U.PORTO

FEUP FACULDADE DE ENGENHARIA
UNIVERSIDADE DO PORTO

Dye-sensitized Solar Cells: Improving Lifetime Stability and Performance

Dissertation presented to the Faculty of Engineering of the University of Porto
for obtaining the degree of
Doctor in Chemical and Biological Engineering
by

José Miguel Lopes Maçaira Nogueira

Adélio Miguel Magalhães Mendes, Full Professor – Supervisor

Luísa Manuela Madureira Andrade Silva, Assistant Researcher – Co-supervisor

Lepabe
Laboratory for Process Engineering,
Environment, Biotechnology and Energy

Department of Chemical Engineering,
Faculty of Engineering, University of Porto, Portugal

2016

Agradecimentos / Acknowledgements

Queria também agradecer aos (muitos!) colegas de trabalho do grupo de investigação "Solar" (LEPABE, FEUP) liderado pelo Prof. Adélio Mendes, cujo trabalho se desenvolve na UPTEC – Centro de Inovação. Este é um grupo ímpar, multidisciplinar e em constante crescimento onde o ambiente descontraído e condições de trabalho são propícias à excelência dos projectos de I&D.

Aos meus amigos da FEUP pelo companheirismo de sempre, pelos bons momentos passados e pela amizade! Ao João Carneiro, Diana Olariu, Ali Emami, João Silva, Paula Dias, João Mendes, Sara Paula, André Santos, André Maia, Marta Pimenta, Ana Duarte, António Leal, Ricardo Teixeira e Isabel Gomes. Aos meus amigos alfacinhas, João Robalo e Joana Do Vale pelos momentos inesquecíveis que passamos nestes anos, pela cumplicidade e amizade! Aos meus amigos de Espinho, Godinho, Hugo, Jonathan, Mário e Miguel. Amigos de sempre e para sempre! Nestes últimos anos a dedicação aos respectivos trabalhos retirou-nos tempo de convívio, mas não o brilho especial de quando nos juntamos.

Um agradecimento especial à minha família. Fazer parte dela é um privilégio e uma responsabilidade. Obrigado pelos momentos especiais, pelos pilares e valores inabaláveis que têm passado de geração em geração. Uma palavra especial ao Jaime e Marisa, pelas tertúlias com vista de mar que duram até de manhã! Obrigado Tio pelas conversas profundas e intensas! Pelas vivências partilhadas! Um obrigado também à Leonor por nos fazeres trabalhar num futuro melhor. Aos meus sogros, Helena Doutel e Luis Costa pelo apoio constante, pela amizade e pelos bons momentos passados.

Aos meus pais, Fernando Nogueira e Maria de Lurdes Maçaira, por serem uma referência de vida, pelo vosso apoio incondicional. Tudo o que sou hoje se deve a vocês. Ao meu irmão, Pedro Maçaira Nogueira, por cresceres comigo, pela cumplicidade, pela personalidade e pelo apoio. Parceiro para a vida!
Por fim, à minha mulher Erica Doutel Costa, o amor da minha vida. Obrigado por seres como és, única! Obrigado por partilhares a tua vida comigo.

A todos que, de uma forma ou de outra, contribuíram para o atingir de mais um objectivo. O meu sincero e humilde obrigado!

To my lovely wife

Preface

In September 2011 Prof. Adélio Mendes (FEUP) challenged me for developing a glass-to-glass laser sealing by applying his idea of what we later named of scan pattern. This technology was applied to dye-sensitized solar cells, and then what became by being an optimization work evolved into my PhD thesis. This dissertation is submitted for the degree of Doctor of Philosophy at University of Porto – Faculty of Engineering (FEUP). The present work was developed in Laboratory for Process Engineering, Environment, Biotechnology and Energy (LEPABE), at the Chemical Department of FEUP, and at the facilities of EFACEC in Maia. The work was supervised by Professor Adélio Mendes and co-supervised Dr. Luísa Andrade from LEPABE–FEUP.

From this PhD work resulted the publication of 5 scientific articles and 1 international patent. 1 more scientific article is under revision.

Contents

Dye-sensitized Solar Cells: Improving Lifetime
Stability and Performance

Chapter 3. Laser Sealed Dye-Sensitized Solar Cells: Efficiency and long term stability analysis

Chapter 4. Temperature Role in the Recombination Reaction on Dye-Sensitized Solar Cells

Chapter 5. Modeling, Simulation and Design of Dye-Sensitized Solar Cells

Chapter 6. High efficient DSC photoelectrode using a SiO_2 scaffold layer coated with a 3 nm TiO_2 film

Abstract

Global energy demand is increasing rapidly and by 2030 it is projected that energy consumption will grow 50 %. The Earth serious environmental problems dictate that there is urgency in use clean, secure and affordable energy sources. Photovoltaic (PV) energy is believed to meet these requirements, but up to now PV technology struggles to economically compete with other energy sources. This work studies dye-sensitized solar cells (DSCs), a technology that promises low cost PV energy generation. In particular it addresses the two main bottlenecks that prevent DSC technology to become a commercial alternative; these bottlenecks are lifetime stability and performance.

Concerning stability, encapsulation was identified as critical to obtain stable DSC devices. A new sealing process was developed based on laser assisted glass frit melting. The feasibility of the laser sealing process is investigated and the operating conditions were optimized for sealing DSCs. The sealed samples were subjected to stringent encapsulation tests according to international standards. Accelerated ageing was used to assess the lifetime stability of the laser sealed DSCs and compared with the devices sealed using common polymer materials. The developed laser assisted sealing allowed studying the temperature effect on DSCs performance, in a wide temperature range between - 5 to 105 ºC. The activation energies for the recombination reaction were determined and its dependence on the semiconductor/electrolyte interfaces discussed.

Phenomenological modelling was used as a simulation tool to assess the two main electrochemical processes that rule the DSC performance: electron transport and recombination. The model was used to describe how transport and recombination influence the solar cell efficiency and the optimum design of the photoelectrode (PE).

Finally, a new PE architecture was developed for increasing DSC efficiency. The new architecture aimed at increasing the specific photoelectrode surface area, the transparency and decreasing electron recombination. The developed PE is made of a mesoporous SiO_2 scaffold layer coated with a TiO_2 film deposited by atomic layer deposition (ALD). The parameters used at the ALD were optimized and the TiO_2 film thickness that originates the most efficient device determined. The new PE architecture was compared with commercial TiO_2 films, and future enhancements in DSC design were discussed.

Resumo

A procura global de energia está a aumentar rapidamente prevendo-se que até 2030 o seu consumo cresça 50 %. Os graves problemas ambientais do planeta reforçam a urgência em encontrar fontes de energia limpas, seguras e economicamente viáveis. Existe a espectativa de que a energia fotovoltaica (PV) possa cumprir estes requisitos, mas até agora esta tem tido dificuldade em competir economicamente com outras fontes de energia. Este trabalho foca-se no estudo de células solares sensibilizadas por corante (DSCs), uma tecnologia que promete produção de energia elétrica a baixo custo. São abordadas em particular as duas principais limitações que impedem que a tecnologia DSC se torne uma alternativa comercialmente viável: estabilidade a longo prazo e eficiência.

No que diz respeito à estabilidade, o encapsulamento das células foi identificado como fundamental para a obtenção de dispositivos DSC estáveis a longo prazo. Foi desenvolvido um novo processo de selagem baseado na fusão de vidro auxiliada por laser. A viabilidade técnica do processo de selagem laser é investigada e as condições de operação otimizadas. As amostras seladas foram submetidas a testes rigorosos de encapsulação de acordo com normas internacionais. De forma a avaliar a estabilidade a longo prazo da solução desenvolvida, foram realizados testes de envelhecimento acelerado em células seladas a laser e em células seladas com o polímero normalmente empregue.

O processo de selagem laser desenvolvido permitiu também estudar o efeito da temperatura no desempenho das DSCs numa gama alargada de temperaturas entre -5 e 105 °C. As energias de ativação para a reação de recombinação foram determinadas e foi analisada a sua dependência das interfaces semicondutor/eletrólito presentes na célula solar.

De forma a avaliar os dois processos eletroquímicos que regem o desempenho das células DSC, transporte e recombinação de eletrões, foi utilizado um modelo fenomenológico como ferramenta de simulação. O modelo foi usado para descrever de que forma os fenómenos de transporte e recombinação eletrónicos influenciam a eficiência da célula solar e o design ótimo do seu fotoelétrodo (PE).

Por fim, foi desenvolvida uma nova arquitetura para o fotoelétrodo de forma a aumentar a eficiência das DSCs. O novo PE visava aumentar a área de superfície

disponível, a transparência e diminuir a recombinação dos eletrões. O PE desenvolvido é constituído por uma camada mesoporosa de SiO_2 cuja superfície interna é coberta por um filme fino de TiO_2 depositado por camada atómica (ALD). Os parâmetros do processo ALD foram otimizados e a influência da espessura do filme de TiO_2 no desempenho DSCs foi estudada e discutida. O novo PE é comparado com filmes de TiO_2 comerciais e foram discutidas implicações futuras no *design* das células DSC.

Abbreviations and Symbols

Abbreviation	Definition	Units
A	active area of the solar cell	m^2
ALD	atomic layer deposition	
AM	air mass	
A_s	specific superficial area	m^2·g^{-1}
BET	Brunauer-Emmett-Teller	
BHJ	Barrett-Joyner-Halenda	
BIPV	building integrated photovoltaics	
c_μ	chemical capacitance	F
C_{CE}	double layer capacitance at the platinum/TCO interface.	F
CE	counter electrode	
C_i	concentration of species i	M
$C_{TCO/EL}$	double layer capacitance at exposed TCO/electrolyte interface	F
Da	dimensionless number (equivalent to Damkölher number)	
D_{eff}	effective diffusion coefficient of electrons	m^2·s^{-1}
D_i	diffusion coefficient of species	m^2·s^{-1}
D_k	Knudsen diffusivity	m^2·s^{-1}
d_p	pore size	m
D_{ref}	reference diffusion coefficient	m^2·s^{-1}
DSC	dye-sensitized solar cell	
d_{SiO_2}	SiO$_2$ nanoparticle diameter	m
E	energy	J
E^0_{redox}	standard redox energy	J
E_a	activation energy	eV
E_{cb}	conduction band energy	J
E_{cbc}	corrected conduction band energy	J
EDS	energy-dispersive X-ray spectroscopy	

E_f	Fermi energy	J
E_f^{eq}	dark equilibrium Fermi energy	J
E_g	bandgap energy	J
EIS	electrochemical impedance spectroscopy	
E^{OC}_{redox}	open circuit redox energy	J
E_{redox}	redox energy	J
F	Faraday constant (F = 96 485,3399 C·mol^{-1})	C· mol^{-1}
FF	fill factor	
FTO	fluorine-doped Tin oxide	
G_i	generation rate of specie i	m^{-3}·s^{-1}
H	Planck constant (h = 6.62606896×10^{-34} J·s)	J·s
HOMO	highest occupied molecular orbital	
I	electric current	A
I_s	incident photon flux	m^2·s^{-1}
J_0	exchange current density at the counter electrode	A·m^{-2}
J_i	current density of species i	A·m^{-2}
J_{rec}	recombination current	A·m^{-2}
J_{sc}	short circuit current density	A·m^{-2}
k_B	Boltzmann constant	J·K^{-1}
k_r	recombination reaction rate constant	m$^{-3(1-\beta)}$·s^{-1}
l	position coordinate in the SiO$_2$ mesoporous layer	m
LAGF	laser assisted glass frit	
L_f	thickness of the DSC mesoporous layer	m
L_n	electrons diffusion length	m
LUMO	highest unoccupied molecular orbital	
MFC-C	N$_2$ flowrate in ALD vacuum chamber	cm^3·s^{-1}
MFC-R	N$_2$ flowrate in ALD reactor	cm^3·s^{-1}
N_{CB}	effective density of states in the TiO$_2$ conduction band	m^{-3}
n_{eq}	dark equilibrium electron density	m^{-3}
NHE	normal hydrogen electrode	

n_i	density of specie i	m^{-3}
N_i	number of moles of specie i	mol
NP	nanoparticles	
n_{ref}	reference particle density	m^{-3}
P	pressure	atm
PCE	power conversion efficiency	%
PE	photoelectrode	
PV	photovoltaic	
q	elementary charge ($q = 1.60217646 \times 10^{-19}$ C)	C
Q_{frit}	quality of the glass frit sealing	
Q_i	flux of specie i	m^{-3}·s^{-1}
R	ideal gas constant ($R = 8.314472$ J·K^{-1}·mol^{-1})	J·K^{-1}·mol^{-1}
R_c	contact and wire series resistances	Ω
R_{ce}	charge-transfer resistance at the counter electrode	Ω
R_{ext}	load parameter: external resistance	Ω
R_i	recombination rate of species i	m^{-3}·s^{-1}
R_k	electron recombination resistance	Ω
R_p	shunt resistances	Ω
R_{series}	external series resistances	Ω
R_{TCO}	transparent conductive oxide sheet resistance	Ω
$R_{TCO/EL}$	charge transfer resistance at exposed TCO/electrolyte interface	Ω
R_w	electron transport resistance	Ω
SEM	scanning electron microscopy	
STP	standard conditions of temperature and pressure (273.15 K, 10^5 Pa)	
T	temperature	K
t	time	s
TCO	thin conductive oxide	
T_g	transition temperature	K
TIP	titanium isopropoxide	

$t_{purge,i}$	ALD purge time of component i	
T_s	softening temperature	K
UV	ultra-violet	
V_{cb}	conduction band potential	V
V_{cbc}	corrected conduction band potential	V
V_{ext}	external cell potential	V
V_f	fermi level potential	V
V_{int}	internal cell potential	V
V_{oc}	open-circuit potential	V
wt.	weight	
X	position coordinate in the TiO_2 mesoporous layer	m
X	coded factors for the design matrix of the DOE	
X_f	coverage factor of SiO_2 porous layer with TiO_2 film	%
Z'	real part of impedance	Ω
Z''	imaginary part of impedance	Ω
Z_d	Warburg element of the Nernst diffusion of I_3^- within electrolyte	Ω

Greek symbol	**Definition**	**Units**
γ	coordinate of shrinking core position	m
α	wavelength-dependent absorption coefficient	m^{-1}
β	recombination reaction order	
Δt_i	ALD pulse time of component i	s
ΔV_{cb}	shift in the conduction band potential, V	V
ΔV_{int}	variation of the applied potential, V	V
ε	porosity	
ζ	symmetry coefficient	
η	solar to energy conversion efficiency	%
η_{inj}	electron injection efficiency	%
η_{Pt}	electrochemical overpotential at Pt electrode	V
θ	dimensionless time variable	

λ	wavelength	m
ξ	tortuosity	
ρ_i	molar density of specie i	$mol \cdot m^{-3}$
τ_{e^-}	electron lifetime	s
τ_{min}^p	minimum time required for the full coverage SiO_2 porous layer with TiO_2 film	s
τ_{tr}	electron transport time	s
φ	dimensionless number	
ϕ	dimensionless number (Equivalent to Thiele modulus)	
ψ	thermal expansion coefficient	$°C^{-1}$

Superscript	Definition
*	dimensionless variable
0^-	external point of the current collector
0^+	xx coordinate close to the photoanode
init	initial conditions
p	pulse
t	total

Subscripts	Definition
c^+	cations
CB	conduction band
CE	counter electrode
e^-	electrons
ht	high temperature
I^-	iodide
I_3^-	triiodide
lt	low temperature
MPP	maximum power point
OC	open-circuit
SC	short-circuit
VB	valence band

CHAPTER 1

Introduction

"The stone age didn't end because they ran out of stones."

Unknown author

Introduction

World energy consumption will increase 56 % before 2040 driven by the economic growth and increasing population in developing countries and in emerging economies such as China and India[1] – Figure 1.1. Relatively high oil prices, as well as concerns about the environmental impact of the fossil fuels combustion and strong government incentives, have made the harvest of energy from renewable sources the fastest growing energy source according to the International Energy Outlook of 2013[1].
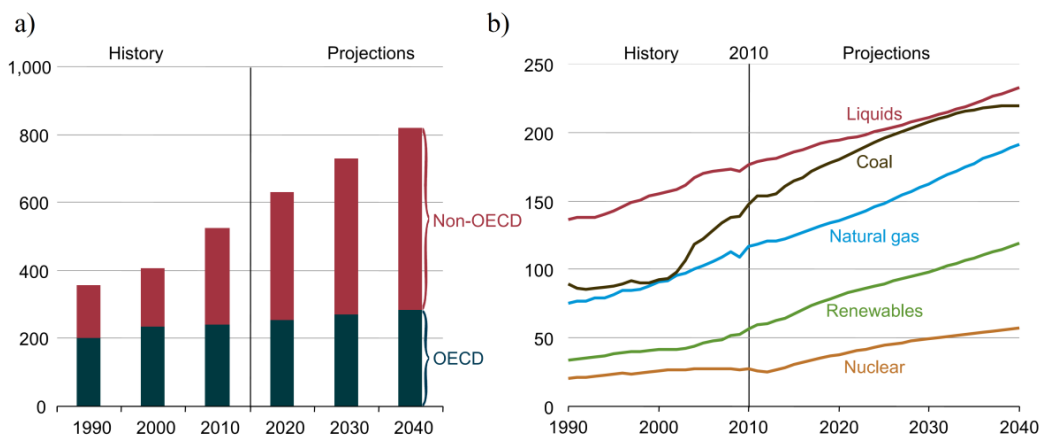
Figure 1.1 a) World total energy consumption in OECD and non-OECD countries and b) by fuel type, from 1990 with projections to 2040 (ordinate scale in quadrillion Btu, equivalent to TJ) (adapted from International Energy Outlook 2013[1])

The total energy generation from renewable sources has increased 2.5 % per year and it is expected to grow from 19 %, recorded in 2008, to 28 % in 2040[1] – Figure 1.2b). In particular, solar energy is the fastest growing segment of technologies for harvest energy from renewable sources and photovoltaic (PV) market is expected to grow up to 450 GW of installed capacity until 2019, according to the global market outlook for solar power[2] – Figure 1.2.
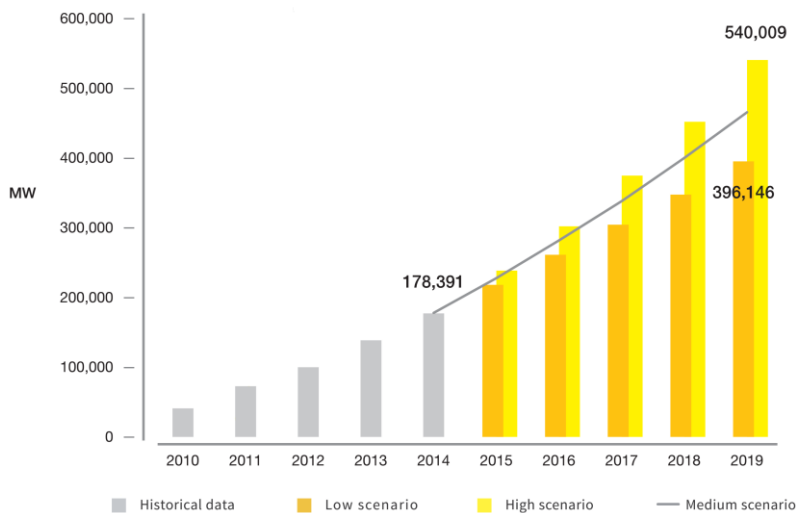
Figure 1.2 Solar PV cumulative market scenarios until 2019 (adapted from Global market outlook for solar power 2015-2019 [2])

Solar energy is the most abundant renewable energy source, and undoubtedly can be regarded as safe, inexhaustible and reliable at a human scale. The total solar power available to the planet Earth exceeds by a factor of 1500 the total human power consumption[3]. There is huge economic potential in solar energy; however, it is highly dependent on the cost of PV devices. Obviously the PV market evolution will make use of the most competitive solar panels at the time, most likely the first generation crystalline and polycrystalline silicon solar panels (c-Si). These devices at lab scale can achieve up to 25 % sun to power conversion efficiency (PCE, η) and their recent progressively lower prices reflects its industrial establishment that, undoubtedly, makes use of the today's semiconductor industry infrastructures. However, the high production and environmental costs led to a constant progress in the development and establishment of new PV technologies (Figure 1.3) aiming to avoid the drawbacks of

the c-Si solar panels. Some established semiconductor based technologies comprise gallium arsenide tin film solar cells (GaAs, $\eta \approx 24$ %), copper-indium-gallium-(di)selenide (CIGS, $\eta \approx 20$ %), cadmium-telluride (CdTe, $\eta \approx 17$ %) and amorphous/nanocrystalline silicon ($\eta \approx 10$ %) solar cells[4]. This second generation of thin film technologies have had an important role in the PV installation capacity up to now[5]. However, they share the same performance and cost limitations as conventional Si devices. After approximately 20 years of research and development, third generation thin film solar devices are starting to emerge in the marketplace. This new generation of photovoltaic systems includes semiconductor quantum dots (QDPV, $\eta \approx 6 - 10$ %)[6], organic semiconductors (OPV, $\eta \approx 10$ %)[4, 7] and dye sensitized solar cells (DSCs, $\eta \approx 14$ %)[8]. These new technologies benefit from their low processing costs and environmental impact and thus short payback time when compared to the conventional solar devices. At present stage, third generation PV technologies are still far behind the efficiency values of the conventional Si-based solar cells (~ 20 %); nevertheless, the promise of low processing costs and usage of available environmental-friendly raw materials make them subject to an intensive research and development.
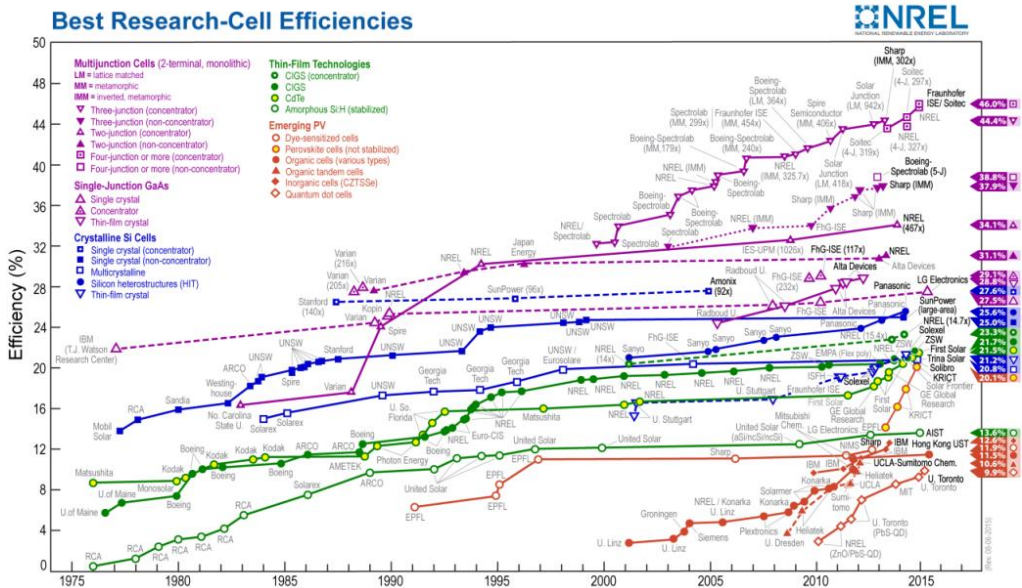
Figure 1.3 Best research solar cell efficiencies (courtesy of the National Renewable Energy Laboratory, Golden, CO[9]).

Dye sensitized solar cells (DSCs) present themselves as a very promising photovoltaic technology. They are made of cheap components that are non-toxic and world-wide available and offer distinctive features such as semi-transparency, multi-colour range possibilities, flexibility and lightweight applications, but also good performance under low light conditions and different solar incident angles[10-12] – Figure 1.4. These unique characteristics open a new possibility of applications and markets where conventional solar devices will never be able to penetrate, *e.g.* low-power consumer electronics, outdoor or indoor recreational and building integrated photovoltaics (BIPV) applications. In fact, the DSC technology has recently been used by several companies in showcase applications by Glass2Energy, DyePower, Solaronix, Sony, Fujikura, Panasonic, G24i, Dyesol, 3G Solar and Toyota-Asin.

Figure 1.4. Glass façade composed by 300 m^2 of dye-sensitized solar cells demonstration modules in EPFL's SwissTech Convention Center, Lausanne, Switzerland (adapted from[13]) .

However, for the DSC technology to become a competitive alternative to the present PV technologies, major breakthroughs are necessary mainly concerning the two critical aspects of any PV device: power conversion efficiency and lifetime.

Regarding the device lifetime, at least 25 years of constant power conversion efficiency should be guaranteed for outdoor applications. This aspect has caught researchers' attention in order to enhance DSCs' stability and thus many reports are being published concerning improvements on the stability and new sealing methods[14-19]. Then, several methods were proposed to enhance the efficiency of DSCs[20-23], being one of the most promising the use of nanostructured materials as photoelectrodes to enhance light harvesting and charge extraction to improve photocurrent, photovoltage and fill factor.

1.1 Dye Sensitized Solar Cells: Operating principles & State of the art

In 1991 O'Regan and Grätzel proposed the first bulk heterojuntion photoelectrochemical solar cell with 7 % power conversion efficiency, taking advantage of the three-dimensional TiO_2 photoelectrode film and using a ruthenium dye as sensitizer[24]. DSCs mimic natural photosynthesis and differ from conventional p-n junction devices because light collection and charge transport are separated in the cell. Light absorption occurs in the chemisorbed sensitizer molecule, while electron transport occurs in the semiconductor TiO_2 - Figure 1.5.
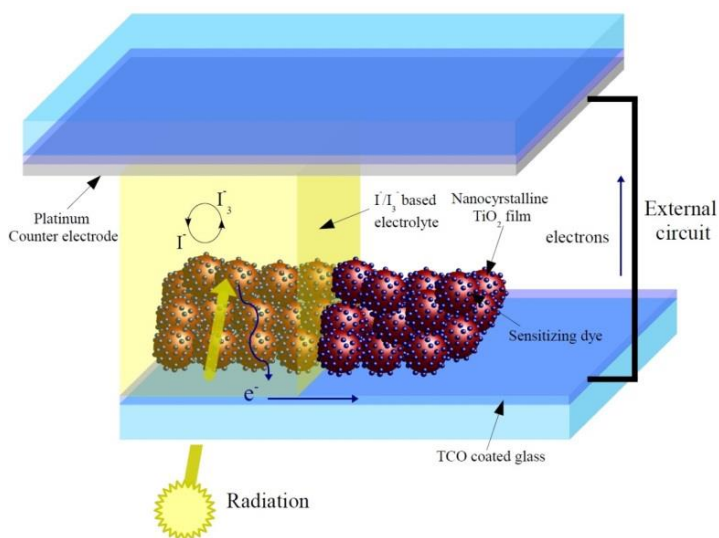
Figure 1.5. Representation of the working principles of DSCs.

The photoelectrode is a mesoporous oxide layer composed of nanometer-sized particles. Attached to the surface of the oxide is a monolayer of dye responsible for light absorption. The optical absorbance that occurs in the dye molecules results in excitation of an electron from the highest occupied molecular orbital (HOMO) to the lowest unoccupied molecular orbital (LUMO)[25]. The photogenerated electrons are transferred to the conduction band of the semiconductor oxide and percolate through the semiconductor network, being collected at the transparent conducting oxide. The oxidized dye is regenerated by electron donation from the electrolyte solution containing a redox couple, typically of iodide/triiodide. The triiodide ions formed in the semiconductor's surface during the redox reaction diffuse to the Pt-catalyzed counter-electrode, where they are reduced back to iodide by the electrons from the external circuit. The efficiency (η) of the solar cell is determined by its current-voltage characteristics, specifically the open-circuit photovoltage (V_{oc}), the photogenerated current density measured under short-circuit conditions (J_{sc}), light irradiance (I_s) and the fill factor of the cell (FF), which depends on the series resistances and on the shunt resistances in the cell[26] :

$$\eta = \frac{J_{sc}V_{oc}}{I_s}\text{FF}$$

(1.1)

The short-circuit photocurrent (J_{sc}) is essentially related to the amount of sunlight harvested in the visible part of the solar spectrum by the sensitizer. Consequently, dye molecules play a critical role in photon capture and for this reason the progress in DSCs have been closely followed by the constant development of new porphyrin and organic sensitizers that have high extinction coefficients and broader optical absorption spectra. These have even supplanted the commonly used Ru(II) polypyridil sensitizers in liquid but also in solid-state electrolyte DSCs[14, 20, 27-35].

The open-circuit voltage (V_{oc}) is related to the energy difference between the quasi-Fermi level of electrons in the semiconductor and the chemical potential of the redox mediator in the electrolyte[36]. The most common electrolyte in high performance DSCs uses the triiodide/iodide (I_3^-/ I^-) redox couple[27,37,38]. Despite the excellent results achieved so far using this redox couple, it presents some drawbacks such as the corrosion of several current collectors and partial absorption of visible light around 430

nm, resulting in a voltage loss[39]. To mitigate these effects several alternatives have been studied[35, 40-43]. Good results have been reported using an amorphous organic hole-transport material (HTM), spiro-OMeTAD (2,2',7,7'-tetrakis(N,N-di-p-methoxyphenyl-amine)9,9'-spirobifluorene)[44] and cobalt based (Co (II/III) tri(bypiridyl)) non-corrosive electrolyte. These new hole transport materials yielded impressive results, reaching PCEs higher than 14 % and V_{oc} of 1 V for liquid-state DSCs and 7.2 % and 965 mV for solid-state devices [8,20,45-50]. Other materials like processable p-type direct bandgap $CsSnI_3$ semiconductor have been used very recently for hole conduction, aiming to replace the liquid iodide/triiodide based electrolyte. This hole conductor yielded record efficiencies of 8.5 % for solid state DSCs[51]. A very interesting and underexplored class of materials of organometallic halide pervoskite have also been used as sensitizers in liquid electrolyte-based photoelectrochemical cells with conversion efficiencies from 3.5 to 6.5 %[52, 53]. These materials provide excellent support for binding organic and inorganic components to form a molecular composite that not only acts as a sensitized, but also as a hole and electron conductor. Recently $CsSnI_3$ perovskite was shown to be an efficient hole conductor in a solid state DSC achieving 8.5 % efficiency[51]. Another specific perovskite, a methylamonium lead iodide chloride ($CH_3NH_3PbI_2Cl$), was used as the light absorbing material in conjunction with TiO_2 as transparent n-type component and spiro-OMeTAD as p-type hole conductor. The device achieved 8 % efficiencies[54]. Interestingly, the authors found out that by replacing the TiO_2 by an insulating framework of Al_2O_3 the power to conversion efficiency was improved to almost 11 %. Apparently the perovskite material employed is a much better electron conductor than the TiO_2, and the Al_2O_3 only acts as a "scaffold" to support and provide surface area for the perovkite to be coated on. Other record-breaking work proposed an innovative platform that includes a three dimensional nanocomposite and bilayer architecture with an inorganic-organic hybrid heterojuntion[55]: the use of TiO_2 /$CH_3NH_3PbI_3$ /polymeric HTMs / Au system boosted efficiencies of solid state perovskites solar cells up to 20 %. Although this devices have very high efficiencies, they have not yet proven stable enough for commercialization[56].

The main processes in a DSC system are light absorption, charge injection, electron transport and collection and electrolyte diffusion. Since 1991 most of the improvements in DSCs efficiency have been achieved through major improvements in molecular sensitizers and redox electrolytes[57]. However, directly or indirectly all of above mentioned phenomena strongly depend on the photoelectrode. In particular, the two competing processes that rule the performance of a DSC are electron transport in the mesoporous semiconductor and recombination losses in the semiconductor/electrolyte interface[58]. Both effects have been widely studied mainly using electrochemical impedance spectroscopy (EIS) but there are challenges that still remain particularly in the photoanode[36,59-66]. Consequently new photoanode structure models are needed to suppress electron recombination and to enhance light harvesting but keeping the cell's transparency characteristics.

The ideal photoelectrode should have a high surface area to ensure high dye loading and efficient light harvesting. Even though a greater amount of electrons are photogenerated, there is also a higher probability of electrons to recombine in the interface semiconductor/electrolyte – dark current – since the pathway to get the current collector is also higher. Thus, the electron transport in the photoelectrodes plays a very important role in the electron collection efficiency since it directly influences the dark current[67]. The electron transport is essentially governed by a diffusion mechanism and it is controlled by hoping phenomena limited by the low conductivity of TiO_2 nanoparticles and their multiple grain boundaries[68]. Good electrolyte diffusion should also be guaranteed in the photoelectrode; however liquid electrolytes tend to have low viscosities, so its diffusion in the photoelectrode should not be a performance-limiting process in DSCs.

Researchers have proposed several strategies to address the transport limiting process, such as using bare 1-D nano-structures composed by TiO_2, SnO, or ZnO to increase electron mobility in the photoelectrode[69,70]. Although these structures provide direct pathways for electrons to reach the collecting substrate, the inefficient dye adsorption of this type of structures do not generate enough electrons to produce high photocurrents. A common-sense development was to mix high surface area nanoparticles with high conductive 1-D structures and create hybrid photoelectrodes[71],

in a way they can benefit from the advantages of each structure. Other approach consists in creating hierarchically ordered photoelectrodes with large aggregate particles composed by smaller ones[72-74]; this strategy aims to achieve high surface areas, guaranteed by small particles, and efficient electrolyte diffusion, provided by macropores created by the larger aggregates. These photoelectrodes benefit from a good light scattering effect, resulting in high performance devices. Another interesting approach was to use highly conductive host backbones to serve as charge extraction support to the high surface area nanoparticles[21,75,76]. The idea of having a 3-D TCO collecting substrate has great potential because, if carefully optimized, it should be able to create a DSC where every generated electron can be collected. Following this idea of increasing the photoelectrode conductivity, graphene has also been used in DSCs[77-81]. Benefiting from its high electrical conductivity and having a work function close to the one of TiO_2 (4.42 - 4.5 eV *vs*. 4.5 eV, respectively), graphene should enhance electron mobility and extraction in DSCs. These various approaches are described and discussed below.

1.2 Nanostructured photoelectrodes

Nano science has opened the door to the development of new nanostructured materials and concepts that were not available before[82-85]. Nanostructures such as nanoparticles[83,86,87], nanowires[88-92], nanotubes[88,89,93-96], nanorods[97-99] and nanobelts[100] have been developed in the last decade for use in an array of applications in electronics, sensor devices, optoelectronics, photovoltaic and photocatalysis[84]. Nanomaterials can have very high specific surface areas even up to several hundred of $m^2 \cdot g^{-1}$ [101,102]. Photoelectrodes of nanomaterials allow the adsorption of a large amount of sensitizer molecules in a monolayer configuration; the dye coated area relates to the photocurrent generated by the DSC device. Nanosize materials also affect the way electrons are transported through the photoelectrode structure. Unlike p-n junction solar cells, in DSCs there is no macroscopic electrostatic potential gradient in the film, fact caused by the small size of the individual colloidal particles and by the presence of concentrated electrolytes. This means that in the nanoparticle film the governing

electron transport process is diffusion, contrary to the drift process seen in p-n junction solar cells for carrier separation in the presence of an electrical field[25,103].

The most common material found in DSC's photoelectrode is anatase TiO_2. This commercial metal oxide has typically surface areas between 40-100 m^2 and an electric resistivity in the order of 1 to 10^2 $\Omega \cdot cm$ [104, 105].

1.2.1   Electron transport in nanostructured photoelectrodes

The typical electron diffusion coefficient in TiO_2 nanoparticle film, 5×10^{-5} $cm^2 \cdot s^{-1}$, is found to be several orders of magnitude below single crystal (bulk) values[106-108]. The higher electron mobility and diffusion coefficients in single crystals are related to their higher electron concentrations (caused either by illumination or application of external voltage)[67,109]. The values determined for the electron diffusion coefficients point out the fact that diffusion is much slower in nanostructured materials than in single crystals; this is related to the multicrystalline nature of these structures that creates electron traps and consequently limit the lifetime of the excited electrons[67]. Although still subject of some debate[67,110,111], it is generally accepted that electron transport occurs by the combination of two phenomena: percolation through a network of sites and thermal accessibility to energy states. Therefore, morphological parameters such as porosity, surface area, pore size, particle diameter, shape and elemental crystal size and orientation within the nanostructures have an important impact on the electron diffusion coefficient but also in the energetic properties of the material, such as the distribution of trap energy or electronic concentration.

The electron transport and recombination properties can be studied by several techniques, including photocurrent/photovoltage transient techniques[112,113], intensity modulated photocurrent spectroscopy (IMPS)/intensity modulated photovoltage spectroscopy (IMVS)[106,114] and by electrochemical impedance spectroscopy (EIS)[59,115]. In particular EIS is a powerful technique for investigating the kinetic processes of DSCs. Electron transport and chemical potential in the semiconductor film, electron recombination in the photoelectrode/electrolyte interface, charge transfer at the counter electrode and the diffusion of the redox species in the electrolyte can be well distinguished based on the impedance response of the system as a function of

frequency. Compared to the other techniques, EIS has the potential to allow obtaining most parameters that reflect the kinetic processes of the device. Making use of the Nyquist plots, the impedance data is fitted by an adequate equivalent circuit and the electron transport and recombination properties parameters are estimated. From these experiments three main parameters can be obtained: the recombination resistance, R_k, transport resistance, R_w and chemical capacitance of the semiconductor C_μ. In this way the electron diffusion length, L_n, and the electron lifetime, τ_{e-}, can be determined by using the following equations[65]:

$$\tau_{e-} = R_k C_\mu \tag{1.2}$$

$$L_n = L_f \sqrt{\frac{R_k}{R_w}} \tag{1.3}$$

$$L_n = \sqrt{\tau_n D_{eff}} \tag{1.4}$$

where D_{eff} is the electron diffusion coefficient and L_f is the semiconductor film thickness. Combining eq.(1.2) and eq.(1.3) the effective diffusion coefficient of electrons in the semiconductor can be determined by:

$$D_{eff} = \left(\frac{R_k}{R_w}\right)\left(\frac{L_f^2}{\tau_n}\right) \tag{1.5}$$

Using the electron diffusion coefficient the electron transport time, τ_{tr}, can be determined by[116,117]:

$$\tau_{tr} = \frac{L_f^2}{D_{eff}} \tag{1.6}$$

This value indicates for how long an electron can percolate through the semiconductor before recombining with electrolyte. Before the electrons can be collected at the FTO substrate there is the possibility of recombination with the electrolyte, so an electron collecting rate at the FTO substrate should be defined[20]. Based on the two processes that rule the performance of a DSC, recombination and transport, a collection efficiency, η_{cc}, can be determined by[118]:

$$\eta_{cc} = \frac{\left[-L_n\alpha \cosh\left(\frac{L_f}{L_n}\right) + \sinh\left(\frac{L_f}{L_n}\right) + L_n\alpha e^{-\alpha L_f}\right] L_n\alpha}{\left(1 - L_n{}^2\alpha^2\right)\left(1 - e^{-\alpha L_f}\right) \cosh\left(\frac{L_f}{L_n}\right)} \tag{1.7}$$

where α is the photoelectrode film absorption coefficient.

1.2.2 1-D nanostructures

Considerable attention has been given to the fact that morphological features can have a clear impact in the performance of photoelectrodes in dye-sensitized solar cells, mainly in the electron transport effectiveness and the electron recombination with electrolyte. Particular interest is given to 1-D nanostructures that are believed to improve electron transport by providing direct pathways throughout the structure of the photoelectrode to the collecting substrate. The so-called 1-D structures include nanotubes, nanowires and nanofibers that can be composed by several metal oxide materials such as TiO_2 ZnO or SnO_2[69,70]. Generally, these materials have higher diffusion coefficients than non-ordered nanostructures and are meant to give electron diffusion lengths larger than film thickness. These structures can be used directly as photoelectrodes with dye molecules adsorbed in their surface – Figure 1.6 a) – or by adding metal oxide nanoparticles to the 1-D structure – Figure 1.6 b). Table 1.1 presents the diffusion coefficients as well as the corresponding cell performance characteristic values for several DSCs produced with photoelectrodes based on 1-D nanostructures. The values presented in Table 1.1 show that 1-D nanostructures present higher values of diffusion coefficients than nanoparticle based structures, meaning that generated electrons can move and reach the collecting substrate faster. However the overall DSC performance is far from the ones obtained using the conventional TiO_2 nanoparticle film. This is mainly attributed to the comparatively low internal surface area available for the adsorption of dye molecules.
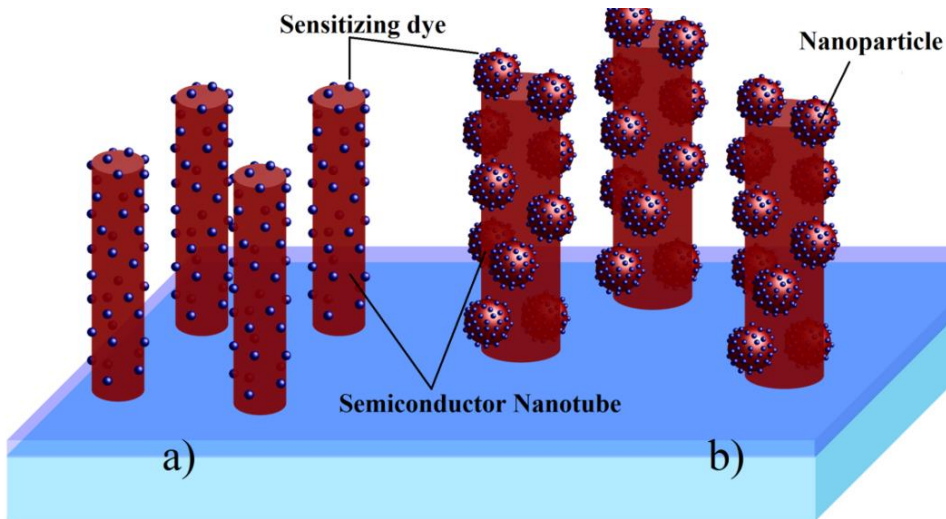
Figure 1.6 a) Schematic of 1-D nanostructures with sensitizing dye adsorbed on the surface; b) 1-D nanostructures decorated with semiconductor nanoparticles.

Table 1.1 1-D nanostructured DSC performance values and electron diffusion coefficients.

1-D Nanostructure	Ref.	Cell performance				Diffusion coefficient
		η / %	J_{sc} / mA·cm^{-2}	V_{oc} / mV	FF	D_{eff} / cm^2·s^{-1}
N719 TiO$_2$ NP	[119]	5.00	11.3	670	0.660	7.2×10^{-5}
Mercurochrome-sensitized ZnO nanowire	[119]	0.84	3.40	500	0.490	1.8×10^{-3}
Mercurochrome-sensitized ZnO nanowire/ NP composite	[119]	2.20	6.30	610	0.580	2.1×10^{-4}
TiO$_2$ NP/nanotubes, 10 wt. %	[71]	3.10	8.33	630	0.600	7.1×10^{-4}
TiO$_2$ nanorods	[120]	0.56	2.22	575	0.440	3.3×10^{-7}
TiO$_2$ nanorods coated with ZnO nanoparticles	[120]	0.83	3.57	545	0.430	8.0×10^{-6}
TiO$_2$ nanorods coated with TiO$_2$ nanoparticles	[120]	0.19	0.71	592	0.470	4.3×10^{-6}

Kang *et al.*[121] were one of the first authors to report good performance values with semi-transparent DSCs using a photoelectrode composed only by nanotubes. They produced nanotube arrays with external diameter of 295 nm, tube lengths of 6–15 μm and wall thickness of 21–41 nm, respectively – Figure 1.7. The incorporation of this material in a DSC configuration exhibited a V_{oc} of 610 mV, a J_{sc} of 8.26 mA·cm^{-2} and a fill factor of 0.70, giving an overall power conversion efficiency of 3.5 %. Although

these results are an improvement for nanotube-based DSC photoelectrodes, the TiO_2 nanoparticle-based DSCs still presents higher performance. As mentioned earlier, the low surface area of these types of 1-D nanotube arrays can explain the relatively low efficiency of the corresponding DSC devices.
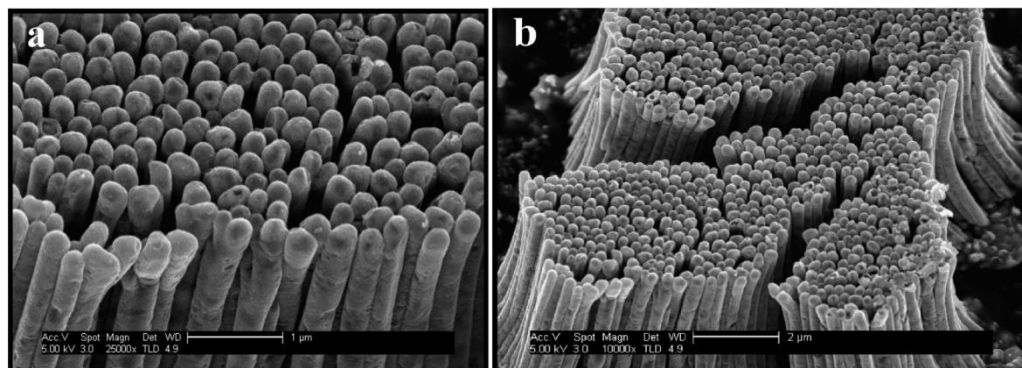
Figure 1.7 Field emission-SEM images TiO_2 nanotubes [121].

To overcome the low surface area that 1-D nanostructures have compared with nanoparticle films, some researchers combined both structures in order to take advantage of the benefits of each of them[122,123]. Gan *et al.*[123] created a hybrid structure combining vertically aligned ZnO nanowires (NW) with TiO_2 nanoparticles (NP) attached. ZnO has similar band gap of 3.2 eV[124] but electron mobility up to two orders of magnitude higher than TiO_2: $(0.1 - 4)$ $cm^2 \cdot (V \cdot s)^{-1}$ *vs.* 65 $cm^2 \cdot (V \cdot s)^{-1}$ at 25 ºC, respectively[70,105, 125-127]. This makes ZnO a particularly interesting metal oxide to compete with TiO_2 in DSCs. The high value of D_{eff} of ZnO NW – based DSC substantiates that the electrons injected from excited dye molecules can travel faster and therefore are collected more efficiently - Figure 1.7. However, the low value of J_{sc} in the bare ZnO electrode confirms the low surface area of these 1-D aligned nanostructures. Incorporating TiO_2 NPs with inherent high surface areas in the ZnO nanowires, an increase in the current density from 1.60 to 3.54 $mA \cdot cm^{-2}$ was obtained by these authors. The hybrid cell revealed a D_{eff} value of 6.92×10^{-4} $cm^2 \cdot s^{-1}$ that falls between those of the bare ZnO film $(2.8 \times 10^{-3}$ $cm^2 \cdot s^{-1})$ and the TiO_2 NP electrode $(\approx 5 \times 10^{-5}$ $cm^2 \cdot s^{-1})$ – Table 1.2. Actually, it is almost fifteen times larger than the D_{eff} of TiO_2 NP film, showing that the hybrid electrode combines the advantages of both structures:

improved electron transport along the vertically aligned nanowire array and increased surface area provided by the TiO_2 NP. Nevertheless, the performance of the hybrid cell (2.2 %) is still far from the nanoparticle-based DSC (5 % in Table 1.1), mainly because the surface area provided by the hybrid solution is still low compared to a similar thickness film constituted only by nanoparticles. This fact was caused by the low coverage of the nanowires with nanoparticles as shown in Figure 1.8 and Table 1.2, as well as the low thickness of the hybrid photoanode (3 μm). Nonetheless, better results can be expected if an optimization is performed to balance the ratio between the vertically aligned structures and the quantity of nanoparticles attached to their surface.
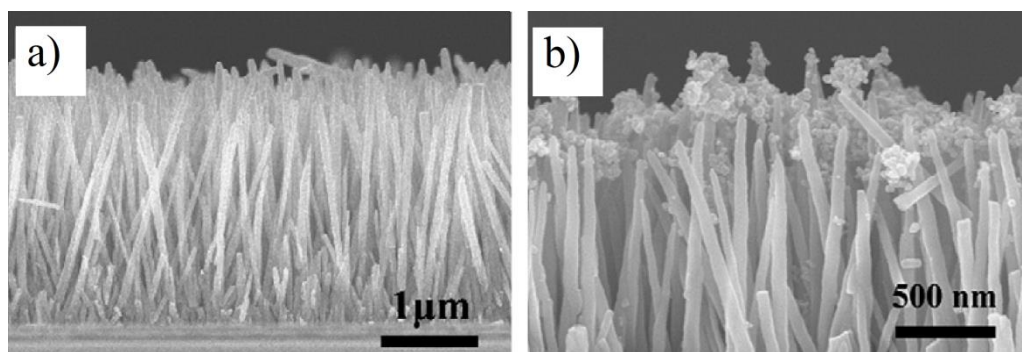
Figure 1.8 SEM images of vertically aligned nanowires: (a) without and (b) with NP attached to its surface [123].

Table 1.2 DSC performance parameters and diffusion coefficients, correspondent to devices using the photoelectrodes presented in Figure 1.8**.**

Electrode	J_{sc} mA·cm^2	V_{oc} / mV	FF	η / %	τ / ms	D_{eff} / cm^2·s^{-1}
TiO_2 NP						2.52×10^{-5}
ZnO NW	1.60	610	0.40	0.390	84.0	2.80×10^{-3}
ZnO NW/TiO_2 NP	3.54	600	0.37	0.790	57.3	6.92×10^{-4}

A common strategy to achieve high electron mobility but also high surface area is blending 1-D nanostructures, such as TiO_2 nanotubes, with TiO_2 nanoparticles; this way the photoelectrode can benefit from both the high conductive 1-D nanostructure and from the high surface area available for dye adsorption – Figure 1.9.
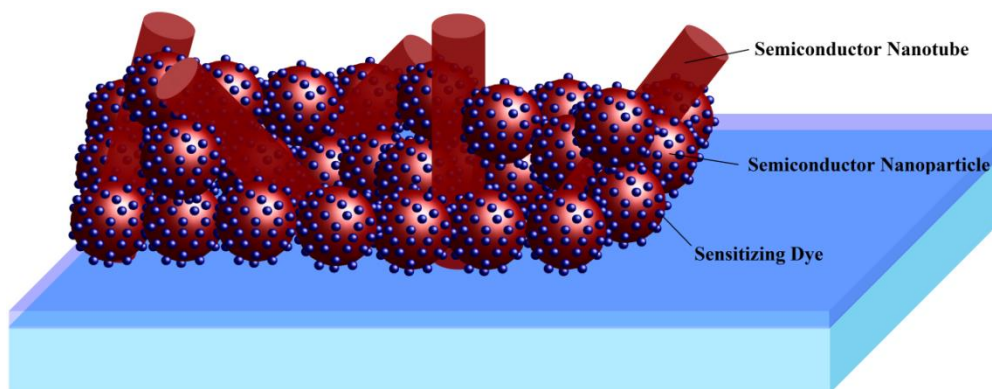
Figure 1.9 Schematic of 1-D nanostructures blended with metal oxide particles.

Zhong *et al.*[71] showed that it is possible to increase the photovoltaic performance of DSCs by blending different concentrations of TiO_2 nanotubes into a TiO_2 mesoporous film. These authors blended anodic TiO_2 nanotubes with different concentrations into a P25 based TiO_2 mesoporous film and studied the electron transport properties of the film and the recombination phenomena by electrochemical impedance spectroscopy – Figure 1.10. Although this study uses a low performance TiO_2 reference electrode (0 wt. % of nanotubes) it provides complete EIS data allowing to withdraw important conclusions about the use of nanotubes in DSC photoelectrodes.
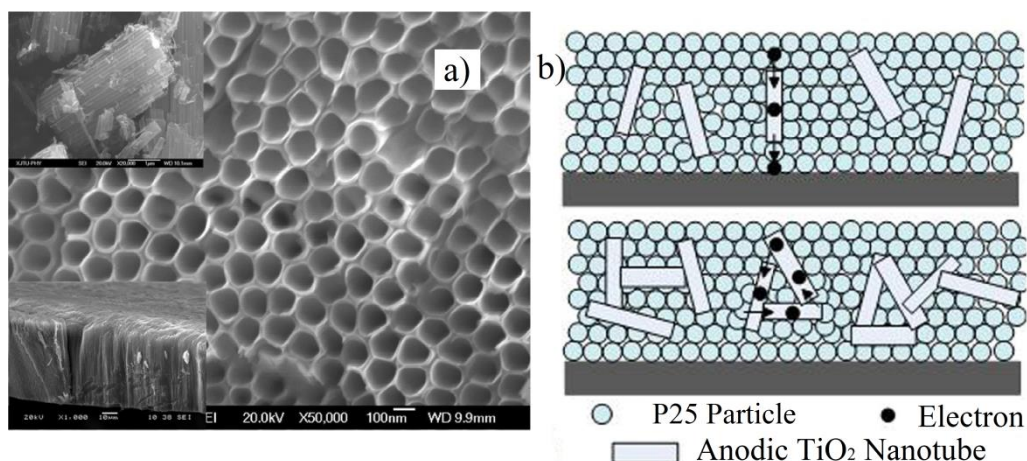
Figure 1.10 (a) SEM micrograph of nanotubes sinthetized by Zhong *et al.*[71]; (b) Schematic diagram of the electron transport in the hybrid TiO_2 film.

The same authors optimized the concentration of nanotubes blended in the photoelectrode film, increasing electron transport and slowing the electron recombination. Figure 1.11 presents the electron properties of DSCs with different nanotube concentrations. There is a correlation between the device's efficiency and the electron diffusion coefficient, electron diffusion length and ultimately with the electron collection efficiency. The interpretation of the diffusion length, L_n, reflects the main phenomena occurring in DSCs: the electron transport and electron recombination. For a nanotubes concentration of 10 wt. %, η and D_{eff} present maximum values. For a blending level of 10 wt. % nanotubes dispersed in the TiO$_2$ particles supply shorter paths for electron transport than the disordered interconnected TiO$_2$ nanoparticles. For a 30 wt. % nanotubes concentration, the decrease in the device efficiency is followed by the decrease of the electron diffusion coefficient and electron diffusion length due to the increase of the electron transport time. So, in this specific case, the concentration of TiO$_2$ nanotubes might be acting as trap centers that difficult transportation to FTO substrate. Although the TiO$_2$ nanotubes are more conductive than TiO$_2$ nanoparticles, above a certain concentration the increase of nanotubes does not result in higher electron diffusion coefficients in the film. For concentrations higher than 30 wt. %, the electron lifetime increases even though the global efficiency of the device decreases. In fact, the ratio between electron lifetime and transit time becomes constant, meaning that the recombination resistance decreases at the same level of the transport resistance increases; thus the electron diffusion length remains approximately constant. Therefore, the low photocurrent density explains the efficiency decrease since the inclusion of nanotubes above 30 wt. % strongly diminishes the available surface area for dye adsorption.
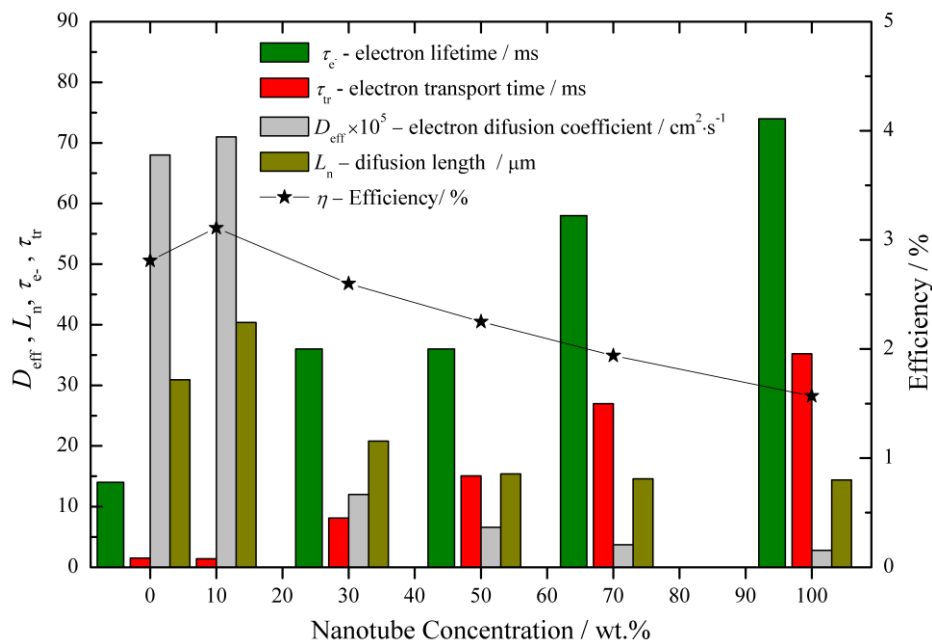
Figure 1.11 Electron transport properties and DSC performance value of DSCs with different nanotube concentrations (adapted from[71]).

1.2.3 3-D hierarchically ordered nanostructures

The key aspects of a photoelectrode structure are large surface area, necessary to ensure high loading of dye molecules that will generate electrons, and sufficiently large pores with excellent interconnectivity for efficient electrolyte diffusion. Additionally, the defect level and the number of particle boundaries must be low to suppress electron loss by recombination with the electrolyte and allow a good electron transport to the collecting substrate. However, in a standard TiO_2 nanostructure high surface area and large pores are not compatible. Even if an increase of the surface area is important to adsorb a great amount of dye, it simultaneously decreases the average pore size, thus limiting the diffusion of the redox species in the nanostructure. As stated before, 1-D vertically aligned structures solve the electron transport issue and facilitate the electrolyte diffusion throughout the photoelectrode, but do not ensure enough dye loading that could result in high performance devices. This way, 3-D hierarchical pore structures are very interesting as they have several scales of pores. Indeed, such

materials are of great interest as they provide high surface areas and large pore sizes at the same time: nanometer pores that ensure high amount of adsorbed dye molecules - Figure 1.12 (II) – and large micro or mesopores that allow fast electrolyte diffusion - Figure 1.12 (I)[72-74].
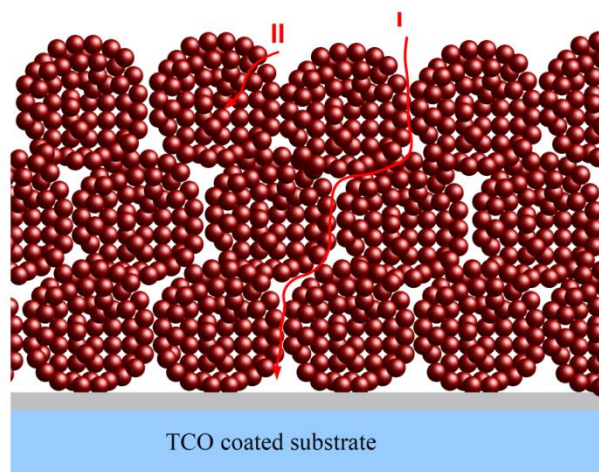
Figure 1.12 Schematic representation of a hierarchical nanoparticle film, having two different scale pores: (I) meso/macropores and (II) smaller nanopores.

Kim *et al.*[128] developed a solvothermal method for preparing crystallized TiO_2 sphere with ultrahigh surface areas up to 117.9 $m^2 \cdot g^{-1}$ and a well-defined nanoporous structure. The strategy used for the preparation of these spheres involves a two-step approach. First, the controlled hydrolysis reaction (equation 1.8) is carried out to form the TiO_2:

$$Ti\{OCH(CH_3)_2\}_4 + 2H_2O \longrightarrow TiO_2 + 4(CH_3)_2CHOH \qquad (1.8)$$
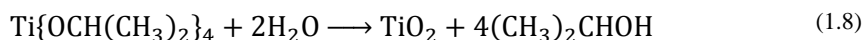
This reaction produces TiO_2 spheres in the amorphous phase and with a smooth surface without any pores - Figure 1.13a). The shape and size of the spheres can be controlled by the conditions of the hydrolysis reaction[128]. Then, the formed spheres are collected and washed with ethanol, and transferred to a titanium autoclave containing ethanol to conduct a hydrothermal reaction. The temperature is raised to 240 ℃ and held for 6 h; by this means the amorphous spheres are converted to a crystallized structure with high porosity - Figure 1.13b) and c).
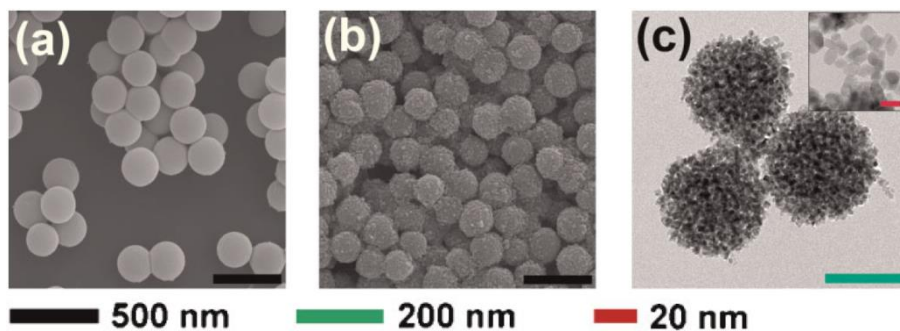
Figure 1.13 SEM micrographs of the spheres synthesized by Kim *et al.*[128]: a) before and b) after the hydrothermal treatment and c) TEM image with detail showing the porosity of the spheres.

The produced spheres have a diameter of 250 nm. The Brunauer-Emmett-Teller (BET) surface area of these structures was measured to be up to 117.9 $m^2 \cdot g^{-1}$, which is 1.7 times higher than the usual surface area of a P25 film. This is an indication of the high internal surface area built in the spheres. The authors also measured the pore size distribution and found that, as expected, the spheres exhibit a bimodal pore size distribution. The N_2 adsorption-desorption isotherms showed that the TiO_2 nanoparticle film has mainly pores of 29 nm, while the spheres show pores with average pore sizes of 9 nm and 55 nm. The smaller pores are inside the nanoporous sphere, visible in Figure 1.13c), and they are responsible for the high surface area of the final structure. The 55 nm sized pores are originated by the interstitial voids formed by the close-packed 250 nm spheres and they are responsible for the electrolyte diffusion improvement throughout the film. The internal pore of ~ 9 nm did not affect the diffusion of the electrolyte probably because the diffusion length is only ≈125 nm (half of the bead diameter = 250 nm). The spheres were used to prepare TiO_2 electrodes with thicknesses in the range of 10 – 10.3 μm. The resulting DSCs revealed a high J_{sc} of 14.6 $mA \cdot cm^{-2}$, a V_{oc} of 804 mV, a FF of 0.72 and an efficiency of $\eta = 8.44$ %. These values are considerable better than the results obtained for a standard nanoparticle TiO_2 film: J_{sc} of 12.7 $mA \cdot cm^{-2}$, a V_{oc} of 811 mV, a FF of 0.72 and an efficiency of $\eta = 7.40$ %. The main difference between both types of DSCs is the short-circuit current density J_{sc} that was considerably enhanced. This increase is mainly ascribed to the increased amount of adsorbed dye molecules in semiconductor structure – 140.4 $μmol \cdot cm^{-2}$ for

the cell equipped with the new photoelectrode and 122.1 µmol·cm^{-2} for the conventional cell. Additionally, the produced photocurrent should also benefit from scattering effect of the larger 250 nm particles in the photoelectrode. The same authors added to the previous photoelectrode a 500 nm interfacial TiO_2 layer to decrease the electron recombination at the FTO/electrolyte interface. The TiO_2 spheres were then treated with $TiCl_4$ and, finally, the photoelectrode outer surface was coated with hollow TiO_2 nanoparticles to act as scattering layer. The final DSC device showed an excellent result of 19.6 mA·cm^{-2} of J_{sc}, a V_{oc} of 766 mV, a FF of 0.69 and an efficiency of η = 10.52 %.

Sauvage *et al.*[23] reported a single titania layer based on the same principle, using mesoporous beads of 830 nm – Figure 1.14. The reported bead film had 89 m^2·g^{-1} and a mean pore size of 23 nm. The beads showed a mesoporous structure from the surface to the core and therefore the interior titania nanoparticles remain highly accessible to both chemisorption of dye molecules and electrolyte diffusion. The authors also presented evidences that inside the beads exist densely packed TiO_2 grains, having each grain contact with the neighbouring ones. This aspect is responsible for the increase of electron lifetime and enhanced electron mobility, reducing the electron recombination effect with the electrolyte.
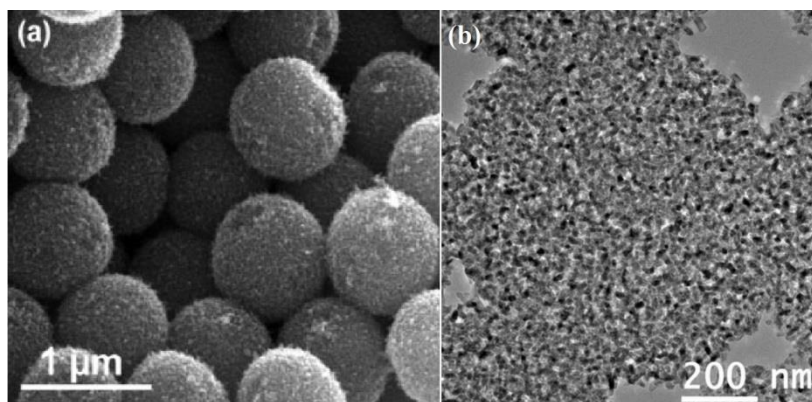
Figure 1.14 SEM micrographs of the obtained beads prepared by Sauvage *et al.*[23] showing: (a) their close packing in the film and (b) the high mesoporosity to the core.

The authors reported 10.6 % efficiency and an IPCE of 92 % at a wavelength of 570 nm with a 12 μm single bead film and using a heteroleptic tiophene-based dye (C101 dye). However, using the standard N719 dye with the above mentioned semiconductor structure resulted in a DSC with only 8.3 % efficiency. This allows concluding that the morphology and chemical nature of both nanoparticle film and dye molecule must be optimized for each other. The same authors found that the solar cells prepared with bead film showed enhanced electron lifetime, electron diffusion coefficients and diffusion length compared to a P25 film. The superior performance of the beads was mainly attributed to the close packing of grains and crystal intergrowth within the mesoporous titania beads. Similarly to what Kim *et al.* [128] have done, a triple layer DSC was prepared by Sauvage *et al.*[23], combining mesoporous beads with a transparent P25 TiO_2 interfacial layer and a light scattering layer on top of the beads, rendering an impressive J_{sc} of 19.90 mA·cm^{-2} , a V_{oc} of 724 mV, a FF of 0.77 and an η of 11.2 %. Even though the higher efficiency obtained based on a complex structure it is impressive that a single 12 μm film of TiO_2 beads gave 10.6 % PCE.

1.2.4   3-D template based backbones

Other types of hierarchical systems include structures with different length scales with different physical properties, *e.g.* systems including larger backbones with several pore and crystal sizes. It was reported to be possible to create hierarchical structures with individual control over the macro and mesostructure morphologies and dimensions, by infiltration of mesoporous amorphous silica in macroporous ceramic[129] or titania backbones[130].
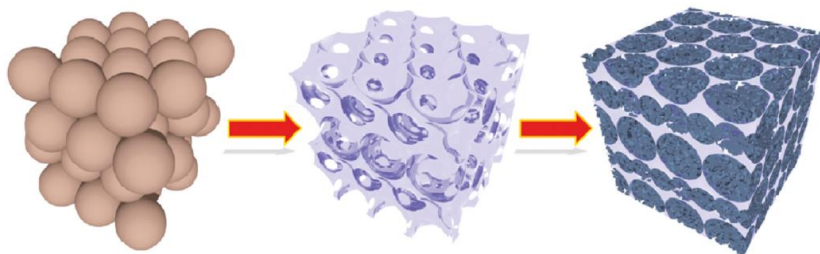
Figure 1.15 Schematic representation of the preparation method of hierarchical titania frameworks. A template material, such as polystyrene spheres, is impregnated with a titania solution precursor that after the hydrolization reaction is calcinated to form the crystallized anatase backbone, adapted from[76].

This approach was later used to create fully crystalline hierarchical titania backbones, as reported by Kuo *et al.*[131]. This work revealed a novel multi-scale TiO_2 nanostructure, composed by a TiO_2 blocking layer at the FTO surface and an inverse opal main structure. Then, organized transport channels were created between contacting spherical voids of the TiO_2 inverse opal and then TiO_2 nanoparticles were coated on the spherical surfaces of the voids – Figure 1.16. The TiO_2 inverse opal film was created by coating the blocking layer with polystyrene spheres (PS) with 100 nm of diameter. The PS template was infiltrated by electrochemical deposition of TiO_2 – Figure 1.16a) – and a close packing of PS spheres was obtained – Figure 1.16b). Afterwards, the resulting PS template was removed by calcination to obtain a crystalline inverse opal anatase scaffold opal Figure 1.16 c) and d). Then, this structure was treated with $TiCl_4$ in order to introduce TiO_2 NP into the structure and then to originate a larger surface area photoanode.
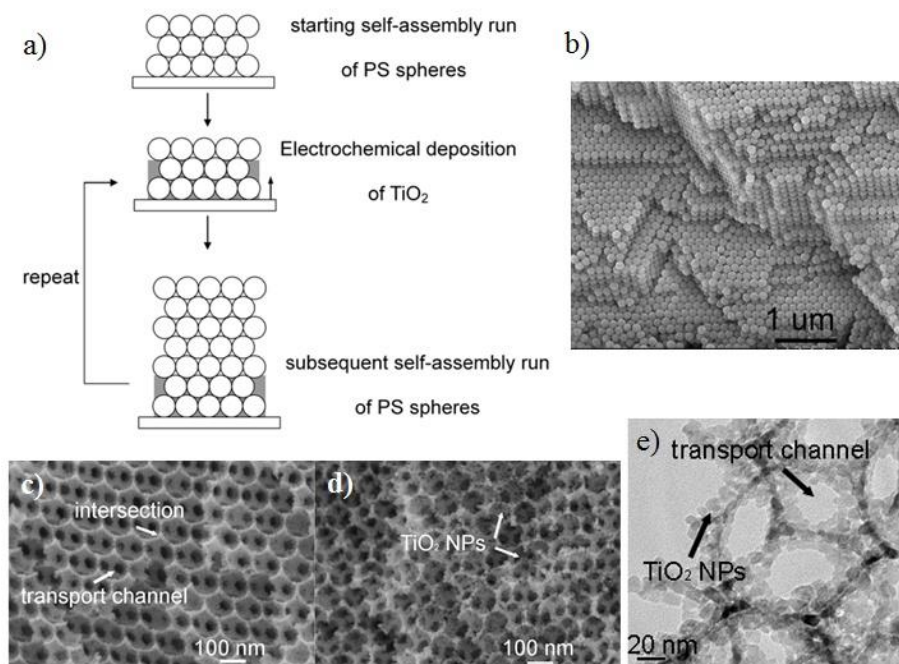
Figure 1.16 a) Schematic representation of the synthesis method of a highly ordered multi-scale nanostructure of TiO$_2$ proposed by Kuo *et al.*[131]; b) Film composed by the polystyrene opals revealing their close packing; SEM micrographs of the TiO$_2$ inverse opal c) before and d) after TiCl$_4$ treatment; e) TEM images of the TiO$_2$ nanoparticle decorated inverse opal revealing the coating of the macroporous transport channels. Adapted from[131].

Figure 1.16 c) and d) present SEM pictures of the anatase inverse opal structure before and after the TiCl$_4$ treatment. These figures show TiO$_2$ NP of 10–15 nm attached to the backbone, as well as the transport channel openings of 30~50 nm for dye solution and electrolyte penetration. Similarly to the bead structures presented before, these features are believed to enhance the load of dye molecules and electrolyte diffusion within the structure. The TEM picture presented in Figure 1.16 e) shows that TiO$_2$ NP are well crystallized and well connected, characteristics that are essential for a good electron transport through the structure. Because the NP are organized and attached to the walls of the main large pores, they have excellent access to the electrolyte. The fabricated TiO$_2$ nanostructure was assembled in a DSC configuration, yielding a J_{sc} of 8.2 mA·cm^{-2}, a V_{oc} of 720 mV, a FF of 0.62 and an efficiency of $\eta =$ 3.7 %. Although offering many potential advantages, the structure proposed by Kuo *et*

al.[131] still has low performance. Unfortunately, the authors did not present results on the surface area of the developed hierarchical structure, which may be the cause of the reported low efficiency. This issue could be addressed coating the surface area of the voids created by the PS spheres with a higher amount of TiO_2 NP.

A similar approach was reported by Mandlmeier *et al.*[76]. The authors created a similar highly crystalline macroporous inverse opal backbone but using polymethylmethacrylate (PMMA) spheres and a titania precursor for solution impregnation. The spheres diameter was 200 nm, two times the size of the spheres used by Kuo *et al.*[131]. This originated voids in the macroporous crystalline titania structure also twice the size and the intervoid connection was determined to be around 50-70 nm. The obtained scaffold can be seen in Figure 1.17a) and with detail in Figure 1.17b). After impregnation with titania precursor solution and calcination at 450 ºC, the hierarchical film consists of crystalline anatase – Figure 1.17 c) and d) – with crystal size larger than 20 nm in the macroporous scaffold walls and 4–6 nm in the mesoporous walls; these values have been confirmed by HRTEM and X-ray scattering. Thus, in the same hierarchical structure there are two crystal sizes: larger sizes in the walls of the macroporous backbone and smaller ones in the mesoporous anatase filling. The authors concluded that the highly crystalline scaffold had a strong effect in the crystallization of the mesoporous filling, acting as a nucleation site for further crystallization of the initially amorphous phase[76]. Besides this, the macroporous backbone has a stabilization effect in the mesoporous material embedded in its structure, preventing pore shrinkage due to heating. Thus, the final size of the mesoporous is even 50 % larger than the same material when applied on a flat surface. Mandlmeier *et al.*[76] also performed nitrogen adsorption experiments and determined that the macroporous scaffold exhibited a type II isotherm, typical for porous materials with macropores, and a surface area of 64 $m^2 \cdot g^{-1}$ – Figure 1.17e) curve A. After impregnation with titania solution, the hierarchical structure have a completely different adsorption behaviour, exhibiting a type IV isotherm with a surface area of 154 $m^2 \cdot g^{-1}$ - Figure 1.17e) curve B. This behaviour, suggests the existence of different pore sizes, ranging from micro to meso and macropores. The narrow hysteresis between the adsorption and desorption isotherms indicate a good pore distribution and its shape

indicates mostly mesoporosity[132]. Although Figure 1.17e) shows very similar isotherms for the hierarchical film (isotherm B) and for a standard mesoporous film grown in a flat surface (isotherm C), the pore size distributions, shown in Figure 1.17e) and f) are different and the average pore diameter are 6.1 nm and 5.1 nm, respectively. Additionally, a decrease in surface area from 210 $m^2 \cdot g^{-1}$ for the mesoporous film grown in the flat surface to 174 $m^2 \cdot g^{-1}$ for the hierarchical film was also observed. The increase in pore size up to 20 % confirms the non-shrinking effect described earlier due to the nanoparticles embedded in the macroporous backbone.
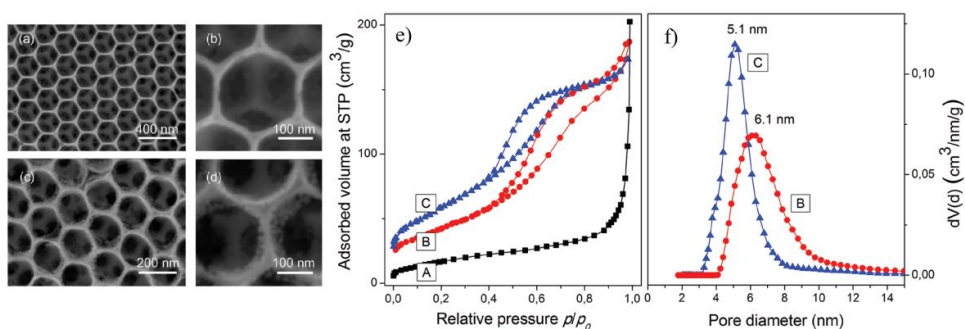
Figure 1.17 SEM images of macroporous scaffold created by Mandlmeier *et al.*[76]: before (a and b) and after (c and d) TiO_2 NP infiltration. e) Nitrogen adsorption/desorption isotherms (A - macroporous scaffold; B - macroporous scaffold with TiO_2 NP infiltration; C - reference mesoporous TiO_2 film); and f) pore size distribution of the macroporous scaffold material (B) and the reference mesoporous TiO_2 (C).

Using this hierarchical titania layer as photoelectrode in a DSC the authors achieved $J_{sc} = 7.17$ mA·cm^{-2}, $V_{oc} = 780$ mV, FF = 0.71 and an efficiency of $\eta = 4.0$ %. This result compared to the single mesoporous titania backbone film (J_{sc} of 0.97 mA·cm^{-2}, a V_{oc} of 980 mV, a FF of 0.52 and an efficiency of $\eta = 0.4$ %) represents an improvement of nearly ten times. Nonetheless, the performance is very limited compared for instance to the above mentioned beads by Kim *et al.*[128] or by Sauvage *et al.*[23], who reported a performance of ~ 10 % PCE in DSCs.

It is important to holdback that there is no clear relation between the photoelectrode surface area and the performance of the DSC. In fact, Sauvage *et al.*[23] used 400 nm spherical beads with 89 $m^2 \cdot g^{-1}$ and achieved ~10 % PCE; Kim *et al.*[128]

used smaller size beads (250 nm) with larger surface area (117 $m^2 \cdot g^{-1}$) and obtained also ~ 10 % with similar film thickness (10-12 μm); Mandlmeier *et al.*[76] prepared a porous photoelectrode with the largest surface area which did not surpass 4 % PCE DSC even if they have used a film with nearly half of the thickness used by the previous two authors (5.5 μm) and no additional scattering layer. On the other hand, there is a clear impact of the morphological parameters of the porous semiconductor on the DSC performance even though the relation between both is not always clear; it is still missing a deeper understanding in how the morphological features of the porous material influences the working kinetics of DSCs. Electrochemical impedance spectroscopy can play an important role in unraveling this relation but works describing a systematic electrochemical analysis on the new hierarchically ordered photoanodes are very scarce. A very recent report by Cho *et al.* [75] described the preparation of a similar hierarchical structure as described by Kuo *et al.* [131] and Mandlmeier *et al.* [76]. The authors studied the influence of the template colloidal particles diameter in the final macroporous structure and its role in the electron transport properties in the final DSC device. The thickness of the electrode was changed by controlling the macroporous inverse opal support and the diameter of the mesopores was controlled using different sizes of template colloidal particles. Several complete DSC devices were prepared and Figure 1.18 presents the corresponding DSC performance values, the adsorbed amount of dye in the photoelectrode and the charge transfer resistance in the TiO_2 interface, R_k, (determined by EIS) as a function of the mesoscale pore diameter. It can be observed that the pore diameter and the DSC performance are inversely proportional. This happens because the pore diameter increase corresponds to the diminishing of the surface area available for dye adsorption and, consequently, the decrease of the short-circuit current density. At this stage, the specific surface area available for dye adsorption governs the DSC performance. Electrochemical impedance spectroscopy showed lower charge transfer resistances at the TiO_2 interfaces for smaller mesopore diameters, implying that the electron/electrolyte recombination resistance was higher in photoelectrodes with 35 nm pore size.
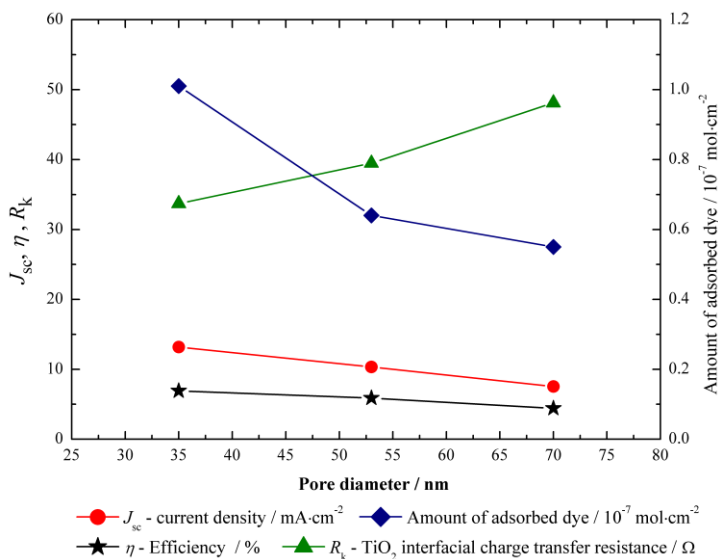
Figure 1.18 DSC performance values as a function of the mesoscale pore diameter of the photoelectrode (adapted from[75]).

The challenge of increasing the amount of adsorbed dye molecules and increase the electron transport through the semiconductor to the FTO collecting substrate still remains. Nonetheless, hierarchical structures using template techniques are very promising because they give control over the whole pore structure of the photoelectrode. However, more kinetic data such as electron diffusion coefficients, electron diffusion lengths and ionic diffusion coefficients should be determined and correlated to the morphological features of the nanostructures in order to optimize the photoelectrode structure and maximize efficiency.

As was described throughout this review work, the increase of the specific surface area to enhance dye adsorption in TiO_2 nanostructures does not pose great challenge. What is not trivial is to increase the adsorbed amount of dye without increasing the electron/electrolyte recombination rate; indeed this should be the reason why most of the 3-D strategies up to now did not produce high performance devices. The electronic loss by recombination is induced mainly by slow electron transport through the photoelectrode. Bearing this in mind, Tétreault *et al.*[21] followed the idea of using templating techniques to build macroporous backbones. In this case, besides using TiO_2 a thin conductive material of SnO_2 or Al/ZnO was also used to coat the template

material – Figure 1.19. By using polystyrene spheres they created a macroporous structure with well-defined morphological characteristics. Then, by atomic layer deposition (ALD) they created a 3-D TCO macroporous scaffold. Comparing this backbone to the previously described TiO_2 ones, this shows the clear advantage of having higher electron mobility and thus to offer a 3-D network for electron collection.
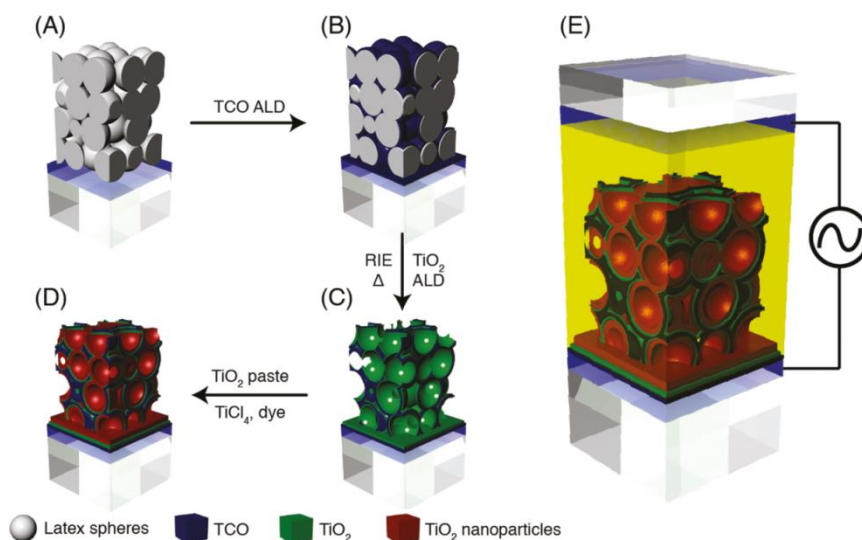
Figure 1.19 Schematic diagram for the fabrication method of the 3-D host passivation guest dye sensitized solar cell.

To avoid the electron recombination at the TCO backbone/electrolyte interface, this structure was then protected with a dense passivating TiO_2 thin layer, once again deposited by ALD. Afterwards, the backbone was filled with 17 nm anatase nanoparticles to ensure high surface area. This approach targeted high dye loadings and injection dynamics of typical anatase nanoparticles-based DSC. Figure 1.20 shows SEM micrographs of such structures where the good connection between the TCO backbone and the flat TCO substrate can be seen – Figure 1.20 a) and c). This electronic connection ensures efficient charge extraction throughout the photoelectrode. The inherent disordered structure caused by the template spheres creates an open structure that, according to the authors, only uses a small fraction of the 3-D film (~10 %), leaving enough volume to be filled with small TiO_2 particles with high superficial surface area for dye adsorption. Figure 1.20 c) confirms that the

TCO backbone is well coated in both sides by the dense passivation TiO_2 layer that should enable the TCO chemical stability and preventing electron recombination.
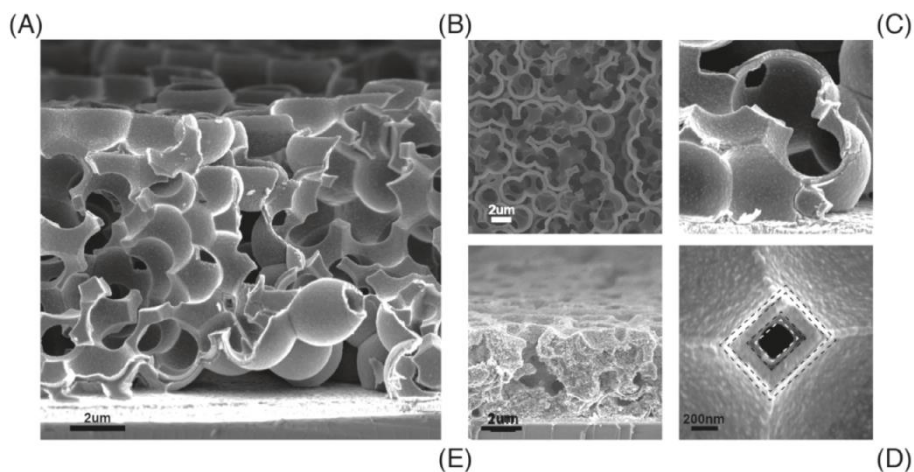
Figure 1.20 SEM micrograph of a self-assembled 3-D Al:ZnO TiO_2 host-passivation guest DSC photoanode: a) cross sectional view of the 3-D backbone; b) top view of the 3-D backbone; c) high-magnification micrograph showing the TiO_2 covered 3-D macroporous Al:ZnO host in direct contact with the front FTO electrode; d) high magnification micrograph showing the 3-D backbone coated with dense TiO_2 inside and outside; and e) complete photoanode after infiltration and calcination of the TiO_2 nanoparticle paste[21].

Using this new 3-D material concept Tétreault *et al.*[21] prepared DSCs based on TiO_2, SnO_2 and Al/ZnO 3-D host photoelectrodes in combination with Z907 dye. The best result was found using SnO_2 host backbone, rendering devices with J_{sc} of 10.4 mA·cm^{-2}, a V_{oc} of 803 mV, a FF of 0.70 and an η of 5.8 %. These results showed an increase of almost 100 mV when comparing with the Z907 best performing devices[133]. The electron mobility was also measured using electrochemical impedance spectroscopy and the authors found that in fact the Al/ZnO and SnO_2 films have electron diffusion coefficients six orders of magnitude higher than TiO_2 nanoparticles films (6.19 cm^2·s^{-1} and 0.423 cm^2·s^{-1}, respectively, compared to 6×10^{-6} cm^2·s^{-1} for the TiO_2 NP film).

Table 1.3 compares these results with those obtained by Kuo *et al.*[131] and Mandlmeier *et al.*[76]. Despite using similar template techniques to create a TiO_2 macroporous backbone, Kuo and Mandlmeier did not report DSC efficiencies higher

than 4 %. The difference between their and Tétreault *et al.*[21] results might be in the electron diffusion coefficient. Since the three authors followed the same architecture concept, it can be concluded that the higher performance observed is due to the higher electron mobility in the Al/ZnO and SnO_2 hosts. The findings by these authors should motivate studies to determine the influence of these highly conductive host backbones and their interaction with semiconductor particles, particularly their influence in the injection dynamics and in the overall kinetics of DSCs.

Table 1.3 Influence of the macroporous template backbone material on DSC performance.

Author	Host Material	V_{oc}	J_{sc} / mA·cm^{-2}	FF	Efficiency / %
Kuo *et al.*[131]	TiO_2	720	8.2	0.62	3.7
Mandlmeier *et al.*[76]	TiO_2	780	7.17	0.71	4.0
	TiO_2	791	6.9	0.73	4.0
Tétreault *et al.*[21]	Al/ZnO	842	7.5	0.77	4.9
	SnO_2	803	10.4	0.70	5.8

In a recent work, Crossland *et al.*[134] followed this idea, and disclosed the synthesis method for a mesoporous TiO_2 crystals that deliver enhanced mobility and optoelectronic device performance. This innovative work showed that mesoporous single-crystal (MSC) semiconductor could provide long range electronic connectivity and structural coherence. Using TiO_2 MSCs films processed under 150 ºC, the authors fabricated all solid state devices with 7.3 % efficiency. This result is quite remarkable, taking into account that TiO_2 nano-crystalline films are usually processed at 500 ºC to improve electrical connection between nanoparticles. The synthesis process is based on a templating technique, which uses silica beads with tuneable sizes from 20 to 250 nm that act as host backbone. The template material is first "seeded" with a titanium precursor, TiF_4, and only then is immersed in the reaction vessel. The reaction, hydrothermal growth of TiF_4 in the presence of hydrofluoric acid, is then carried out in the template pores. The acid stabilizes the precursor and significantly decreases the nucleation rate, allowing the synthesis of a high surface area (70 m^2·g^{-1}) single crystal

of anatase TiO_2. These single crystals benefit from a much higher electron conductivity of 1.5×10^{-5} S·cm^{-1} comparing to 2.2×10^{-7} S·cm^{-1} measured for a TiO_2 nanoparticle sintered film. Obviously, with very similar surface area (70 *vs*. 75 m^2·g^{-1} for TiO_2 MSCs and nanoparticles, respectively) and electrical conductivity two orders of magnitude higher, the mesoporous TiO_2 single crystals are an excellent candidate for replacing TiO_2 nanoparticle films in DSCs. These results, for a solid state device, surpass all the other template based techniques discussed so far, even more because they were tested with liquid electrolytes.

1.2.5 Hybrid TiO_2/Graphene nanostructures

In the last couple of years graphene has attracted enormous attention because of its unique properties and array of applications[135-138]. With a theoretical surface area of 2630 m^2·g^{-1}, graphene is an ideal support material with enhanced interfacial contact even when used in small amounts[139]. Its electron mobility of 10^4 cm^2·V^{-1} [135] at room temperature means that graphene has an excellent ability to transport electrons. These facts have made it very attractive for incorporation in photocatalytic mesoporous films [140-143] and in DSC's counter electrode[144-146], where its electrocatalytic properties have been put to use to substitute the expensive platinum catalyst. Recently, graphene has also been incorporated in DSC's photoelectrodes – Figure 1.21[77-81]. Fourier transform infrared spectroscopy (FT-IR) experimental results of pure TiO_2 and graphene-TiO_2 hybrid films showed that Ti-O-C bonds are formed, indicating the chemical interaction between surface hydroxyl groups of TiO_2 and functional groups of graphene oxide[147]. Experimental data also shows that the presence of graphene in the TiO_2 photoelectrode also increases the total amount of dye adsorbed in the film[78,147,148]. This fact is explained by these authors based on the huge surface area of graphene that provides more anchoring sites for TiO_2. But in fact, and similarly to what happens in photocatalytic studies where there are π-π conjugations between methylene blue molecules and the aromatic rings of graphene oxide sheets, a chemical interaction between sensitizing dye and graphene might exist, helping to explain the higher amount of adsorbed dye in hybrid films[80,147,149].

Graphene is produced mainly by the chemical oxidation method resulting in graphene oxide (GO)[150,151], which can be then reduced either chemically or thermally. However, reduced graphene oxide (RGO) contains oxygen functional groups (-OH and =O) on the planes and –COOH and carbonyl groups in the periphery of the planes[144, 145]. This, along with the lattice surface defects created during the exfoliation process, is believed to be responsible for the electrocatalytic behaviour of graphene[152-154]. Because of GO electrocatalytic properties and its high extinction coefficient[155], RGO should be handled carefully when used in the photoelectrode of DSCs; if not properly reduced, the remaining oxygen containing groups could promote recombination of electrons with electrolyte. In high amounts, graphene can also compete with the sensitizer molecules on light absorption and thus decrease the performance of DSCs. Therefore, the successful introduction of graphene in the photoelectrodes of DSCs depends on a careful balance between its conductive ability and electrocatalytic behaviour.
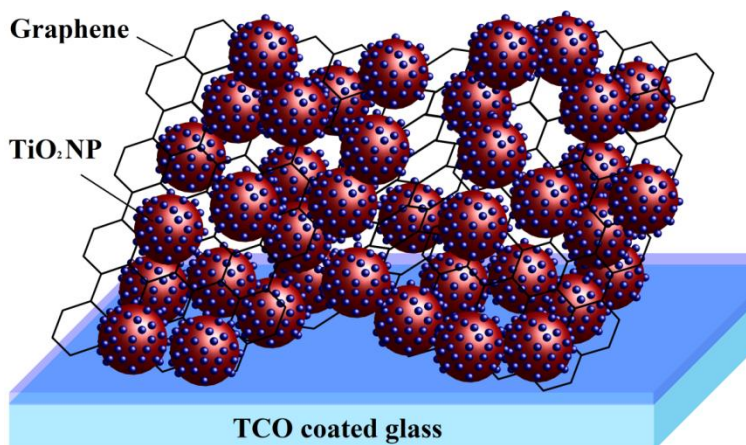
Figure 1.21 Schematic representation of a TiO_2/graphene hybrid photoanode.

Tang *et al.*[78] reported the development of a photoanode where exfoliated graphene sheets (GS) were attached to a TiO_2 nanoparticles matrix - Figure 1.22. The authors used a molecular grafting method where the graphene sheets were chemically exfoliated and chemisorbed in the TiO_2 matrix. By controlling the oxidation time, it was possible to achieve a highly efficient electronic conductive film and thus a good attachment between the GO and the nanoparticles. In fact, the determined resistivity of

a GO/TiO$_2$ decreased by more than two orders of magnitude from $2.1 \pm 0.9 \times 10^5$ Ω to $3.6 \pm 0.9 \times 10^2$ Ω[78]. These authors determined that the GO provided additional and more efficient electronic transport paths but also increased the dye loading of the film, leading to a photocurrent increase.
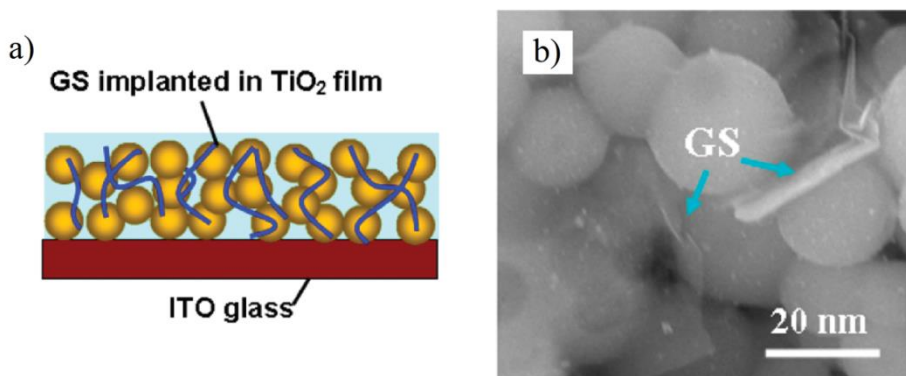
Figure 1.22 Schematic representation of a TiO$_2$ film with GS attached (left) and SEM micrographs of the prepared film with detail to the graphene sheet attached to the TiO$_2$[78].

Sun *et al.* [77] developed a method where graphene was dispersed using Nafion® and then incorporated in TiO$_2$ particles by a heterogeneous coagulation particles. Because the opposite zeta potentials of P25 particles (~15 mV) and graphene (-42 mV) there is a strong electrostatic attractive force that binds the TiO$_2$ NP to the surface of the graphene. The authors succeeded to coat graphene sheets with TiO$_2$ resulting in a composite structure with a P25 to graphene ratio of 200:1(w/w). The DSC with P25 nanoparticles showed a J_{sc} of 5.04 mA·cm^{-2} and η of 2.70 %. In the presence of 0.5 wt. % of graphene the J_{sc} increased 66 % to 8.38 mA·cm^{-2}, resulting in an efficiency of 4.28 %. The authors ascribe this enhanced performance to an increase in dye adsorption due to the creation of surface morphologies with more sites available and an extended electron lifetime since electrons travel through long mean free paths without recombining.

Yang *et al.*[79] successfully incorporated graphene in TiO$_2$ nanostructure to form 2D graphene bridges in DSCs. The authors reported an optimum result for graphene oxide content of 0.6 wt. % that originated a DSC with a J_{sc} of 16.29 mA·cm^{-2}, a V_{oc} of 690

mV, a FF of 0.62 and a η of 6.97 %. This result represent an increase of 45 % in the short-circuit current density and 39 % in the conversion efficiency, when compared to a P25 film-based DSC, shown in Figure 1.22. Comparing this result to DSCs equipped with a photoanode containing CNTs prepared by the same method and weight percentage – 0.4 % – a huge difference emerges since CNT devices perform significantly worse: J_{sc} of 3.35 mA·cm^{-2}, V_{oc} of 420 mV, FF of 0.41 and η of 0.58 %. The Fermi level of a CNT is between its conduction band (CB, -4.5 eV *vs.* vacuum) and its valence band. Besides, its CB is below the CB of TiO$_2$ (-4 eV *vs.* vacuum) resulting in a decrease of the V_{oc}. In opposition, graphene is a zero band material [156] and its work function is calculated to be higher than CNT value (4.42 to 4.5 eV *vs.* vacuum)[77,157,158]. This makes graphene perfect to be introduced in the TiO$_2$ structure because the apparent Fermi Level is not decreased. This fact explains why in the Yang *et al.* results the V_{oc} was not affected by the introduction of graphene (up to 0.4 wt. %) as can be seen in Figure 1.23. The unaffected V_{oc} and the enhanced efficiency mean that graphene increased charge transport and partially suppressed electron recombination with the electrolyte. In higher concentrations graphene starts to compete with the sensitized TiO$_2$ nanoparticle for light absorption and becomes a recombination center for electrons; consequently the DSC performance is affected – Figure 1.23.
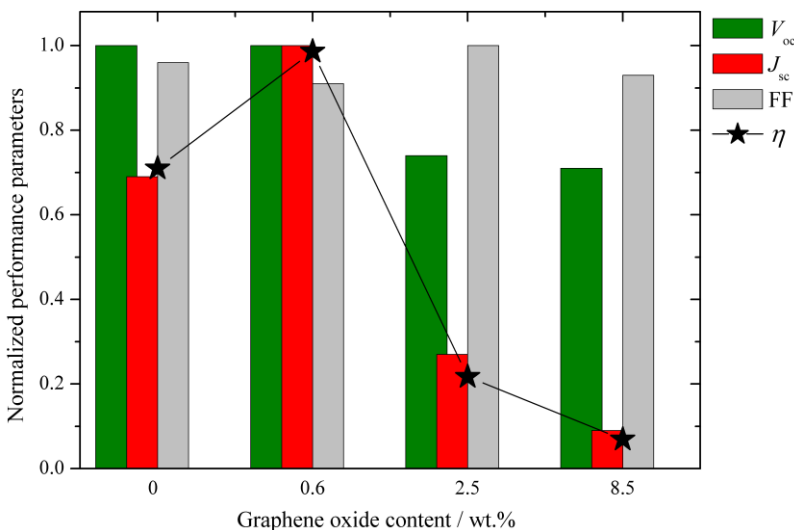
Figure 1.23 TiO$_2$/graphene hybrid DSC normalized performance values *vs.* different graphene oxide contents present in the photoanode.

1.2.6 Outlook for high performance photoelectrode

Morphological features have a great impact in the performance of photoelectrodes in dye sensitized solar cells, mainly determined by changes in the electron transport effectiveness, surface area available for dye loading and pore diameter for electrolyte diffusion.

1-D nanostructures provide direct pathways for electron transport and when used as photoelectrodes improve the electron diffusion length, electron lifetime and diffusion coefficient. However, they have a fundamental disadvantage: they do not provide the necessary specific surface area for dye adsorption, resulting in DSCs with poor efficiencies (~0.5 %). To overcome this challenge researchers began coating the 1-D nanostructures with nanoparticles or blended 1-D nanostructures in nanoparticles films for taking advantage of the characteristics of both structures: high surface area of the nanoparticles and high electron transport characteristics of the 1-D structures. However, again relatively low efficiency values have been reported using these structures (~3 %).

3-D hierarchical pore structures are very interesting as they have several scales of pores. Hierarchically structured metal oxides have nanometer pores that ensure high amount of adsorbed dye molecules and large micro or mesopores, allowing good electrolyte diffusion. A hierarchically bead-made film shows enhanced electron lifetimes, electron diffusion coefficients and diffusion lengths compared to a P25 film. The superior performance of the beads, with an efficiency of ~11 %, was mainly attributed to the close packing of grains and crystal intergrowth within the mesoporous titania beads. Another type of hierarchical systems includes structures with different length scales of two different morphological characteristics, for example, pore diameter and crystal size of a larger backbone. It was reported to be possible to create hierarchical structures where there is individual control over the macro and meso structures morphologies and dimensions by infiltration of mesoporous amorphous silica in macroporous ceramics or in titania backbones. The most promising technique in this category of hierarchical films is the one proposed by Tréteault *et al.*[21] that used the template idea to create a 3-D TCO macroporous scaffold by atomic layer

deposition. Although the relatively low efficiency (~6 %) attained so far, the idea of creating a 3-D network as electron collecting substrate has great potential. The key parameters of this structure are the compact TiO_2 layer coating of the TCO macroporous scaffold to avoid electron recombination with the electrolyte and the proper filling of the structure with TiO_2 NP to achieve good adsorption of sensitizing molecules. A different idea was proposed and tested successfully by Crossland *et al.*[134] In this work a mesoporous TiO_2 single crystal with high surface area and considerable higher electrical conductivity delivered a remarkable 7.3 % energy efficiency when inserted in a solid state solar cell. By demonstrating that MSCs displayed higher electron conductivities than nanocrystalline TiO_2, while eliminating the thermal sintering treatment, this work opened the door for a new kind of photoelectrodes in DSCs, multijunction device fabrication, temperature-sensitive substrate choice, and reduced device fabrication costs.

Finally, some reports concerning the use of graphene in combination with TiO_2 photoelectrodes show that graphene enhances the DSC performance when used in very low amounts (~0.5 wt. %). This material promises to bring the photoelectrodes of DSCs to the next level of development. The presence of graphene-bridges in a TiO_2 NP photoelectrode provides: i) a higher electron mobility; ii) higher amount of adsorbed dye; and iii) decreases the electron recombination with electrolyte, improving the overall solar cell efficiency. Due to its electrocatalytic properties and high extinction coefficient, when graphene is used in higher concentrations (>0.5 wt. %) and it is not properly reduced, it competes with the sensitizer for light absorption and acts as a recombination centre.

The challenge of increasing both the amount of adsorbed dye molecules and the electron transport through the semiconductor to the FTO collecting substrate still remains. More kinetic data such as electron diffusion coefficients, electron diffusion lengths and ionic diffusion coefficients should be determined and correlated to the morphological features of the nanostructures to optimize the photoelectrode and maximize efficiency. This state of art review aims to motivate other studies to investigate different materials and structures for photoelectrodes applications. Highly conductive host backbones and graphene structures are identified as promising for

increasing the overall kinetics of DSCs and thus their influence and interaction with different metal oxide particles should be deeply understood.

1.3 Long term stability of DSCs

The commercial success of any PV technology depends on the reliability, energy efficiency and cost of the devices. The degradation pathways of real PV system devices can occur at system, module, cell and molecular levels as illustrated in Figure 1.24. Large solar power plants are controlled by complex operational centers that integrate information from weather stations and grid operators to maximize profit without destabilizing the electricity grid.
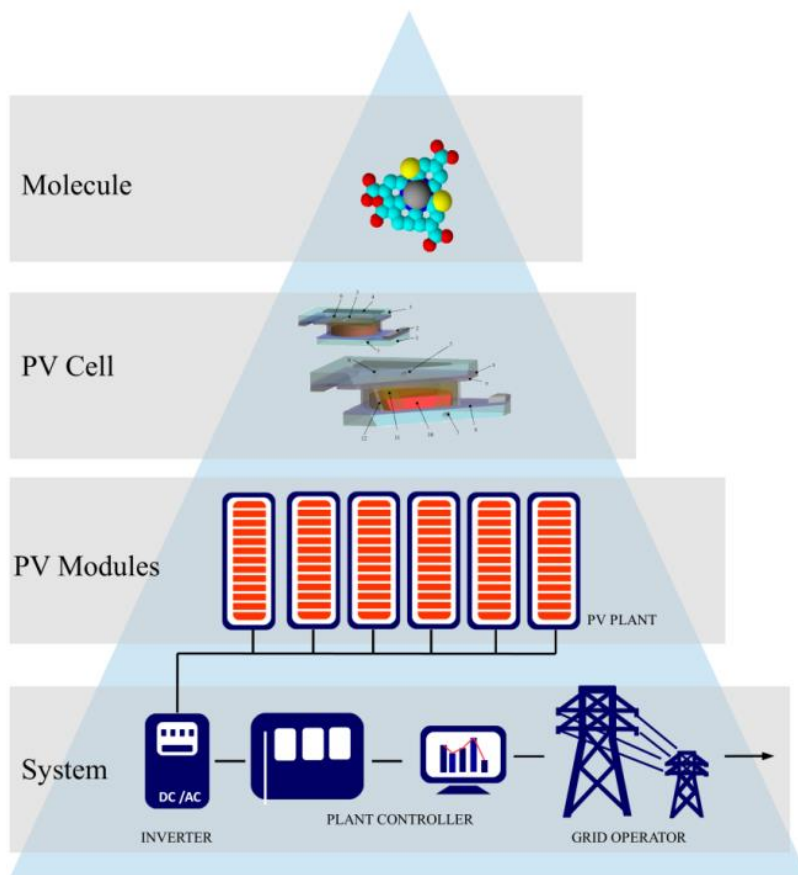

Figure 1.24 Illustration of the different levels where degradation of PV fields can occur: system, module, cell and molecular levels.

For DSC technology to become a real commercial alternative to fossil fuels, at least 25 year of constant power conversion efficiency should be guaranteed for outdoor applications. Therefore, any product based on DSC technology must comply to stringent standards such as IEC 61646 for thin-film PV modules[159]. The standard comprises series of accelerated stress tests aiming duplicating the expected failures in a shorter time frame compared to outdoor exposure. The tests include thermal cycles, damp heat tests, humidity freeze and mechanical loads, among others. The degradation mechanisms occurring at the DSC device can be categorized into two main levels, as shown in Figure 1.24: at the DSC device or at the molecular level. Degradation at the cell level deals with sealing failures, which allows contaminants to enter the cell and in severe cases electrolyte leakage; both mechanisms are considered critical factors that determine long term stability of the solar cell[160]. The degradation at the molecular level deals with deactivation of the inner components of the cell, which in most of the cases are related to external contamination, like water and oxygen[160-162]. The specific degradation processes have been subjected to much scrutiny in the scientific community and are usually assigned to dye desorption[163-165], electron recombination at the photoelectrode[166-168], degradation of the counter electrode[169-171], decrease in triiodide concentration[169, 172, 173], water and oxygen inside the cell[174-177] and UV light exposure[163, 165, 178]. These mechanisms are usually triggered by external factors like light intensity, temperature and moisture, which in turn stress a critical pre-requisite of the DSC cell: the encapsulation of the liquid electrolyte. Consequently, the sealing reliability of DSCs is considered a key pre-requisite that a DSC cell must fulfil to be suitable for real outdoor testing[165]. Besides, unreliable cell tightness questions the stability studies on molecular level of the inner components employed in the solar cell.

The commonly employed sealing materials are thermoplastic polymers, such as Surlyn®, that are unreliable at temperatures above 60 ºC due to its low softening temperature (~60-70 ºC)[165]. Above this temperature it is known to be permeable to oxygen and continuous exposure to light and temperature cycling eventually causes sealing failure[160]. Although it is widely used by research teams all around the world in laboratory test cells, this sealant is not appropriate for stable operation in real outdoor conditions[174, 179, 180].

1.4 Scope of the thesis

DSC technology is a promising candidate for low cost renewable electricity generation. However, there are technical limitations that prevent commercialization of the technology. Two main aspects are identified as critical for DSCs to emerge in the PV market: lifetime stability and energy efficiency. The work developed in this thesis targets these limitations, by creating robust engineering solutions to the DSC industrialization constraints.

This work is divided in seven chapters. In **Chapter 1**, modern society energy paradigm is revisited and perspectives for energy harvesting from renewable sources are discussed: particular emphasis is given to the DSC technology potential. An overview of the operation principles is given, as well as state-of-the-art DSC configurations. The influence of the photoelectrode morphology in the DSC performance is analysed and the best strategies to improve DSC efficiency and stability are identified.

Chapter 2 focuses on the development and optimization of a sealing process for obtaining stable DSC devices. An innovative sealing process based on laser assisted glass melting was developed and optimized for DSC sealing.

The following chapter, **Chapter 3**, compares the laser-assisted glass sealing process against the commonly used sealing method concerning performance and stability. **Chapter 4** aims at understanding and quantifying the recombination process at TiO_2/electrolyte and FTO/electrolyte interfaces and their dependence with temperature. The developed laser assisted sealing allows studying the temperature effect in DSC performance up to 105 ºC, the highest temperature ever considered in kinetic studies of liquid state DSCs.

Chapter 5 concerns modelling, simulation and design of DSCs. A phenomenological model is used to describe transport and recombination processes affecting the DSC performance, and in which way they can be tuned to optimize its operation. This chapter provides a useful framework in the exploration of new concepts and designs for improving DSCs performance.

Chapter 6 displays the development of innovative photoelectrode architecture for DSCs. The new PE aims at increasing DSCs efficiency by targeting the transport and recombination limitations of the commonly employed TiO_2 nanoparticle films.

Finally, **Chapter 7** lays out the main conclusions of the thesis, along with future work ideas, suggestions and guidelines.

Acknowledgements

References

1.   P. H. J. Conti, *International Energy Outlook 2013*, U.S. Energy Administration, 2013.

2.   F. T. Manoel Rekinger, SolarPower Europe, *Global Market Outlook for Solar Power 2015-2019*, SolarPower Europe, 2015.

3.   U. N. D. Programme, *World energy assement: Energy and the challenge of sustainability* United Nations Development Programme, 2000.

4.   M. A. Green, K. Emery, Y. Hishikawa, W. Warta and E. D. Dunlop, *Progress in Photovoltaics: Research and Applications*, 2012, **20**, 12-20.

5.   J. Ciesielska, *Global Market Outlook for Photovolatics until 2015*, 2011.

6.   T. Sugaya, O. Numakami, R. Oshima, S. Furue, H. Komaki, T. Amano, K. Matsubara, Y. Okano and S. Niki, *Energy & Environmental Science*, 2012, **5**, 6233-6237.

7.   J. D. Servaites, M. A. Ratner and T. J. Marks, *Energy & Environmental Science*, 2011, **4**, 4410-4422.

8.   K. Kakiage, Y. Aoyama, T. Yano, K. Oya, J.-i. Fujisawa and M. Hanaya, *Chem. Commun.*, 2015.

9.   Best research solar cell efficiencies chart, http://www.nrel.gov/ncpv/images/efficiency_chart.jpg, Accessed October, 2015.

10. L. M. Goncalves, V. d. Z. Bermudez, H. A. Ribeiro and A. M. Mendes, *Energy & Environmental Science*, 2008, **1**, 655-667.

11. M. K. Nazeeruddin, E. Baranoff and M. Grätzel, *Solar Energy*, 2011, **85**, 1172-1178.

12. M. Grätzel, *Journal of Photochemistry and Photobiology C: Photochemistry Reviews*, 2003, **4**, 145-153.

13. Report: The Cutting Edge of Research – EPFL's SwissTech Convention Center, http://www.detail-online.com/inspiration/report-the-cutting-edge-of-research-%E2%80%93-epfl%E2%80%99s-swisstech-convention-center-111842.html, Accessed Ocotber 2015.

14. J.-H. Yum, S.-J. Moon, C. S. Karthikeyan, H. Wietasch, M. Thelakkat, S. M. Zakeeruddin, M. K. Nazeeruddin and M. Grätzel, *Nano Energy*, 2012, **1**, 6-12.

15. D. Kuang, C. Klein, S. Ito, J. E. Moser, R. Humphry-Baker, N. Evans, F. Duriaux, C. Grätzel, S. M. Zakeeruddin and M. Grätzel, *Advanced Materials*, 2007, **19**, 1133-1137.

16. L. Andrade, S. M. Zakeeruddin, M. K. Nazeeruddin, H. A. Ribeiro, A. Mendes and M. Grätzel, *ChemPhysChem*, 2009, **10**, 1117-1124.

17. F. Ribeiro, J. Maçaira, R. Cruz, J. Gabriel, L. Andrade and A. Mendes, *Solar Energy Materials and Solar Cells*, 2012, **96**, 43-49.

18. J. Wu, S. Hao, Z. Lan, J. Lin, M. Huang, Y. Huang, P. Li, S. Yin and T. Sato, *J. Am. Chem. Soc.*, 2008, **130**, 11568-11569.

19. W. Wu, J. Li, F. Guo, L. Zhang, Y. Long and J. Hua, *Renewable Energy*, 2010, **35**, 1724-1728.

20. A. Yella, H.-W. Lee, H. N. Tsao, C. Yi, A. K. Chandiran, M. K. Nazeeruddin, E. W.-G. Diau, C.-Y. Yeh, S. M. Zakeeruddin and M. Grätzel, *Science*, 2011, **334**, 629-634.

21. N. Tétreault, É. Arsenault, L.-P. Heiniger, N. Soheilnia, J. Brillet, T. Moehl, S.

Zakeeruddin, G. A. Ozin and M. Grätzel, *Nano Letters*, 2011, **11**, 4579-4584.

22. J.-Y. Liao, H.-P. Lin, H.-Y. Chen, D.-B. Kuang and C.-Y. Su, *Journal of Materials Chemistry*, 2012, **22**, 1627-1633.

23. F. d. r. Sauvage, D. Chen, P. Comte, F. Huang, L.-P. Heiniger, Y.-B. Cheng, R. A. Caruso and M. Graetzel, *ACS Nano*, 2010, **4**, 4420-4425.

24. B. O'Regan and M. Grätzel, *Nature*, 1991, **353**, 737-740.

25. A. Hagfeldt and M. Grätzel, *Acc. Chem. Res.*, 2000, **33**, 269-277.

26. L. R. Andrade, H. A.; Mendes, A, *Dye - Sensitized Solar Cells: an Overview, in Energy Production and Storage: Inorganic Chemical Strategies for a Warming World*, John Wiley & Sons, Ltd, Chichester, UK, 2010.

27. F. Gao, Y. Wang, D. Shi, J. Zhang, M. K. Wang, X. Y. Jing, R. Humphry-Baker, P. Wang, S. M. Zakeeruddin and M. Gratzel, *Journal of the American Chemical Society*, 2008, **130**, 10720-10728.

28. F. Gao, Y. Wang, J. Zhang, D. Shi, M. Wang, R. Humphry-Baker, P. Wang, S. Zakeeruddin and M. Grätzel, *Chem. Commun.*, 2008, 2635-2637.

29. M. Nazeeruddin, P. Péchy and M. Grätzel, *Chem. Commun.*, 1997, 1705-1706.

30. M. Nazeeruddin, A. Kay, I. Rodicio, R. Humphry-Baker, E. Mueller, P. Liska, N. Vlachopoulos and M. Grätzel, *J. Am. Chem. Soc.*, 1993, **115**, 6382-6390.

31. M. K. Nazeeruddin, T. Bessho, L. Cevey, S. Ito, C. Klein, F. De Angelis, S. Fantacci, P. Comte, P. Liska, H. Imai and M. Graetzel, *Journal of Photochemistry and Photobiology A: Chemistry*, 2007, **185**, 331-337.

32. V. Shklover, M.-K. Nazeeruddin, S. M. Zakeeruddin, C. Barbe, A. Kay, T. Haibach, W. Steurer, R. Hermann, H.-U. Nissen and M. Gratzel, *Chemistry of Materials*, 1997, **9**, 430-439.

33. W. Zhou, B. Zhao, P. Shen, S. Jiang, H. Huang, L. Deng and S. Tan, *Dyes and Pigments*, 2011, **91**, 404-412.

34. H.-H. Chou, C.-Y. Hsu, Y.-C. Hsu, Y.-S. Lin, J. T. Lin and C. Tsai, *Tetrahedron*, 2012, **68**, 767-773.

35. C. Teng, X. Yang, C. Yuan, C. Li, R. Chen, H. Tian, S. Li, A. Hagfeldt and L. Sun, *Organic Letters*, 2009, **11**, 5542-5545.

36.   L. Andrade, J. Sousa, H. A. Ribeiro and A. Mendes, *Solar Energy*, 2011, **85**, 781-793.

37.   Y. Chiba, A. Islam, Y. Watanabe, R. Komiya, N. Koide and L. Han, *Japanese Journal of Applied Physics, Part 2: Letters*, 2006, **45**, L638-L640.

38.   M. Nazeeruddin, P. Pechy, T. Renouard, S. Zakeeruddin, R. Humphry-Baker, P. Comte, P. Liska, L. Cevey, E. Costa, V. Shklover, L. Spiccia, G. Deacon, C. Bignozzi and M. Grätzel, *J. Am. Chem. Soc.*, 2001, **123**, 1613-1624.

39.   A. Martinson, T. Hamann, M. Pellin and J. Hupp, *Chemistry - A European Journal*, 2008, **14**, 4458-4467.

40.   M. Wang, N. Chamberland, L. Breau, J.-E. Moser, R. Humphry-Baker, B. Marsan, S. M. Zakeeruddin and M. Grätzel, *Nat Chem*, 2010, **2**, 385-389.

41.   Z. Zhang, P. Chen, T. N. Murakami, S. M. Zakeeruddin and M. Grätzel, *Advanced Functional Materials*, 2008, **18**, 341-346.

42.   B. Bergeron, A. Marton, G. Oskam and G. Meyer, *J. Phys. Chem. B*, 2005, **109**, 937-943.

43.   G. Oskam, B. Bergeron, G. Meyer and P. Searson, *J. Phys. Chem. B*, 2001, **105**, 6867-6873.

44.   U. Bach, D. Lupo, P. Comte, J. Moser, F. Weissortel, J. Salbeck, H. Spreitzer and M. Grätzel, *Nature*, 1998, **395**, 583-585.

45.   H. Nusbaumer, J. E. Moser, S. M. Zakeeruddin, M. K. Nazeeruddin and M. Gratzel, *J. Phys. Chem. B*, 2001, **105**, 10461-10464.

46.   S. Sapp, C. Elliott, C. Contado, S. Caramori and C. Bignozzi, *J. Am. Chem. Soc.*, 2002, **124**, 11215-11222.

47.   H. Nusbaumer, S. Zakeeruddin, J. Moser and M. Grätzel, *Chemistry - A European Journal*, 2003, **9**, 3756-3763.

48.   P. Cameron, L. Peter, S. Zakeeruddin and M. Grätzel, *Coordination Chemistry Reviews*, 2004, **248**, 1447-1453.

49.   S. Nakade, Y. Makimoto, W. Kubo, T. Kitamura, Y. Wada and S. Yanagida, *J. Phys. Chem. B*, 2005, **109**, 3488-3493.

50.   J. Burschka, A. Dualeh, F. Kessler, E. Baranoff, N.-L. Cevey-Ha, C. Yi, M. K. Nazeeruddin and M. Grätzel, *Journal of the American Chemical Society*, 2011,

133, 18042-18045.

51.   I. Chung, B. Lee, J. He, R. P. H. Chang and M. G. Kanatzidis, *Nature*, 2012, **485**, 486-489.

52.   A. Kojima, K. Teshima, Y. Shirai and T. Miyasaka, *Journal of the American Chemical Society*, 2009, **131**, 6050-6051.

53.   J.-H. Im, C.-R. Lee, J.-W. Lee, S.-W. Park and N.-G. Park, *Nanoscale*, 2011, **3**, 4088-4093.

54.   M. M. Lee, J. Teuscher, T. Miyasaka, T. N. Murakami and H. J. Snaith, *Science*, 2012, **338**, 643-647.

55.   J. H. Heo, S. H. Im, J. H. Noh, T. N. Mandal, C.-S. Lim, J. A. Chang, Y. H. Lee, H.-j. Kim, A. Sarkar, K. NazeeruddinMd, M. Gratzel and S. I. Seok, *Nat Photon*, 2013, **7**, 486-491.

56.   G. Niu, X. Guo and L. Wang, *Journal of Materials Chemistry A*, 2015.

57.   M. D. McGehee, *Science*, 2011, **334**, 607-608.

58.   M. Gratzel, *Inorganic Chemistry*, 2005, **44**, 6841-6851.

59.   J. Bisquert, M. Gratzel, Q. Wang and F. Fabregat-Santiago, *The Journal of Physical Chemistry B*, 2006, **110**, 11284-11290.

60.   F. Fabregat-Santiago, J. Bisquert, G. Garcia-Belmonte, G. Boschloo and A. Hagfeldt, *Solar Energy Materials and Solar Cells*, 2005, **87**, 117-131.

61.   J. Bisquert, F. Fabregat-Santiago, I. n. Mora-SeroÌ•, G. Garcia-Belmonte and S. GimeÌ•nez, *The Journal of Physical Chemistry C*, 2009, **113**, 17278-17290.

62.   J. Villanueva-Cab, G. Oskam and J. A. Anta, *Solar Energy Materials and Solar Cells*, 2010, **94**, 45-50.

63.   S. A. Haque, Y. Tachibana, D. R. Klug and J. R. Durrant, *J. Phys. Chem. B*, 1998, **102**, 1745-1749.

64.   J. Bisquert and V. S. Vikhrenko, *The Journal of Physical Chemistry B*, 2004, **108**, 2313-2322.

65.   J. Bisquert, *The Journal of Physical Chemistry B*, 2002, **106**, 325-333.

66.   J. Bisquert, *Journal of Electroanalytical Chemistry*, 2010, **646**, 43-51.

67.   J. A. Anta, *Current Opinion in Colloid & Interface Science*, 2012, **17**, 124-131.

68.   N. Tetreault and M. Gratzel, *Energy & Environmental Science*, 2012.

69.   A. B. F. Martinson, M. r. S. Góes, F. Fabregat-Santiago, J. Bisquert, M. J. Pellin and J. T. Hupp, *The Journal of Physical Chemistry A*, 2009, **113**, 4015-4021.

70.   P. Tiwana, P. Docampo, M. B. Johnston, H. J. Snaith and L. M. Herz, *ACS Nano*, 2011, **5**, 5158-5166.

71.   P. Zhong, W. Que, J. Zhang, Q. Jia, W. Wang, Y. Liao and X. Hu, *Journal of Alloys and Compounds*, 2011, **509**, 7808-7813.

72.   Y. Wang and F. Caruso, *Advanced Functional Materials*, 2004, **14**, 1012-1018.

73.   Y. Zhao and X. S. J. Z. L. J. C. Y. Z. S. Y. L. D. Zhu, *ChemPhysChem*, 2007, **8**, 856-861.

74.   W. Fan, M. A. Snyder, S. Kumar, P.-S. Lee, W. C. Yoo, A. V. McCormick, R. Lee Penn, A. Stein and M. Tsapatsis, *Nat Mater*, 2008, **7**, 984-991.

75.   C.-Y. Cho and J. H. Moon, *Langmuir*, 2012, **28**, 9372–9377.

76.   B. Mandlmeier, J. M. Szeifert, D. Fattakhova-Rohlfing, H. Amenitsch and T. Bein, *Journal of the American Chemical Society*, 2011, **133**, 17274-17282.

77.   S. Sun, L. Gao and Y. Liu, *Applied Physics Letters*, 2010, **96**, 083113.

78.   Y.-B. Tang, C.-S. Lee, J. Xu, Z.-T. Liu, Z.-H. Chen, Z. He, Y.-L. Cao, G. Yuan, H. Song, L. Chen, L. Luo, H.-M. Cheng, W.-J. Zhang, I. Bello and S.-T. Lee, *ACS Nano*, 2010, **4**, 3482-3488.

79.   N. Yang, J. Zhai, D. Wang, Y. Chen and L. Jiang, *ACS Nano*, 2010, **4**, 887-894.

80.   M.-Y. Yen, M.-C. Hsiao, S.-H. Liao, P.-I. Liu, H.-M. Tsai, C.-C. M. Ma, N.-W. Pu and M.-D. Ger, *Carbon*, 2011, **49**, 3597-3606.

81.   S. R. Kim, M. K. Parvez and M. Chhowalla, *Chemical Physics Letters*, 2009, **483**, 124-127.

82.   M. F. Ashby, P. J. Ferreira and D. L. Schodek, in *Nanomaterials, Nanotechnologies and Design*, Butterworth-Heinemann, Boston, 2009, pp. 1-16.

83.   A. S. Edelstein, in *Encyclopedia of Materials: Science and Technology (Second Edition)*, eds. K. H. J. B. Editors-in-Chief: , W. C. Robert, C. F. Merton, I. Bernard, J. K. Edward, M. Subhash and V. Patrick, Elsevier, Oxford, 2001, pp. 5916-5927.

84.   in *Frontiers of Nanoscience*, ed. W. Gerhard, Elsevier, 2009, vol. Volume 1, p.

ii.

85.   B. Bhushan, *Springer Handbook of Nanotechnology*, Springer, 2010.

86.   C. A. F. Daniel L. Fedlheim, *Metal Nanoparticles: Synthesis, Characterization, and Applications*, CRC, 2001.

87.   P. R. Solanki, A. Kaushik, V. V. Agrawal and B. D. Malhotra, *NPG Asia Mater*, 2011, **3**, 17-24.

88.   K. D. Sattler, *Handbook of Nanophysics: Nanotubes and Nanowires*, CRC, 2010.

89.   X. Sun and M. S. Saha, ed. J. Zhang, Springer London, 2008, pp. 655-714.

90.   D. K. Ferry, *Science*, 2008, **319**, 579-580.

91.   R. Yan, P. Pausauskie, J. Huang and P. Yang, *Proceedings of the National Academy of Sciences*, 2009, **106**, 21045-21050.

92.   C. Cheng and H. J. Fan, *Nano Today*, 2012, **7**, 327-343.

93.   R. H. Baughman, C. Cui, A. A. Zakhidov, Z. Iqbal, J. N. Barisci, G. M. Spinks, G. G. Wallace, A. Mazzoldi, D. De Rossi, A. G. Rinzler, O. Jaschinski, S. Roth and M. Kertesz, *Science*, 1999, **284**, 1340-1344.

94.   A. Salehi-Khojin, K. Y. Lin, C. R. Field and R. I. Masel, *Science*, 2010, **329**, 1327-1330.

95.   F. M. Toma, A. Sartorel, M. Iurlo, M. Carraro, P. Parisse, C. Maccato, S. Rapino, B. R. Gonzalez, H. Amenitsch, T. Da Ros, L. Casalis, A. Goldoni, M. Marcaccio, G. Scorrano, G. Scoles, F. Paolucci, M. Prato and M. Bonchio, *Nat Chem*, 2010, **2**, 826-831.

96.   B. Y. Lee, M. G. Sung, J. Lee, K. Y. Baik, Y.-K. Kwon, M.-S. Lee and S. Hong, *ACS Nano*, 2011, **5**, 4373-4379.

97.   X. Wang, X. Chen, L. Gao, H. Zheng, M. Ji, C. Tang, T. Shen and Z. Zhang, *Journal of Materials Chemistry*, 2004, **14**, 905-907.

98.   J. R. Morber, Y. Ding, M. S. Haluska, Y. Li, J. P. Liu, Z. L. Wang and R. L. Snyder, *The Journal of Physical Chemistry B*, 2006, **110**, 21672-21679.

99.   A. M. More, T. P. Gujar, J. L. Gunjakar, C. D. Lokhande and O. S. Joo, *Applied Surface Science*, 2008, **255**, 2682-2687.

100.   Z. W. Pan, Z. R. Dai and Z. L. Wang, *Science*, 2001, **291**, 1947-1949.

101. Z. Zhang, S. Brown, J. B. M. Goodall, X. Weng, K. Thompson, K. Gong, S. Kellici, R. J. H. Clark, J. R. G. Evans and J. A. Darr, *Journal of Alloys and Compounds*, 2009, **476**, 451-456.

102. D. Chen, L. Cao, F. Huang, P. Imperial, Y. B. Cheng and R. A. Caruso, *Journal of the American Chemical Society*, 2010, **132**, 4438-4444.

103. Q. Zhang and G. Cao, *Nano Today*, 2011, **6**, 91-109.

104. B. Huber, A. Brodyanski, M. Scheib, A. Orendorz, C. Ziegler and H. Gnaser, *Thin Solid Films*, 2005, **472**, 114-124.

105. K. Madhusudan Reddy, S. V. Manorama and A. Ramachandra Reddy, *Materials Chemistry and Physics*, 2003, **78**, 239-245.

106. L. Dloczik, O. Ileperuma, I. Lauermann, L. M. Peter, E. A. Ponomarev, G. Redmond, N. J. Shaw and I. Uhlendorf, *J. Phys. Chem. B*, 1997, **101**, 10281-10289.

107. A. C. Fisher, L. M. Peter, E. A. Ponomarev, A. B. Walker and K. G. U. Wijayantha, *The Journal of Physical Chemistry B*, 2000, **104**, 949-958.

108. L. Forro, O. Chauvet, D. Emin, L. Zuppiroli, H. Berger and F. Lévy, *Journal of Applied Physics*, 1994, **75**, 633-635.

109. F. Cao, G. Oskam, G. J. Meyer and P. C. Searson, *Journal of Physical Chemistry*, 1996, **100**, 17021-17027.

110. J. Bisquert, *The Journal of Physical Chemistry B*, 2004, **108**, 2323-2332.

111. J. Bisquert and I. n. Mora-Seró, *The Journal of Physical Chemistry Letters*, 2009, **1**, 450-456.

112. J. van de Lagemaat and A. J. Frank, *The Journal of Physical Chemistry B*, 2001, **105**, 11194-11205.

113. N. Kopidakis, K. D. Benkstein, J. van de Lagemaat and A. J. Frank, *The Journal of Physical Chemistry B*, 2003, **107**, 11307-11315.

114. C. Chen, M. Wang and K. Wang, *The Journal of Physical Chemistry C*, 2009, **113**, 1624-1631.

115. Q. Wang, S. Ito, M. Gratzel, F. Fabregat-Santiago, I. Mora-Sero, J. Bisquert, T. Bessho and H. Imai, *J. Phys. Chem. B*, 2006, **110**, 25210-25221.

116. K. Fan, T. Peng, J. Chen and K. Dai, *Journal of Power Sources*, 2011, **196**,

2939-2944.

117. A. Hagfeldt, G. Boschloo, L. Sun, L. Kloo and H. Pettersson, *Chemical Reviews*, 2010, **110**, 6595-6663.

118. L. Bertoluzzi and S. Ma, *Physical Chemistry Chemical Physics*, 2013, **15**, 4283-4285.

119. C.-H. Ku and J.-J. Wu, *Applied Physics Letters*, 2007, **91**, 093117.

120. M. Samadpour, N. Taghavinia, A. Iraji-zad, M. Marandi and F. Tajabadi, *Eur. Phys. J.-Appl. Phys*, 2012, **57**.

121. T.-S. Kang, A. P. Smith, B. E. Taylor and M. F. Durstock, *Nano Letters*, 2009, **9**, 601-606.

122. D. K.-P. Wong, C.-H. Ku, Y.-R. Chen, G.-R. Chen and J.-J. Wu, *ChemPhysChem*, 2009, **10**, 2698-2702.

123. X. Gan, X. Li, X. Gao, F. Zhuge and W. Yu, *Thin Solid Films*, 2010, **518**, 4809-4812.

124. R. Zhang, A. A. Elzatahry, S. S. Al-Deyab and D. Zhao, *Nano Today*, 2012, **7**, 344-366.

125. A. Moezzi, A. M. McDonagh and M. B. Cortie, *Chemical Engineering Journal*, 2012, **185–186**, 1-22.

126. R. R. Hasiguti and E. Yagi, *Physical Review B*, 1994, **49**, 7251-7256.

127. L.-c. Ji, L. Huang, Y. Liu, Y.-q. Xie, F. Liu, A.-y. Liu and W.-z. Shi, *Thin Solid Films*, 2011, **519**, 3789-3791.

128. Y. J. Kim, M. H. Lee, H. J. Kim, G. Lim, Y. S. Choi, N.-G. Park, K. Kim and W. I. Lee, *Advanced Materials*, 2009, **21**, 3668-3673.

129. S. Costacurta, L. Biasetto, E. Pippel, J. Woltersdorf and P. Colombo, *Journal of the American Ceramic Society*, 2007, **90**, 2172-2177.

130. P. C. Angelomé, M. C. Fuertes and G. J. A. A. Soler-Illia, *Advanced Materials*, 2006, **18**, 2397-2402.

131. C. Kuo and S. Lu, *Nanotechnology*, 2008, **19**, 095705.

132. G.-S. Shao, L. Liu, T.-Y. Ma and Z.-Y. Yuan, *Chemical Engineering Journal*, 2011, **174**, 452-460.

133. Y. Cao, Y. Bai, Q. Yu, Y. Cheng, S. Liu, D. Shi, F. Gao and P. Wang, *The*

Journal of Physical Chemistry C, 2009, **113**, 6290-6297.

134. E. J. W. Crossland, N. Noel, V. Sivaram, T. Leijtens, J. A. Alexander-Webber and H. J. Snaith, *Nature*, 2013, **495**, 215-219.

135. K. S. Novoselov, A. K. Geim, S. V. Morozov, D. Jiang, Y. Zhang, S. V. Dubonos, I. V. Grigorieva and A. A. Firsov, *Science*, 2004, **306**, 666-669.

136. Z.-S. Wu, G. Zhou, L.-C. Yin, W. Ren, F. Li and H.-M. Cheng, *Nano Energy*, 2012, **1**, 107-131.

137. S. Yang, X. Feng and K. Müllen, *Advanced Materials*, 2011, **23**, 3575-3579.

138. M. F. Craciun, S. Russo, M. Yamamoto and S. Tarucha, *Nano Today*, 2011, **6**, 42-60.

139. A. Peigney, C. Laurent, E. Flahaut, R. R. Bacsa and A. Rousset, *Carbon*, 2001, **39**, 507-514.

140. I. C. Robin, A. Jouini, C. Tavares, J. Rothman, G. Feuillet, D. Ehrentraut and T. Fukuda, *J Korean Phys Soc*, 2008, **53**, 2888-2892.

141. Y. H. Ng, I. V. Lightcap, K. Goodwin, M. Matsumura and P. V. Kamat, *The Journal of Physical Chemistry Letters*, 2010, **1**, 2222-2227.

142. N. J. Bell, Y. H. Ng, A. Du, H. Coster, S. C. Smith and R. Amal, *The Journal of Physical Chemistry C*, 2011, **115**, 6004-6009.

143. J. Du, X. Lai, N. Yang, J. Zhai, D. Kisailus, F. Su, D. Wang and L. Jiang, *ACS Nano*, 2010, **5**, 590-596.

144. D. W. Zhang, X. D. Li, H. B. Li, S. Chen, Z. Sun, X. J. Yin and S. M. Huang, *Carbon*, 2011, **49**, 5382-5388.

145. R. Cruz, D. A. Pacheco Tanaka and A. Mendes, *Solar Energy*, 2012, **86**, 716-724.

146. M.-H. Yeh, C.-L. Sun, J.-S. Su, L.-Y. Lin, C.-P. Lee, C.-Y. Chen, C.-G. Wu, R. Vittal and K.-C. Ho, *Carbon*, 2012, **50**, 4192-4202.

147. T.-D. Nguyen-Phan, V. H. Pham, E. W. Shin, H.-D. Pham, S. Kim, J. S. Chung, E. J. Kim and S. H. Hur, *Chemical Engineering Journal*, 2011, **170**, 226-232.

148. B. Tang and G. Hu, *Journal of Power Sources*, 2012, **220**, 95-102.

149. Z. Liu, J. T. Robinson, X. Sun and H. Dai, *Journal of the American Chemical Society*, 2008, **130**, 10876-10877.

150. D. Li, M. B. Muller, S. Gilje, R. B. Kaner and G. G. Wallace, *Nat Nano*, 2008, **3**, 101-105.

151. G. I. Titelman, V. Gelman, S. Bron, R. L. Khalfin, Y. Cohen and H. Bianco-Peled, *Carbon*, 2005, **43**, 641-649.

152. T. N. Murakami and M. Grätzel, *Inorganica Chimica Acta*, 2008, **361**, 572-580.

153. K. Imoto, K. Takahashi, T. Yamaguchi, T. Komura, J.-i. Nakamura and K. Murata, *Solar Energy Materials and Solar Cells*, 2003, **79**, 459-469.

154. L. Kavan, J. H. Yum and M. Grätzel, *ACS Nano*, 2010, **5**, 165-172.

155. A. Gray, M. Balooch, S. Allegret, S. D. Gendt and W.-E. Wang, *Journal of Applied Physics*, 2008, **104**, 053109.

156. M. Freitag, *Nat Nano*, 2008, **3**, 455-457.

157. R. Czerw, B. Foley, D. Tekleab, A. Rubio, P. M. Ajayan and D. L. Carroll, *Physical Review B*, 2002, **66**, 033408.

158. J. W. G. Wilder, L. C. Venema, A. G. Rinzler, R. E. Smalley and C. Dekker, *Nature*, 1998, **391**, 59-62.

159. IEC-61646, *Thin-film terrestrial photovoltaic (PV) modules - Design qualification and type approval*, 2008.

160. M. I. Asghar, K. Miettunen, J. Halme, P. Vahermaa, M. Toivola, K. Aitola and P. Lund, *Energy & Environmental Science*, 2010, **3**, 418-426.

161. R. Harikisun and H. Desilvestro, *Solar Energy*, 2011, **85**, 1179-1188.

162. L. Tao, Z. Huo, Y. Ding, Y. Li, S. Dai, L. Wang, J. Zhu, X. Pan, B. Zhang, J. Yao, M. K. Nazeeruddin and M. Gratzel, *Journal of Materials Chemistry A*, 2015, **3**, 2344-2352.

163. P. M. Sommeling, M. Späth, H. J. P. Smit, N. J. Bakker and J. M. Kroon, *Journal of Photochemistry and Photobiology A: Chemistry*, 2004, **164**, 137-144.

164. P. Wang, S. Zakeeruddin, J. Moser, M. Nazeeruddin, T. Sekiguchi and M. Grätzel, *Nat Mater*, 2003, **2**, 402-407.

165. A. Hinsch, J. Kroon, R. Kern, I. Uhlendorf, J. Holzbock, A. Meyer and J. Ferber, *Progress in Photovoltaics: Research and Applications*, 2001, **9**, 425-438.

166. M. Toivola, J. Halme, L. Peltokorpi and P. Lund, *International Journal of Photoenergy*, 2009, **2009**, 15.

167. K. Miettunen, J. Halme and P. Lund, *The Journal of Physical Chemistry C*, 2009, **113**, 10297-10302.

168. M. Ikegami, J. Suzuki, K. Teshima, M. Kawaraya and T. Miyasaka, *Solar Energy Materials and Solar Cells*, 2009, **93**, 836-839.

169. W. J. Lee, E. Ramasamy, D. Y. Lee and J. S. Song, *Solar Energy Materials and Solar Cells*, 2008, **92**, 814-818.

170. E. Ramasamy, W. J. Lee, D. Y. Lee and J. S. Song, *Applied Physics Letters*, 2007, **90**, 173103.

171. N. Papageorgiou, W. Maier and M. Grätzel, *Journal of The Electrochemical Society*, 1997, **144**, 876-884.

172. W. Kubo, S. Kambe, S. Nakade, T. Kitamura, K. Hanabusa, Y. Wada and S. Yanagida, *The Journal of Physical Chemistry B*, 2003, **107**, 4374-4381.

173. B. Macht, M. Turrión, A. Barkschat, P. Salvador, K. Ellmer and H. Tributsch, *Solar Energy Materials and Solar Cells*, 2002, **73**, 163-173.

174. F. O. Lenzmann and J. M. Kroon, *Advances in OptoElectronics*, 2007, **2007**, ID 65073.

175. J. M. Kroon, N. J. Bakker, H. J. P. Smit, P. Liska, K. R. Thampi, P. Wang, S. M. Zakeeruddin, M. Grätzel, A. Hinsch, S. Hore, U. Würfel, R. Sastrawan, J. R. Durrant, E. Palomares, H. Pettersson, T. Gruszecki, J. Walter, K. Skupien and G. E. Tulloch, *Progress in Photovoltaics: Research and Applications*, 2007, **15**, 1-18.

176. H. Greijer Agrell, J. Lindgren and A. Hagfeldt, *Solar Energy*, 2003, **75**, 169-180.

177. H. Pettersson and T. Gruszecki, *Solar Energy Materials and Solar Cells*, 2001, **70**, 203-212.

178. M. K. I. Senevirathna, P. K. D. D. P. Pitigala, E. V. A. Premalal, K. Tennakone, G. R. A. Kumara and A. Konno, *Solar Energy Materials and Solar Cells*, 2007, **91**, 544-547.

179. M. Ye, X. Wen, M. Wang, J. Iocozzia, N. Zhang, C. Lin and Z. Lin, *Materials Today*, 2015, **18**, 155-162.

180. F. Kong, S. Dai and K. Wang, *Advances in OptoElectronics*, 2007, **2007**, 75384.

CHAPTER 2

Development and Optimization of a laser sealing process for DSC devices

"No man is an island"

John Donne

Adapted from the peer-reviewed article

F. Ribeiro, **J. Maçaira**, R. Cruz, J. Gabriel, L. Andrade, A. Mendes, *Laser assisted glass frit sealing of dye-sensitized solar cells.* Solar Energy Materials and Solar Cells, 2012. **96**(1): p. 43-49.

and international patent

A. Mendes, L. Andrade**,** J. Mendes, F. Ribeiro, **J. Nogueira** "*Substrate and electrode for solar cells and the corresponding manufacturing process*", PCT/IB2012/051376 and WO2012/127443, 2012.

2

Development and Optimization of a Laser Sealing Process for DSC devices

2.1 Introduction

Long-term stability is a basic requirement for all solar cell technologies. Despite all the efforts to enhance DSCs performance, long-term stability is still a major issue that limits market implementation. In fact, for building-integrated photovoltaic (BIPV) applications it is expectable that DSCs performance remains stable for no less than 25 years[1]. The long-term stability problem of DSCs is directly related to the commonly employed sealing methods, which use thermoplastic sealants such as Surlyn® or Bynel®. Although being the most used sealants, they originate poor device encapsulation with consequent contamination with external oxygen and humidity and electrolyte leakage, which result in quite reduced DSC lifetime.

Other sealing methods are also used to encapsulate DSCs[2-7], such as the thermo-compressive glass frit bonding process[8, 9]. This sealing method is quite interesting since it has been demonstrated that lead-free glass frits are thermal and mechanical stable barriers, as well as chemically inert towards the electrolyte. However, the thermo-compressive method requires the use of high processing temperatures (> 440 °C) and long process times with mechanical pressure to ensure an appropriate sealing[2,9]. This

results in high manufacturing costs and process complexity, which compromises the expected low cost of DSCs.

The present work focuses on the development of an innovative laser-assisted glass frit sealing process. It is proposed a cost-effective, fast and leak-free sealing process for DSCs. Lasers are used in a wide range of bonding processes[10-13], such as low temperature direct glass bonding[14] and pulsed laser for direct joining glass substrates[11]. However, these processes cannot be used in DSCs devices since photoelectrode and counter-electrode should be spaced by *ca*. 40 µm. In the present work an intermediate layer is used that acts simultaneously as spacer and as sealing layer. This bonding layer consists of a commercial low melting point glass frit paste that upon laser melting allows glass-glass-glass sealing. This glass sealing has to be performed at a substrate temperature such as tensions originated by differential thermal expansions are dissipated. This temperature is, however, significantly lower than the temperature required in thermo-compressive bonding methods. The feasibility of this laser-assisted glass frit paste sealing procedure is investigated and the optimized laser operating conditions are discussed. Different tests were performed to the sealed samples and conclusions are drawn concerning the quality of the implemented solutions.

2.2 Materials and methods

2.2.1   Glass frit sealant

The presence of a liquid electrolyte in DSCs requires that a hermetic sealing is obtained to reach long term stability. Thus, the sealing material has to meet several requirements[15]:

- chemical stability in contact with the corrosive liquid electrolyte;
- excellent barrier properties and particularly no permeability towards water and oxygen;
- good adhesion to the TCO glass;
- processing compatibility with DSC components (maximum process temperatures of PE and CE are *ca*. 500 ºC and 450 ºC, respectively);
- thermal expansion similar to the TCO glass substrates;

- low melting point;
- high absorbance to the wavelength of the laser beam.

Glass frits are glass powders usually milled into grain sizes lower than 15 μm. Then, they are transformed into a printable paste by mixing organic binders and solvents. A mixture of a lead-free bismuth borosilicate-based glass frit paste (AGC-ASAHI glass Company, Ltd) was used – Table 2.1. According to the manufacturer, the glass paste has a thermal expansion coefficient (ψ) of 7.5×10^{-6} °C^{-1}, which closely matches the standard glass substrates of DSCs (soda-lime glass, 8.3×10^{-6} °C^{-1} to 8.9×10^{-6} °C^{-1} [16]). This characteristic is particularly important because the final PV device is subjected to temperature variations that cause materials to expand and contract throughout its lifetime; these mechanical expansions stress the bonding interface usually causing micro fissures that eventually originate sealing failures[16]. Figure 2.1 shows the particle size distribution of the glass paste used (Beckman Coulter LS^{TM} 230 particle size analyzer). A bimodal distribution was determined with particle sizes between 30 nm and 3.0 μm.

Table 2.1 Properties of the chosen glass paste (as provided from manufacturer)

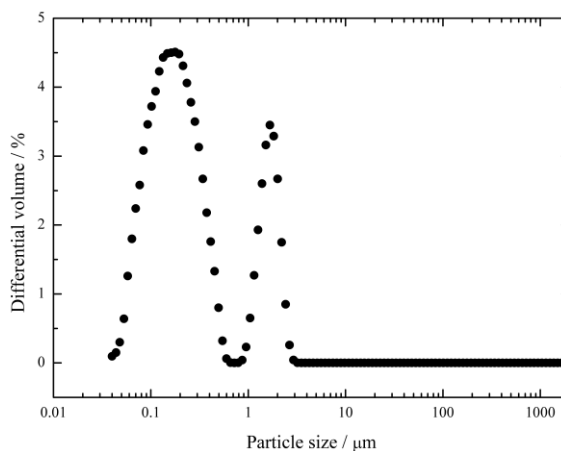| Glass paste	Glass type	Firing condition/ °C-min	ψ x10^{-6} / °C^{-1}	T_g / °C	T_s / °C	Viscosity / Pa·s
5115HT1	$SiO_2 \cdot BiO_3 \cdot ZnO$	450-10	7.5	355	415	140

Figure 2.1 Size distribution of the glass frit particles present in the glass paste.

The glass substrates used were 2.2 mm thick soda-lime based (TEC15 from Dyesol, Ltd) coated with a conductive fluorine doped tin dioxide layer, SnO_2:F (*ca.* 500 nm and 15Ω·□$^{-1}$). Before deposition of the glass paste on the glass substrates, these were washed sequentially with a detergent solution (Alconox®, VWR) in an ultrasonic cleaner (Amsonic TTC 2530) at 55 ºC for 15 min, followed by ultrasonic cleaning in deionized water at room temperature and dried with air at 50 ºC. Afterwards, they were additionally cleaned for 20 min in a UV/O_3 system (UVO-Cleaner® model 42-220). The glass paste was homogenized on a mixer mill (Retsch® MM mill) using a zirconium oxide grinding jar with zirconium oxide balls before use. The deposition of the glass paste was done by screen-printing using a screen made of a stainless steel net 200 mesh/in coated with a suitable resin. This printing technique provides precise deposition of the glass paste perimeter with the shape and dimensions required to form the seal and spacer of the solar cell. Glass paste rectangles with dimensions of 18.5 × 8.5 mm^2 and 0.8 mm width were screen-printed on the FTO face of the glass substrates. The printed height of the glass paste was about 40 μm, which provides adequate gap between sealed electrodes to hold the PE and CE materials.

2.2.2   Glass paste thermal conditioning

Before the electrode assembly and the actual sealing, a thermal conditioning of the glass paste was carried out. The electrodes were fired at 450 ºC during 10 min, according to the manufacturer specifications shown in Table 2.1. Nonetheless the thermal conditioning had to be optimized beyond manufacturer specifications to get a void-free sealing cord between both FTO-coated glass substrates. Figure 2.2 shows the thermal conditioning tests conducted for obtaining a void-free sealing cord between both FTO-coated glass substrates. Organic binders and volatile solvents present in the glass paste provide an appropriate rheology suitable to the screen-printing deposition process; however, they are not required for the glass-glass bonding process. If traces of solvents and organics are still present in the paste when the glass/glass frit melting takes place, the final sealing between glasses will have voids left by the evaporation of these components, which compromise its robustness. Therefore the pre-conditioning step is crucial for obtaining a void-free sealing cord between both FTO-coated glass

substrates. The thermal conditioning tests performed, shown in Figure 2.2, started with the manufacturer specifications (test A, 450 ºC during 10 min) and were gradually upgraded to get a sealing cord free of voids (test E). Figure 2.3 shows images comparing the final appearance of a glass cord submitted to test A heating profile (Figure 2.3 a and c) and test E (Figure 2.3b and d). It was found out that intermediate steps are essential for efficiently remove all solvents and organics from the glass paste. The best thermal conditioning profile (test E) considers a step at 250 ºC for 30 min to drive out the solvents, followed by an organic burn out at 350 ºC for 30 min and glass frit glazing at 470 ºC for 30 min until the surface has a glossy appearance.
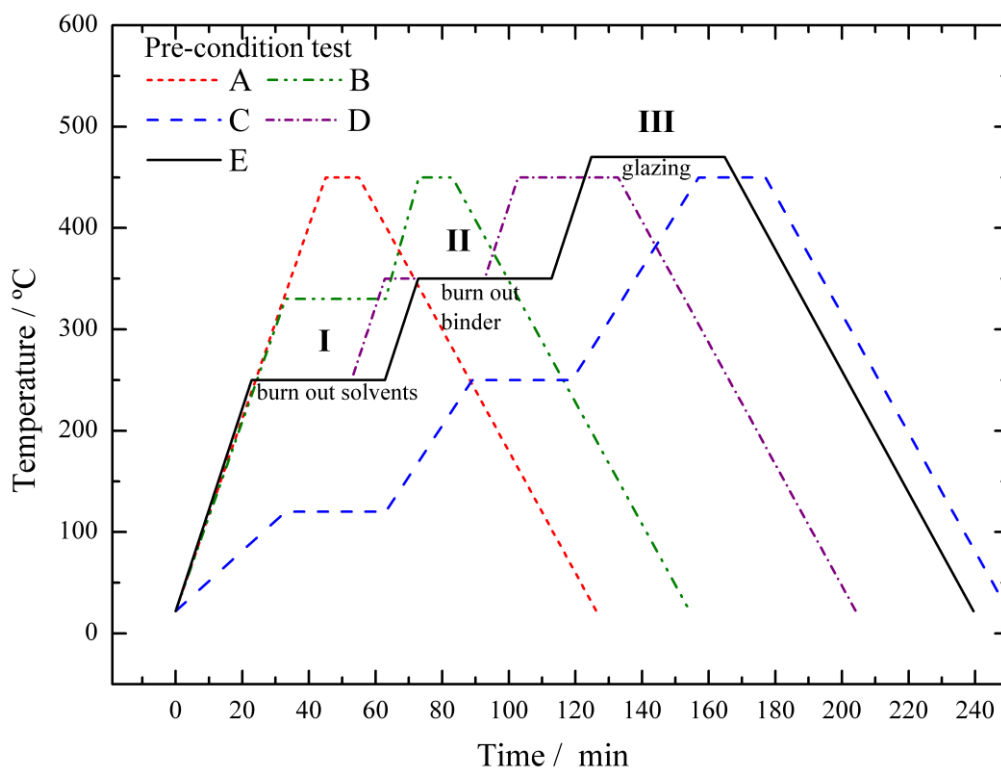

Figure 2.2 Optimization of the thermal conditioning history applied to the printed glass paste.
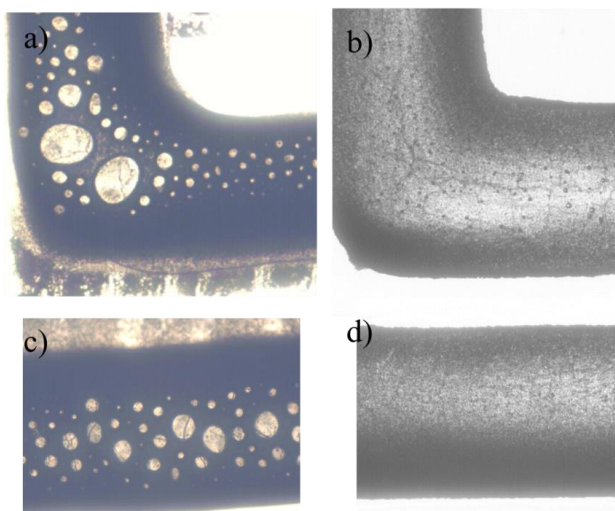
Figure 2.3 Micrographs (50x) taken to the laser assisted sealed sample with glass paste thermal conditioning: a) and c) according to manufacturer specifications (test A in Figure 2.2); b) and d) with the optimized thermal conditioning (test E in Figure 2.2).

2.2.3 LaserBox equipment

The sealing process takes place in an in-house made "LaserBox" equipment shown schematically in Figure 2.4. LaserBox comprises a laser source connected to a laser-scan head using an optic fiber and a controlled heating plate. Ytterbium fiber-delivery laser diode array (IPG photonics) with a wavelength of 1080 nm was used. The 2D optical scan head directs the laser beam through f-theta lens to the sample on top of the heating plate. The scan head software application Waverunner® allows controlling the laser shooting pattern as well as the beam velocity. An in-house developed National Instruments LabVIEW® application was used to control and acquire the laser source parameters during operation (laser power, firing time, laser temperature, *etc.*) – Figure B.1 and B.2 in shown appendix. Parallel to the laser and scan head control software, a PID algorithm ran in another LabVIEW® application to control the heated plate temperature (T_5) and to acquire the signal of four K-type thermocouples that were placed in different locations of the sample (T_1 to T_4) to record the temperature histories during the sealing process. A picture of the LaserBox is shown in Figure 2.5.
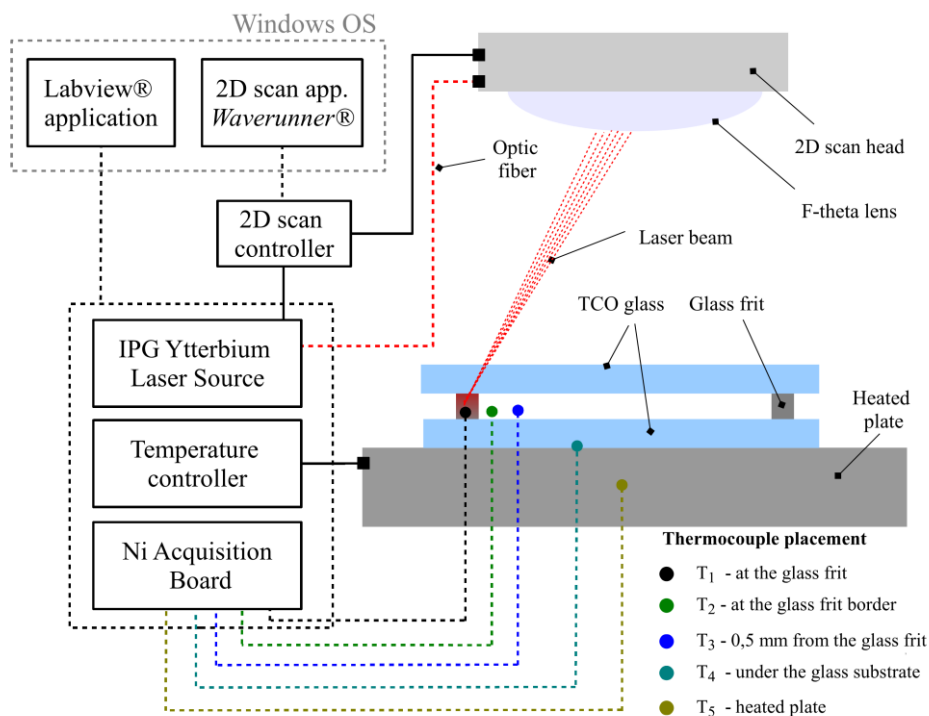
Figure 2.4 Schematic diagram of the LaserBox used for sealing DSC devices.

Figure 2.5 Photograph of the LaserBox equipment where the laser assisted sealing process is conducted.

2.2.4　Sealing Procedure

Following the glass paste thermal conditioning, the substrates with the glass paste (Figure 2.6a) were aligned and assembled together (Figure 2.6b). The sandwiched cells were then transferred to the "LaserBox" and placed on the controlled heating plate. A heating rate of 10 °C·min^{-1} was applied up to end temperature to avoid the formation of internal tensions in the glass substrates during the laser sealing process[16]. After thermal equilibration of the sealing cell is obtained, the laser beam is pointed to the glass frit perimeter and fired following a specific scan pattern described elsewhere[17].

After laser sealing, the heating plate is turned off and samples cool down to room temperature. For comparison purposes, Surlyn® sealed cells were also prepared. Commercial Surlyn® sealing film with thickness of 25 μm (Meltonix 1170-25, Solaronix) was laser cut (Versalaser VLS 2.30) to match the exact dimensions of the glass paste cord used in the laser assisted sealing method. Glass substrates were sealed in a hot press at 160 ºC, by applying 10 bar for 20 seconds.
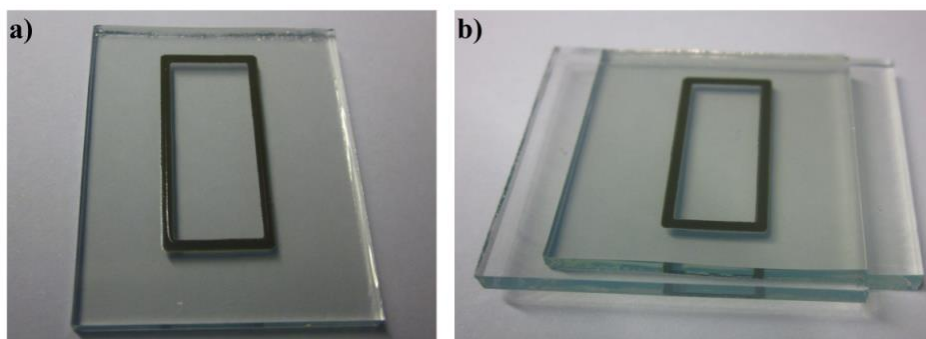
Figure 2.6 Picture of FTO glass substrates a) with printed glass paste and b) the assembled glass substrates spaced by glass frit sealant.

2.2.5　Thermal cycling tests

To determine the ability of the sealed samples to withstand thermal mismatch, fatigue and other stresses caused by repeated temperature changes, temperature cycling tests were conducted in a thermal chamber Aralab FitoClima 300 (Figure 2.7a). The test followed the international standard IEC 61646 for thin-film terrestrial PV modules, which requires 200 cycles to be performed. Each cycle consists on temperature ranging

from -40 ℃ to 85 ℃, with heating and cooling rates of 1.5 ℃·min⁻¹and 10 min of dwell time - Figure 2.7.
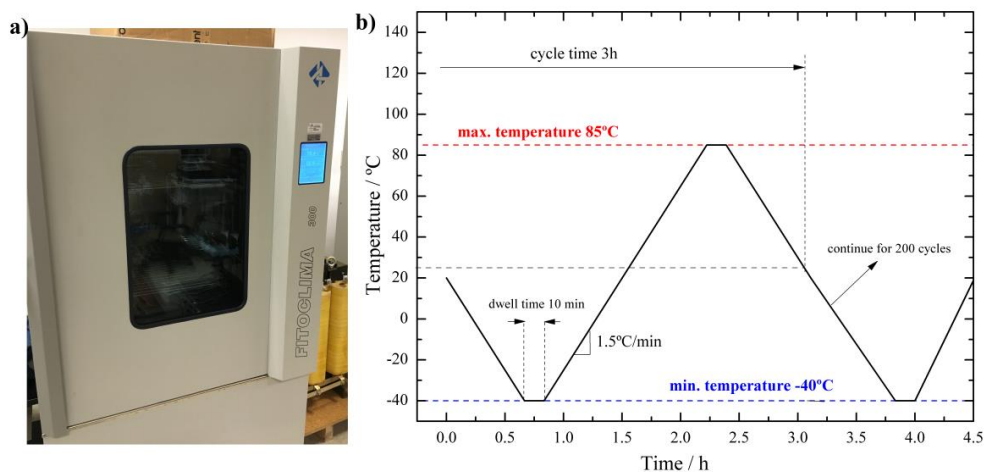
Figure 2.7 a) Thermal chamber Aralab FitoClima 300 where thermal cycling tests were performed and b) cycle characteristics according to international standard IEC 61646.

2.2.6 Leak and shear stress tests

Leak tests were performed using helium gas to determine the effectiveness and tightness of the seal. There are several standard leakage tests but none of them refer to photovoltaic devices such as DSCs. Therefore, the tests performed followed a procedure described in the MIL-STD-883H test method standard (method 1014.13-A1) for microcircuits suitable for use within military and aerospace electronic systems (US Department of Defense). The experimental apparatus required for the procedure is shown in Figure 2.8 and considers a pressure chamber (C_1), a vacuum chamber (C_2) and a mass spectrometer-type leak detector (Alcatel, ASM 142 D). The volume of the chamber used for leak rate measurement should be held to the minimum practical, since this chamber volume has an adverse effect on sensitivity limits.
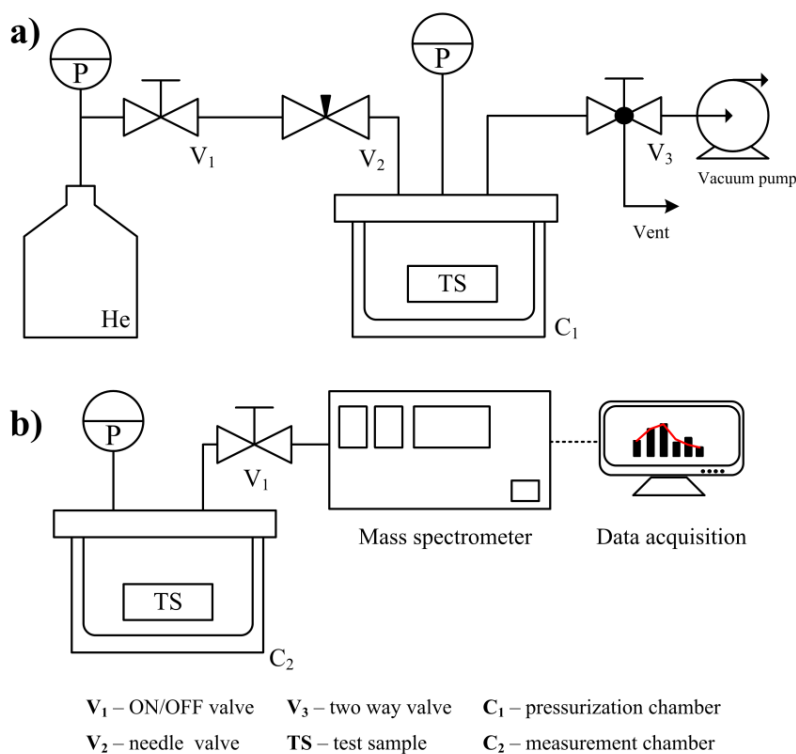
Figure 2.8 Experimental setup for leak rate determination according to the MIL-STD-883H test method standard: a) pressurization step and b) helium leak measurement.

The sealed device is placed in chamber C_1 to which is applied vacuum and then pressurized with a tracer gas of 97.5 ± 2.5 % purity helium for the required time (t_1) and pressure (P_1). The pressure is then relieved and each specimen transferred (the transfer must occur within a maximum interval of time of t_2) to the next chamber (C_2), which is connected to the evacuating system and a mass-spectrometer leak detector. When the chamber is evacuated, any tracer gas which was previously forced into the specimen inner volume will thus be drawn out and analyzed by the leak detector (R_1). The cells were tested using the appropriate conditions specified in the MIL-STD-883H standard (Table 2.2) for the cavity volume of the package under test (~0.006 cm^3): 75 Psia (5.2 bar) for 4 h and maximum dwell time of 1 h.

Table 2.2 Leak test conditions according to MIL-STD-883H

Package volume/ cm^3	Pressure / Psia $\pm$ 2	Minimum exposure time (t_1) / h	Maximum dwell (t_2) / h	Reject limit atm cm^3/s He
<0.05	75	2	1	5 x 10^{-8}
>0.05 - <0.5	**75**	**4**	**1**	**5 x 10^{-8}**
>0.5 - <1.0	45	2	1	1 x 10^{-7}
>1.0 - <10.0	45	5	1	5 x 10^{-8}
>10.0 - <20.0	45	10	1	5 x 10^{-8}

The shear stress tests are essential to assess the mechanical resistance of the devices. They are particularly important to determine the future PV device ability to withstand wind, snow and ice loads. The tests were performed according to International standard ISO 13445 ("Adhesives – Determination of shear stress of adhesive bonds between rigid substrates by block-shear method"). The test specimens were 90 x 30 mm^2 glass devices sealed with 43 mm^2 of glass frit. They were subjected to mechanical shear tests by a universal traction equipment (*TIRA GmbH* universal machine) with a load cell *Typ 32 500N* from *HBM*. The traction equipment was set to 5 mm/min and a maximum transducer load of 500 N.

2.2.7 DSC performance characterization

The prepared DSCs were characterized by their current-voltage (*I-V*) curves and electrochemical impedance spectroscopy (EIS). *I-V* characteristic curves were obtained in a setup equipped with a 1600 W xenon light source (Oriel class B solar simulator, Newport, USA) with variable light intensity, from 10 to 100 mW·cm^{-2} (0.1 to 1 sun light intensity), and using a 1.5 air mass filter (Newport, USA). The simulator was calibrated using a single crystal Si photodiode (Newport, USA). The *I-V* characteristics of the solar cells were obtained applying an external potential load and measuring the generated photocurrent using an AUTOLAB electrochemical station. This station was also used to characterize the cells trough EIS. The frequency range for EIS measurements was from 100 kHz to 0.05 Hz with an AC modulation signal of 10 mV. EIS measurements were carried out in dark and at the open circuit potential (V_{oc}) measured at 1 sun.

2.3 Results and Discussion

2.3.1   Response surface methodology

The LaserBox equipment has several operating parameters and a systematic optimization should be followed to obtain the best operating conditions. A response surface methodology (RSM) implemented in commercial software (JMP 8.0.2, SAS software) was applied. This method combines mathematical and statistic tools for studying in an effective way processes where responses are dependent on several operating variables[18]. In this work the central composite design (CCD) method was considered for fitting the second order models obtained. The quality of the glass frit sealing (Q_{frit}) obtained after the laser-assisted bonding process was chosen for the working function; the glass frit quality was assessed visually and rated from 1 (worst) to 10 (best). The visual assessment took into account the final aspect of the sealed cells in terms of: damaged glass, cracks in the sealing cord, burned glass frit and bubble formation. The factors identified that affect the process response and considered for the optimization are: temperature of the heating plate where the glass samples are placed (T_p), laser power (P_l) and laser-scanning velocity (v_l). Table 2.3 shows the design factors and levels. A three factor central composite design was built with three center points. For generating the design matrices (shown in Appendix, Table A1) coded factors (X_i) ranging from -1 to +1 were used. The coded factors are computed from their actual values (x_i), middle value and the semi-variation interval as shown in equation (2.1)[19].

Table 2.3 CCD factors and respective levels.

Factor	Symbol	Level		
		-1	**0**	**1**
T_p / °C	x_1	280	305	330
P_l / W	x_2	20	35	50
v_l / mm·s^{-1}	x_3	300	400	500

$$X_1 = \frac{x_1 - 305}{25}; \ X_2 = \frac{x_2 - 35}{15}; \ X_3 = \frac{x_3 - 400}{100}; \qquad (2.1)$$

2.3.2 Process Modeling

A second order polynomial equation was fitted to the process response:

$$y = a_0 + \sum_{i=1}^{3} a_i X_i + \sum_{i=1}^{3} \sum_{j=1}^{3} \left(a_{ij} X_i X_j + a_{ii} X_i^2 \right) \qquad (2.2)$$

where y is the process response, X_i are the dimensionless process factors, a_0 is the interception coefficient, a_i are the coefficients related to the dimensionless factors X_i, a_{ij} correspond to the cross interaction between different factors and a_{ii} are the coefficients related to the quadratic effects (curvature)[20].

A standard least squares analysis was performed and the *p*-values (Prob > *F*) were used to assess the relevance of each factor to the process response, where a *p*-value smaller than 0.05 indicates a high relevance and between 0.05 and 0.15 indicates a marginal relevance. Finally, if *p*-values are higher than 0.15 the corresponding parameter has a negligible effect on the response [18]. Following this criterion the heating plate temperature (X_1) was removed from the initial model. The final model is then:

$$y = 5.700 + 2.306X_2 - 1.944X_2^2 - 1.444X_3^2 \qquad (2.3)$$

where all factors have a *p*-value smaller than 0.01.

The fitting model can be used to predict the response values within the range of the factors.

Figure 2.9 compares the predicted with the experimental results for the same operating conditions – parity plot. The plot indicates a good agreement with the experimental results.
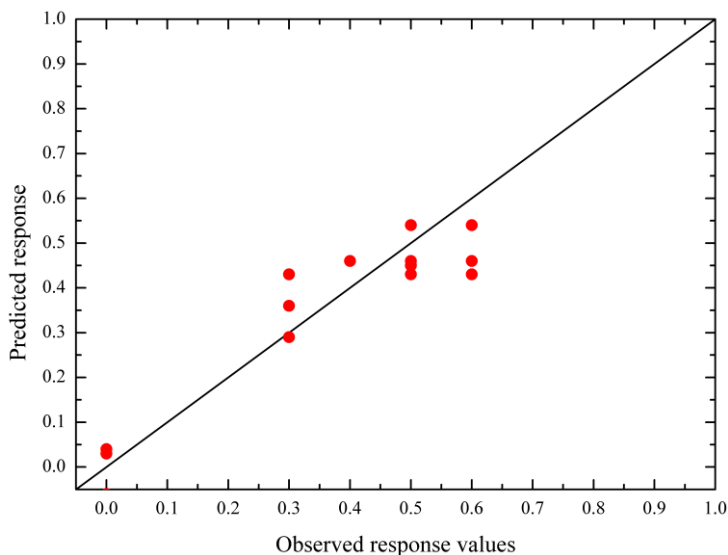
Figure 2.9. Parity graph concerning the sealing process optimization (R^2=0.87).

Based on the interpolating model, the operating conditions that produce the best glass bonding are given in Table 2.4. Although the temperature of the heating plate was not included in the model it was decided to perform the sealing at the highest possible temperature, *i.e.* 330 °C. For the optimal operating conditions, the laser beam completes a sealing loop in about 1.8 seconds. The predicted sealing quality for the operating conditions is 6.3 ± 1.0.

Table 2.4 Determined optimal operating conditions and predicted response.

Factor	value	Q_{frit}
Laser Power / W	44	
		6.3 ± 1.0
Laser scan velocity / mm·s^{-1}	400	

A new run was performed using the optimized operating conditions, resulting in very good sealed samples with high reproducibility. The experimental results were rated with relative sealing quality of 7. Figure 2.10 shows the laser sealed glass substrates sealed, alongside with a Surlyn® sealed sample for comparison.
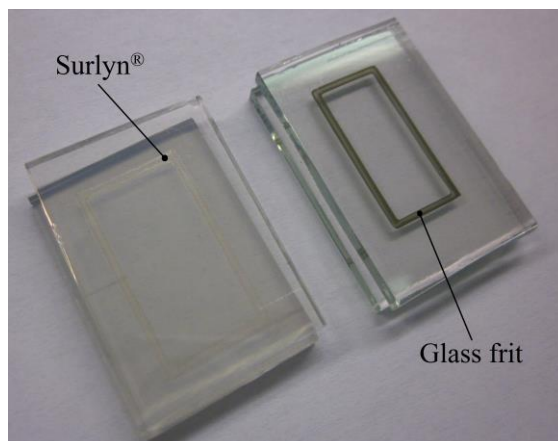
Figure 2.10 Pictures of the laser assisted sealed sample and Surlyn® sealed glass.

2.3.3   Influence of the operating conditions

The fitting equation (2.3) can be used to study the influence of the operating conditions concerning the quality of the final glass frit bonding. Figure 2.11 shows the relative sealing quality as a function of the laser velocity and laser power. Accordingly, it can be concluded that the most relevant factor in the final sealing quality is the laser power at which the sealing process takes place. Plotting the relative sealing quality as a function of the laser velocity and the laser power, a quality peak can be observed for 44 W and 400 mm·s^{-1}, respectively. Moreover, an increase of laser power during the sealing process should be followed by a laser velocity increase balancing the amount of heat delivered to the glass frit cord.
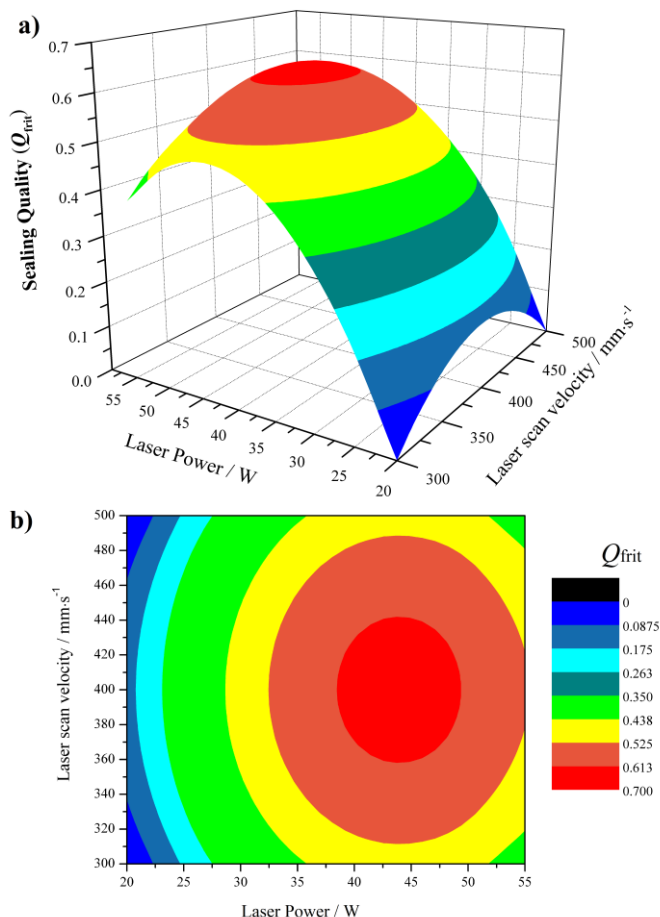
Figure 2.11 Relative sealing quality as a function of laser velocity and laser power.

2.3.4   Temperature history during the laser sealing process

Temperature history readings were obtained during the sealing process at several sample positions (T_1 to T_5) according to Figure 2.4. Figure 2.12 shows that, due to the used scan pattern[17], each position of the glass frit is hit by the laser *ca*. 14 times during the sealing of the sample. The temperature on the border of the cord (T_2) is lower than at the center of the cord (T_1), where the laser beam hits directly the paste. Lateral heating caused by the laser beam is already quite small at 1 mm away from the glass cord - Figure 2.12b. The glass paste heats significantly more than the glass substrate, due to its high absorbance in the near infra-red part of the spectrum (wavelength of the laser is 1080 nm). The optical characteristics of the glass paste and the bare TCO glass

were obtained by spectrophotometry (Shimadzu UV-3600) and their absorbance spectrum is presented in Figure 2.13.
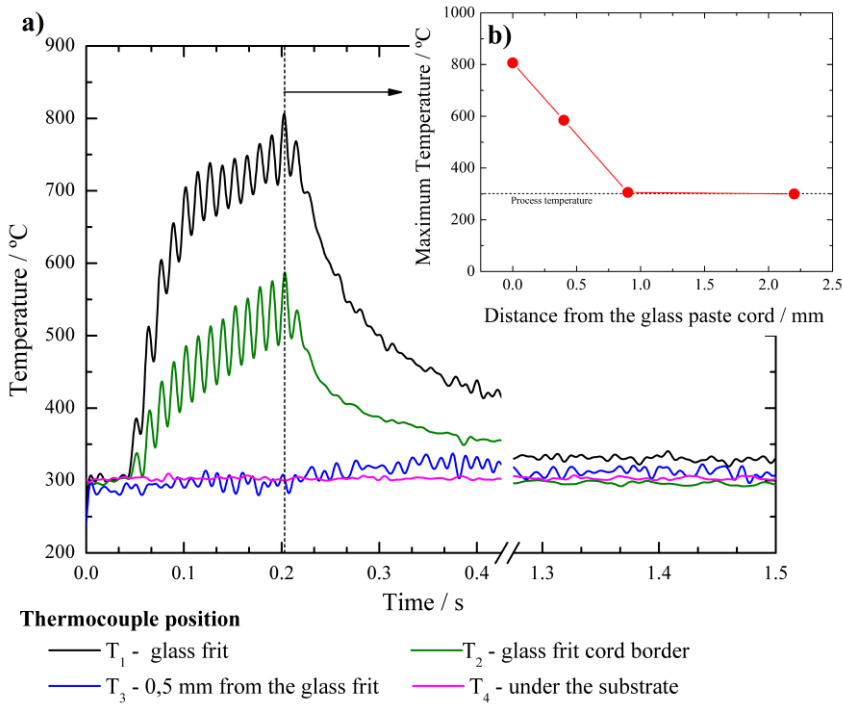

Figure 2.12 a) Temperature histories during the laser assisted sealing process, measured at different positions from the glass frit; and b) Maximum temperature recorded by the thermocouples as a function of their relative position.
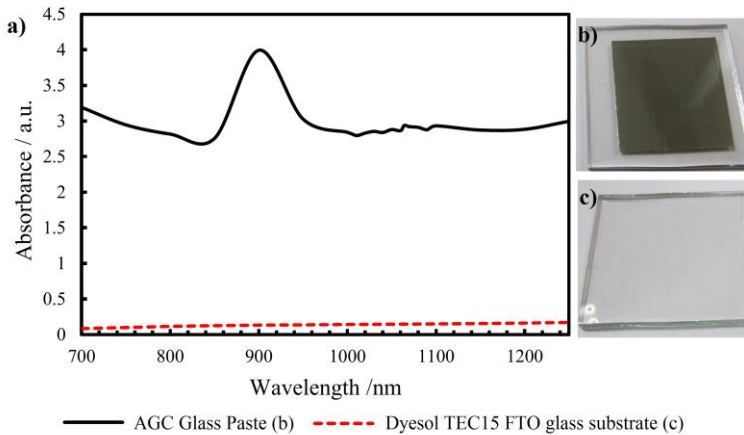
Figure 2.13 a) Near IR absorbance spectrum for the used glass paste b) and glass substrate c).

2.3.5   SEM and elemental analysis

The sealed samples were characterized by scanning electron microscopy (SEM) analysis. A glass-sealed device sealed at the best operating conditions was sectioned, polished and analyzed by SEM – Figure 2.14. The glass frit cord is free of occluded gas and has an excellent contact with both substrates with no cracks between the glass frit sealant and glass substrates. The distance between the glass substrates is 36 μm, which results in an appropriate gap between electrodes to host DSC inner components (typical TiO_2 photoanode thickness ranges from 2 to 20 μm[21, 22]).

Figure 2.14 SEM micrograph of a cross section of the glass frit cord prepared by the laser assisted process.

Elemental analysis performed along a sealed sample (Figure 2.15) confirmed the glass frit composition provided by the manufacturer: it is mainly composed of bismuth oxide matrix embedded with particles of silica, aluminum and zinc oxide. The main constituents of glass are silica, sodium and magnesium.

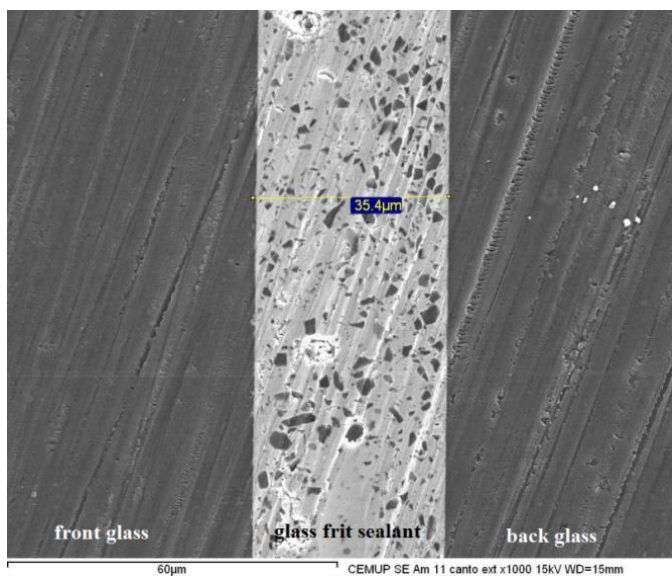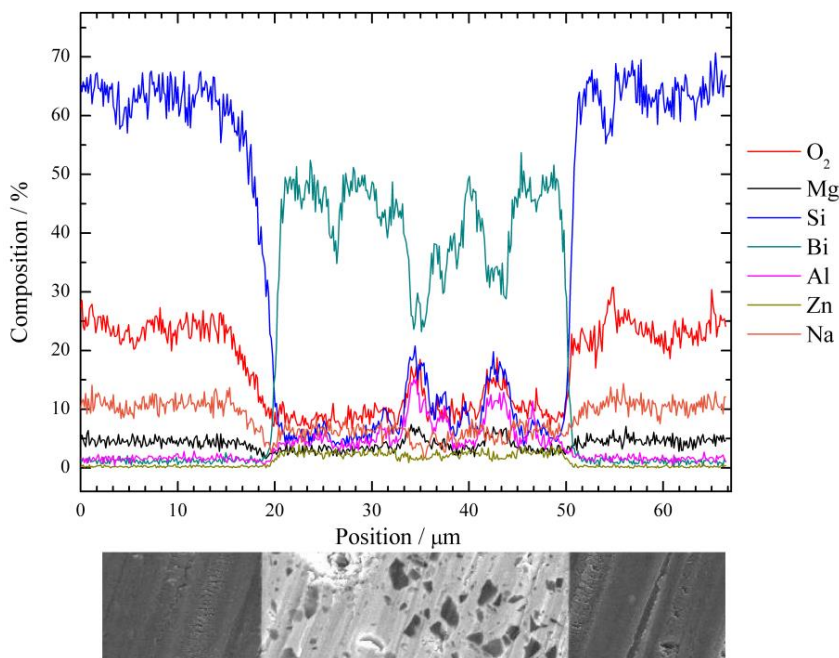**Figure 2.15** Elemental analysis profile of a cross section of a glass bonding layer using the laser assisted sealing process.

2.3.6   Leak and shear stress tests

The laser-sealed cells were tested for leakage according to standard MIL-STD-883H described previously in section 2.2.6. For comparison, Surlyn® sealed cells of similar dimensions (as shown in Figure 2.10) were also tested. Briefly, helium tracer gas was forced into the specimen inner volume, and then drawn out and analyzed by a calibrated helium mass spectrometer. Four types of analysis were performed: blank tests (air), FTO glass, Surlyn® sealed glass and laser sealed glass (LAGF). The Surlyn® sealed devices were tested right after preparation (as described in section 2.2.4); the LAGF samples were tested after enduring temperature cycling tests (200 cycles, from -40 to 85ºC as described in section 2.2.5). The results, presented in Figure 2.16, showed that the Surlyn® sealed samples exhibited the largest leakages, above the rejection limit required by standard MIL-STD-883H.   The laser sealed samples passed the encapsulation standard, even after 200 cycles of thermal cycles according to IEC 61646 for thin-film terrestrial PV modules. The results of leakage rate of LAGF

samples are comparable with plain FTO glass, which confirms the excellent encapsulation properties of the developed sealing process.
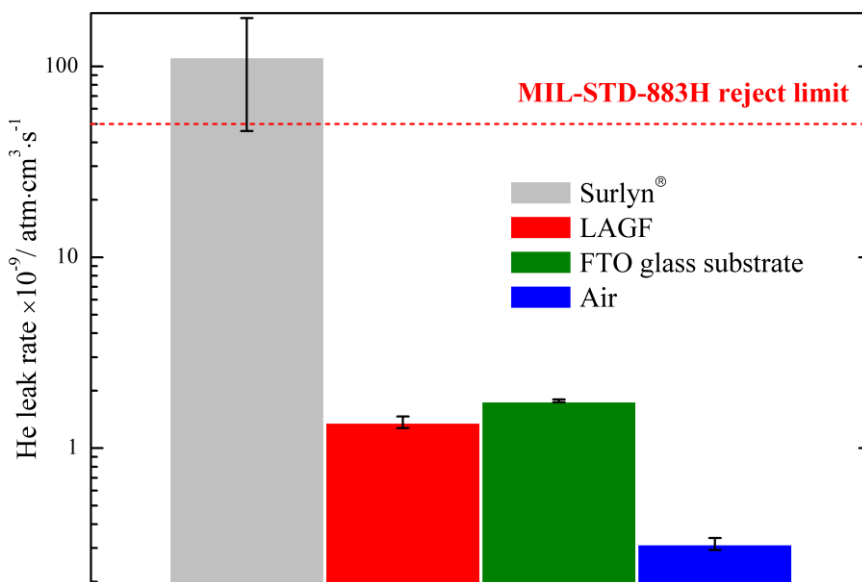
Figure 2.16 Blank leakage rate and leakage rate obtained with Surlyn® and laser-assisted sealed devices (LAGF).

The strength tests are essential to evaluate the sealing process since the bonding process must be strong enough to allow the scale up of the DSC technology. The glass frit bonding layer is tested in different segments lengths and in different directions as described in ISO 13445 (section 2.2.6). The results showed that the maximum shear stress that the glass sealed samples (18.5×8.5 mm^2 with 43 mm^2 of sealed glass frit) withstands is *ca*. 250 N. This means that the glass paste sealed cord withstands *ca*. 5.8 N·mm^{-2}. The requirement for edge seal strength for glass in buildings according to European norm EN 1279-4 is shown in Figure 2.17: sealant failure corresponds to breakage of sealant inside the red triangle. The laser sealed samples clearly passed the specified requirements, which clears the developed sealing for use as seal in BIPV.
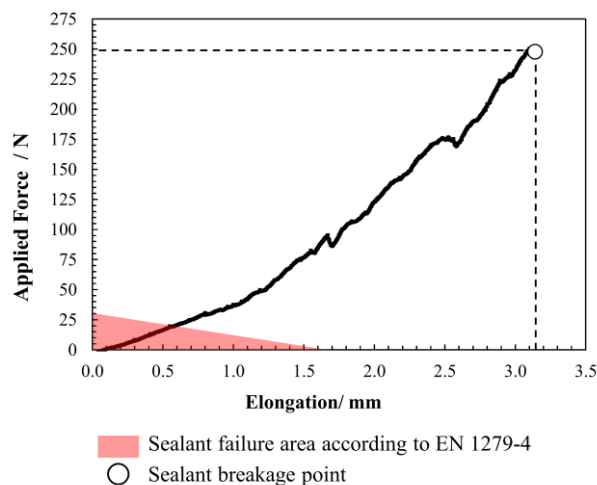
Figure 2.17 Applied force *vs*. elongation of laser sealed glass samples with 43 mm^2 of sealed area; the red triangle corresponds to the sealant failure area according to EN 1279-4.

2.4 Integration of the laser assisted process in the fabrication of DSCs

Figure 2.18 sketches a DSC and its correspondent components numbered from 1 to 10. The DSC is constituted by two sheets of glass (1 and 8) coated with a thin layer of a transparent conductive oxide (TCO, 4) usually fluorine doped tin oxide (FTO, SnO_2-F). In one of the glass sheets is deposited the mesoporous semiconductor layer (7), usually titanium dioxide where a quantity of dye molecules is adsorbed. The catalyst layer (3), normally platinum, is employed to ensure the reduction reaction of triiodide to iodide. The inner volume of the cell is filled with a liquid electrolyte (6), and is delimited by the sealing perimeter (5) that encapsulates the device and ensures the spacing between both electrodes. The counter electrode glass substrate (1) has two drilled channels (9) that connect the interior of the cell with the outside. These channels are used to perform the dye adsorption into the semiconductor (7) and electrolyte filling of the cell and are sealed using Surlyn$^®$ polymer covered by a glass lamella (10). The electrical connection to the external circuit is performed using conductive metal lines, usually of silver (2). Figure 2.18a) and b) illustrates a laser sealed dye-sensitized solar cell.
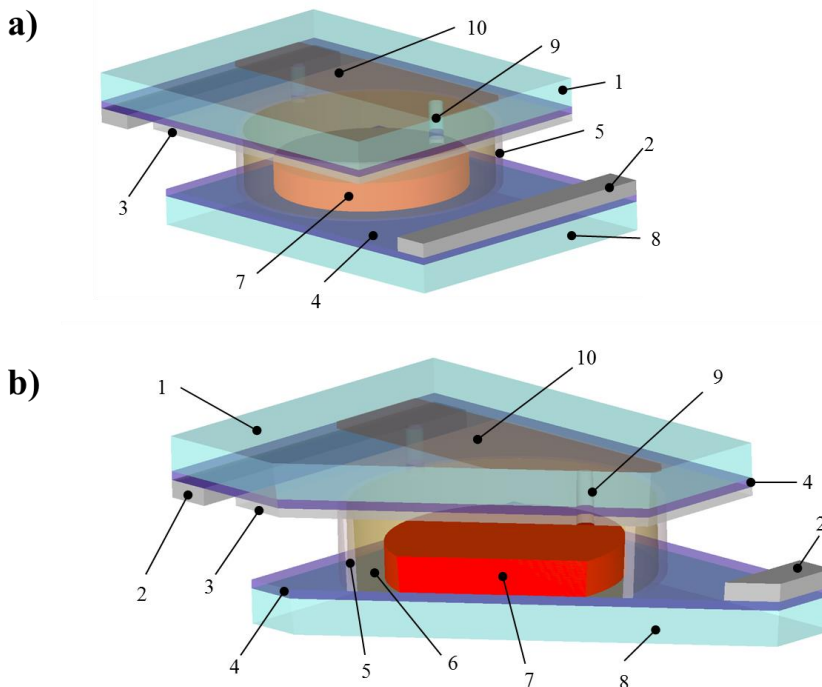
Figure 2.18 Schematic of a laser sealed dye-sensitized solar cell a) top and cross b) sectional views. 1 – counter electrode glass; 2 – electrical contact; 3 – platinum catalyst; 4 – TCO; 5 – glass frit sealing; 6 – electrolyte; 7 – TiO_2 with adsorbed sensitizer; 8 – photoelectrode glass 9 – filling hole; 10 – filling hole cover.

The optimized experimental procedure for preparing dye sensitized solar cells is summarized in Figure 2.19. Briefly, the procedure is divided into five main steps: glass preparation; screen-printing of materials and sintering; laser assisted sealing; dye adsorption; and electrolyte filling. It begins with the preparation of the glass substrates where the photo- and counter-electrodes of the solar cell will be applied. The glass must be cut to match the final dimensions of the solar cell, and then cleaned for removing any solid particles and organic compounds. For the cleaning step, a distilled water/detergent mixture is used as washing bath in an ultrasound-cleaning machine (Amsonic *TTC 2530*) followed by a UV-O_3 (UVO Cleaner model 42-220) cleaning unit, both illustrated in Figure 2.20.
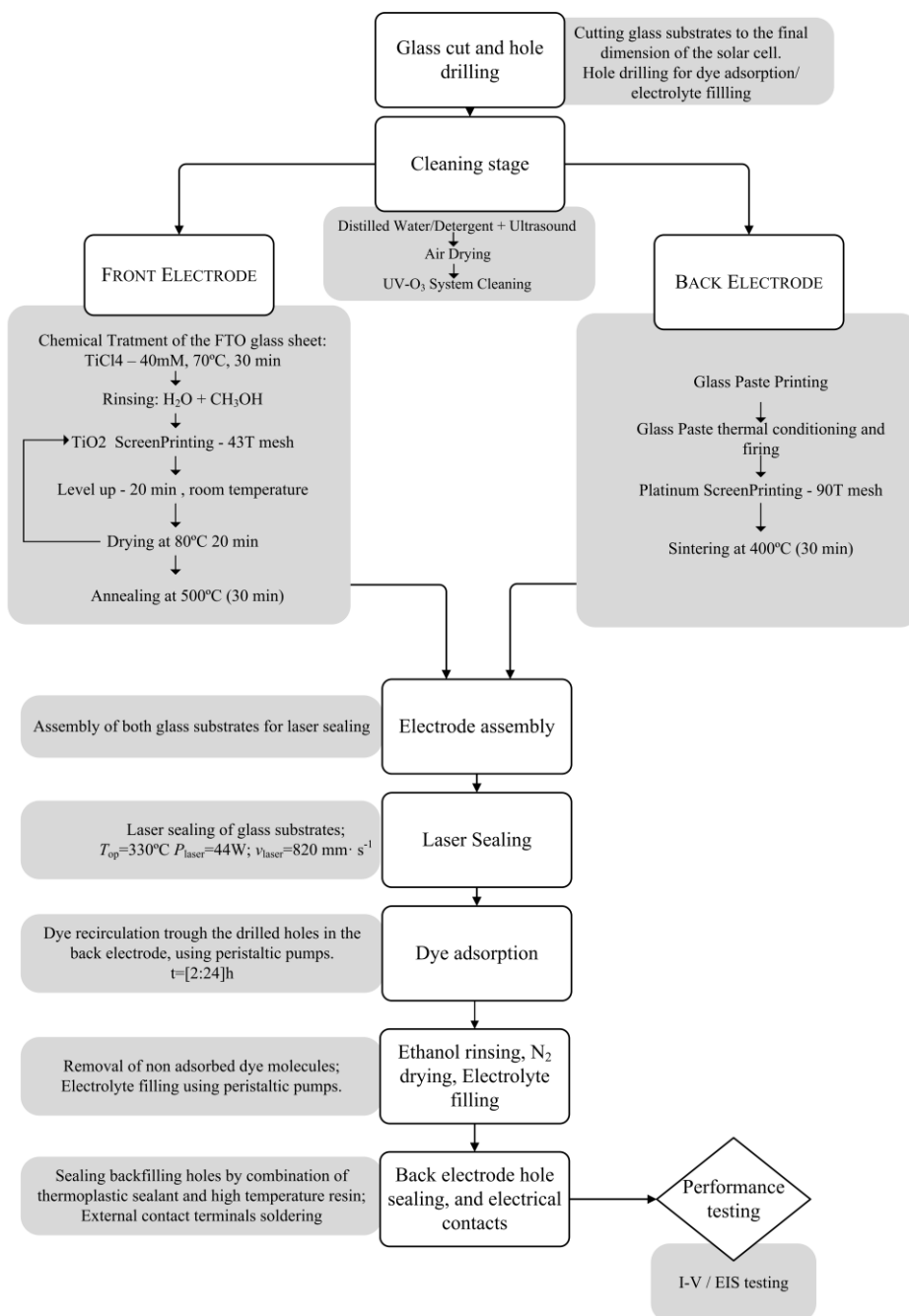
Figure 2.19 Schematic diagram of the experimental procedure for producing laser sealed DSCs.

Figure 2.20 a) Ultrasounds cleaning machine (Amsonic TTC 2530) and b) UV-O$_3$ cleaning unit (UVO Cleaner model 42-220).

After the cleaning step, the sealing material is applied by screen-printing (Rokuprint® screen printer) to the FTO glass substrates – Figure 2.21a). This technique allows a reproducible and fast deposition that is easily adaptable for different configurations and scalable for larger areas. The catalyst layer, usually a platinum paste, and the sealing material, a glass frit paste, are printed and fired sequentially on the same glass sheet, and titanium dioxide paste is printed and fired on the other glass sheet. The firing steps are carried out in a furnace (Nabertherm Gmbh model GF75 - Figure 2.21b) to remove solvents and binders present in the printed component and for sintering. Each material follows a defined sintering program, usually as recommended by the manufacturer.
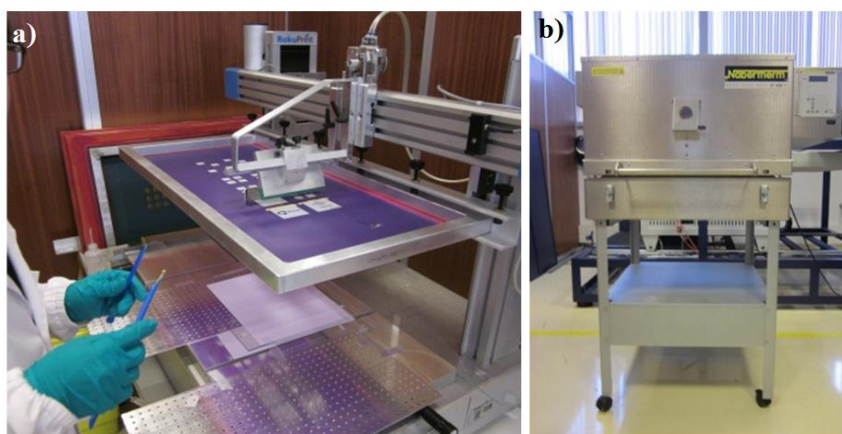
Figure 2.21 a) Rokuprint® screen printer used for printing the components of the solar cell and b) Nabertherm® furnace used for firing the printed materials.

After sealing, the samples are left to cool to the room temperate. At this stage they are glass sealed cells made of a FTO glass substrate coated with a sintered layer of titanium dioxide nanoparticles and a FTO glass substrate coated with a sintered thin layer of platinum catalyst. A dye solution is then pumped through the holes and adsorb to the inner surface of the titanium dioxide layer. After allowing the dye to adsorb to the photoelectrode, ethanol is passed through the cell to remove the unabsorbed dye molecules; nitrogen is passed at the end to dry out the cell. Finally, the cell is filled with the redox electrolyte and the holes are sealed. Figure 2.22a and b) show pictures of glass sealed dye sensitized solar cells of 2 cm^2 to 230 cm^2 of sealed area.
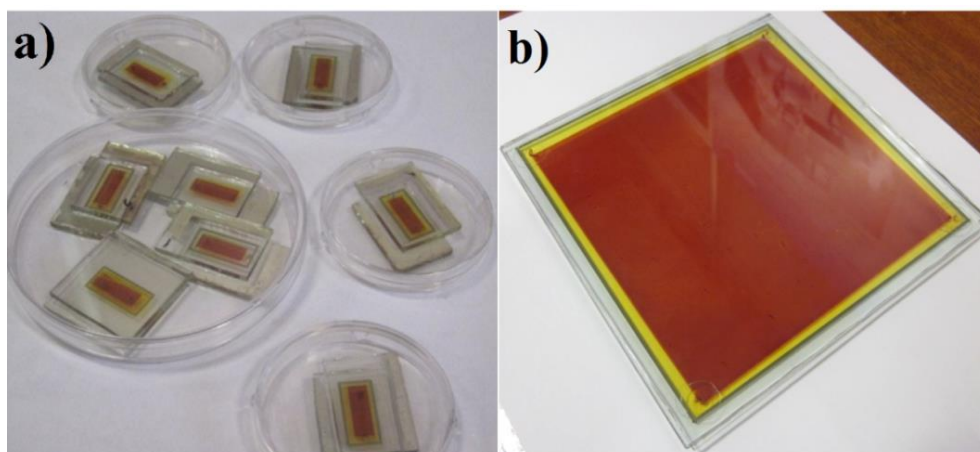
Figure 2.22 10×20 mm^2 (a) and 150×150 mm^2 (b) DSCs prepared by the described experimental procedure.

2.4.1   Sealing process influence on performance of DSC devices

The performance of a dye-sensitized solar cell sealed by the laser assisted glass frit method (LAGF) was compared to a device sealed using the conventional thermoplastic sealant (Surlyn®) - Figure 2.23. The corresponding photovoltaic parameters (short-circuit current density, J_{sc}; open circuit voltage, V_{oc}; fill factor, FF; and efficiency, η) are presented in Table 2.5.
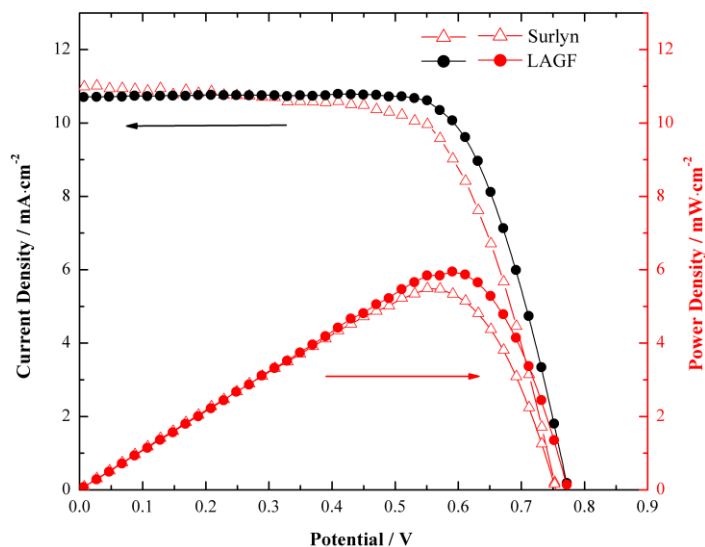
Figure 2.23   *I-V* (black) and power curves (red) of the prepared DSCs sealed by Surlyn® sealed and laser assisted glass frit sealed DSCs.

Table 2.5 DSC Performance parameters for Surlyn® sealed and laser assisted glass frit sealed DSCs.

Sealing method	Performance parameters			
	V_{oc} /V	J_{sc} / mA·cm^{-2}	FF	η / %
LAGF	0.78 ± 0.02	10.7 ± 0.05	0.71 ± 0.06	6.07 ± 0.05
Surlyn®	0.76 ± 0.04	11.0 ± 0.09	0.66 ± 0.04	5.60 ± 0.03

Although the performance parameters in Table 2.5 show there are no significant differences between both types of DSCs, to further study any possible degradation caused by the laser sealing process, the devices were analyzed by EIS. This technique allows time resolving the electrochemical processes in a DSC. Figure 2.25 shows the Nyquist (a) and Bode (b) plots obtained under dark conditions, at V_{oc} of the DSCs (-0.78 V and -0.76 V for LAGF and Surlyn®, respectively). The experimental data was fitted to appropriated electrical analogues, namely a simplified transmission line model[22,23], using ZView® (Scribner Associates Inc.). This model, proposed by Bisquert *et al.*[24], is widely used to describe the transport and recombination kinetic in DSCs.

Because the EIS analysis was conducted at the open circuit potential of the cells (V_{oc}), electron transport resistance through the TiO$_2$ layer was considered negligible. The electrical analogue is presented in Figure 2.24.
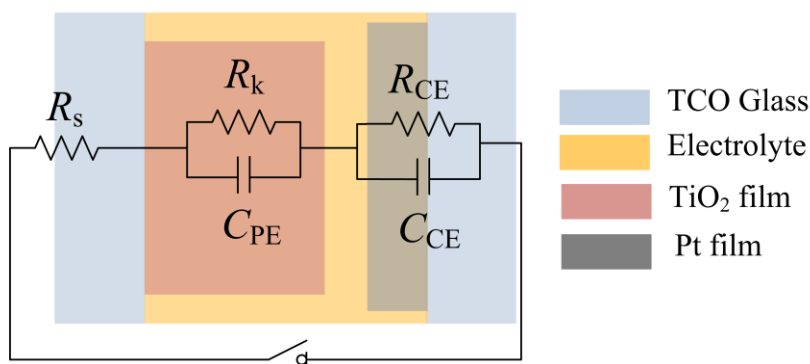
Figure 2.24 Simplified transmission line model used to fit EIS experimental data of DSCs. R_s – series resistances; R_k – recombination resistance; C_{PE} – chemical capacitance at the TiO$_2$ anode; R_{CE} – charge transfer at platinum/TCO interface; C_{CE} double layer capacitance at the platinum/TCO interface.

The Bode plot shows two frequency peaks, corresponding to the electron recombination at the photoelectrode (low frequency) and to the reduction reaction occurring at the platinum counter-electrode (high frequency). In the case of Surlyn® sealed cells the second peak is located at slightly higher frequency than the LAGF cell. This and the larger first semicircle in the Nyquist plot show that the performance of the counter electrode is marginally better in the case of the LAGF cell than in the Surlyn® sealed cell. The model parameters are shown in Table 2.6. The fitted parameters do not suggest any significant difference in both types of devices. Therefore it should be concluded that the glass sealing method allows preparing cells with the same energy efficiency of the Surlyn®-sealed cells.
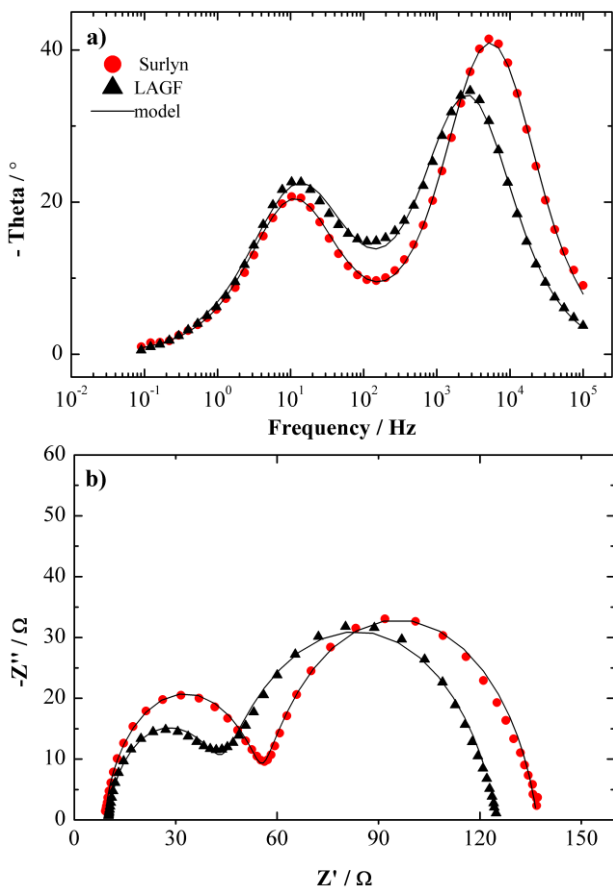
Figure 2.25 Bode a) and Nyquist b) plots obtained under dark conditions, at the V_{oc} of the DSCs (-0.78 V and -0.76V for LAGF and Surlyn®, respectively).

Table 2.6 Results obtained by fitting the EIS experimental data to the presented equivalent circuit for Surlyn® sealed and laser assisted glass frit sealed DSCs.

Sealing method	R_s /Ω	R_{CE} /Ω	C_{CE} /F	R_k /Ω	C_{PE} /F	τ_{e^-} / ms
Surlyn®	9.071	46.33	3.91×10^{-6}	80.02	4.79×10^{-4}	23.6
LAGF	10.03	32.79	1.02×10^{-5}	82.17	5.68×10^{-4}	23.4

2.5 Conclusions

Laser assisted glass encapsulation was evaluated for sealing DSC devices. A response surface methodology allowed optimizing the process parameters, where the laser power was identified as the most important factor in the process. The empiric model obtained, relating the sealing quality and the process parameters, showed a good agreement with the experimental results. Glass samples sealed by the developed process passed the following standards:

- Helium leak tests : MIL-STD-883H, "Encapsulation suitable for microcircuits for use within military and aerospace electronic systems" ;

- Thermal cycling tests : IEC 61646, "International standard for thin-film terrestrial PV modules";

- Shear strength tests: ISO 13445, "Adhesives - Determination of shear strength of adhesive bonds between rigid substrates by the block-shear method"; and EN 1279-4, "Glass in Buildings - Insulating glass units, requirements for sealants".

The substrate temperature (330 ℃) at which the laser assisted sealing takes place is lower than the maximum tolerable temperature of commonly used materials in the photoelectrode and counter-electrode layers of DSC devices, *i.e.* titanium dioxide photoelectrode (~500 °C) and platinum counter-electrode (~450 °C). The photovoltaic characterization (*I-V* and EIS analysis) of the DSCs prepared with the laser assisted glass frit sealant were similar to those obtained with the cells sealed with Surlyn®, showing no evidence that the sealing process influences the performance of DSCs. These results showed that the developed sealing process is suitable for DSC technology, and brings promise of long term stability for the technology.

Acknowledgments

References

1.   N. Kato, K. Higuchi, H. Tanaka, J. Nakajima, T. Sano and T. Toyoda, *Solar Energy Materials and Solar Cells*, 2011, **95**, 301-305.

2.   R. Sastrawan, J. Beier, U. Belledin, S. Hemming, A. Hinsch, R. Kern, C. Vetter, F. M. Petrat, A. Prodi-Schwab, P. Lechner and W. Hoffmann, *Solar Energy Materials and Solar Cells*, 2006, **90**, 1680-1691.

3.   W. J. Lee, E. Ramasamy, D. Y. Lee and J. S. Song, *J. Photochem. Photobiol. A-Chem.*, 2006, **183**, 133-137.

4.   A. J. Bard and L. R. Faulkner, *Electrochemical methods fundamentals and applications*, John Wiley & Sons, New York, 1980.

5.   H. Matsui, K. Okada, T. Kitamura and N. Tanabe, *Solar Energy Materials and Solar Cells*, 2009, **93**, 1110-1115.

6.   F. C. Krebs, *Solar Energy Materials and Solar Cells*, 2006, **90**, 3633-3643.

7.   K. Maeda, K. Teramura, D. Lu, T. Takata, N. Saito, Y. Inoue and K. Domen, *Nature*, 2006, **440**, 295-295.

8.   R. Knechtel, *Microsyst Technol*, 2005, **12**, 63-68.

9.   K. Itoh and J. O. M. Bockris, *Journal of The Electrochemical Society*, 1984, **131**, 1266-1271.

10. K. F. Tamrin, Y. Nukman and S. S. Zakariyah, *Materials and Manufacturing Processes*, 2013, **28**, 857-871.

11. W. Watanabe, S. Onda, T. Tamaki and K. Itoh, *Applied Physics B: Lasers and Optics*, 2007, **87**, 85-89.

12. A. Mathieu, R. Shabadi, A. Deschamps, M. Suery, S. Matte, D. Grevey and E. Cicala, *Optics & Laser Technology*, 2007, **39**, 652-661.

13. V. M. Aroutiounian, V. M. Arakelyan, G. E. Shahnazaryan, G. M. Stepanyan, J. A. Turner and O. Khaselev, *International Journal of Hydrogen Energy*, 2002, **27**, 33-38.

14. D. Ando, K. Oishi, T. Nakamura and S. Umeda, *Proc Ieee Micr Elect*, 1997, 186-190.

15. C. J. Brabec, V. Dyakonov, J. Parisi and N. S. Sariciftci, *Organic Photovoltaics: Concepts and Realization*, Springer Berlin Heidelberg, 2013.

16. E. L. Bourhis, *Glass: Mechanics and Technology*, Wiley, 2008.

17. PCT/IB2012/051376, 2012.

18. D. C. Montgomery, *Design and analysis of experiments*, John Wiley & Sons, New York [etc], 2001.

19. R. H. Myers and D. C. Montgomery, *Response surface methodology process and product optimization using designed experiments*, John Wiley & Sons, New York, 2002.

20. P. J. W. M.J. Anderson, *RSM Simplified: Optimizing Processes Using Response Surface Methods For Design of Experiments*, Productivity Press, New York, 2005.

21. M. Ni, M. K. H. Leung and D. Y. C. Leung, *The Canadian Journal of Chemical Engineering*, 2008, **86**, 35-42.

22. L. Andrade, S. M. Zakeeruddin, M. K. Nazeeruddin, H. A. Ribeiro, A. Mendes and M. Grätzel, *ChemPhysChem*, 2009, **10**, 1117-1124.

23. J. Bisquert, M. Gratzel, Q. Wang and F. Fabregat-Santiago, *The Journal of Physical Chemistry B*, 2006, **110**, 11284-11290.

24. J. Bisquert, *The Journal of Physical Chemistry B*, 2002, **106**, 325-333.

CHAPTER 3

Laser sealed DSCs: Efficiency and Long term stability

"Many of life's failures are people who did not realize how close they were to success when
they gave up"
Thomas A. Edison

3

Laser sealed DSCs: Efficiency and Long term stability

Abstract

Long-term stability is still a major issue that limits dye-sensitized solar cells (DSCs) market implementation. The stability problem of the DSC design is directly related to the common sealing methods, which use thermoplastic sealants, such as Surlyn® or Bynel®. This work follows previous developments by the research group [1-3] on laser assisted glass frit sealing and demonstrates that the developed sealing process originates stable and efficient DSC devices. To assess the stability of the prepared devices, accelerated ageing was performed during 1000 h, at 63±2 °C, visible light intensity of 765 W·m^{-2} and resistive electrical load close the maximum power point of the cells (~0.6 V). Laser sealed DSCs showed remarkable stability with negligible efficiency loss compared to the Surlyn® sealed devices (*ca*. 2 % *vs*. 44 % loss of initial efficiency, respectively). The main degradation mechanism of thermoplastic sealed devices was ascribed to electrolyte leakage and external moisture contamination. These results show that efficient encapsulation methods are crucial to DSC stability and that the developed sealing process can bring stable and efficient DSCs to the PV market.

3.1 Introduction

Besides offering favorable performance-to-cost ratio, emerging photovoltaic technologies must guarantee device stability. Dye sensitized solar cells (DSCs) have low manufacturing costs, use environmental friendly materials and show distinctive characteristics that make them worth to invest[4-6]. Contrary to crystalline silicon (c-Si) photovoltaic (PV) devices, DSCs work especially well under low light levels (0.3 - 0.5 sun)[7, 8], such as light intensity typically available in the facades of buildings. Their ability to convert light into electricity while maintaining some transparency, unlike other PV technologies, make them particularly interesting for building integrated photovoltaics (BIPV) [9]. The operation of DSCs comprises dye excitation and electron injection into TiO_2 conduction band, charge transport through TiO_2 porous network to the SnO_2-F substrate and dye regeneration by the redox electrolyte[10]. These photo/electrochemical processes rely on the chemical compatibility of all DSC components. Graetzel *et al.*[11] showed that the redox system I_3^-/I^- combined with ruthenium dyes can achieve 20 years of molecular stability[11]. However, this intrinsic stability can only be accomplished if no electrolyte leakage or external contaminants penetrate into the cell. In fact, it has been shown that DSCs durability is highly dependent on efficient cell encapsulation and it is the most common reason for long-term stability failure[12,13]. The commonly employed sealants for encapsulating DSCs are polymers, such as Surlyn® and Bynel®, which have some permeability towards oxygen and moisture[14]; their relatively low softening point makes them unreliable sealants at temperatures above 50 – 60 ºC, which prevent their use in commercial DSC applications [9,13,15].

This work reports accelerated aging tests in DSCs fabricated by our previously developed laser assisted glass sealing process[1-3]. Although the laser process produces excellent glass to glass bonding, the technology is not yet fully developed for sealing the electrolyte filling holes; therefore these were sealed combining Surlyn® thermoplastic sealant and high temperature resistant resin. For comparison, Surlyn® sealed DSC devices were also tested.

The aging tests were conducted at 63±2 ºC, under 765 W·m^{-2} of continuous illumination and resistive electrical load close the maximum power point of the cells (~ 0.6 V). The devices were characterized every 200 hours, during the aging period of 1000 h, by intensity-voltage (*I-V*) and electrochemical impedance spectroscopy (EIS) analysis.

3.2 Material and Methods

3.2.1   Laser sealed DSC fabrication

Laser sealed DSCs were prepared as described elsewhere [1-3] (Chapter 2, section 2.4). Briefly, the photoelectrodes were prepared on 2.2 mm thick, 7 Ω·□$^{-1}$ SnO$_2$-F (FTO) coated glass substrates from Solaronix®. First, the glasses were washed sequentially with a detergent solution (Alconox®, VWR) in an ultrasonic cleaner (Amsonic TTC) at 55 ºC for 15 min, followed by ultrasonic cleaning in deionized water at room temperature and dried with air at 50 ºC.

A TiO$_2$ blocking layer is deposited above the FTO layer by atomic layer deposition (ALD – Beneq Oy thin film system TFS200). Deposition of TiO$_2$ was carried out at 225 °C using titanium isopropoxide (TIP, feeding tank at 45 ºC) and H$_2$O (feeding tank at 20 ºC). 250 cycles (~7.5 nm) of TiO$_2$ were deposited under a nitrogen flow of 300 cm^3·min^{-1}, with a pulse/purge lengths of 2 s / 20 s for TIP and 1 s / 3 s for H$_2$O. Then, samples were coated with a porous TiO$_2$ photelectrode layer by sequentially screen-printing 3 layers of a commercial TiO$_2$ paste (Ti-Nanoxide T/SP from Solaronix®), followed by drying at 100 ºC for 5 minutes, and annealing at 475 ºC for 15 min in an infrared electrical oven (Nabertherm Gmbh model GF75). After firing, the samples were treated with a 40 mM TiCl$_4$ aqueous solution at 70 ºC for 20 minutes, before being sintered at 475 ºC for 30 min.

The counter electrodes, prepared on the same type of glass substrates and cleaned as described before, were drilled previously with two holes of 1 mm diameter. A commercial platinum based paste (Platisol T/SP from Solaronix®) was applied on the glass substrate by screen-printing followed by annealing at 400 ºC for 15 minutes. The two electrodes are then assembled and sealed using the developed laser assisted glass

frit method. Dye adsorption in the porous TiO_2 photoelectrode was obtained by recirculating a dye solution (0.5 mM N719, 5 M chenodeoxycholic acid in ethanol) for 12 hours using a peristaltic pump (Ismatec®, Reglo Digital MS-4/8), followed by ethanol rinsing, nitrogen drying, electrolyte filling (high stability Iodolyte Z-150 from Solaronix®) and hole sealing combining Surlyn® thermoplastic sealant (Meltonix 1170-60, Solaronix) and high temperature resistant resin (Pattex® Nural 22 from Henkel). Electrical bus bars and electrical wires were soldered to the FTO surface of photo and counter-electrodes, respectively, using an ultrasonic soldering unit (MBR electronics model USS-9210); the soldered bus bars were protected by high temperature resistant resin to prevent corrosion caused by the heat and moisture. The front glass substrate of the cells was covered with a UV cutoff filter (Solaronix® UV filter adhesive film).

Surlyn® sealed cells followed the same fabrication procedure, except for the laser assisted sealing. Commercial Surlyn® sealing film with thickness of 25 μm (Meltonix 1170-25, Solaronix) was used. Glass substrates were sealed using a hot press at 160 ºC, by applying 10 bar for 20 s. No additional sealing was added (such as high temperature resins commonly employed to add robustness to Surlyn® sealed devices [15]). Images of DSCs sealed with the laser process (a) and Surlyn® (b) are shown in Figure 3.1.
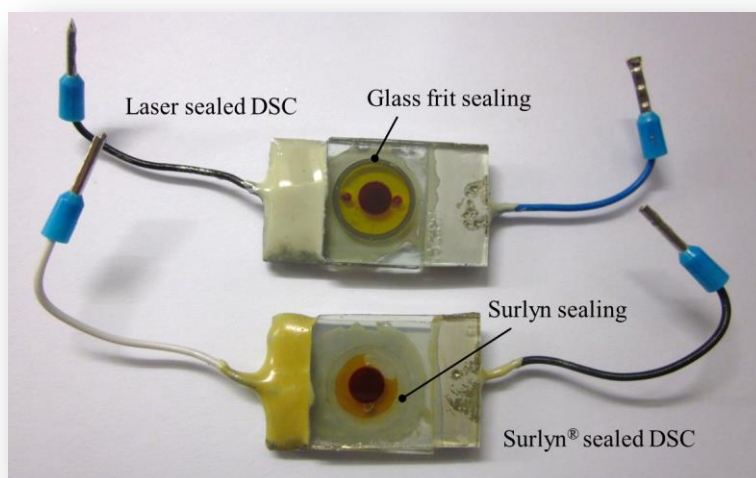
Figure 3.1 Images of the prepared Surlyn® and laser sealed DSCs after the ageing test.

3.2.2 *I-V* and EIS characterization

DSCs were characterized periodically based on recorded *I-V* curves, using a setup equipped with a 150 W xenon light source (Oriel class A solar simulator, Newport, USA) with variable light intensity, from 10 to 1000 W·m^{-2} (0.1 to 1 sun light intensity), and using a 1.5 air mass filter (Newport, USA). The simulator was calibrated using a single crystal Si photodiode (Newport, USA). The *I-V* characteristics of the solar cells were obtained applying an external potential load and measuring the generated photocurrent using an AUTOLAB electrochemical station (PGSTAT 302 N). This station was also used to characterize the cells based on electrochemical impedance spectra. The frequency range for the electrochemical impedance spectroscopy (EIS) measurements was from 100 kHz to 0.05 Hz with an AC modulation signal of 10 mV. The experimental EIS data was fitted to appropriate electrical analogues, namely a simplified transmission line model[16, 17], shown in Figure 3.2, using the commercial software ZView® (Scribner Associates Inc.).
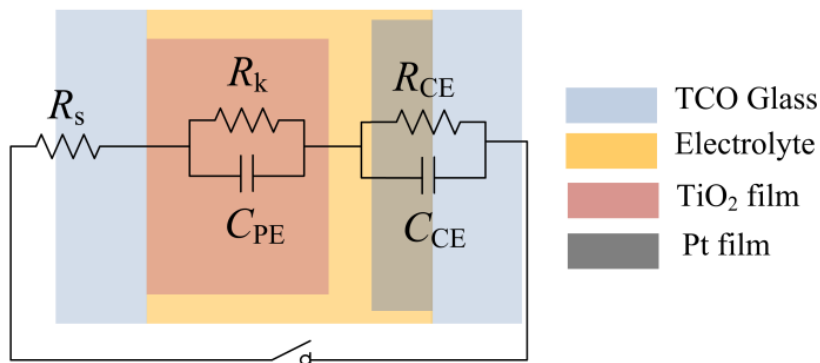
Figure 3.2 Simplified transmission line model used to fit EIS experimental data of DSCs. R_s – series resistances; R_k – recombination resistance; C_{PE} – chemical capacitance at the TiO$_2$ anode; R_{CE} – charge transfer at platinum/TCO interface; C_{CE} double layer capacitance at the platinum/TCO interface.

3.2.3 Accelerated ageing tests

Accelerated ageing tests were performed with continuous light illumination, temperature control and resistive electric load, in a closed test chamber (Atlas SUNTEST XLS+), shown in Figure 3.3, during 1000 h. The ageing conditions were

chosen to mimic harsh outdoor conditions: light intensity was set to 765 $W \cdot m^{-2}$, temperature set point of 60 ℃ and resistive electrical load close to the cells maximum power point (0.6 V). Although equipment temperature set point was 60 ℃, the real value oscillated between 61 ℃ and 65 ℃ (63±2 ℃). To apply a resistive electrical load to the test cells, metal bus bars and a resistor were assembled in a parallel electrical circuit, as shown in Figure 3.4.
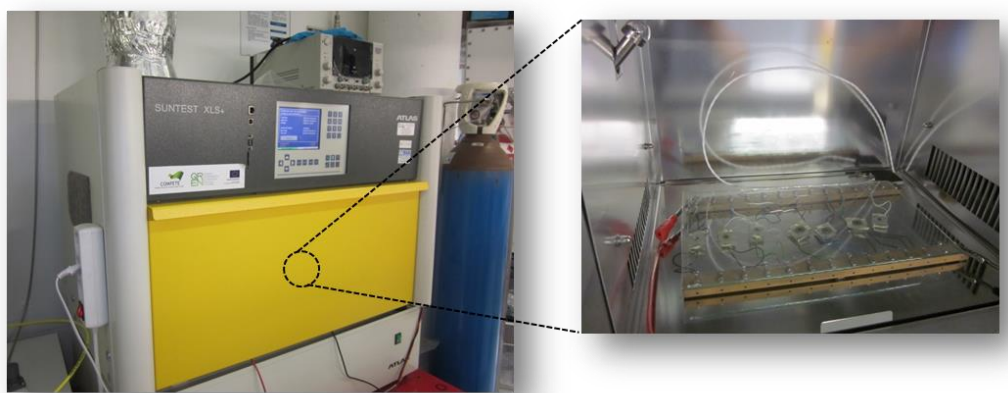
Figure 3.3 Image of the accelerated aging test chamber, and detail of the interior of the chamber loaded with DSCs.
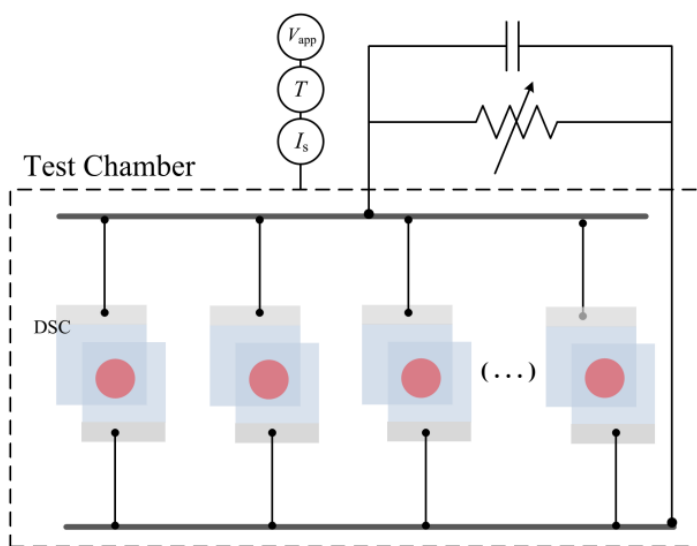
Figure 3.4 Scheme of the experimental setup used for the accelerated aging tests.

3.3 Results and Discussion

3.3.1   Photovoltaic performance

During the aging test, the DSCs were taken from the ageing chamber each 200 hours for *I-V* and EIS characterization. Figure 3.5 shows the normalized solar to electrical energy conversion efficiency (η), open circuit potential (V_{oc}), short circuit current density (J_{sc}) and fill factor (*FF*) of the tested DSCs sealed with Surlyn® and with glass frit. The results presented are the average of 4 DSC samples for each sealing method. The laser assisted glass frit DSCs (LAGF) exhibit excellent stability during the accelerated aging test; LAGF cells retained almost 98 % of their initial efficiency. On contrary, Surlyn® sealed DSCs showed *ca*. 34 % efficiency loss after 1000 h.

Analyzing the performance parameters shown in Figure 3.5 it can be concluded that the degradation of the Surlyn® sealed cells results mainly from a loss of *ca*. 13 % on V_{oc}. Particularly, after 400 h of ageing, all photovoltaic parameters showed a steady and constant decrease; this was assigned to partial leakage of electrolyte and external moisture penetration of the Surlyn® sealed devices. LAGF cells showed a minor decrease of J_{sc} (-5.1 %) and FF (-7.4 %), that was compensated with a 8.3 % increase in the V_{oc}; this resulted in a remarkable stability of the initial efficiency of *ca*. 98 %, something seldom seen in aged DSCs [15,18,19].

Figure 3.6 shows the *I-V* curves of Surlyn® sealed (a) and laser sealed DSCs (b) before and after the complete 1000 h ageing test. The *I-V* curves of Surlyn® sealed DSCs show a large V_{oc} decrease, alongside with a dark current increase, which indicates higher electron/electrolyte recombination rate. Contrarily, LAGF showed similar curves before and after the test, with a slight decrease in dark current.
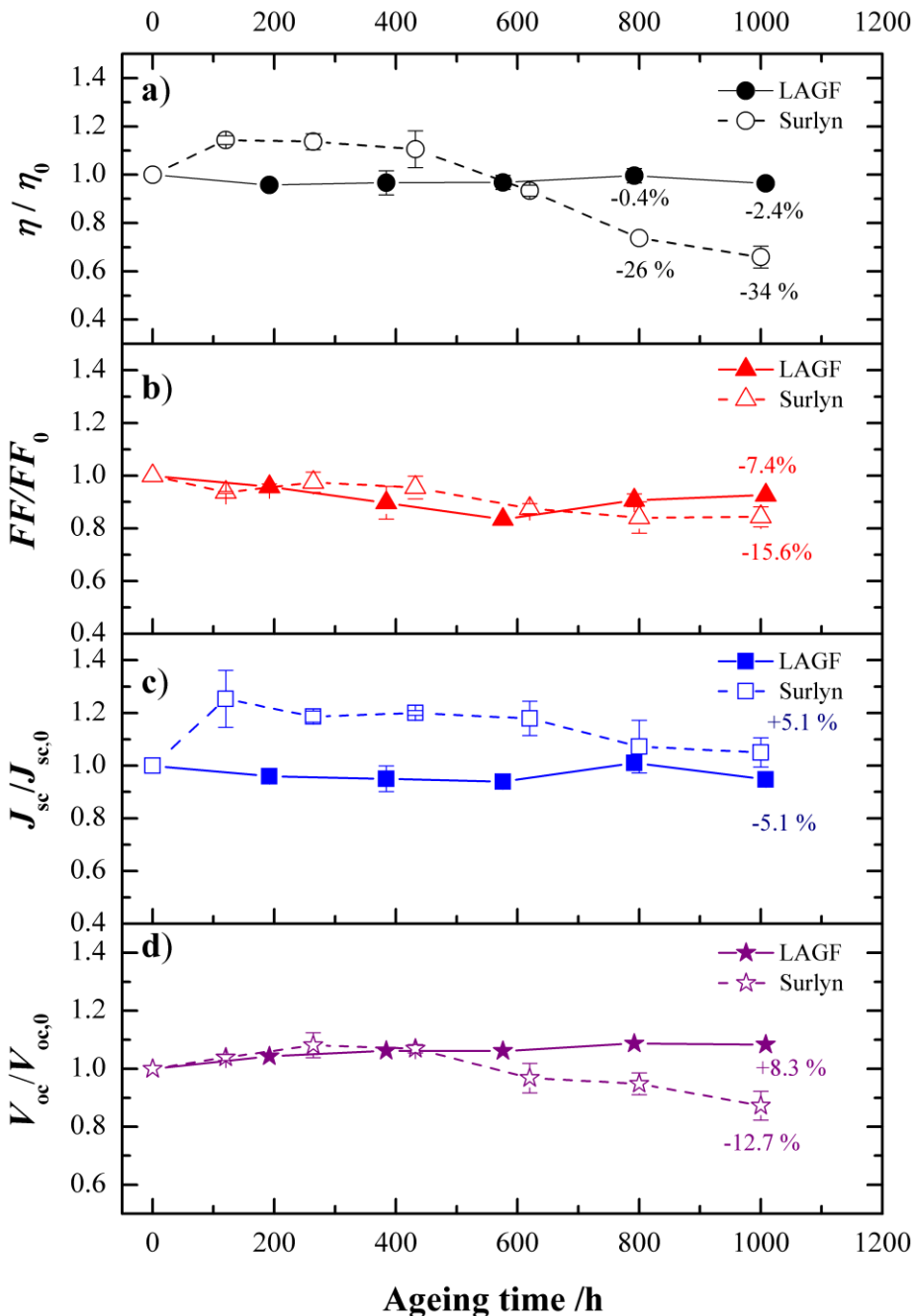
Figure 3.5 Normalized performance parameters history of DSCs based on Surlyn® sealing and laser assisted glass frit sealing (LAGF) during 1000 h under 765 W·m^{-2} light soaking, 63±2 ℃ and 0.6 V resistive load. The error bars refer to the standard deviation of 4 samples.
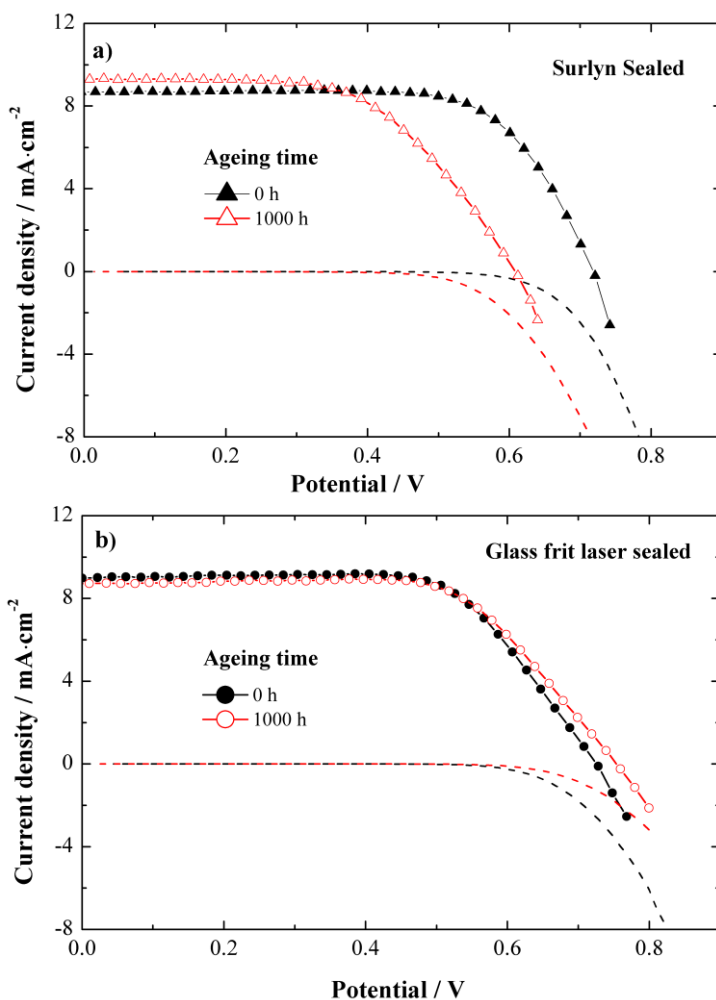
Figure 3.6 *I-V* curves obtained at 0.85 sun and dark conditions, for Surlyn® sealed (a) and laser sealed DSCs (b) before and after the 1000h of the aging test.

The performance parameters of the devices (η, V_{oc}, J_{sc} and FF) before and after the aging test are shown in Table 3.1. Besides a reduction in the V_{oc} value (~ 13 %) cells show also *ca*. 16 % reduction in FF, indicating massive series resistance increase; these two factors suggest that in Surlyn® sealed devices recombination and series resistances play a key role in the final efficiency loss (34 %). Globally, the performance parameters of the LAFG cells showed different ageing behavior and proved to be more resistant than Surlyn® sealed cells to the aging test.

Table 3.1. Performance parameters of Surlyn® and laser sealed (LAGF) DSCs before and after 1000 h of accelerated ageing.

Sealing method	Ageing time / h	Performance parameters				
		V_{oc} /V	J_{sc} / mA·cm^{-2}	FF	η / %	$\Delta\eta$ / %
LAGF	0	0.72 ± 0.05	9.00 ± 0.17	0.67 ± 0.07	5.02 ± 0.07	-2.4
	1000	0.78 ± 0.01	8.54 ± 0.24	0.62 ± 0.01	4.90 ± 0.02	
Surlyn®	0	0.72 ± 0.01	8.47 ± 0.06	0.70 ± 0.03	5.03 ± 0.16	-34
	1000	0.63 ± 0.03	9.11 ± 0.63	0.59 ± 0.18	3.32 ± 0.09	

3.3.2 Electrochemical impedance spectroscopy

Conventional accelerated aging tests record the photovoltaic performance history of solar cells, but give little information about the source of the performance loss. EIS analysis allows penetrating deeper in the sources of efficiency loss and it was performed in the tested devices. Figure 3.7 and Figure 3.8 show the parameters determined by fitting EIS experimental data to appropriated electrical analogues shown in Figure 3.2. Relatively to the counter electrode (CE), Surlyn® sealed cells showed an increase of 52 % in charge transfer resistance of the CE (R_{CE}) and a decrease of 60 % in the CE capacitance (C_{CE}); this indicates degradation in the platinum counter electrode performance. In opposition, LAGF cells showed 13 % increase in R_{CE} and negligible loss in C_{CE}, which indicate significantly less degradation in the platinized electrode.

In terms of photoelectrode (PE) there are distinct trends in both device types: in Surlyn® sealed devices there is 59 % decrease in charge transfer resistance (R_{PE}) followed by 21 % decrease in the chemical capacitance of TiO_2 film (C_{PE}). On the other hand, laser sealed cells show an opposite trend in R_{PE} (+69 %) and similar change in C_{PE} (-31 %). Charge transfer resistance in the TiO_2 film (R_{PE}) relates to the electron/electrolyte recombination reaction rates; this electrochemical reaction depends on several factors, such as temperature, I_3^- concentration in electrolyte and electron concentration in TiO_2 conduction band. The R_{PE} trend in Surlyn® devices shows that recombination rate increases with aging, contrary to LAGF cells where the trend is exactly the opposite. Figure 3.5 shows that the decrease in the photovoltaic
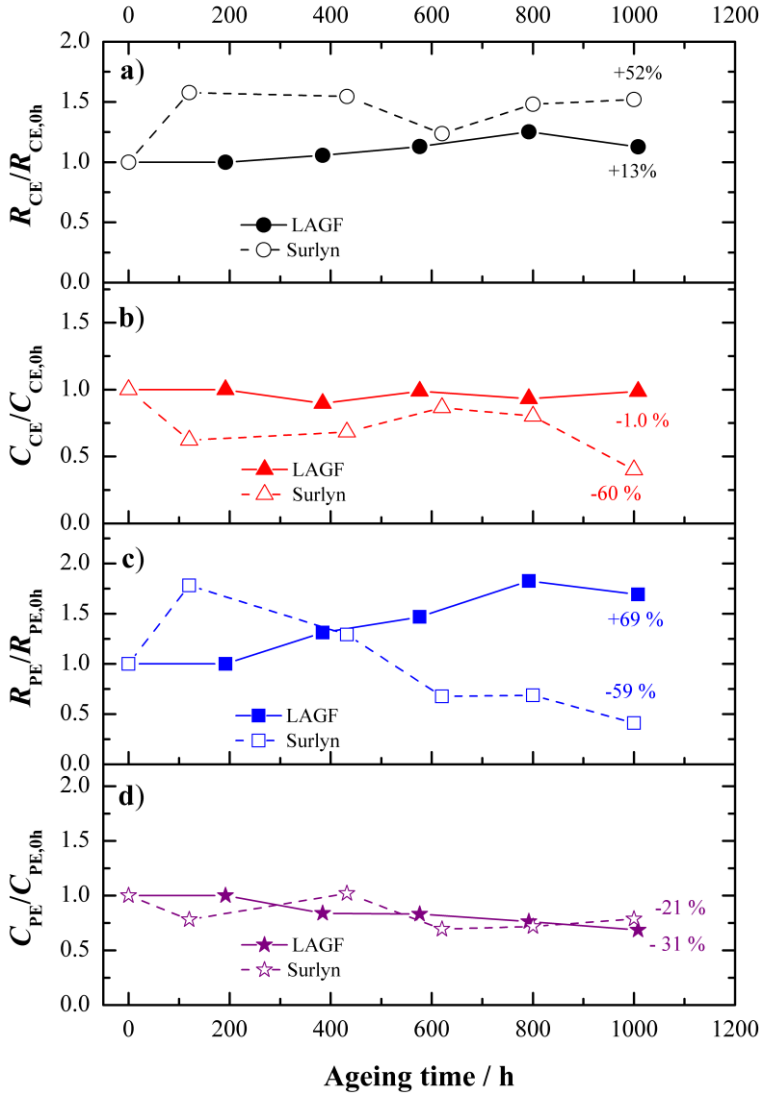
Figure 3.7 Fitted EIS parameters history for Surlyn® sealed and LAGF DSCs. R_k – recombination resistance; C_{PE} – chemical capacitance at the TiO$_2$ anode; R_{CE} – charge transfer resistance at platinum/TCO interface; C_{CE} double layer capacitance at the platinum/TCO interface.

performance of Surlyn® devices (mainly driven by the V_{oc} and FF), is particular steep after *ca.* 400 hours of ageing, which matches closely to the decrease of R_{PE}. This shows that at this point, something led to an irreversible increase in recombination and degradation of performance of the cells, which in this case is ascribed to electrolyte leakage. This is further confirmed by data presented in Figure 3.8. In the Surlyn®

sealed cells, series resistances (R_s) increase and electron lifetime (τ_{e-}) decrease confirm that instant 400 h is a critical moment when series resistances and recombination cause the performance drop of Surlyn® sealed cells. Comparatively, LAGF cells show a remarkable R_s and τ_{e-} stability, which in turn contribute to their performance steadiness.
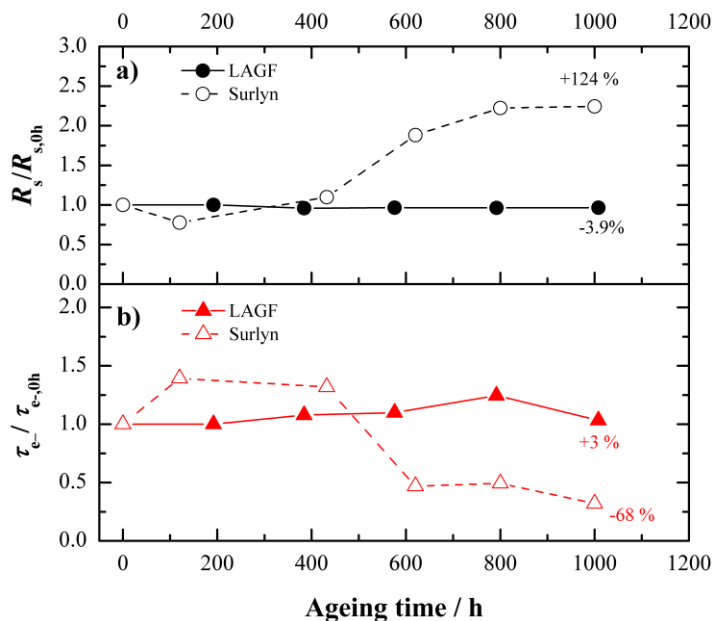
Figure 3.8 Fitted EIS parameters history for Surlyn® sealed and LAGF DSCs R_s – series resistances; τ_{e-} - electron lifetime.

Figure 3.9 shows Bode and Nyquist plots of Surlyn® and LAGF cells before and after the 1000 h ageing test. The simplified transmission line model presented in Figure 3.2 fits well the EIS experimental data. The bode plot from Surlyn® cells (Figure 3.9a) shows that first peak shifts to higher frequencies, indicating a smaller recombination resistance in TiO_2/electrolyte interface; this is confirmed by the Nyquist plot (Figure 3.9a) where the 1000 h analysis results in smaller second Nyquist semicircle. It is also possible to observe an increase in the displacement of the first semicircle to higher resistances, which indicates the increase of the series resistances, as explained before. In turn, LAGF cells display a second semicircle with a larger diameter that results from an increase of electron lifetime; this shows that the recombination in LAFG is lower, and thus its efficiency is maintained.
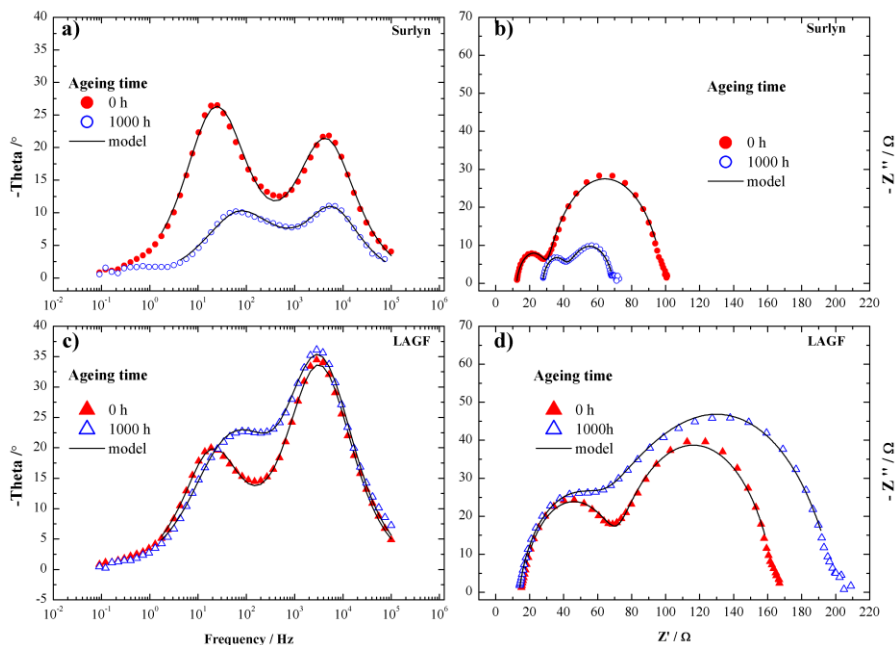
Figure 3.9 Bode (a, c) and Nyquist (b, d) plots for Surlyn® sealed cells (a, b) and LAGF cells (c, d) obtained under dark conditions, at the V_{oc} of the cell, before and after the ageing test (1000 h, 765 W·m⁻², 63±2 ºC, ~0.6 V resistive electrical load).

Table 3.2 shows the EIS fitted parameters, before (0 h) and (1000 h) the ageing test. Altogether, the EIS data show that the degradation process of the Surlyn® sealed cells is mainly related to τ_{e^-} and R_s, explained the largest variation compared to their initial value and with LAGF cells.

Table 3.2 Parameters obtained by fitting the EIS experimental data to the presented equivalent circuit for Surlyn® sealed and LAGF DSCs, before and after ageing test.

Sealing method		LAGF			Surlyn®		
Ageing time / h		0	1000	Δ	0	1000	Δ
	R_{CE} / Ω	32.8	28.53	+13%	46.3	70.4	+52%
	C_{CE} / F	1.02×10^{-5}	1.01×10^{-5}	-1.0%	3.91×10^{-6}	1.56×10^{-6}	-60%
EIS	R_{PE} / Ω	82.2	139	+69%	80.0	32.8	-59%
fit	C_{PE} / F	5.68×10^{-4}	3.87×10^{-4}	-32%	4.79×10^{-4}	3.74×10^{-4}	-22 %
	R_s / Ω	10.0	9.6	**-3.9%**	9.07	20.3	**+124%**
	τ_{e^-} / ms	23.4	32.5	**+3.0%**	23.6	16.1	**-68%**

3.4 Conclusions

Laser assisted glass frit (LAGF) sealed DSCs were tested for stability against DSCs sealed with the commonly employed Surlyn® polymer. Accelerated ageing was carried out during 1000 hours under continuous illumination (765 W·m^{-2}), at 63±2 °C, and applying an electrical resistive load close to the maximum power point (~ 0.6 V) of the cells. The results showed significant differences in stability: after 1000 h of test Surlyn® sealed cells presented 34 % energy efficiency degradation; in turn LAGF cells exhibited negligible efficiency loss (-2.4 %). The degradation occurring after *ca.* 400 hours of test was assigned to electrolyte leakage and moisture penetration inside the Surlyn® sealed cells; this has a negative impact in the cell operation and leads to a constant decrease in V_{oc} and *FF* of the cells that cause efficiency degradation. Oppositely, in LAGF cells, the slight loss of current (-5 %) was balanced by an increase in the V_{oc} (+8 %) that allowed efficiency steadiness. EIS showed that series resistances and recombination were the main causes of performance loss in Surlyn® sealed cells. In turn, LAGF cells showed nearly no R_s degradation (-3.9 %) and less recombination (+3 % in τ_e) after 1000 h of test, which contributed to performance durability of the cells.

These results showed that efficient encapsulation is crucial for obtaining long term stable DSCs. The developed laser assisted glass sealing process produces stable DSC devices, with negligible efficiency loss under the accelerated ageing tested conditions. In turn, Surlyn® by itself cannot guarantee efficient encapsulation, therefore not providing durability for DSC devices.

Acknowledgements

References

1.   PCT/IB2012/051376, 2012.

2.   F. R. J.Maçaira , L.Andrade, J.Gabriel, A.Mendes presented in part at the CHEMPOR 2011 : 11th International Chemical and Biological Engineering Conference, Lisbon, Portugal, 5-7 September, 2011.

3.   F. Ribeiro, Maçaira,J. , Cruz, R., Gabriel, J., Andrade, L., Mendes, A., *Solar Energy Materials and Solar Cells*, 2012, **96**, 43-49.

4.   J. Maçaira, L. Andrade and A. Mendes, *Renewable and Sustainable Energy Reviews*, 2013, **27**, 334-349.

5.   L. M. Goncalves, V. d. Z. Bermudez, H. A. Ribeiro and A. M. Mendes, *Energy & Environmental Science*, 2008, **1**, 655-667.

6.   M. I. Asghar, K. Miettunen, J. Halme, P. Vahermaa, M. Toivola, K. Aitola and P. Lund, *Energy & Environmental Science*, 2010, **3**, 418-426.

7.   T. M. W. J. Bandara, W. J. M. J. S. R. Jayasundara, H. D. N. S. Fernado, M. A. K. L. Dissanayake, L. A. A. De Silva, I. Albinsson, M. Furlani and B. E. Mellander, *Journal of Applied Electrochemistry*, 2015, **45**, 289-298.

8.   C.-P. Lee, C.-A. Lin, T.-C. Wei, M.-L. Tsai, Y. Meng, C.-T. Li, K.-C. Ho, C.-I. Wu, S.-P. Lau and J.-H. He, *Nano Energy*, 2015, **18**, 109-117.

9.   A. Fakharuddin, R. Jose, T. M. Brown, F. Fabregat-Santiago and J. Bisquert, *Energy & Environmental Science*, 2014, **7**, 3952-3981.

10. B. E. Hardin, H. J. Snaith and M. D. McGehee, *Nat Photon*, 2012, **6**, 162-169.

11. M. Grätzel, *Comptes Rendus Chimie*, 2006, **9**, 578-583.

12. T. Toyoda, T. Sano, J. Nakajima, S. Doi, S. Fukumoto, A. Ito, T. Tohyama, M. Yoshida, T. Kanagawa, T. Motohiro, T. Shiga, K. Higuchi, H. Tanaka, Y. Takeda, T. Fukano, N. Katoh, A. Takeichi, K. Takechi and M. Shiozawa, *Journal of Photochemistry and Photobiology A: Chemistry*, 2004, **164**, 203-207.

13. N. Jiang, T. Sumitomo, T. Lee, A. Pellaroque, O. Bellon, D. Milliken and H. Desilvestro, *Solar Energy Materials and Solar Cells*, 2013, **119**, 36-50.

14. A. G. Kontos, T. Stergiopoulos, V. Likodimos, D. Milliken, H. Desilvesto, G. Tulloch and P. Falaras, *The Journal of Physical Chemistry C*, 2013, **117**, 8636-8646.

15. R. Harikisun and H. Desilvestro, *Solar Energy*, 2011, **85**, 1179-1188.

16. J. Bisquert, M. Gratzel, Q. Wang and F. Fabregat-Santiago, *The Journal of Physical Chemistry B*, 2006, **110**, 11284-11290.

17. L. Andrade, S. M. Zakeeruddin, M. K. Nazeeruddin, H. A. Ribeiro, A. Mendes and M. Grätzel, *ChemPhysChem*, 2009, **10**, 1117-1124.

18. L. Tao, Z. Huo, Y. Ding, Y. Li, S. Dai, L. Wang, J. Zhu, X. Pan, B. Zhang, J. Yao, M. K. Nazeeruddin and M. Gratzel, *Journal of Materials Chemistry A*, 2015, **3**, 2344-2352.

19. D. Perganti, A. G. Kontos, T. Stergiopoulos, V. Likodimos, J. Farnell, D. Milliken, H. Desilvestro and P. Falaras, *Electrochimica Acta*, 2015, **179**, 241-249.

CHAPTER 4

Temperature Role in the Recombination Reaction on Dye-Sensitized Solar Cells

"In the middle of difficulty lies opportunity"

Albert Einstein

4

Temperature Role in the Recombination Reaction on Dye Sensitized Solar Cells

Abstract

The performance of photovoltaic (PV) devices as a function of temperature is crucial for technical development and for accurate commercial information. Along with solar irradiance, temperature is the most important operating factor of PV devices performance. Normally it is wide accepted that dye sensitized solar cells (DSC) show minimal energy efficiency dependence with temperature (20 °C – 60 °C). The energy efficiency in DSCs depends on light absorption, charge transport (ohmic resistances) and recombination rates. In this work the recombination reaction kinetics is studied within a wide temperature range. A unique laser assisted sealing technique that allows studying the temperature effect between -5 ºC and 105 ºC without electrolyte leakage or external contamination was used. To the best of our knowledge, this is the highest operating temperature ever considered in kinetic studies of liquid state DSCs. The electrochemical reaction between electrons and triiodide/iodide ions is shown to be the most important factor to determine the energy efficiency of DSCs as a function of temperature. It was concluded that the activation energy of the recombination reactions depends on the interface where it happens – TiO_2/electrolyte and SnO_2-F/electrolyte - and on the temperature. It was found that besides temperature having a deep influence in the recombination reaction rate, the energy of the injecting electron is also critical. These conclusions should provide solid ground for further developments in the DSCs and perovskite solar cell fields, and allow a better comparison between the energy efficiency of different PV technologies for a range of operating temperatures.

4.1 Introduction

Alongside with solar irradiance, temperature is probably the most important outdoor variable that affects the conversion efficiency of PV devices. However, temperature studies on DSCs are scarce and usually limited to temperatures up to 60 ºC[1-3]. Moreover, the glass substrates normally used to assemble DSCs are poor thermal conductors, resulting that real temperature value are usually lower than anticipated by typical temperature control setups; solar simulators irradiance also increase the glass temperature (absorbance of *ca.* 20 %), which makes it difficult to have a good control over the temperature analysis. To the best knowledge of the authors, all reported studies have not considered these effects and should lack of accuracy making our knowledge on the temperature effect on DSCs performance just qualitative.

Generally, conduction band shift of the TiO_2 film, recombination and charges transport kinetics are in a DSC the phenomena that have the greatest contribution for its performance dependence on the temperature[4-6]. Charge recombination corresponds to the undesirable reaction of generated electrons with electrolyte species, ultimately ruling the final performance of DSCs. This reaction involves either free conduction band electrons or electrons trapped in lower energy states[7]. Electronic traps are sites within the semiconductor (energetically localized in the bandgap) that restrict the movement of electrons. They are caused either by chemical impurities, morphological defects or imperfections in the regular spacing of the atoms[8]. The driving force for recombination is related to the energy level where electrons are located in the TiO_2 and temperature, both related to the rate constant, $k_r(T)$, and the electron concentration[9,10]. As V_{oc} changes, the Fermi level (E_F) in TiO_2 moves towards or away from the conduction band edge (E_{CB}); when the Fermi level moves up, the respective electron traps below are filled. Taking this into consideration, it can be expected that the activation energy (E_a) of recombination is proportional to (E_{CB}-E_F)[11]. However, recombination processes do not take place only at TiO_2/electrolyte interface; they can occur by reaction of electrolyte species with generated electrons that can be located either in the TiO_2 photoelectrode or in the transparent conductive oxide (TCO) –

Figure 4.1a). This information is well known in the DSC community, and several passivation methodologies have been developed to decrease recombination[12-17]. The most successful strategies include the use of blocking layers over the TCO film[15,16,18-20] the use of TiO_2 sols applied to the mesoporous TiO_2 layer[21, 22]; and more recently the use an encapsulation layer by atomic layer deposition (ALD) of TiO_2 applied over the dyed semiconductor [17]. These approaches were developed to prevent recombination by different mechanisms, and although proved effective, studies that link temperature effects with recombination rates are rare.

Usually the recombination kinetics is well characterized by electrochemical impedance spectroscopy (EIS) and its magnitude can be analyzed by fitting the experimental data to appropriate electrical analogues[23,24]. The electron lifetime (τ_{e^-}) can be extracted and thus the recombination rate constant ($k_r = 1/\tau_{e^-}$) in the solar cell can be calculated. This powerful analytical technique has proven invaluable during the DSC technological development; unfortunately, by itself, it does not allow distinguishing different recombination reaction pathways, *i.e.* at TiO_2 or SnO_2-F interface – Figure 4.1b).
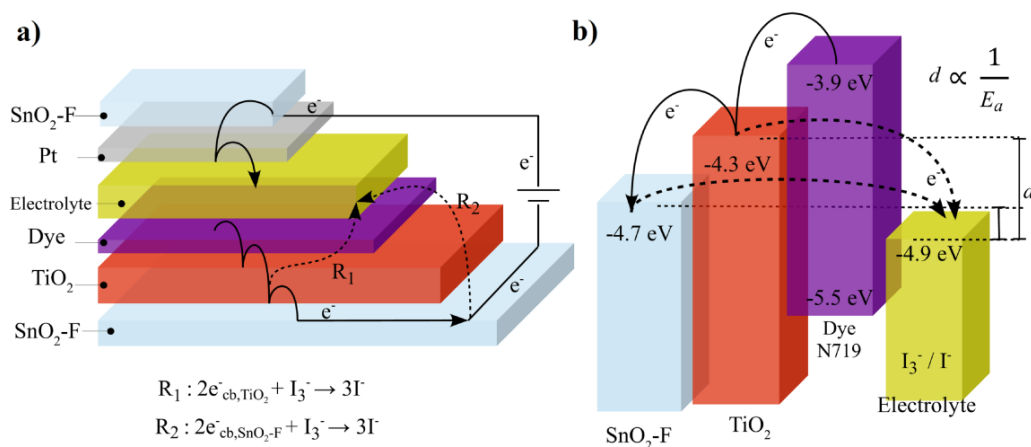
Figure 4.1 a) Schematic representation of the working principles at a dye sensitized solar cell; and b) diagram of energy levels of each functional layer in the DSC. The full arrows represent electron pathways through the device; the dashed arrows represent the main loss reaction mechanisms due to recombination through TiO_2 or SnO_2-F interfaces (R_1 and R_2, respectively). The actual energy levels may change upon assembling.

The present work aims understanding and quantifying the recombination at TiO$_2$/electrolyte and FTO/electrolyte interfaces and their dependence with temperature. This should provide valuable information for the development of more efficient materials, solar cell architectures and to better predict temperature influence on PV output of future commercial applications. An experimental setup was developed that accurately controls the inner temperature of DSC devices, allowing their characterization as a function of the temperature. Laser assisted glass sealing, reported elsewhere[25,26], was used to make the solar cells hermetic, even up to the boiling point of the electrolyte; the setup and sealing process allows to obtain very accurate characterizing results between -5 ºC and 105 ºC. The temperature influences in *I-V* curves as well as in the electrochemical kinetics of the solar cell was determined and are discussed. It was developed an experimental methodology that distinguishes the recombination occurring at TiO$_2$/interface from recombination occurring at TCO (SnO$_2$-F) interface; to do so the exposed TCO area to electrolyte was progressively increased to deliberately cause changes in the recombination rate constant. This allows quantifying the temperature influence for both recombination pathways and its implications in solar cells operation and respective architecture design.

4.2 Material and Methods

4.2.1   Laser sealed DSCs and half-cell fabrication

In the present work two types of devices were fabricated: DSCs and half-cells – Figure 4.2 and Figure 4.3. DSCs are made of two electrodes: the photo electrode (PE) and the counter electrode (CE); the electrolyte in between contains the iodide/triiodide redox pair. PE and CE are each applied on glass coated with a transparent conducting oxide (TCO); the PE includes a mesoporous TiO$_2$ film sensitized with a dye responsible for light absorption. The CE consists of a nanometric platinum layer applied on the TCO surface and responsible for catalyzing the reduction of triiodide to iodide. A half-cell configuration consists of two identical TCO glasses coated with the relevant material, separated the electrolyte. They mimic the phenomena in a DSC allowing evaluating the CE and electrolyte behaviors without the interference of the

sensitized porous TiO$_2$ layer; in the present work they are used to study the electrochemical reaction of electrons with electrolyte species over a specific interface. Half-cells made with thin films of SnO$_2$-F, Pt, and TiO$_2$ were assembled to study the recombination reaction as a function of temperature. The preparation of both devices (DSCs and half-cells) is described as follows.

Photoelectrodes were prepared on 2.2 mm thick, 7 $\Omega \cdot \square^{-1}$ SnO$_2$-F (FTO) coated glass substrates from Solaronix®. First, the glasses were washed sequentially with a detergent solution (Alconox®, VWR) in an ultrasonic cleaner (Amsonic TTC) at 55 ºC for 15 min, followed by ultrasonic cleaning in deionized water at room temperature, rinsed with ethanol and dried with air at 50 ºC. Then, samples were coated with a porous TiO$_2$ layer by screen-printing a commercial TiO$_2$ paste (Ti-Nanoxide T/SP from Solaronix®), followed by drying at 100 ºC for 5 minutes. To control the final thickness of the transparent layer of TiO$_2$, the screen-printing and drying procedures were repeated as necessary to get the desired thickness (12 μm-thick photoelectrodes were obtained with three screen-printing cycles). Samples were annealed at 475 ºC for 15 min in an infrared electrical oven (Nabertherm Gmbh model GF75). After firing, the samples were treated with a 40 mM TiCl$_4$ aqueous solution at 70 ºC for 20 minutes, before being sintered at 475 ºC for 30 min. In cells where blocking layer is required, a thin and compact layer of TiO$_2$ above the FTO layer was applied immersing the FTO glasses in a 40 mM TiCl$_4$ aqueous solution at 70 ºC for 20 minutes; after washing with water and ethanol, the samples were dried with a nitrogen flow. The counter electrodes, prepared on the same type of glass substrates and cleaned as described before, were drilled previously with two holes of 1 mm diameter. A commercial platinum based paste (Platisol T/SP from Solaronix®) was applied on the glass substrate by screen-printing followed by annealing at 400 ºC for 15 minutes.

Both DSCs and half cells devices, the two electrodes were assembled and sealed using a laser assisted glass frit method[25]. To control the exposed SnO$_2$-F area to electrolyte, the glass frit-sealing perimeter was varied from 5 to 12 mm (see Figure 4.18), without changing the total distance to the electrical contact; this way the electron lifetime can be controlled without changing the series resistances. Dye adsorption in the porous TiO$_2$ photoelectrode was obtained by recirculating a dye solution (0.5 mM

N719, 5 M chenodeoxycholic acid in ethanol) for 12 hours using a peristaltic pump (Ismatec®, Reglo Digital MS-4/8), followed by ethanol rinsing, nitrogen drying, electrolyte filling (high stability iodolyte Z-150 from Solaronix®) and hole sealing by a combination of thermoplastic sealant (Surlyn®, Dupont) and high temperature resistant resin (Pattex® Nural 22 from Henkel). Solder bus bars and electrical wires were applied to the FTO surface of the photo and counter-electrodes, respectively, using an ultrasonic soldering unit (MBR electronics model USS-9210); the soldered bus bars were protected by high temperature resistant resin to prevent corrosion caused by the heat and moisture. The described manufacture process produced devices resistant at least to 120 ºC, without electrolyte leakage. The DSCs manufactured have between 5 and 6 % efficiency (25ºC, 100 mW·cm^{-2}, 1.5 air mass filter) which is a typical efficiency value in devices prepared with a non-volatile electrolyte (Iodolyte Z150 – Solaronix) based on methoxypropionitrile (MPN), which is known to produced stable but less efficient devices than acetonitrile based electrolytes.
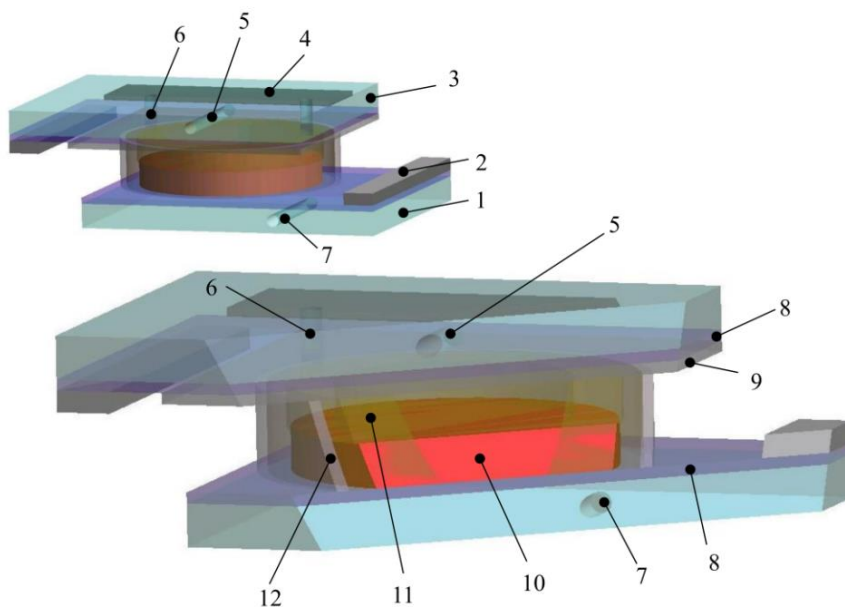
Figure 4.2 Schematics of the manufactured DSC device (not in scale): 1 – Photoelectrode glass; 2 – electrical contact; 3 – counter-electrode glass; 4 – filling hole cover; 5 – drilled hole for temperature measurement, T_2; 6 –filling hole; 7 - drilled hole for temperature measurement, T_1; 8 – TCO; 9 – platinum catalyst; 10 – TiO$_2$ with adsorbed sensitizer; 11 – electrolyte; 12 – glass frit sealing.
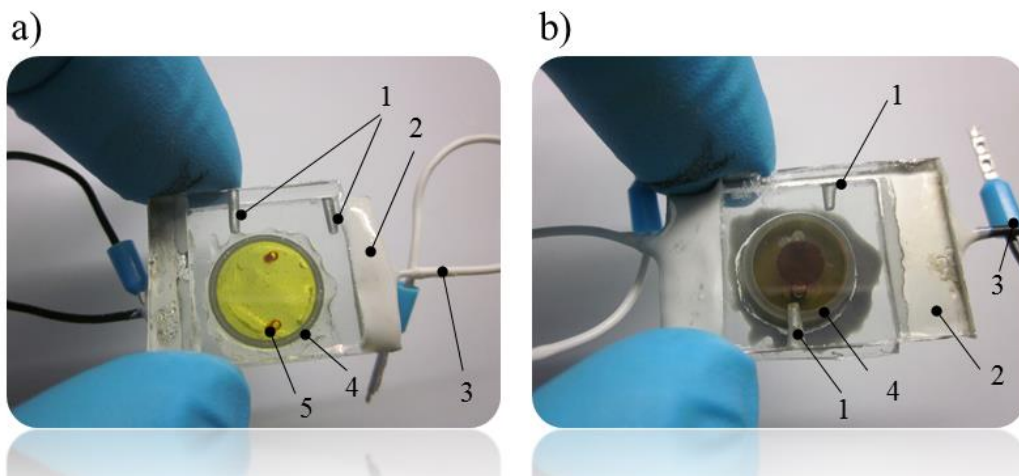
Figure 4.3 Pictures of the laser sealed: (a) half-cells and (b) dye-sensitized solar cells: 1 – drilled hole for temperature measurement; 2 – electrical contact; 3 – electrical terminal; 4 – glass frit sealing; 5 – electrolyte filling hole.

4.2.2 Experimental Setup

The experimental *I-V* characteristics were obtained in a setup equipped with a 150 W xenon light source (Oriel class A solar simulator, Newport, USA) with variable light intensity, from 10 to 100 mW·cm^{-2} (0.1 to 1 sun light intensity), and using a 1.5 air mass filter (Newport, USA). The simulator was calibrated using a single crystal Si photodiode (Newport, USA). The *I-V* characteristics of the solar cell were obtained applying an external potential load and measuring the generated photocurrent using an AUTOLAB electrochemical station. This station was also used to characterize the cells through EIS. The frequency range for EIS measurements was from 100 kHz to 0.05 Hz with an AC modulation signal of 10 mV. EIS measurements were carried out in dark and at the open circuit potential measured at 25ºC (V_{oc}, 25ºC) for DSCs and at 0 V for half-cells. The operation temperature of the solar cell was controlled using an in-house made experimental setup, shown in Figure 4.4 and Figure 4.5, based on a peltier device (Marlow Industries, model RC12-6) connected to a Keithley DC power supply (Model 2425C). A PID algorithm was run on a National Instruments LabVIEW application shown in appendix B, Figure B3. Four K-type thermocouples were placed in different locations: in a drilled axial hole in the photoelectrode glass (T_1), in the counter electrode glass (T_2) and at aluminum slabs connected to the cold and hot side (T_3 and

T_4, respectively) of the thermo-electrical element (peltier module). All heat transfer interfaces were filled with thermal conducting paste to maximize the heat transfer. When a potential difference is applied to the thermo-electrical element (4), a temperature difference is created between both sides (T_3 and T_4) of the peltier device.

By using a PID algorithm it is possible to accurately control temperature at the DSC (T_3). The heat-dissipating surface (T_4) of the peltier device was cooled using a thermal fluid from a thermostatic bath (Julabo model ME, Germany) (5). Under illumination, and without temperature control, the temperature inside the DSC can increase more than 10 ℃ in a few minutes. Figure 4.6 show that when the temperature control is turned on, the system immediately responds to correct the temperature to the desired set-point.
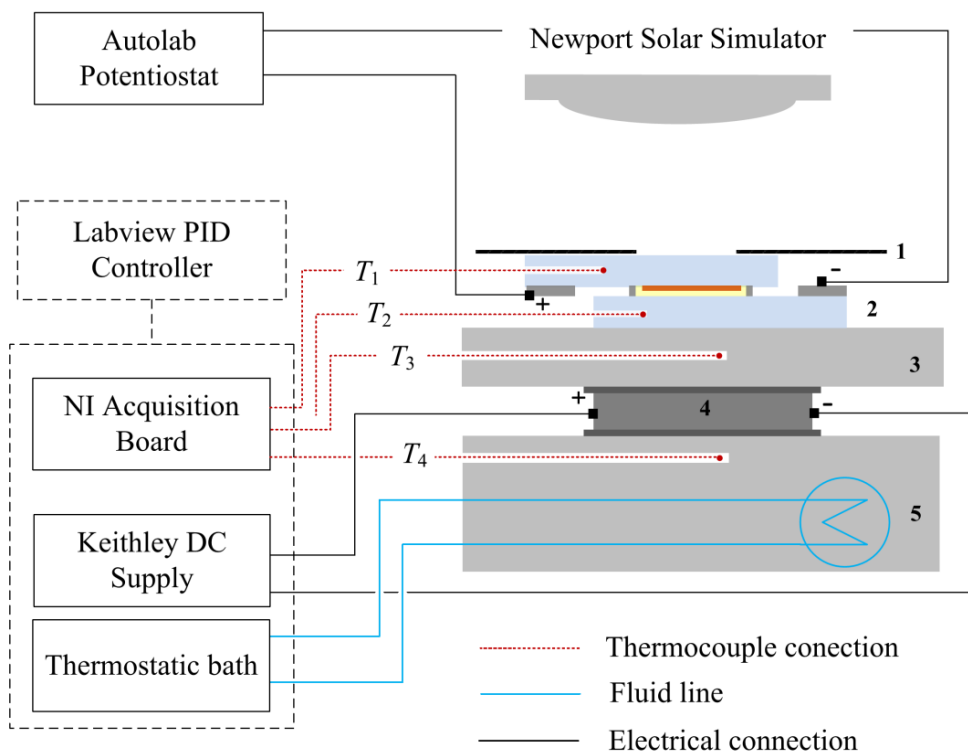
Figure 4.4 Experimental setup used for temperature control of an under illumination DSC between -10 °C and 105 °C. 1- thermal insulator black mask; 2- DSC; 3- aluminum slab; 4- peltier device; 5- aluminum slab with drilled thermal fluid circuit.
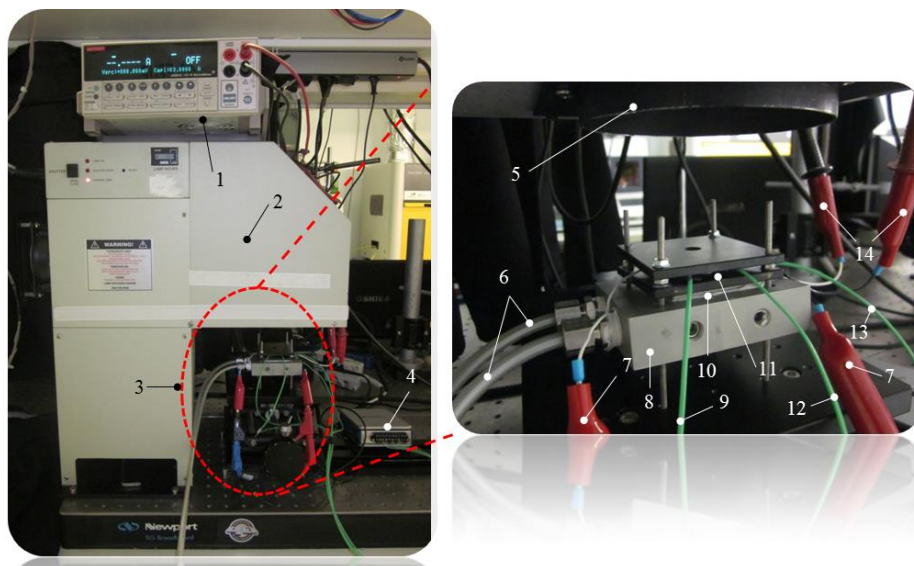
Figure 4.5 Experimental setup used for temperature control of an under illumination DSC between -5 °C and 105 °C. 1–Keithley DC supply; 2–Newport solar simulator; 3– temperature control unit; 4– NI acquisition board; 5– solar simulator; 6– cooling fluid lines; 7– DSC electrical connections to autolab potentiostat; 8– aluminum slab with drilled thermal fluid circuit; 9 – thermocouple T_2 ; 10 – peltier device; 11 – DSC; 12– thermocouple T_1; thermocouple T_3; 14 – electrical connections from peltier device to Keithley DC supply.
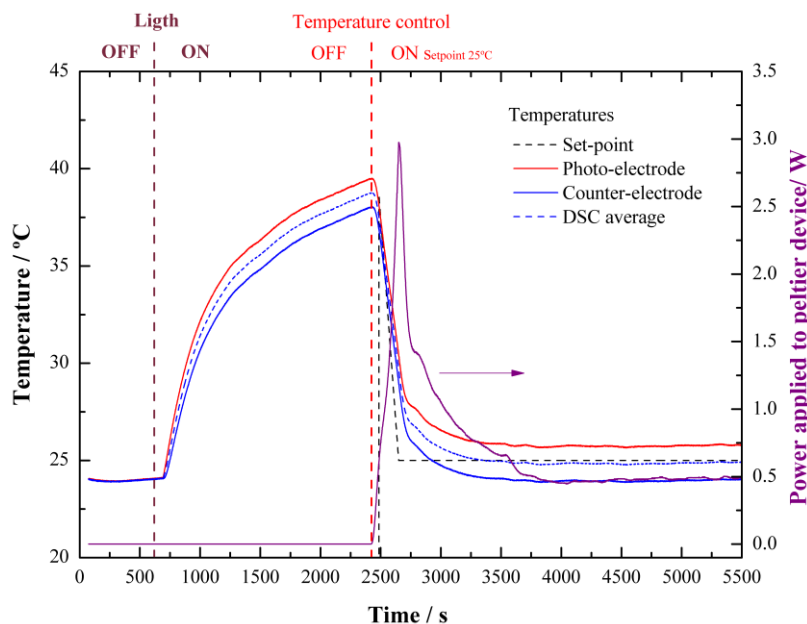
Figure 4.6 Temperature measurements of an illuminated DSC (100 mW·cm^{-2}, AM 1.5) with and without temperature control (temperature set point = 25ºC).
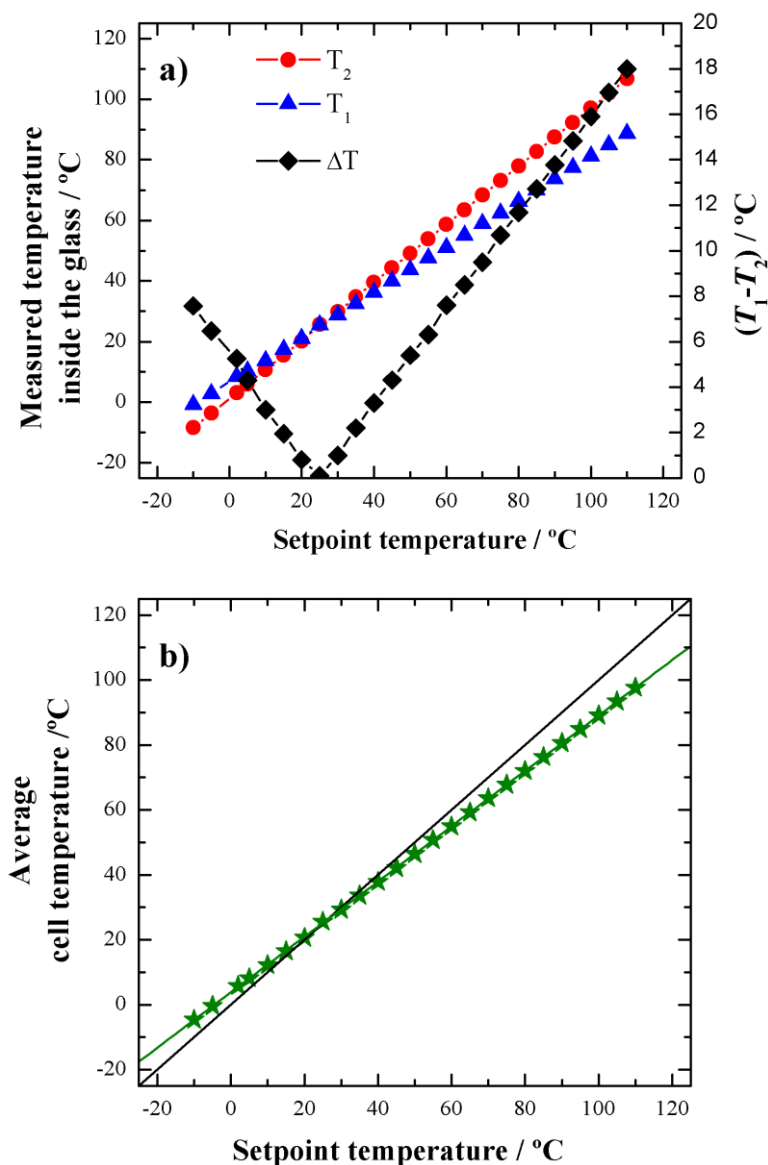
Figure 4.7 Temperature values from: a) T_1 (photoelectrode), T_2 (counter electrode), calculated temperature difference between electrodes; and b) average cell temperature *vs.* set point temperature.

Figure 4.7 shows the temperature readings of a DSC device under illumination. Typically the temperature difference between the counter-electrode side (T_2) and the peltier cold side (T_3) is less than 1 ºC, as the heat conduction of the aluminium slab is quite high. However, the temperature difference between the glass substrates of both electrodes of the solar cell can be relatively high, especially at low or high

temperatures. Above a set point of 50 ℃ the temperature gap starts widening and it can go up to 20 ℃ at 110 ℃; this illustrates the low thermal conductivity of the glass substrates. Although the gap between both electrodes is filled with liquid electrolyte, there is always a temperature gradient inside the cell, particularly at temperatures far from room temperatures. This fact highlights the importance of taking correct temperature readings when analyzing the temperature effect. In all results presented in this work the temperature was corrected to the average cell temperature calculated by the readings taken inside both glass electrodes of the solar cell (T_1 and T_2).

4.3 Results and Discussion

4.3.1 Temperature influence in DSC performance

I-V and EIS analysis were conducted in several batches of DSCs, from set point temperatures ranging from -5 ℃ to 105 ℃. V_{oc}, J_{sc}, FF and η were read for each temperature using the average of three devices; these parameter were used to characterize the performance of the cells and are now on called performance parameters. The photoconversion efficiency (η) of the solar cell was determined by its current-voltage characteristics, specifically the open-circuit photovoltage (V_{oc}), the photogenerated current density measured under short-circuit conditions (J_{sc}), the intensity of incident light (I_s) and the fill factor of the cell (FF). The current and voltage output of the DSC result from a balance between charge generation flux and recombination flux. The effect of temperature in the *I-V* curves of a typical DSC batch is presented in Figure 4.8. The *I-V* curves have been normalized with respect to V_{oc} and J_{sc} obtained at 25 ℃. As the temperature rises, there is a decrease in both V_{oc} and J_{sc} values, leading to a decrease in the performance.
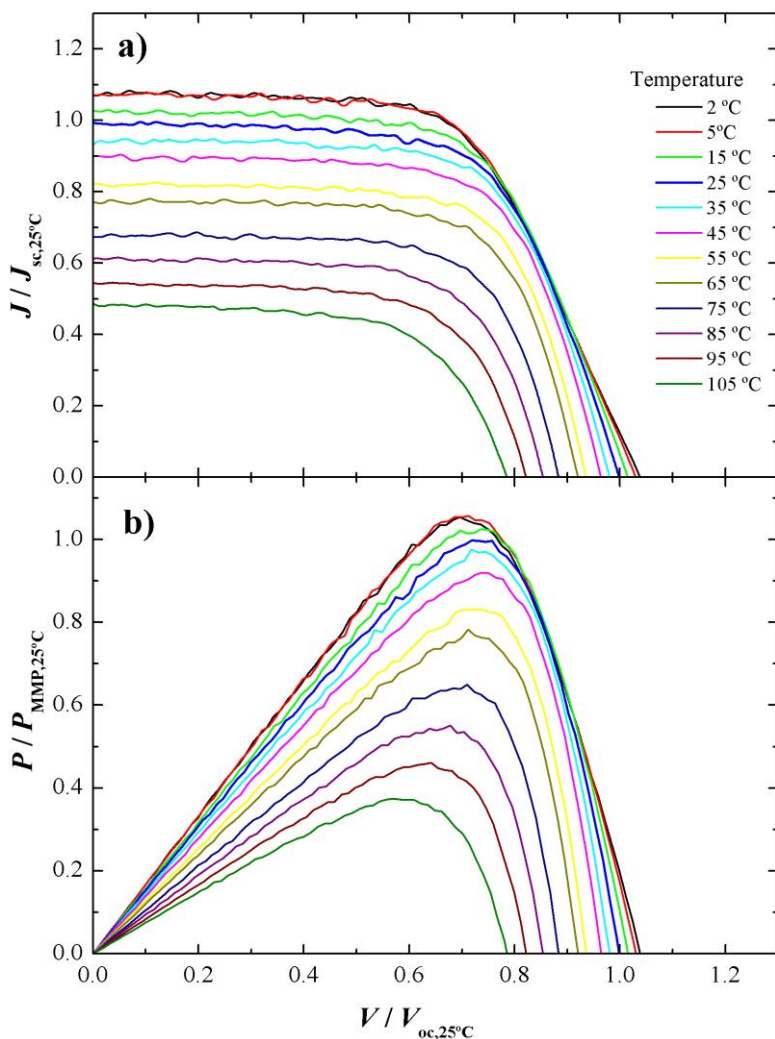
Figure 4.8 (a) *I-V* and (b) power curves normalized to the corresponding values at 25°C. ($V_{oc,25°C}$ = 0.77 V ; $J_{sc,25°C}$ = 9.4 mA·cm^{-2}; FF$_{25°C}$ = 0.65 ; $\eta_{25°C}$ = 4.8 %), as a function of the temperature.

Figure 4.9 shows the performance parameters, normalized by the corresponding values obtained at 25 °C, as a function of the temperature. FF appears to be the only parameter that has some increase with temperature. It can be clearly seen that there are different decrease rates of V_{oc} and J_{sc} as a function of the temperature; the short circuit current has a higher decrease with temperature than the open circuit voltage. FF is the ratio between the maximum power density and the product of V_{oc} and J_{sc}; because the V_{oc} decreases with temperature at a higher rate than J_{sc}, there is a higher FF for higher

temperatures. In this particular batch of cells, the efficiency is approximately constant with temperature up to *ca*. 50 ℃. Considering 25 ℃ as the reference temperature, at 50 ℃ these cells retained about 91 % of the efficiency; at 70 ℃, 70 % and at 100 ℃, only *ca*. 30 %.
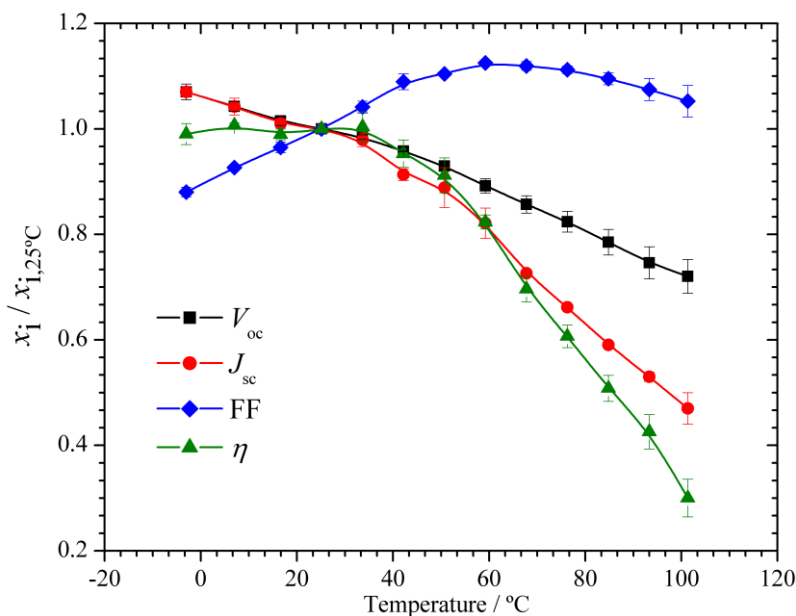
Figure 4.9 Performance parameters normalized to the corresponding values 25 ℃ values ($V_{oc,25℃}$ = 0.77 V ; $J_{sc,25℃}$ = 9.4 mA·cm^{-2}), as a function of the operating temperature. Lines were added for readability.

To check whether this loss of efficiency was reversible, the *I-V* characterization was repeated at 25 ℃ after the samples underwent the highest temperature analysis (Figure 4.10 and Table 4.1). The performance of DSCs showed excellent temperature resistance: there was a decrease in $J_{sc,}$ but an increase in the FF that resulted in a higher efficiency (5.83 % *vs*. 6.01 % before and after the tests, respectively). The V_{oc} showed no meaningful changes before and after the tests. The DSCs also showed less than 15 % total efficiency degradation after over 1000 hours of storage at room temperature in dark conditions, after conducting the temperature tests – Figure 4.11. This was mainly due to a decrease in the J_{sc}, which in turn is probably caused by dye desorption from TiO$_2$ film occurred at high temperatures, a known phenomenon with the N719/I$_3^-$ system[27,28]; the V_{oc} and FF showed remarkable stability with no particular degradation.

These results show that, in the described analysis conditions and up to 100 °C, there is no internal degradation of the solar cell components, which attests the thermal resistance and sealing quality of the prepared DSCs; this allows a correct analysis of the temperature influence.
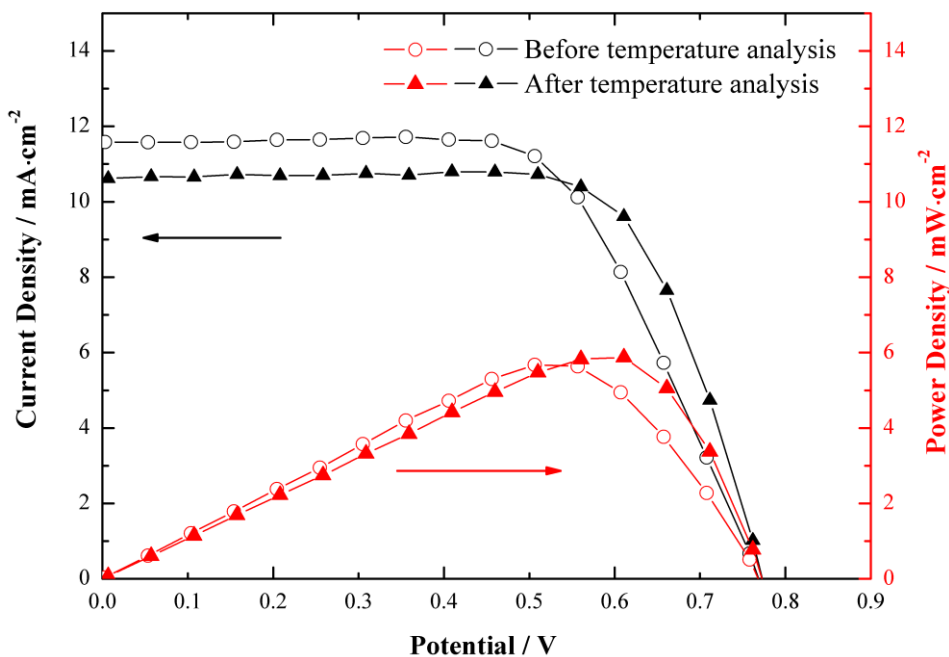
Figure 4.10 *I-V* and power density curves for a DSC before and after sustaining the temperature analysis range from 0 to 100 °C. Lines were added for readability.

Table 4.1 Performance parameters, obtained at 25 °C, of samples that underwent the temperature analysis, before and after the tests.

Parameter	Before temperature tests	After temperature tests
V_{oc} / V	0.77 ± 0.03	0.77 ± 0.02
J_{sc} / mA·cm^{-2}	11.3 ± 0.25	10.8 ± 0.19
MMP / mW·cm^{-2}	5.72 ± 0.16	5.95 ± 0.13
FF	0.66 ± 0.12	0.71 ± 0.18
η / %	5.83 ± 0.05	6.07 ± 0.04
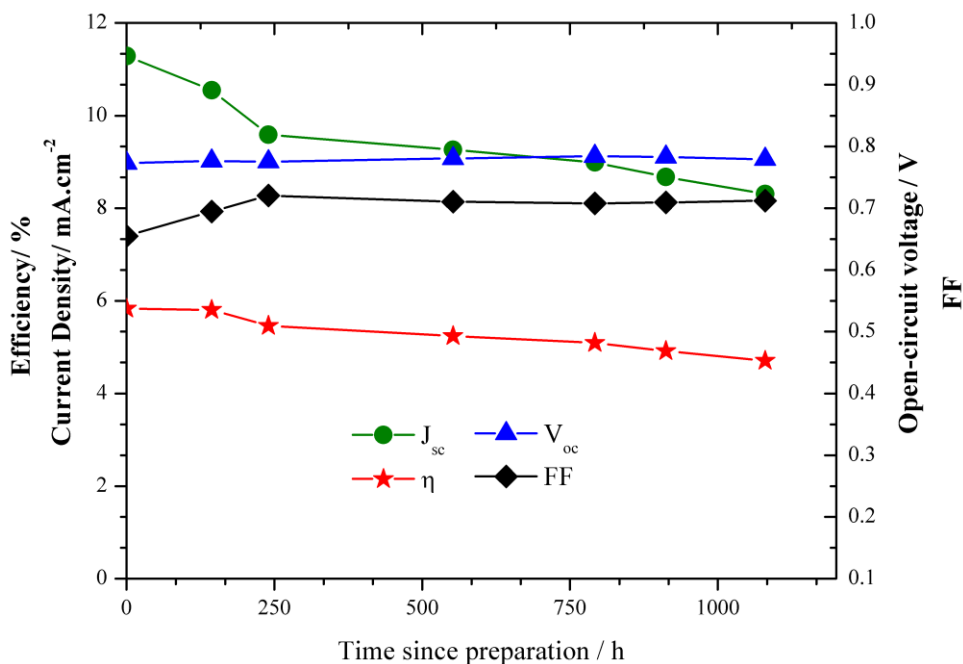
Figure 4.11 Performance parameters *vs.* time since preparation of samples that underwent the temperature analysis (0 to 100 ºC): V_{oc} – open circuit voltage; J_{sc} – short circuit current density; FF – fill factor; η - photo conversion efficiency. Lines were added for readability.

The DSC efficiency dependence on the temperature is normally assigned to the conduction band shifts in the TiO_2 photoelectrode, recombination and charge transport processes [29, 30]. Temperature controlled EIS experiments were conducted in platinum half cells, in order to characterize the temperature influence at the counter electrode during the operation of the DSCs. Bode and Nyquist diagrams are shown for platinum half cells in Figure 4.4, obtained at 0 V and under dark conditions for different temperatures; the electrochemical reaction at the platinum catalyst layer and electrolyte was then assessed. The Bode diagram shows two frequency peaks, one at low frequencies, corresponding to the diffusion of ionic species in the electrolyte (I^- and I_3^-), and another at high frequencies, ascribed to the electrochemical reaction at the platinum counter electrode with the electrolyte[31-33]. The operating temperature causes a slight frequency shift in the low frequency peak, and a moderate shift in the high frequency peak, suggesting a higher temperature influence in the charge transfer

process occurring at the Pt/electrolyte interface than in the electrolyte diffusion processes. This behavior is also observed in the Nyquist plot (Figure 4.4b): the first semicircle corresponds to the resistance associated to the electrochemical reaction of triiodide to iodide, and the second semicircle to the electrolyte diffusion in the liquid electrolyte.
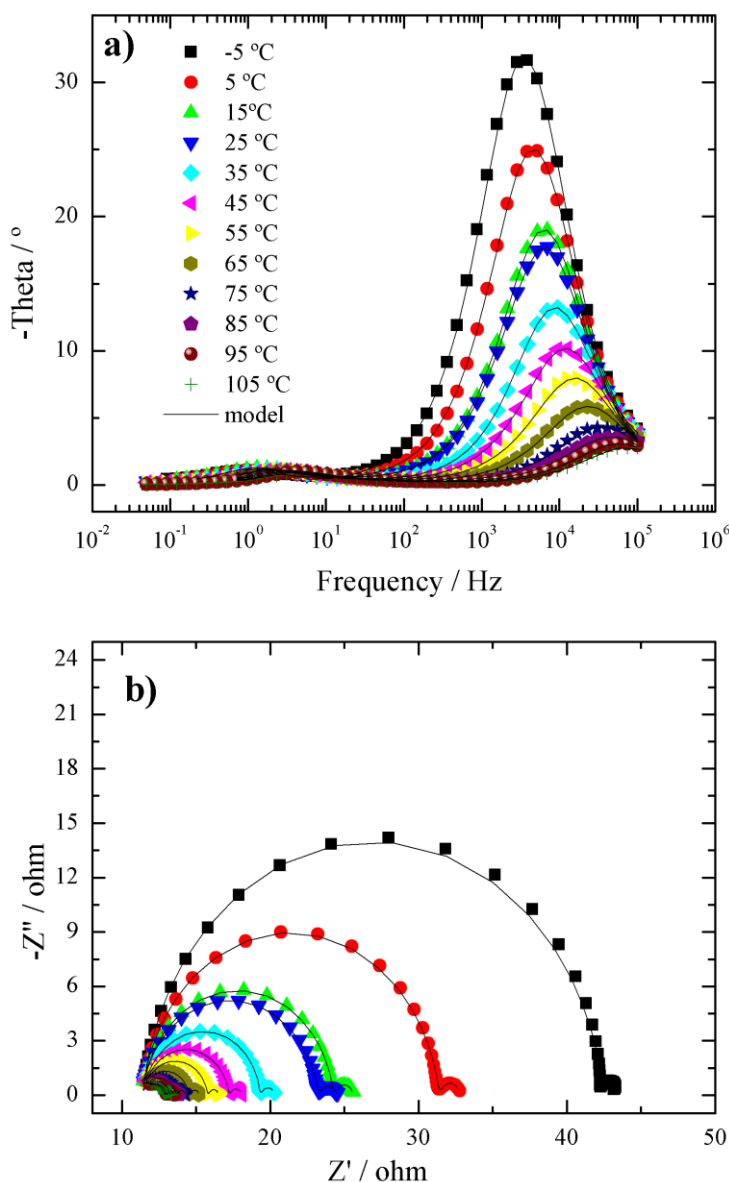
Figure 4.12 Platinum half-cell Bode (a) and Nyquist (b) plots obtained in dark conditions at 0 V in in the temperature range -5 to 105 ºC.

From the Nyquist plot it can be seen that the first semicircle changes considerably with temperature while the second semicircle changes only slightly. To understand and quantify this influence, the EIS experimental data was fitted to an equivalent electrical analogue based on a Randles-type circuit (presented in Figure 4.13), using ZView® (Scribner Associates Inc.)[34,35]. The fitting results are shown in Figure 4.14, where the charge transfer resistance (R_{CE}), chemical capacitance of the counter electrode (C_{CE}), and ionic diffusion coefficient ($D_{I_3^-}$) are plotted against temperature. R_{CE} displays an exponential trend with temperature as expected from the Butler-Volmer equation; the electrolyte diffusion shows an exponential increase with temperature as well, whereas the counter electrode electrochemical capacitance remains relatively constant, unsurprisingly, as the reaction surface area is unchanged by temperature[36]. These results suggest that temperature has a highly beneficial effect regarding to the counter electrode operation. In DSCs, the electrochemical reaction at the counter electrode is basically the same that might happen at the photoelectrode when generated electrons undesirably react with electrolyte species present in the porous film of titanium dioxide; this prejudicial reaction, typically called recombination reaction, is believed to be the main limiting factor of efficiency, not only in DSCs but in the majority of solar technologies[37-39]. The fundamental difference between both reactions is the source of electrons and the interface where the electrochemical reactions take place. At the counter electrode the triiodide reduction reaction takes place catalyzed by platinized layer applied on the SnO_2:F substrate; iodine diffuse then to the photoelectrode for regenerating the oxidized dye. Direct reduction of triiodide may happen at the photoelectrode – external recombination, which limits the total current and voltage and thus the final efficiency of the device. The recombination reaction can occur directly at TiO_2/electrolyte interface (R_1) or at the FTO/electrolyte interface (R_2), as represented in Figure 4.1.
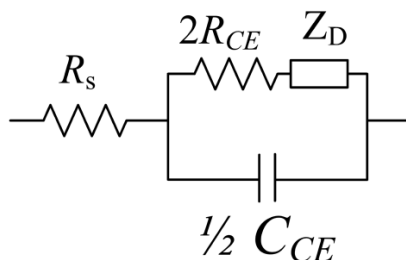
Figure 4.13 Electrical analogue used for fitting the electrochemical impedance spectra of half-cells. R_s – series resistances ; R_{CE} – charge transfer at catalytic interface; C_{CE} double layer capacitance at catalytic interface; Z_d- Nernst diffusion within electrolyte
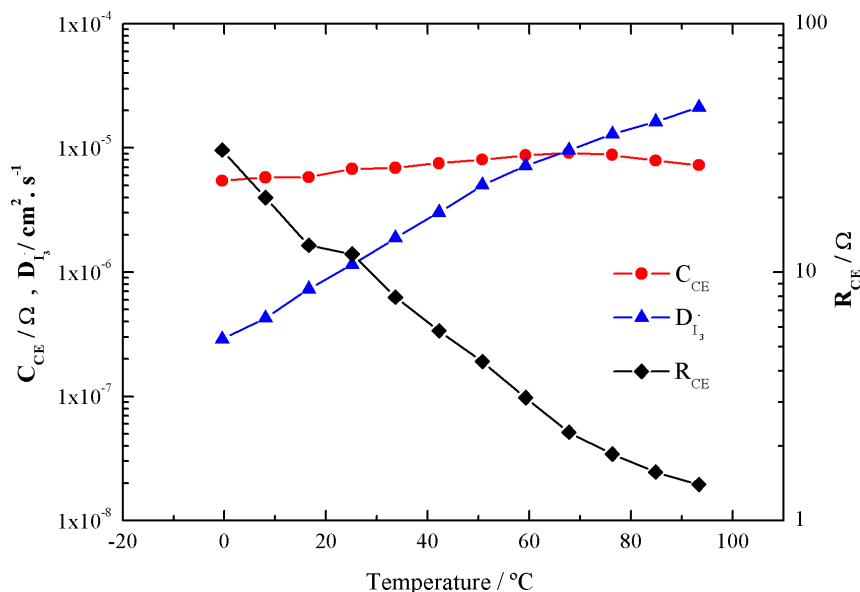
Figure 4.14. Impedance data obtained for a platinum half-cell, at 0 V in dark conditions cells in the temperature range studied. Lines were added for readability.

Figure 4.16 shows for a typical batch of DSCs the EIS results. The experimental data was fitted using appropriated electrical analogues, namely using the transmission line model (presented in Figure 4.15)[40-42]. This model, proposed by Bisquert *et al.*[23], is widely used to describe the transport and recombination kinetic processes in DSCs.
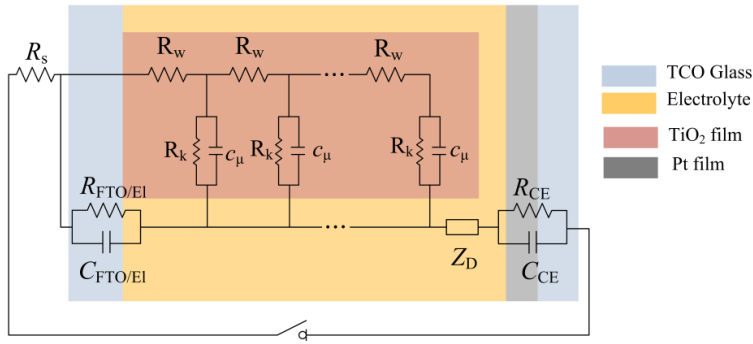
Figure 4.15 Transmission line model used to fit EIS experimental data of DSCs. R_s – series resistances; $R_{TCO/EL}$ – charge transfer resistance at exposed TCO/electrolyte interface; $C_{TCO/EL}$ double layer capacitance at exposed TCO/electrolyte interface; R_k – recombination resistance; R_w – transport resistance; c_μ – chemical capacitance; Z_d- Warburg element of the Nernst diffusion of I_3^- within electrolyte; R_{CE} – charge transfer at platinum/TCO interface; C_{CE} double layer capacitance at the platinum/TCO interface.
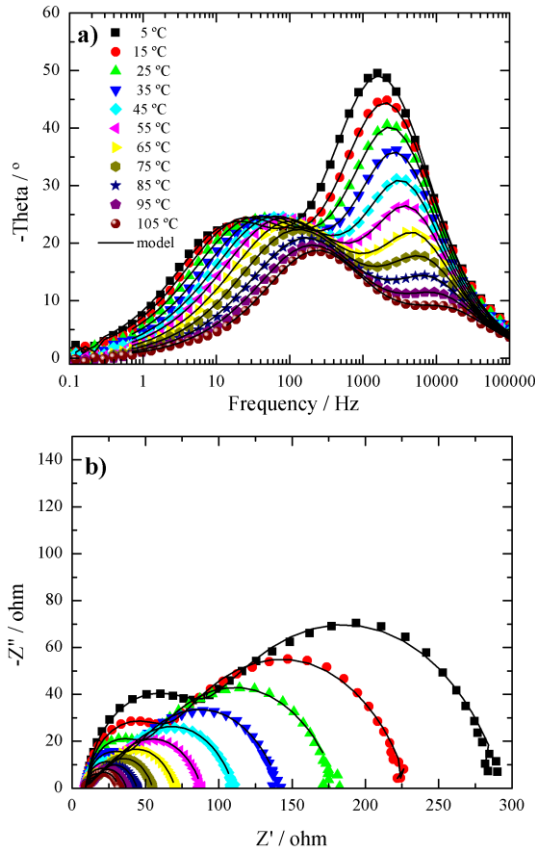
Figure 4.16 Complete DSC Bode (a) and Nyquist (b) plots obtained under dark conditions, at the V_{oc} of the cell at 25 ℃ (-0.78 V) for the temperature range of 5 ℃ to 105 ℃.

The experiments were conducted under dark conditions at the V_{oc} value obtained at 25 ℃ (0.77 V). The Bode diagram shows two frequency peaks, corresponding to the electron transport and recombination at the photoelectrode (low frequency) and to the reduction reaction occurring at the platinum counter electrode (high frequency). Both phase peaks shift to higher frequencies as temperature increases; the shift of the high frequency peak in the Bode diagram and the first semicircle in the Nyquist plot teaches that the counter electrode performance improves with the temperature. Looking at the low frequency peak in the Bode diagram (Figure 4.16a) and the second semicircle in the Nyquist plot (Figure 4.16b) it appears that the electron/electrolyte recombination resistance decreases with the temperature. The calculated parameters from the model fitting [41] are plotted against temperature in Figure 4.17. Transport and recombination related parameters are the photoelectrode capacitance, C_{PE}, electron diffusion coefficient, D_{eff}, recombination resistance, R_k, and electron lifetime, τ_{e-}. While C_{PE} appears to be relatively constant, due to the unchanged reaction surface area, R_k and τ_{e-} decrease exponentially with temperature. This highlights the fact that the recombination reaction is highly enhanced by temperature. However, electron transport, evaluated by D_{eff}, improves with temperature. Considering that the final performance of the solar cell is a balance between electron generation, recombination and transport, there are two opposite effects caused by temperature: on one hand the recombination increases with the temperature; however, the electron transport rate also increases with temperature. Assuming that electron generation rate, conduction band and electrolyte redox potentials are mostly constant with temperature[6], in terms of DSC performance clearly the balance is negative as seen from the global efficiency *vs.* temperature results (Figure 4.8 and Figure 4.9). This highlights that, in terms of temperature dependence, recombination is dominant over the charge transport.
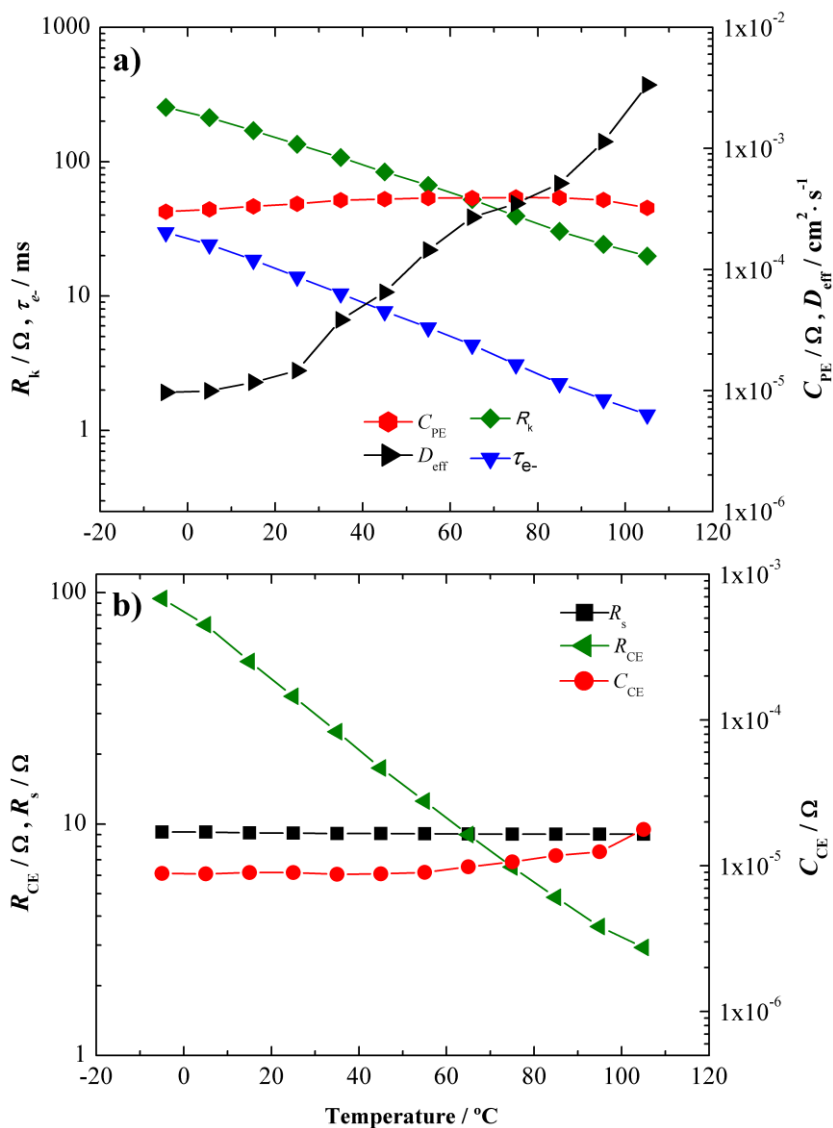
Figure 4.17 Impedance parameters obtained by EIS for complete DSCs cells at 0.78 V under dark conditions, for the temperature range studied. Lines were added for readability.

4.3.2   Recombination and DSC performance as a function of the temperature

To assess the recombination rate at interfaces TiO_2/electrolyte and FTO/electrolyte of the solar cell and their temperature dependence, five batches of DSCs were prepared and analyzed by means of *I-V* and EIS characterization. Each batch, of three identical cells, differs in terms of total recombination rate constant, $k_r(i)$. To experimentally change the total recombination reaction constant, $k_r(1)$ to $k_r(5)$, the perimeter length of the glass frit sealing was varied as displayed by Figure 4.18a); all the remaining solar cell design parameters (such as TiO_2 active area, distance to metallic contacts, etc.) were kept constant. This way it is possible to change the extent of free TCO area in contact with electrolyte, and thus the amount of generated electrons that may recombine with triiodide. It should be emphasized that the total distance from the active area to the metallic contact remains constant; therefore the series resistance in the solar cell is also constant between batches. Because the TiO_2/electrolyte interface is constant for all five batches of cells, it is then possible to assess the temperature effect on the recombination rate constant at the FTO/electrolyte.

Figure 4.18b) plots the electron lifetime against the exposed electrolyte area for DSCs with and without TiO_2 blocking layer. Indeed, the exposed area affects recombination, even in the case of DSCs with TiO_2 blocking layer applied over the SnO_2-F film. This illustrates the importance of minimizing the exposed non-active area to electrolyte, as well as the optimization of blocking layer design. An ideal blocking layer should completely prevent recombination, fact that does not happen according to the results presented in Figure 4.18b). The blocking layer employed was applied by chemical bath deposition of aqueous $TiCl_4$ solution; although this is a common method when preparing high efficient DSCs, it is known that this procedure may produce a defected blocking layer[12,43].
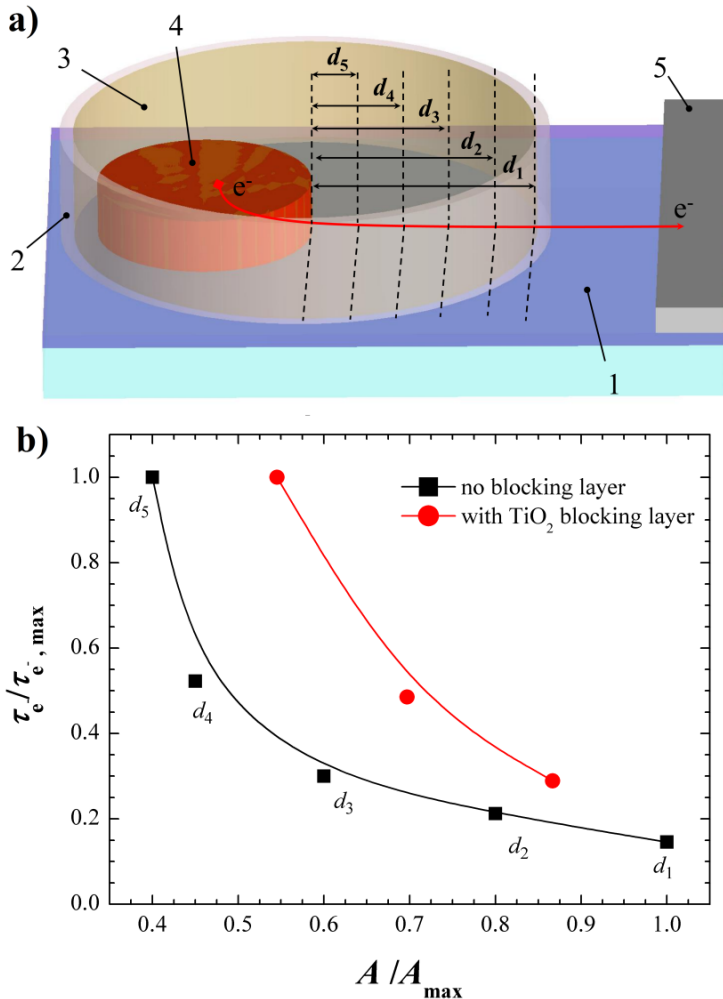
Figure 4.18 a) Schematic diagram showing the methodology to control the FTO/electrolyte exposed reaction interface in the photoelectrode; 1 – TCO; 2 – glass frit sealing; 3 – electrolyte; 4 – TiO_2 with adsorbed sensitizer; 5 – electrical contact; the dashed lines represent the relative positioning of the glass frit sealing. b) Experimental results of electron lifetime versus exposed area of electrolyte to FTO or TiO_2 blocking layer. Lines were added for readability.

Analyzing the *I-V* parameters (normalized by results at 25 °C) for the different DSC batches, Figure 4.19, it is possible to conclude that the trend of each parameter (V_{oc}, J_{sc}, FF and η) depends on the total recombination rate constants; the rate constants were numbered from the highest, $k_r(1)$, to the lowest $k_r(5)$. The results indicate that the total recombination reaction rate increases monotonously with interface area and temperature. This means that even though the prepared solar cells at 25 °C have similar
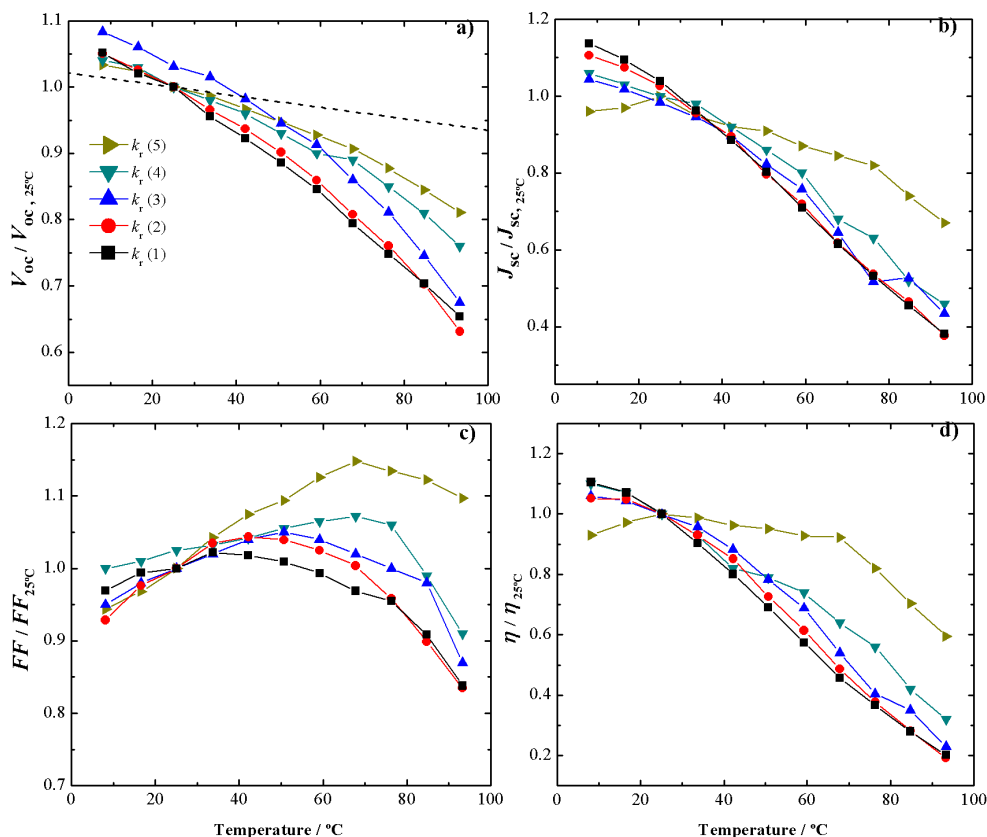
Figure 4.19 *I-V* performance parameters relative to 25 ºC values of five different batches of DSCs differing in the recombination reaction constant k_r(i).The black dashed line in a) corresponds to the theoretical V_{oc} *vs.* temperature trend expected for a cell with no recombination (calculated from the Butler-Volmer equation[44]). Lines were added for readability.

efficiencies (~ 5 % to 6 %), when subjected to different operating temperatures, substantial changes in performance emerge. The differences observed in the FF and efficiency are caused by $V_{oc}(T)$ and $J_{sc}(T)$ values. On one hand, it is expected TiO_2 conduction band down shift to the electrolyte redox potential, reducing in this way the open circuit voltage; however, this shift causes only a slight change as seen Figure 4.19a) (dashed black line, calculated from the Butler-Volmer equation[44]). The difference between the normalized open circuit potential values, V^*_{oc}, predicted by Butler-Volmer and the observed values was assigned to the recombination. On the other hand, J_{sc} is basically determined by the balance between electron generation and recombination. Assuming that the temperature has a negligible effect in the photon

absorption and electron generation processes[45,46], the trend observed in Figure 4.19b) should then be mainly attributed to recombination. It can be concluded that recombination has a preponderant influence in the V_{oc} and J_{sc} evolution with temperature.

The recombination rate constants of the five batches of DSCs were plotted against the inverse of temperature to construct the Arrhenius plot – Figure 4.20a). As expected, the curves corresponding to cells with higher recombination display higher recombination rates. There are clearly two different trends in each curve with a breaking point at *ca*. 40 ºC, which correspond to different activation energy values. The activation energies (E_a) were calculated for each batch of cells, based on two linear fittings. The two E_a values for each batch corresponds to the temperature ranges below ($E_{a,lt}$) and above ($E_{a,ht}$) 40 °C. These values were plotted against the respective rate constants in Figure 4.20b). There are two important observations: i) for both temperature ranges, the activation energies increase with recombination rate; ii) $E_{a,lt}$ is lower than $E_{a,ht}$. This means that more efficient cells, *i.e.* with less recombination (lower k_r), have lower activation energy values. This fact can be explained as follows: in this work to obtain high recombination cells the exposed TCO interface to electrolyte was increased as previously described; this means that for high recombination cells (*i.e.*, $k_r(1)$) most of the recombination interface is SnO_2-F. Oppositely, in low recombination cells (*i.e.*, $k_r(5)$) there is nearly no FTO exposed, and the main recombination reaction proceeds at TiO_2 interface.

The results suggest that the driving force for the electrochemical reaction between electrons and triiodide is related not only with a reaction rate constant, $k_r(T)$, (that is temperature dependent) and chemical concentration of triiodide in electrolyte (that in this case is constant across devices), but also with the energy level of electrons. Given this, when electrons are in a higher energy level (*i.e.* TiO_2 CB, -4.2 eV[47]) the activation energy required for recombination is lower comparing with electrons in lower energy levels (*i.e.* SnO_2-F CB, -4.7 eV[47]). This support the results for the activation energies being lower for TiO_2 dominant cells compared with DSCs with largely exposed TCO. Indeed, these results clearly show that the activation energy barrier rules the recombination process.
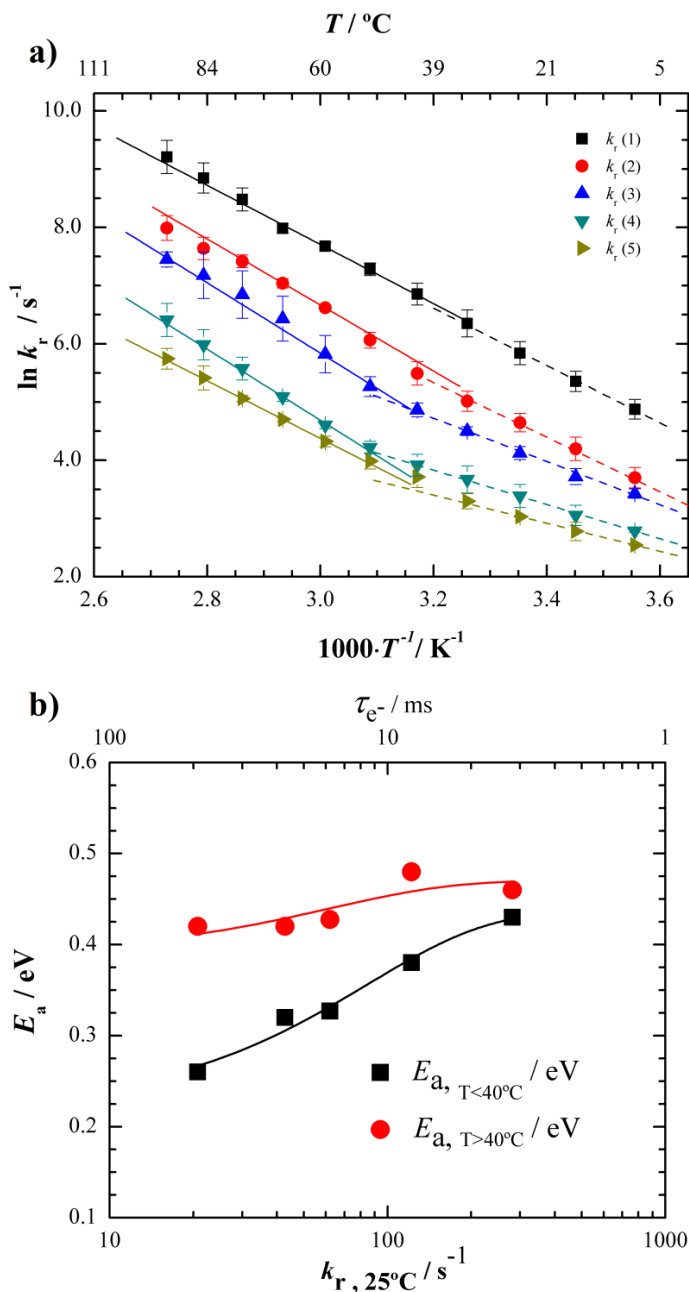
Figure 4.20 Arrhenius plot, with respective linear fittings, for several sets of DSCs with different recombination rate constants; b) Activation energies *vs.* recombination rate constant and respective exponential fits, calculated from the Arrhenius plot trends found for temperatures lower and above 40 °C. The calculated activation energies increase with recombination; an axis displaying the lifetime of electrons is also shown. Lines were added for readability.

Chemical reactions occasionally show an Arrhenius plot with two different linear trends at regions of low and high temperatures, respectively. Typically, this feature is associated with simultaneous and competing reactions or reaction mechanisms involving different activation energies[48], with one reaction being dominant depending on the temperature range. In the present case, to understand the two trends of the DSCs recombination reaction Arrhenius plot, half-cells of FTO (SnO_2-F), TiO_2 and platinum films were prepared and analyzed as described before; the corresponding Arrhenius plot is shown in Figure 4.21. As expected the platinum half-cells show very high reaction rates since platinum is good catalyst for the reduction reaction of triiodide to iodide. The SnO_2-F / SnO_2-F half-cells show two clear distinct trends in the Arrhenius plot: between 30 °C - 40 °C there is very little influence of temperature in the reaction rate, showing very small activation energy in this temperature range. However, for temperatures higher than 40 ºC there is a good linear fit resulting in activation energy of 0.66 eV. Contrarily, in the case of TiO_2/TiO_2 half-cells, the Arrhenius plot does not show multiple trends and the calculated activation energy was found to be 0.47 eV.

To rationalize the shape of the Arrhenius plots for recombination in DSCs, seen in Figure 4.20a), the logarithmic of the average rate constants for SnO_2-F and TiO_2 was plotted -green curve in Figure 4.21. This has a similar shape as the ones from complete DSCs, showing that the influence that temperature has in the recombination process makes a contribution from two distinct recombination mechanisms that occur at the different interfaces of the solar cell.

The data presented at Figure 4.21 shows that at temperatures below 40 ºC, temperature has almost no influence in recombination reaction rate at the TCO interface. This suggests that at low temperature the main recombination reaction mechanism should be between trapped electrons and electrolyte. SnO_2-F trap states, located at energies below the conduction band, could be positioned close and even at lower energies than the redox energy of the electrolyte (energies from SnO_2-F CB and redox energy of electrolyte are close, *ca*. -4.7 and -5.0 eV, respectively[47]), which means that below a certain temperature (40 ºC according to the results of this work) the reaction rate is mostly temperature independent, simply because most electrons do not have sufficient energy to react with the electrolyte. However, in the TiO_2 case, due to

its higher conduction band energy (~ -4.26 eV), most trap states ought to be located above the redox energy of the electrolyte. This means that, for the temperature range studied, most trapped electrons should have enough energy to react with electrolyte species.

The results suggest that there is a shift in the dominant recombination pathway from trapped electrons to electrolyte to CB electrons to electrolyte, which explains the different trends in the Arrhenius plots. The recombination reaction mechanism between CB electrons and electrolyte species requires less activation energy; this is confirmed by the activation energy values presented in Figure 4.20b). As the total recombination increases (higher k_r in abscissas axis of Figure 4.20b), activation requires progressively more energy due to the trapping energy.

The different shapes found in the Arrhenius plots of the platinum half cells can also be explained considering that the catalyst layer consists of platinum nanoparticles deposited on the TCO; SnO_2-F crystals exposed to electrolyte at this surface provide an alternative reaction pathway from the Pt catalyst.

Taking into account the above considerations, the main results concerning recombination *vs.* temperature are compiled in Table 4.2. The cells with low k_r show higher V_{oc} and higher activation energies for recombination reaction that occurs mainly at TiO_2 /electrolyte: $E_{a,lt} = 0.26$ eV and $E_{a,ht} = 0.42$ eV; when the main recombination interface is SnO_2-F/electrolyte (high k_r) the activation energy is found to be $E_{a,lt} = 0.43$ eV and $E_{a,ht} = 0.46$ eV.
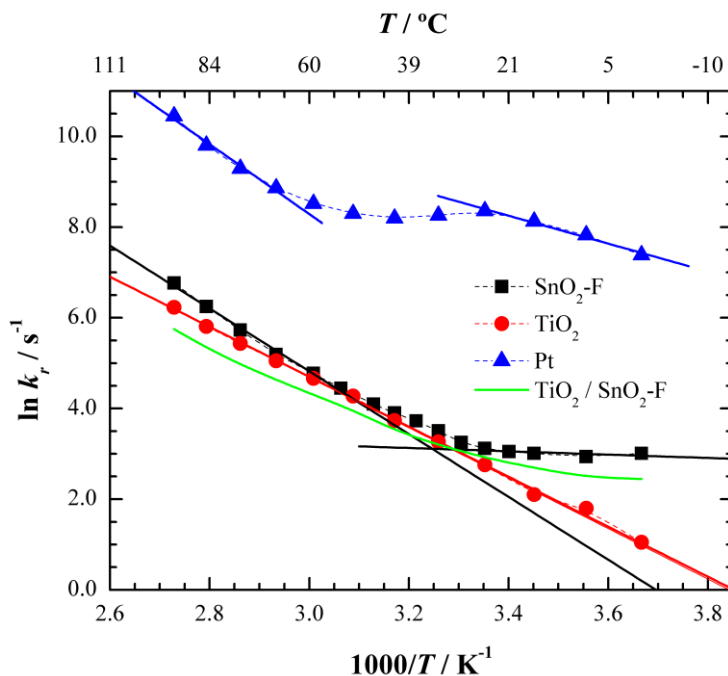
Figure 4.21 Arrhenius plot of recombination reaction (reduction of triiodide) for three types of half-cells: SnO_2-F, TiO_2 blocking layer and Pt. The green curve represents the average between the TiO_2 and SnO_2-F curves.

Table 4.2 Recombination rate constants, open-circuit voltages at 25 ℃, and activation energies calculated for different batches of complete DSCs and half-cells.

Device		$k_{r,25℃}$ / s^{-1}	$V_{oc,25℃}$ / V	$E_{a,lt}$ / eV	$E_{a,ht}$ / eV
DSCs	$k_{r,(1)}$	281	0.719	0.43	0.46
	$k_{r,(2)}$	122	0.727	0.38	0.48
	$k_{r,(3)}$	62.1	0.734	0.33	0.43
	$k_{r,(4)}$	42.8	0.768	0.32	0.42
	$k_{r,(5)}$	20.8	0.770	0.26	0.42
Half-cells	Pt	4257		0.30	0.75
	SnO_2-F	22.64		0.0	0.66
	TiO_2	16.00		0.47	0.47

4.4 Conclusions

DSC performance as a function of the temperature was assessed for a wide range of temperatures, from -5 ºC up to 105 ºC. DSC cells were hermetically sealed using the recently developed laser assisted glass sealing process, which allowed obtaining reliable results. Within the temperature range considered, it was not observed degradation of the components of the solar cells, with full efficiency reversibility (at 25 ºC) in samples tested up to 100 ºC.

The recombination was quantified as a function of temperature and for SnO_2-F/electrolyte and TiO_2/electrolyte interfaces. It was concluded that the electrons energy level significantly affects the recombination reaction: when electrons are in a higher energy level (*i.e.* TiO_2 CB) the driving force for recombination is lower comparing with lower energy level electrons (*i.e.* SnO_2-F CB). Thus, the activation energy was found to be lower for the recombination taking place at TiO_2 interface than SnO_2-F interface with electrolyte (0.47 eV *vs.* 0.66 eV, respectively).

Arrhenius plots for recombination rates in DSCs showed two different activation energies for temperatures below and above *ca.* 40 ºC. To explain this fact, the authors propose a shift in the dominant recombination pathway from trapped electrons/electrolyte to CB electrons/electrolyte. This work shows that recombination depends on both the temperature and semiconductor interfaces present in the solar cell.

Generally temperature has an overall negative effect on the DSC performance; this effect was shown to be governed by the total electron/electrolyte recombination.

Acknowledgements

References

1.   S. R. Raga and F. Fabregat-Santiago, *Physical Chemistry Chemical Physics*, 2013, **15**, 2328-2336.

2.   M. Toivola, L. Peltokorpi, J. Halme and P. Lund, *Solar Energy Materials and Solar Cells*, 2007, **91**, 1733-1742.

3.   M. Berginc, U. Opara Krašovec, M. Jankovec and M. Topič, *Solar Energy Materials and Solar Cells*, 2007, **91**, 821-828.

4.   H. Yang, C. Yu, Q. Song, Y. Xia, F. Li, Z. Chen, X. Li, T. Yi and C. Huang, *Chem. Mater.*, 2006, **18**, 5173-5177.

5.   K. Lobato and L. M. Peter, *The Journal of Physical Chemistry B*, 2006, **110**, 21920-21923.

6.   J. S. Henry, S.-M. Lukas, G. Michael and C. Marco, *Physical Review B (Condensed Matter and Materials Physics)*, 2006, **74**, 045306 045301-045306 045306

7.   M. Wang, P. Chen, R. Humphry-Baker, S. M. Zakeeruddin and M. Gratzel, *ChemPhysChem*, 2009, **10**, 290-299.

8.   R. Memming, *Semiconductor Electrochemistry*, Wiley-VCH, 2001.

9.   M. Bailes, P. J. Cameron, K. Lobato and L. M. Peter, *The Journal of Physical Chemistry B*, 2005, **109**, 15429-15435.

10.   B. O'Regan, L. Xiaoe and T. Ghaddar, *Energy & Environmental Science*, 2012, **5**, 7203-7215.

11.   B. C. O'Regan and J. R. Durrant, *The Journal of Physical Chemistry B*, 2006, **110**, 8544-8547.

12.   P. J. Cameron and L. M. Peter, *The Journal of Physical Chemistry B*, 2003, **107**, 14394-14400.

13.   L. Kavan, N. Tétreault, T. Moehl and M. Grätzel, *The Journal of Physical Chemistry C*, 2014.

14.   L. Kavan, M. Zukalova, O. Vik and D. Havlicek, *ChemPhysChem*, 2014, **15**, 1056-1061.

15.   D. H. Kim, M. Woodroof, K. Lee and G. N. Parsons, *ChemSusChem*, 2013, **6**,

1014-1020.

16. J. Xia, N. Masaki, K. Jiang and S. Yanagida, *The Journal of Physical Chemistry B*, 2006, **110**, 25222-25228.

17. H.-J. Son, C. Prasittichai, J. E. Mondloch, L. Luo, J. Wu, D. W. Kim, O. K. Farha and J. T. Hupp, *Journal of the American Chemical Society*, 2013, **135**, 11529-11532.

18. K.-I. Jang, E. Hong and J. Kim, *Korean J. Chem. Eng.*, 2012, **29**, 356-361.

19. C. Jiang, W. L. Koh, M. Y. Leung, W. Hong, Y. Li and J. Zhang, *Journal of Solid State Chemistry*, 2013, **198**, 197-202.

20. W. Yongzhen, Y. Xudong, C. Han, Z. Kun, Q. Chuanjiang, L. Jian, P. Wenqin, I. Ashraful, B. Enbing, Y. Fei, Y. Maoshu, Z. Peng and H. Liyuan, *Applied Physics Express*, 2014, **7**, 052301.

21. B. C. O'Regan, J. R. Durrant, P. M. Sommeling and N. J. Bakker, *The Journal of Physical Chemistry C*, 2007, **111**, 14001-14010.

22. F. d. r. Sauvage, D. Chen, P. Comte, F. Huang, L.-P. Heiniger, Y.-B. Cheng, R. A. Caruso and M. Graetzel, *ACS Nano*, 2010, **4**, 4420-4425.

23. J. Bisquert, *The Journal of Physical Chemistry B*, 2002, **106**, 325-333.

24. J. Bisquert, *Journal of Electroanalytical Chemistry*, 2010, **646**, 43-51.

25. F. Ribeiro, Maçaira,J. , Cruz, R., Gabriel, J., Andrade, L., Mendes, A., *Solar Energy Materials and Solar Cells*, 2012, **96**, 43-49.

26. PCT/IB2012/051376, 2012.

27. N. Jiang, T. Sumitomo, T. Lee, A. Pellaroque, O. Bellon, D. Milliken and H. Desilvestro, *Solar Energy Materials and Solar Cells*, 2013, **119**, 36-50.

28. N. Kato, K. Higuchi, H. Tanaka, J. Nakajima, T. Sano and T. Toyoda, *Solar Energy Materials and Solar Cells*, 2011, **95**, 301-305.

29. A. Usami, S. Seki, Y. Mita, H. Kobayashi, H. Miyashiro and N. Terada, *Solar Energy Materials and Solar Cells*, 2009, **93**, 840-842.

30. H. J. Snaith and L. Schmidt-Mende, *Advanced Materials*, 2007, **19**, 3187-3200.

31. L. Andrade, J. Sousa, H. A. Ribeiro and A. Mendes, *Solar Energy*, 2011, **85**, 781-793.

32. R. Cruz, D. A. Pacheco Tanaka and A. Mendes, *Solar Energy*, 2012, **86**, 716-

724.

33. F. Fabregat-Santiago, J. Bisquert, G. Garcia-Belmonte, G. Boschloo and A. Hagfeldt, *Solar Energy Materials and Solar Cells*, 2005, **87**, 117-131.

34. R. Cruz, J. P. Araujo, L. Andrade and A. Mendes, *Journal of Materials Chemistry A*, 2014, **2**, 2028-2032.

35. A. Hauch and A. Georg, *Electrochimica Acta*, 2001, **46**, 3457-3466.

36. J. Bisquert, *Physical Chemistry Chemical Physics*, 2003, **5**, 5360-5364.

37. H. J. Snaith, *Advanced Functional Materials*, 2010, **20**, 13-19.

38. B. E. Hardin, H. J. Snaith and M. D. McGehee, *Nat Photon*, 2012, **6**, 162-169.

39. J. Maçaira, L. Andrade and A. Mendes, *Renewable and Sustainable Energy Reviews*, 2013, **27**, 334-349.

40. J. Bisquert, M. Gratzel, Q. Wang and F. Fabregat-Santiago, *The Journal of Physical Chemistry B*, 2006, **110**, 11284-11290.

41. L. Andrade, S. M. Zakeeruddin, M. K. Nazeeruddin, H. A. Ribeiro, A. Mendes and M. Grätzel, *ChemPhysChem*, 2009, **10**, 1117-1124.

42. Q. Wang, J.-E. Moser and M. Grätzel, *The Journal of Physical Chemistry B*, 2005, **109**, 14945-14953.

43. B. Yoo, K.-J. Kim, S.-Y. Bang, M. J. Ko, K. Kim and N.-G. Park, *Journal of Electroanalytical Chemistry*, 2010, **638**, 161-166.

44. J. Macaira, L. Andrade and A. Mendes, *RSC Advances*, 2014, **4**, 2830-2844.

45. M. Grätzel, *Progress in Photovoltaics: Research and Applications*, 2000, **8**, 171-185.

46. M. Grätzel and J.-E. Moser, in *Electron Transfer in Chemistry*, ed. V. Balzani, Wiley-VCH, Weinheim, 2001, vol. 5, ch. Part 3.

47. R. Memming, in *Semiconductor Electrochemistry*, Wiley-VCH Verlag GmbH, 2007, pp. 241-263.

48. L. Masgrau, À. González-Lafont and J. M. Lluch, *Theor Chem Acc*, 2003, **110**, 352-357.

CHAPTER 5

Modeling, Simulation and Design of Dye Sensitized Solar Cells

"Design is not just what it looks like and feels like. Design is how it works"

Steve Jobs

5

Modeling, Simulation and Design of Dye Sensitized Solar Cells

Abstract

It is well known that recombination and transport rule the performance of dye sensitized solar cells (DSCs); although, the influence that these two phenomena have in their performance, particularly in the open circuit-potential (V_{oc}) and in the short circuit current (J_{sc}), is not fully understood. In this paper a phenomenological model is used to describe the quantitative effect that transport and recombination have in the performance of the solar cell and their influence in its optimal design. The model is used to predict the influence of the recombination reaction rate constant (k_r) and diffusion coefficient (D_{eff}) in the V_{oc} and in the J_{sc}, whether a linear or non-linear recombination kinetics is considered. It is provided a methodology for decoupling the conduction band shifts from recombination effect in charge extraction experiments. Results also suggest that the influence of recombination in the V_{oc} and in J_{sc} is highly dependent on the reaction order considered. This fact highlights the importance of considering the reaction order when modeling data obtained by experimental methods. The combined results are analyzed and discussed in terms of the collection efficiency and in the optimization of the photoelectrode thickness. The model provides also a useful framework for exploring new concepts and designs for improving DSCs performance.

5.1 Introduction

The dye sensitized solar cell (DSC) is a potentially low cost photovoltaic technology that recently has achieved 12 % efficiency by two different approaches[1,2]. A very recent work reported an energy conversion efficiency of 15 % for a new sensitized solar cell[3]. This world record has been announced by M. Gräztel at the Hybrid and Organic Photovoltaic conference (HOPV 2013) meeting held in Seville in 2013 and has been certified as 14 % of energy efficiency by Newport Corporation[3]. Dye sensitized solar cells (DSCs) mimic natural photosynthesis and differ from conventional p-n junction devices because light collection and charge transport are separated in the cell[4]. Light absorption occurs in the chemisorbed sensitizer molecule, while electron transport occurs in the semiconductor. The photo conversion energy efficiency (η) of the solar cell is determined by its current-potential characteristics, specifically the open-circuit photopotential (V_{oc}), the photocurrent density measured under short-circuit conditions (J_{sc}), the intensity of incident light (I_s) and the fill factor of the cell (FF). The working principles of DSCs, illustrated in Figure 5.1, can be summarized in the following steps:

a) Light harvesting: photon absorption by dye molecules adsorbed in a monolayer on the surface of the mesoporous semiconductor (typically TiO_2); electrons from the ground state (S) are promoted to the excited state (S*, k_{11}):

$$S \underset{k_{12}}{\overset{hv,k_{11}}{\rightleftharpoons}} S^*$$

(5.1)

b) Injection: the excited electrons are injected into the conduction band of the semiconductor (k_{21}), resulting in the oxidation of the sensitizer (S$^+$):

$$S^* \underset{k_{22}}{\overset{k_{21}}{\rightleftharpoons}} S^+ + e^-_{CB}$$

(5.2)

c) Dye regeneration: reduction of the oxidized sensitizer (S$^+$) to its original state (S) by electron donation from I$^-$ present in the liquid electrolyte, producing I_3^- (k_3):

$$S^+ + \frac{3}{2}I^- \xrightarrow{k_3} \frac{1}{2}I_3^- + S \qquad (5.3)$$

d) Collection: diffusive collection of electrons from the mesoporous semiconductor to the transparent conductive oxide (TCO) where they become available for electrical work in the external circuit;

e) Electrolyte mass transfer: diffusive transport of the reduced I_3^- and oxidized I^- through the pores of the semiconductor to and from the counter electrode (usually coated with a platinum catalyst);

f) Electrolyte regeneration: at the counter electrode the platinum catalyst reduces the oxidized I_3^- back to I^- by reaction with a low energy electron from the external circuit (k_4):

$$I_3^- + 2e^- \xrightarrow{Pt,k_4} 3I^- \qquad (5.4)$$

During this series of reactions, there are also processes that are unfavorable to the DSC performance:

g) Decay of dye excited state: decay of the excited state of the dye (S^+) to the ground state (S) before electron injection in the conduction band of the semiconductor. This reaction (k_{12}) competes directly with the injection step (k_{21});

h) Electron-dye recombination (k_{22}): reaction between the oxidized dye molecules (S^+) and electrons in the conduction band of the TiO_2. This competes with dye regeneration (k_3) and with collection of electrons from the TiO_2 (d);

i) Electron-electrolyte recombination: reaction of conduction band electrons with electrolyte species. This reaction competes with electron collection (d).

$$I_3^- + 2e_{CB}^- \xrightarrow{k_5} 3I^- \qquad (5.5)$$
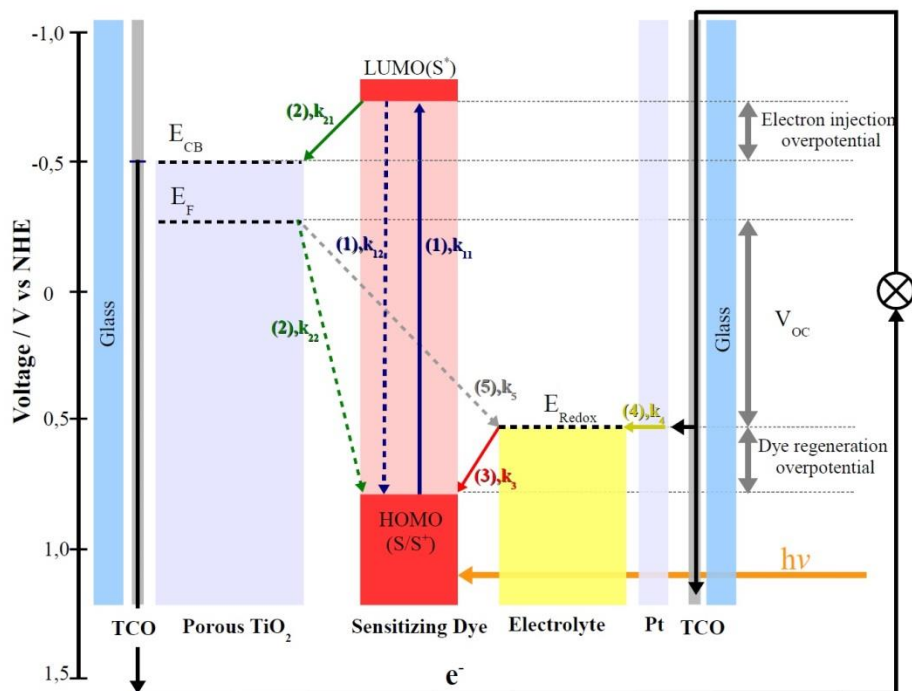
Figure 5.1 Illustration of DSC's working principles. The full arrows represent the forward electron transfer reactions; the dashed arrows represent electron losses routes.

For solar cell to produce electrical energy, the forward electron transfer reactions (k_{11}, k_{21}, k_3 and k_4) must overcome the possible electron lost pathways (k_{12}, k_{22} and k_5). The time constant ranges of each reaction are illustrated in Figure 5.2[5]. The recombination reaction of electrons with electrolyte species (k_5) is considered to be one of the most important energy efficiency bottlenecks. Because the electrolyte is present throughout all the porous structure of the semiconductor, the recombination reaction is affected by the photoelectrode thickness, iodide concentration, dye structure and others[6-9].

The average electron diffusion coefficients in anatase TiO_2 range between 10^{-4} and 10^{-5} $cm^2 \cdot s^{-1}$ [10], resulting in an electron transport time constant (τ_{tr}) for a typical 10 μm thick photoelectrode in the range of few milliseconds. The electron lifetime (τ_{e^-}) corresponding to a recombination reaction constant of k_5 – Figure 5.2, has the same order of magnitude of the electron transport time constant resulting in a direct

competition between these two mechanisms. The current and potential outputs of the DSC are recombination limited, and result from a balance between the charge generation and the recombination fluxes. Controlling charge extraction, by increasing transport, and lowering charge recombination will increase the efficiency of DSCs. Thus, understanding charge recombination and controlling recombination rate constants is of utmost importance. Several studies have been carried out to understand how recombination can been lowered in DSCs, and many articles have been published examining the effect of electrolyte additives, new photoanode architectures, new dyes, surface coatings, among other factors[11-23].
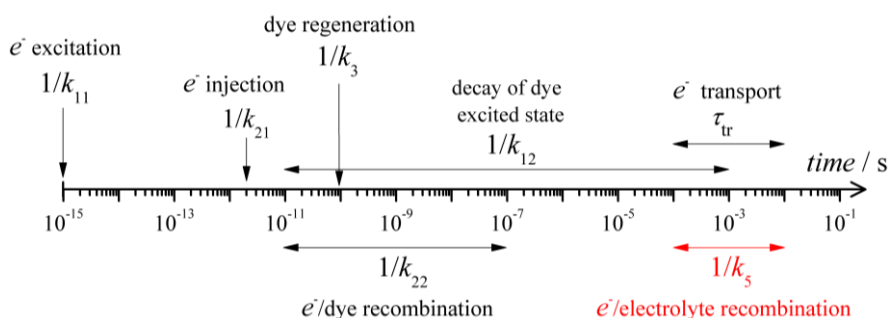
Figure 5.2 Dynamics of the electrochemical processes during DSCs operation; adapted from [5].

In this work a dynamic phenomenological model proposed initially by Andrade *et al.*[24] is used to describe the quantitative effect that transport and recombination have in the performance of the solar cell, and the influence that this has in its design. The model is used to predict the influence of the recombination reaction rate constants (k_r) and diffusion coefficients (D_{eff}) in the V_{oc} and J_{sc}, considering linear or non-linear recombination reaction. The results are helpful, particularly in decoupling phenomena seen in charge extraction experiments that are usually used to assess and compare recombination rates among DSC samples.

5.2 Modeling

The model used in this work is based on the initially proposed model by Andrade *et al.*[24] but taking into account the recombination reaction order parameter *β*. The mobile species considered in the present model are electrons in the conduction band of

TiO_2 and iodide and triiodide ions in the liquid electrolyte. The developed model of an irradiated DSC assumes the following physical and chemical processes:

1) electron generation (from excited dye molecules);
2) electron transport in the porous semiconductor (TiO_2);
3) electron recombination with electrolyte species;
4) oxidation of iodide (inside the pores of TiO_2);
5) and reduction of triiodide (at the platinum catalyst).

It is assumed that the cell is irradiated perpendicularly to the photoelectrode and that each absorbed photon generates one injected electron into the TiO_2 conduction band. All injected electrons are considered from the excited state of the dye, and not from TiO_2 band gap excitation. Reactions (1) and (2) are considered irreversible since their forward kinetic constants are much higher that the corresponding reverse kinetic constants ($k_{11} >> k_{12}$ and $k_{21} >> k_{22}$)[5]. Therefore only one possible mechanism for electron loss is assumed, corresponding to the recombination reaction of electrons with electrolyte species (reaction 5, k_5).

Figure 5.3 illustrates the modeled DSC. The photoelectrode is deposited over the TCO layer, which has an electrical resistance of R_{TCO}, and is made of a film of sintered TiO_2 nanoparticles with thickness L_f and porosity ε. The dye is adsorbed on this mesoporous film of TiO_2 as a monolayer. The dye has a wavelength-dependent light absorption coefficient of $\alpha(\lambda)$. The liquid electrolyte, made of the redox pair I^- / I_3^- (with diffusion coefficients D_{I^-} and $D_{I_3^-}$), is responsible for the regeneration of the dye, transporting low energy electrons from the counter-electrode. The TCO-TiO_2 interface was defined to be at $x = 0$. This interface is modeled as an ideal ohmic contact, meaning that there is no charge transfer resistance at the interface. At the counter electrode, the interface electrolyte-platinum catalyst happens at $x = L$ and the electrochemical reduction of I_3^- was described by the Butler-Volmer equation. The electron transport in the photoelectrode was assumed to be governed by diffusion (negligible convection)[18].
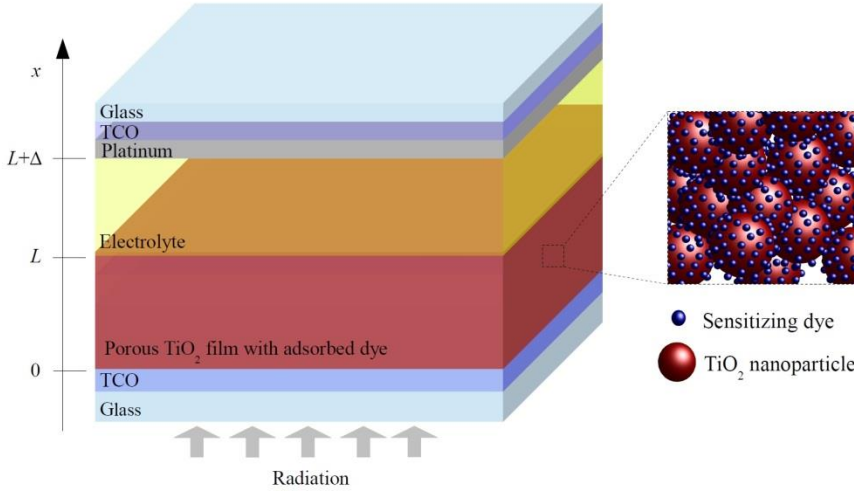
Figure 5.3 Scheme of the modeled DSC.

From the previous assumptions, the continuity and transport equation that describe the mobile species is[24]:

$$-\frac{\partial J_i}{\partial x} + G_i(x) - R_i(x) = \frac{\partial n_i}{\partial t}, \qquad i = \text{e}^-, \text{I}_3^-, \text{I}^- \tag{5.6}$$

The first term on the left hand side of equation (5.6) represents the charge carrier flux. The second and third terms, $G_i(x)$ and $R_i(x)$, represent the generation and recombination rates of species i, respectively. The term on the right hand side of the equation is the time derivative of the species i concentration. The charge carrier flux, J_i, is assumed to occur by diffusion only and is given by the Fick's law[25]:

$$J_i = -D_i \frac{\partial n_i}{\partial x} \tag{5.7}$$

and the generation rate is given by the Beer-Lambert law that relates the absorption of light to the properties of the material through which the light is travelling:

$$G_i = \eta_{inj} \alpha(\lambda) I_0 e^{-\alpha(\lambda)x} \tag{5.8}$$

Each absorbed photon is assumed to produce one injected electron. The developed model considers a uniformly distributed monolayer of dye through the surface area of TiO$_2$. The injection efficiency parameter, η_{inj}, takes into account this phenomenon but also the light reflection and glass and electrolyte absorption losses.

For each two electrons that react with triiodide, three ions of iodide are formed (reaction 5). The recombination rate term can be written as follows[26]:

$$R_{e^-} = k_r\left(n_{e^-}(x,t) - n_{eq}\right)^{\beta} \tag{5.9}$$

The recombination reaction kinetics is subject of much debate and some of the scientific work published so far considers that this reaction follows first-order kinetics:

$$\beta = 1 \; ; k_r = \frac{1}{\tau_{e^-}} \tag{5.10}$$

where k_r is the reacton rate constant and τ_{e^-} is the electron lifetime.

However, several uncertainties surround the recombination kinetics in DSCs and the respective parameters that govern the solar cells behavior. Some models assume that the rate at which electrons are transferred from the conduction band to the redox electrolyte is first order in free electron concentration ($\beta = 1$)[27,28]. However, it has been suggested that deviations from the first order model may arise from the recombination process being mediated by electronic surface states below the TiO_2 conduction band[29-31]. A non-linear model formulation is then being suggested:

$$\beta \neq 1 \; ; \; k_r = k_0 \frac{1}{\tau_{e^-}} \tag{5.11}$$

where k_r is the reaction rate constant, in $m^{-3(1-\beta)} \cdot s^{-1}$, and k_0 is a model constant. The driving force of the recombination reaction is the diference between the generated electrons density, $n_{e^-}(x,t)$, and the dark equilibrium electron density, n_{eq}. This electron density corresponds to the resulting equilibrium bewteen the electron at the fermi level and the redox potential of the electrolyte:

$$n_{eq} = N_{CB} \exp\left[-\frac{E_{CB} - E_{redox}}{k_B T}\right] \tag{5.12}$$

According to the above assumptions the model equations can be written as follows:

Electrons balance

Introducing equations (5.7)–(5.9) into the continuity equation (5.6), the continuity equation for electrons comes:

$$D_{e^-}\frac{\partial^2 n_{e^-}}{\partial x^2} + \eta_{inj}\alpha(\lambda)I_0 e^{-\alpha(\lambda)x} - k_r\left(n_{e^-}(x,t) - n_{eq}\right)^{\beta} = \frac{\partial n_{e^-}}{\partial t} \tag{5.13}$$

Assuming that for $t = 0$ the cell is not illuminated, the electron density is equal to the dark electron density, n_{eq}:

$$t = 0 \quad n_{e^-}(x, 0) = n_{eq} \tag{5.14}$$

A charge balance at the interface $x = 0$ determines that the electron flux at $x=0^+$ equals the electron flux at $x=0^-$. Therefore, the charge balance at this interface is given by $J_{e^-}^{0^+} = J_{e^-}^{0^-}$. Because $J_{e^-}^{0^+}$ corresponds to the diffusive electrons transported through the TiO$_2$, which in steady state is the net current produced by the solar cell, J_{cell}, the boundary condition for $x=0$ is:

$$x = 0 \, ; J_{e^-}^{0^+} = -qD_{e^-} \frac{\partial n_{e^-}}{\partial x} \Big|_{x=0^+} \tag{5.15}$$

where q is the electron elementary charge. At $x=L$ there is no contact between the film of TiO$_2$ nanoparticles and the platinized FTO. Therefore, there are no electrons bridging between the photoelectrode and the counter-electrode. Only iodide and triiodide perform this charge transfer. Thus, the corresponding boundary condition for $x = L$ is:

$$x = L \, ; \frac{\partial n_{e^-}}{\partial x} = 0 \tag{5.16}$$

Iodide and Triiodide balance

Each generated mole of electrons causes the consumption of one mole of I$^-$ ion and the production of half mole of I$_3^-$ that can be reduced back to I$^-$ form either at the platinum layer or due to the recombination reaction (undesirable back reaction). Besides the reduction of triiodide that takes place at the counter-electrode, the oxidation and reduction reactions of the ionic species take place in the photoelectrode porosity. Accordingly to the stoichiometry reactions (5.3) and (5.4) the terms of generation and recombination of triiodide and iodide must be affected by the corresponding coefficients:

$$D_{I^-} \frac{\partial^2 n_{I^-}}{\partial x^2} - \frac{3}{2\varepsilon} \left[\eta_{inj} \alpha(\lambda) I_0 e^{-\alpha(\lambda)x} - k_r \left(n_{e^-}(x,t) - n_{eq} \right)^\beta - \frac{\partial n_{e^-}(x,t)}{\partial t} \right] = \frac{\partial n_{I^-}(x,t)}{\partial t}$$
$$\tag{5.17}$$

$$D_{I_3^-} \frac{\partial^2 n_{I_3^-}}{\partial x^2} + \frac{1}{2\varepsilon} \left[\eta_{inj} \alpha(\lambda) I_0 e^{-\alpha(\lambda)x} - k_r \left(n_{e^-}(x,t) - n_{eq} \right)^\beta - \frac{\partial n_{e^-}(x,t)}{\partial t} \right] = \frac{\partial n_{I_3^-}(x,t)}{\partial t}$$
$$\tag{5.18}$$

At instant $t = 0$, the concentration of iodide and triiodide is known:

$$t = 0 \; : \; n_{I_3^-}(x,0) = n_{I_3^-}^{ini} \; ; \; n_{I^-}(x,0) = n_{I^-}^{ini} \tag{5.19}$$

At the interface of TiO$_2$/TCO, $x = 0$, only electrons are able to flow so the net flux of I$_3^-$ and I$^-$ is zero:

$$x = 0 \; : \; \frac{\partial n_{I_3^-}}{\partial x} = 0 \; ; \; \frac{\partial n_{I^-}}{\partial x} = 0 \tag{5.20}$$

Although there is generation and consumption of both ionic species, their total number of moles remains constant, thus resulting in the following integral boundary condition:

$$x = L : \; \int_0^L n_{I_3^-}(x)dx = n_{I_3^-}^{ini} L \; ; \; \int_0^L n_{I^-}(x)dx = n_{I^-}^{ini} L \tag{5.21}$$

For the three charged species, e$^-$, I$_3^-$ and I$^-$, the initial and boundary conditions, (5.14), (5.15), (5.16) and (5.19)-(5.21), are given and are necessary to solve the three non-linear differential equation system, (5.13), (5.17) and (5.18). However, additional information is needed at $x = 0$ to solve the system: the net current at this interface must be known, J_{cell}. Assuming that the external circuit has no resistances, the electron density generated by the cell, J_{cell}, equals the current density that is returned to the cell via the counter electrode, J_0. Here, electrons participate in the reduction reaction of triiodide to iodide - reaction (5.4) - catalyzed by the platinum catalyst deposited on top of the TCO surface and thus it can be treated as an electrochemical half-cell[32]; the charge transfer can be described by the Butler-Volmer equation. This approach is considered to describe the electrochemical kinetics at this interface $x = L + \Delta$[33,34]:

$$J_{cell} = J_0 \left[\frac{n_{I_3^-}(L)}{n_{I_3^-}^{oc}(L)} e^{\frac{\alpha q \eta_{Pt}}{k_B T}} - \frac{n_{I^-}(L)}{n_{I^-}^{oc}(L)} e^{\frac{-(1-\alpha)q \eta_{Pt}}{k_B T}} \right] \tag{5.22}$$

The Butler-Volmer equation describes the reduction reaction overpotential at the counter-electrode catalyst as a function of the current density. It describes the charge transfer over a metal/electrolyte interface assuming no charge diffusion limitations in the electrolyte. The charge transfer reaction at the platinized interface has a charge transfer resistance, R_{ct}. An overpotential is necessary to drive the reaction at a certain current density, J_{cell}. As stated by equation (5.22), the current density of the cell depends on the exchange current density, J_0, which is the electron's ability to exchange with the solution, but also on the platinum overpotential, η_{Pt}. This value translates the

necessary potential to overcome the energy barrier of the reaction of the electrons with the triiodide. This corresponds to an overall potential loss of the solar cell and must be as low as possible[35,36]. The counter electrode overpotential, η_{Pt}, can be obtained as follows[24]:

$$\Delta V_{int} = \frac{1}{q}\left[E_{CB} + k_B T \ln\frac{n_{e^-(x=0)}}{N_{CB}} - E_{redox}^0 - \frac{k_B T}{2}\ln\frac{n_{I_3^-}^{oc}}{(n_{I^-}^{oc}L)^3} - q\eta_{Pt}\right]$$

$$\eta_{Pt} = \frac{E_{CB} - E_{redox}^{oc}}{q} + \frac{k_B T}{q}\left[\ln\frac{n_{I_3^-}^{oc}}{2(n_{I^-}^{oc}L)^3} + \ln\frac{n_{e^-(x=0)}}{N_{CB}}\right] - \Delta V_{int} \qquad (5.23)$$

Analyzing equation (5.23) is understood that η_{Pt}, and consequently the electrons flux, depends on the internal potential of the solar cell. There are also external resistances that should be accounted for and correlated to the internal resistances; this can be done using Kirchhoff's and Ohm's laws[32]:

$$\Delta V_{int} = (R_s + R_{ext})\left(\frac{R_p}{R_{ext}+R_s+R_p}\right)A\,J_{cell} \qquad (5.24)$$

where R_s is the sum of all external resistances, R_{ext} is the applied load, R_p are the shunt resistances, and A the active area of the DSC. Equation (5.24) should be inserted in the counter electrode overpotential equation (5.23) and then introduced in the Butler-Volmer equation (5.22). Thus the produced current of the solar cell, equation (5.22), can be determined by the applied load, R_{ext}. The external potential given by the device is calculated taking into account the produced current, the applied load and the other resistances taken into account in the model:

$$V_{ext} = R_{ext}\left(\frac{R_p}{R_{ext}+R_s+R_p}\right)A\,\cdot J_{cell} \qquad (5.25)$$

To decrease the number of variables and to improve numerical convergence issues of the numerical methods, the model parameters were made dimensionless respecting to the electron and ionic species parameters and the semiconductor thickness:

$$\varphi = \alpha(\lambda)L, \qquad \theta = \frac{D_{ref}}{L^2}t, \qquad n_i^* = \frac{n_i}{n_{ref}}, \qquad x^* = \frac{x}{L},$$

$$D_i^* = \frac{D_i}{D_{ref}}, \quad j_{cell}^* = \frac{J_{cell}}{J_0}, \qquad Da = \frac{L^2\cdot\eta_{inj}\cdot\alpha(\lambda)\cdot I_0}{D_{ref}\cdot n_{ref}}, \qquad \phi = L\sqrt{L^{3(1-\beta)}\cdot\frac{k_r}{D_{ref}}}$$

Using the above established dimensionless variables, the dimensionless equations and respective initial and boundary conditions can be written as follows for the three modeled species (e$^-$, I$_3^-$ and I$^-$):

Dimensionless Electrons Balance

$$D_{e^-}^* \frac{\partial n_{e^-}^*}{\partial x^{*2}} + \left[Da\, e^{-\varphi x^*} - \phi^2 \left(n_{e^-}^* - n_{eq}^* \right)^\beta \right] = \frac{\partial n_{e^-}^*}{\partial \theta} \tag{5.26}$$

Initial condition:

$$\theta = 0 \; ; \; n_{e^-}^*(x^*, 0) = n_{eq}^* \tag{5.27}$$

Boundary conditions:

$$x^* = 0 \; ; J_{cell}^* = \frac{n_{ref} D_{ref}\, q}{L} \left(D_{e^-} \frac{\partial n_{e^-}^*}{\partial x^*} \Big|_{x=0^+} \right) ; x^* = 1; \; \frac{\partial n_{e^-}^*}{\partial x^*} = 0 \tag{5.28}$$

Dimensionless Triiodide Balance

$$D_{I_3^-}^* \frac{\partial^2 n_{I_3^-}^*}{\partial x^{*2}} + \frac{1}{2\varepsilon} \left[Da\, e^{-\varphi x^*} - \phi^2 \left(n_{e^-}^* - n_{eq}^* \right)^\beta - \frac{\partial n_{e^-}^*}{\partial \theta} \right] = \frac{\partial n_{I_3^-}^*}{\partial \theta} \tag{5.29}$$

Initial condition:

$$\theta = 0 \; ; \; n_{I_3^-}^*(x^*, 0) = n_{I_3^-}^{*\,ini} \tag{5.30}$$

Boundary conditions:

$$x^* = 0 \; ; \frac{\partial n_{I_3^-}^*(0,\theta)}{\partial x^*} = 0 \; ; x^* = 1 \; ; \; \int_0^1 n_{I_3^-}^*(x^*)dx^* = n_{I_3^-}^{*ini} \tag{5.31}$$

Dimensionless Iodide Balance

$$D_{I^-}^* \frac{\partial^2 n_{I^-}^*}{\partial x^{*2}} - \frac{3}{2\varepsilon} \left[Da\, e^{-\varphi x^*} - \phi^2 \left(n_{e^-}^* - n_{eq}^* \right)^\beta - \frac{\partial n_{e^-}^*}{\partial \theta} \right] = \frac{\partial n_{I^-}^*}{\partial \theta} \tag{5.32}$$

Initial condition:

$$\theta = 0 \; ; \; n_{I^-}^*(x^*, 0) = n_{I^-}^{*\,ini} \tag{5.33}$$

Boundary conditions:

$$x^* = 0 \; ; \frac{\partial n_{I^-}^*(0,\theta)}{\partial x^*} = 0 \; ; x^* = 1 \; ; \; \int_0^1 n_{I^-}^*(x^*)dx^* = n_{I^-}^{*ini} \tag{5.34}$$

The system of equations (5.26), (5.29) and (5.32) describes the mobile species concentration profiles with time. The partial differential equations were spatially discretized using the finite differences method. The time integration was accomplished by the numerical package developed by the Lawrence Livermore National Laboratory, LSODA [37] .

5.3 Experimental

5.3.1   Dye sensitized solar cell preparation

   Steady state simulated results were critically compared with experimental results of two DSCs with different photoelectrode thicknesses: device A with 7.5 µm and device B with 12.5 µm. The photoelectrodes were prepared on 2.2 mm thick and 7 $\Omega \cdot \square^{-1}$ FTO coated glass substrates from Solaronix®. First, the glasses were washed sequentially with a detergent solution (Alconox®, VWR) in an ultrasonic bath at 55 ºC for 15 min, followed by ultrasonic cleaning in deionized water at room temperature, rinsed with ethanol and dried with air. To form a thin and compact layer of TiO_2 above the FTO layer, the substrates were immersed in a 40 mM $TiCl_4$ aqueous solution at 70 ºC, for 20 minutes. After washing with water and ethanol, the samples were dried with a nitrogen flow. Then, the samples were coated with porous TiO_2 layer by screen printing a commercial TiO_2 paste (Ti-Nanoxide T/SP from Solaronix®), followed by drying at 80 ºC for 20 minutes. To control the final thickness of the transparent layer of TiO_2, the screen printing procedure (printing and drying) was repeated as necessary to get the desired thickness of photoelectrode. The samples were annealed at 500 ºC for 15 min in an infrared electrical oven. After firing, the samples were again treated with a 40 mM $TiCl_4$ aqueous solution at 70 ºC for 20 minutes, before being sintered at 500 ºC for 30 min. The counter electrodes, prepared on the same type of glass substrates and cleaned as described before, were drilled previously with two holes of 1 mm diameter. A drop of H_2PtCl_6 solution (2 mg of Pt in 1 mL ethanol) was applied on the glass substrate followed by annealing at 400 ºC for 15 minutes. Both electrodes were assembled and sealed using a laser assisted glass frit method described in Chapter 2 [38]. Dye adsorption in the porous TiO_2 was obtained recirculating 1 mM N719 dye solution for 10 hours, followed by ethanol rinsing, nitrogen drying, electrolyte filling (Iodolyte Z-150 from Solaronix®) and hole sealing by thermoplastic sealant (Surlyn®, Dupont).

5.4 Results and Discussion

5.4.1   Current-potential characteristics

The input values of parameters for the simulation step are listed in Table 5.1. For each parameter it is indicated if the value was obtained by fitting to the experimental results (parameters k_r, β and E_c-E_{redox}) or from an independent source.

The experimental *I-V* characteristics were obtained in a set-up equipped with a 1600 W xenon light source (Oriel class B solar simulator, Newport, USA) irradiating 100 mW·cm^{-2} (1 sun light intensity) and using a 1.5 air mass filter (Newport, USA). The simulator was calibrated using a single crystal Si photodiode (Newport, USA). The *I-V* characteristics of the solar cell were obtained applying an external potential bias (electrical load) and measuring the generated photocurrent.

Figure 5.4 plots the experimental and simulated I-V and power curves for the two sets of samples. The experimental and simulated results are in good agreement. Table 5.2 present the experimental and simulated performance parameters; the relative difference between both is smaller than 2 % showing that the model is able to simulate accurately the experimental results.
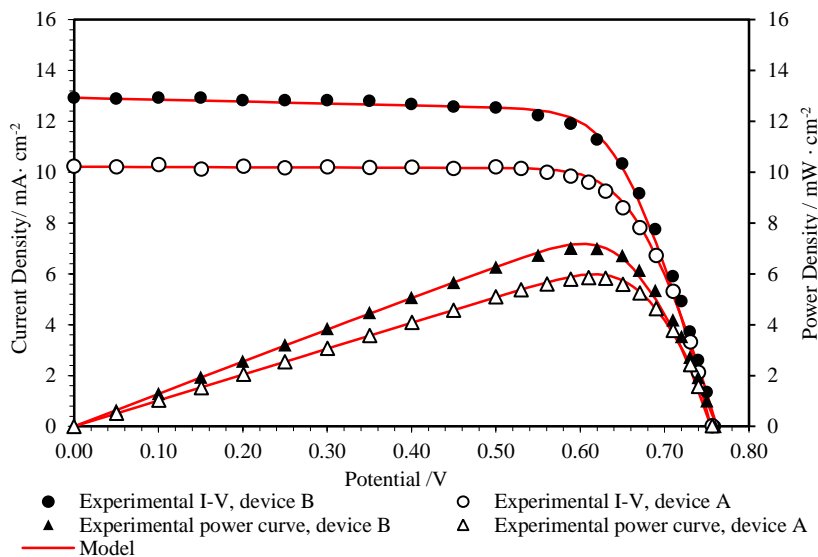

Figure 5.4 Experimental and simulated results *I-V* and power curves for device A and B (photoelectrode with 7.5 µm and 12.5 µm thickness). All other parameters are presented in Table 5.1.

Table 5.1 Input values for the simulation step for devices A and B.

	Parameter	notation	Device A	Device B	Ref
Morphological features	PE Thickness	L_f / μm	7.5	12.5	Measured
	Film Porosity	ε	0.63		Computed
	Active area	A / cm^2	0.158		Measured
Photon absorption/ electron Injection	Incident Photon Flux	I_s / cm$^{-2}\cdot$s^{-1}	1.47×10^{17}		Measured
	Injection Efficiency	η_{inj}	0.90		[39]
	Dye Absorption Coefficient	$\alpha(\lambda)$ / cm^{-1}	1000		Computed
	Temperature	T / K	298		Measured
Initial/boundary concentrations of species	Initial Concentrations	$C^0_{e^-}$	0		-
		$C^0_{I_3^-}$ /mmol$\cdot$dm^{-3}	100.0		Computed
		$C^0_{I^-}$ / mmol$\cdot$dm^{-3}	1100		Computed
	Open-Circuit Concentrations	$C^{oc}_{I_3^-}$ / mmol$\cdot$dm^{-3}	99.00		Computed
		$C^{oc}_{I^-}$ / mmol$\cdot$dm^{-3}	1102		Computed
Diffusion coefficients of species	Diffusion coefficients	$D_{I_3^-}$ / cm$^2\cdot$s^{-1}	4.91×10^{-6}		[24]
		D_{I^-} / cm$^2\cdot$s^{-1}	4.91×10^{-6}		[24]
		D_{eff} / cm$^2\cdot$s^{-1}	1.10×10^{-4}		[24]
Pt Counter electrode	Exchange Current Density	J_0 / mA$\cdot$cm^{-2}	6.81×10^{-2}		Computed
	Symmetry Parameter	ζ	0.78		[32]
Recombination reaction	Reaction order coefficient	β	0.75		Fit
	Rate constant	k_r / m$^{-0.75}\cdot$s^{-1}	8.00	6.62	Fit
Density of States	E_{cb} - E_{redox}	eV	0.93	0.94	Fit
	Effective density of states in the TiO$_2$ conduction band	N_c / cm^{-3}	1.00×10^{21}		[40]
External Resistances	Shunt Resistances	R_p / Ω	76129	14392	Computed
	External Series resistances	R_s / Ω	40	47	Computed

Table 5.2 Performance parameters of the simulated and experimental results.

Semiconductor thickness	12.5 μm			7.5 μm		
Performance Parameter	Simulation	Experimental	(σ / %)	Simulation	Experimental	(σ / %)
J_{sc} / mA·cm^{-2}	12.93	12.95	(0.1)	10.21	10.23	(0.2)
V_{oc} / V	0.75	0.76	(0.6)	0.76	0.76	(0.7)
MMP /mW·cm^{-2}	7.18	7.12	(0.9)	5.98	5.88	(1.7)
V_{mpp} / V	0.61	0.60	(1.2)	0.62	0.62	(0.0)
J_{mpp} / mA·cm^{-2}	11.85	11.89	(0.1)	9.63	9.48	(1.6)
Fill Factor, FF	0.74	0.73	(1.4)	0.77	0.76	(1.2)
Efficiency, η	**7.18**	**7.12**	(0.9)	**5.98**	**5.88**	(1.7)

Even though the model predicts the experimental results reasonably well, there are some deviations, particularly in the maximum power point. The deviation is caused by the difference in the simulated and experimental fill factor. This difference probably relates to the rough estimation made for the shunt resistance. The shunt resistance relates to the back electron transfer across the TiO_2/dye/electrolyte interface, particularly in the dye free areas of the TiO_2 surface and can be estimated from the slope of the experimental *I-V* curve at short circuit[41].

5.4.2 Influence of recombination in DSCs

Controlling the recombination reaction is believed to be the key to developing new materials and cell architectures for high efficient DSCs. Thus the interpretation of the recombination rate constants influence in the working mechanisms of DSCs is of extreme importance[40,42]. In the previous section the model was compared to experimental results and proved to model well the steady state behavior of the prepared DSCs. In this section, the influence of k_r in the performance of the solar cell is assessed. This parameter affects the amount of generated electrons that react back to the electrolyte. Figure 5.5 shows the simulated *I-V* curves for recombination rate constants ranging from 5 to 1000 s^{-1} ($\beta = 1$). Clearly, the *I-V* curve is affected by the

amount of electrons that recombine, which is reflected particularly in the J_{sc} and V_{oc} values.

Figure 5.6 shows the simulated electron density profiles at steady-state conditions and the theoretical photon absorption/electron generation through the TiO$_2$ film according to the Beer-Lambert law. Since solar radiation is assumed to strike the photoanode side of the solar cell (see Figure 5.3), at $x = 0$, most of the electrons are generated near this interface, due to the exponential behavior of the absorption law. For this reason, and also because the transport path for the generated electrons increases from $x = 0$ to 12.5 μm, a larger electron density gradient is seen at the beginning of the film decreasing towards zero at positions close to $x = 12.5$ μm. This indicates that the initial TiO$_2$ layer thickness fraction closer to the illuminated side of the solar cell is the one that contributes the most for the current delivered by the cell. The change in the electron lifetime (assumed first order recombination) has a strong influence in the electron density across the semiconductor. The electron density profiles have been simulated for short-circuit (Figure 5.6), maximum power point (Figure 5.7) and open circuit conditions (Figure 5.8). As expected, for higher recombination rates the concentration of electrons are lower justifying the lower values of J_{sc} (Figure 5.6) and V_{oc} (Figure 5.8) parameters.

Figure 5.5 Simulated *I-V* curves with different recombination reaction rate constants. All other parameters are presented in Table 5.1, device B.

Figure 5.6 Simulated electron density profiles for short circuit conditions with different recombination reaction rate constants. All other parameters are presented in Table 5.1, device B.

Figure 5.7 Simulated electron density profiles for maximum power point with different recombination reaction rate constants. All other parameters are presented in Table 5.1, device B.
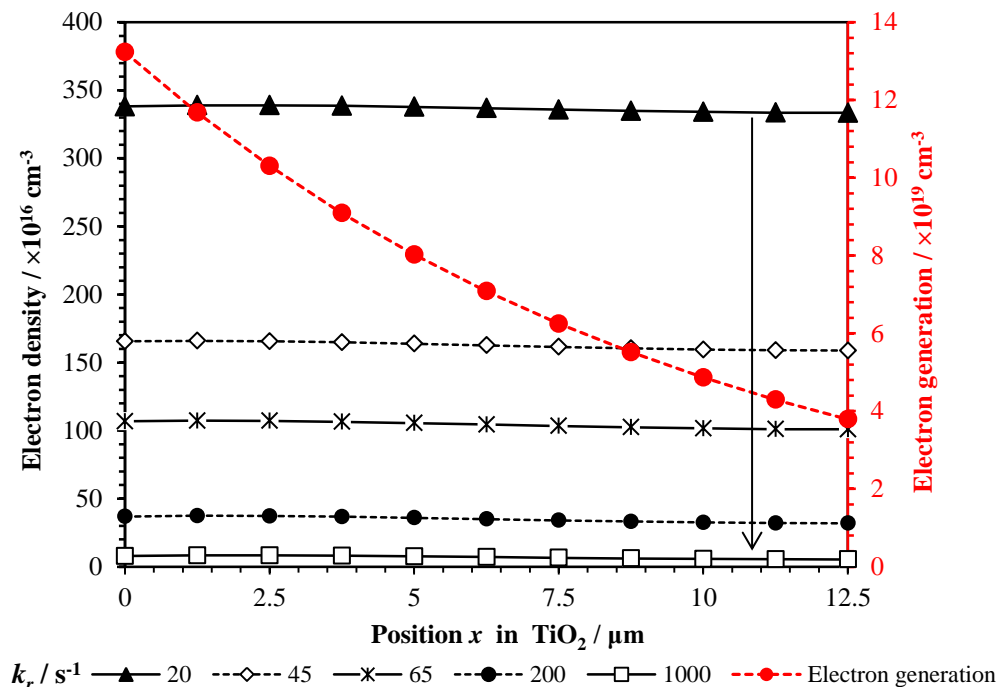
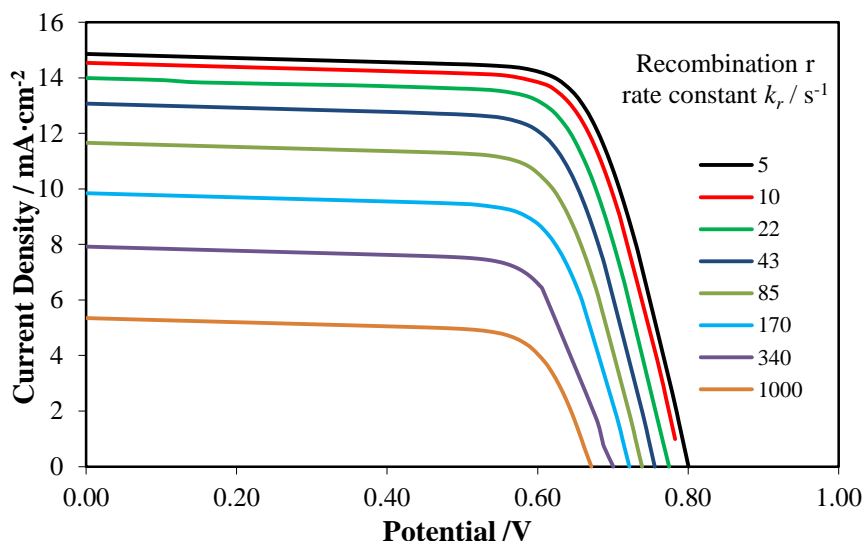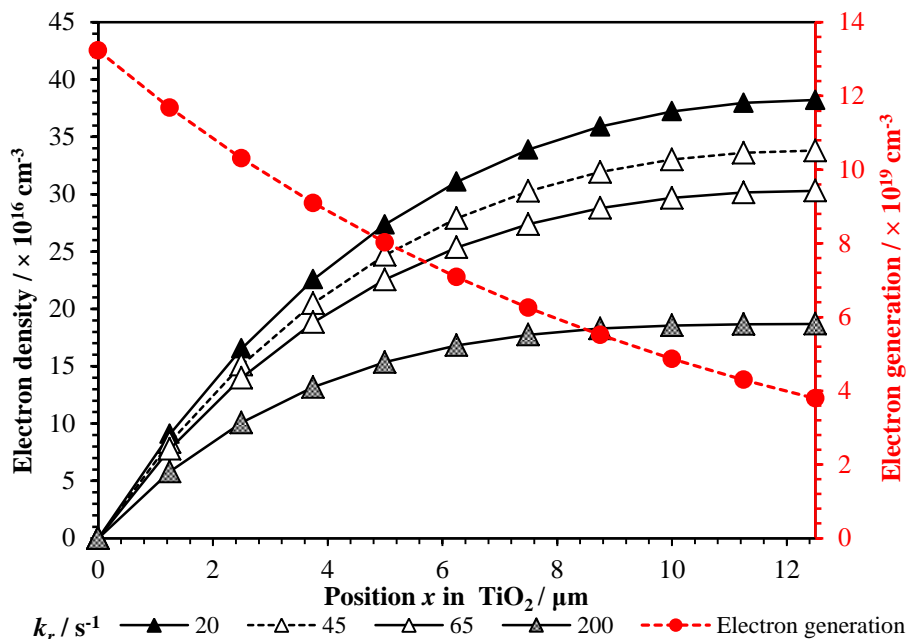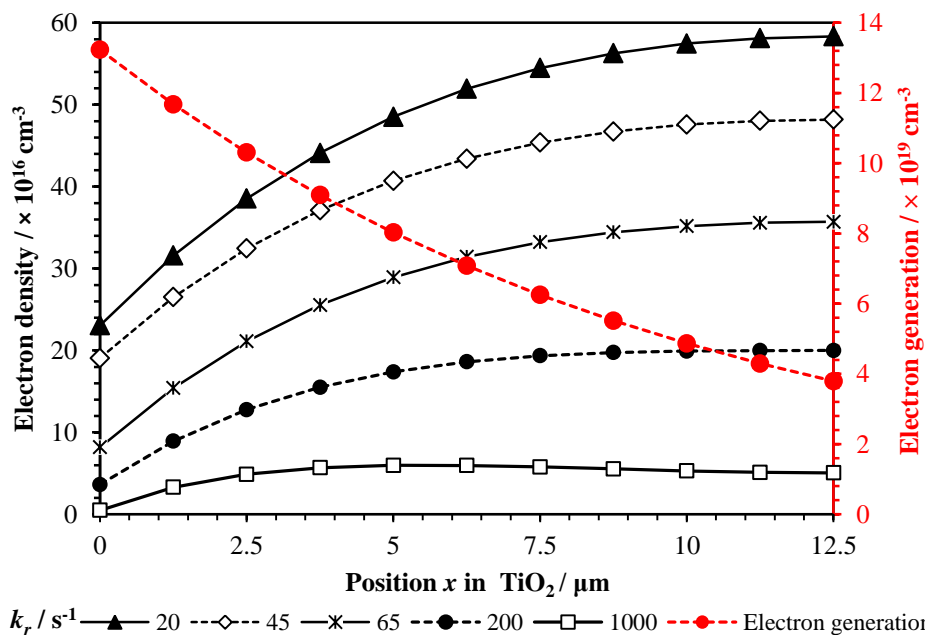**Figure 5.8** Simulated electron density profiles for open circuit conditions with different recombination reaction rate constants. All other parameters are presented in Table 5.1, device B.

At open circuit conditions the recombination flux matches the photocurrent and there are no electrons flowing to the external circuit. At these conditions there is almost no electron gradient, as seen in Figure 5.8, and this equilibrium determines the open circuit potential, $V_{oc,}$ of the device[26]. Therefore, recombination determines the open potential, V_{oc}, of the device and also controls the short circuit current, J_{sc}. The excited electron density profiles in the TiO_2 film, simulated for different electron recombination rates, enlighten the influence that this reaction has in the open potential, V_{oc}, of the solar cell. The electron recombination rate affects the electron flow through the external circuit, and therefore, affects the chemical potential that is built inside the device due to the presence of energy states below the Fermi level of the semiconductor. This way, the amount of electrons that react with the triiodide affects the final potential of the system, as can be confirmed in Figure 5.8 where higher recombination rates reduce the electron density in the device at open circuit conditions and, by doing so, the chemical potential within the device, acts to reduce the final V_{oc} of the solar cell.

The concentration profiles of the ionic species, shown in Figure 5.9, are also influenced by recombination. For an illuminated cell, triiodide is formed where there is photon absorption and consequently electron injection, due to the regeneration reaction of the oxidized dye with iodide, producing triiodide. Therefore electron generation increases the consumption of iodide and consequently the formation of triiodide. By increasing the recombination reaction rate constant, the amount of electrons that react with triiodide is higher, and thus there is an extra consumption of triiodide besides the amount that is produced by the regeneration reaction of iodide with the oxidized dye. However, because there are less electrons flowing to the external circuit and being returned back to the device through the counter electrode, there is an accumulation of triiodide, mainly at the interface $x = 12.5$ μm, where the reduction reaction back to iodide takes place at the platinum catalyst. Along with the extra consumption of triiodide higher k_r also causes higher formation of iodide; because the fraction of iodide consumption due to the dye regeneration is independent of k_r, for higher recombination rates there is an accumulation of I$^-$ verified for $x=0$ – Figure 5.9.

Figure 5.9 Simulated ionic concentration profiles for maximum power point for different recombination reaction rate constants. All other parameters are given in Table 5.1, device B.
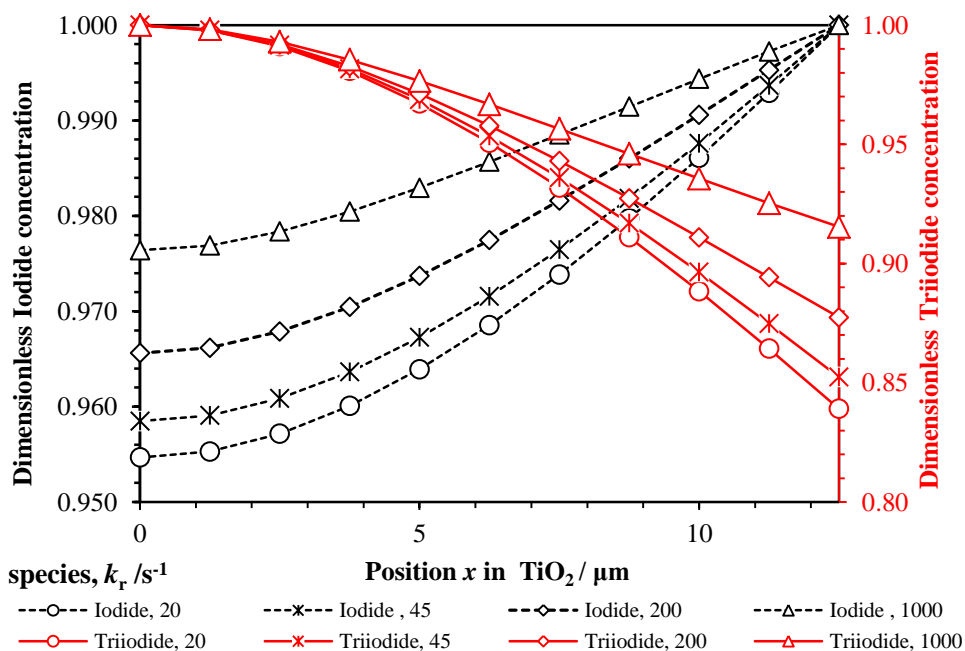
The effect of recombination in the open circuit potential and in the short circuit current is illustrated in Figure 5.10a. In this figure the values of V_{oc} and J_{sc} are plotted as a function of the recombination reaction rate constant for several values of the recombination reaction coefficient β. The V_{oc} shows a logarithmic dependence as a function of the recombination reaction rate constant across all the values of k_r and for all values of β. The effect of the recombination in the V_{oc} becomes higher for lower values of β. However, in the case of the J_{sc}, apparently there are two distinct logarithmic trends: lower recombination rates ($k_r < 50$ s^{-1}) influence less J_{sc} than higher values of k_r. This fact remains true for β values higher than 0.7. For lower values of β (< 0.7) the "non-ideality" trend of J_{sc} tends to disappear and the logarithmic dependence remains constant for all values of k_r. This "non-ideal" trend of J_{sc} *vs.* k_r is verified only for low values of k_r and thus for situations where there is almost no recombination in the DSC. Therefore, at these conditions, the J_{sc} does not appear to be recombination-limited; hence the curves tend to predict the same J_{sc} regardless of the β value, as can be seen in Figure 5.10b). This fact highlights the importance of considering the reaction order especially for high values of k_r, as it is where the β value influences the most the predicted J_{sc}.
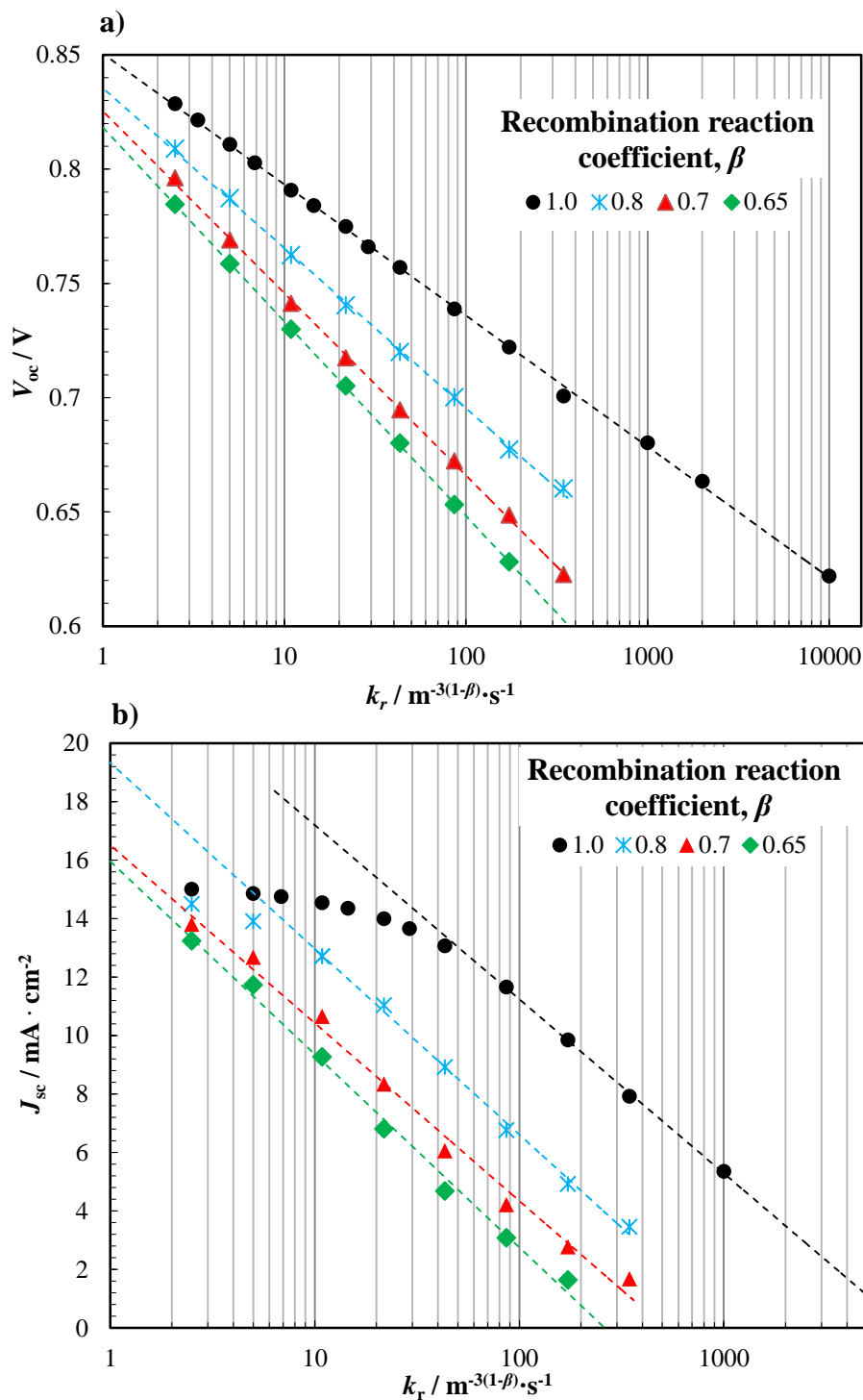
Figure 5.10 Influence of the recombination reaction rate constants in the V_{oc} (a) and J_{sc} (b), considering several values of the recombination reaction coefficient, β. All other parameters are presented in Table 5.1, device B.

5.4.3   Interpretation of recombination in charge extraction experiments

The previous section studied the influence of the recombination effect on J_{sc} and V_{oc}; now, the influence of k_r is discussed in terms of charge concentration. Usually charge extraction experiments are used as a tool to assess limitations in the solar cells[40,43]. The method relies on the optical perturbation of the solar cell and the corresponding measurement of the output transient electrical signals (current or potential) of the device[44,45]. This approach allows researchers to determine critical information about the electron concentration, transport and recombination inside the solar cell. This is particularly interesting for the development of new materials for DSCs as it allows comparing results from different devices and understanding differences in recombination, collection efficiency, conduction band shifts and other factors that have a crucial role in the final performance of the DSC.

In this section the phenomenological model is used to predict the charge concentration in DSCs for a given set of defined parameters, as a function of k_r and $(E_{cb}-E_{redox})$. The independent influence that recombination and conduction band shifts have in the plots of charge concentration versus potential in the DSC is evaluated and discussed. Figure 5.11a) shows the charge density as a function of the applied potential calculated for several values of k_r. The charge concentration shows an exponential increase with the potential applied to the solar cell. Although there is some debate in the academic field, the exponential behavior of charge density versus potential is commonly attributed to the exponential distribution of the trap states below the conduction band edge of TiO_2 that are able to accept electrons[44]. Because recombination with electrolyte species is believed to occur with electrons in the conduction band, a vertical shift up of the charge density curves generally means that recombination decreases, see Figure 5.11a). In this figure, however, the value of $(E_{cb}-E_{redox})$ was kept constant between simulations, which seldom happens experimentally. When comparing recombination rates from experimental charge density results, there is a high probability that a shift in the semiconductor conduction band edge also occurs. The E_{cb} shift is caused by differences in the surface electric field between the

TiO_2 and the electrolyte. It can be caused by several factors, such as electrolyte composition[46-49], surface treatments of TiO_2 [50,51], dye molecular properties[52], dye adsorption methods[40,53], temperature changes[54], among others. In Figure 5.11b) the charge density is plotted versus the applied potential for several values of (E_{cb}-E_{redox}) and for k_r =14 s^{-1}. Figure 5.11b) shows that a relative shift of E_{cb} compared to E_{redox} corresponds to a lateral displacement of the curve in the plot. The maximum attainable V_{oc} is affected mainly by two contributions: (E_{cb}-E_{redox}) and k_r[55]; because k_r has been fixed, the difference in the V_{oc} between simulations corresponds to the actual $\Delta(E_{cb}$-$E_{redox})$ between curves.
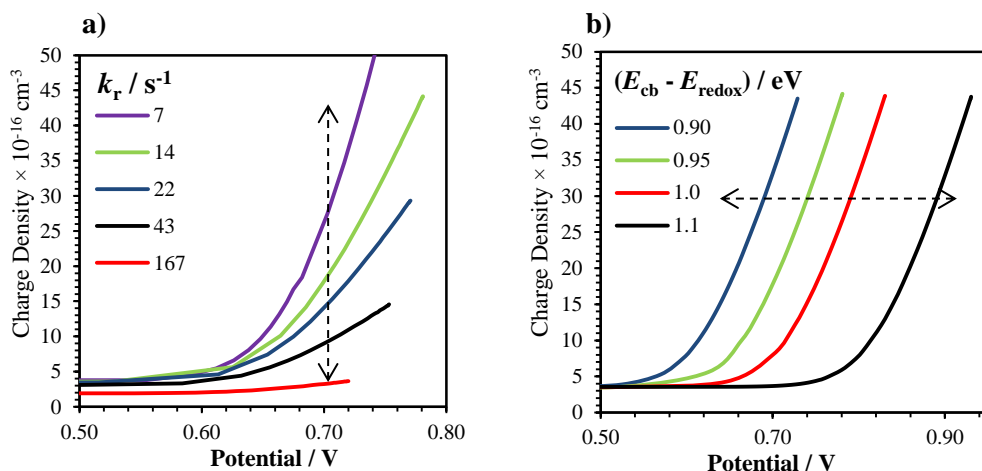
Figure 5.11 a) Simulated data of charge density *vs.* applied potential for several values of k_r and (E_{cb} - E_{redox}) = 0.95 eV, b) Simulated data of charge density *vs.* applied potential for several values of (E_{cb} - E_{redox}) and k_r =14 s^{-1}. All other parameters are given in Table 5.1, device B.

When charge extraction experiments are used to compare recombination between cells the E_{cb} shift can mask the effect of changes in k_r[40,56,57]. Thus, it is crucial knowing how to decouple both processes for assessing the recombination rates taking into account changes in E_{cb}. In Figure 5.12a) changes in k_r and shifts in E_{cb} are considered between simulations. This is an example of what could be expected in experimental results. Direct analysis of the plot does not allow taking conclusions about which curve belongs to solar cells with higher or lower recombination rates.
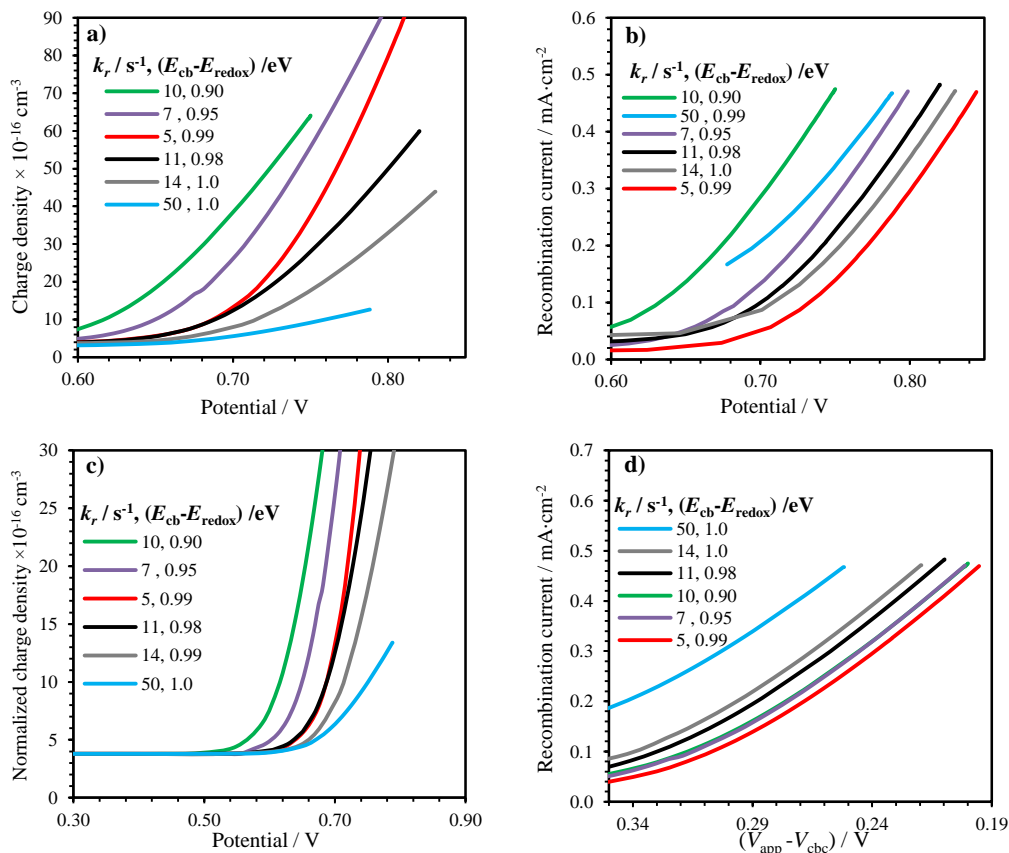
Figure 5.12 a) Simulated data of charge density *vs.* applied potential for several values of (E_{cb}-E_{redox}) and k_r, b) Recombination current *vs.* potential with variable values of (E_{cb}-E_{redox}) and k_r, without correction of E_{cb}, c) Simulated data of normalized charge density *vs.* applied potential for several combinations of (E_{cb}-E_{redox}) and k_r, d) Recombination current *vs.* (V_{app}-V_{cbc}) with variable values of values of (E_{cb}-E_{redox}) and k_r. All other parameters are accordingly with Table 5.1, device B.

In this case, the lateral displacement of the curves caused by the relative change in E_{cb} masks the vertical displacement caused by different recombination rate constants.

The comparison of recombination rate constants between DSCs can be done, accordingly to some reports, by examining plots of the recombination current, J_{rec}, *vs.* potential, calculated by eq. (5.35), and shown in Figure 5.12b) [40]:

$$J_{rec} = \frac{n_{e^-}(V)}{\tau_{e^-}} \tag{5.35}$$

Because recombination current depends only on the concentration of electrons in the conduction band and on the recombination rate constant, this allows separating the

overlap effect of E_{cb} shift. However, plotting J_{rec} versus potential, Figure 5.12b), does not order by recombination current the curves of the plot. Even in this case the effect of lateral displacement by E_{cb} shift is verified. Aiming to completely remove this influence and correctly analyze the data, the conduction band shift should be accounted for. To do that, the recombination currents should be compared for the same value of $(E_f - E_{redox})$, which means that the comparison should be done for the same amount of free electrons able to recombine with electrolyte. This can be done as follows[40]:

a) First the shift in the conduction band edge has to be determined. The total charge density, $n_{e^-}^t$, can be obtained at short circuit conditions for each simulation; then it is subtracted to the $n_{e^-}^t$ at short circuit of a pre-defined standard simulated curve ($k_r = 7$ s^{-1} and $(V_{app}-V_{cbc}) = 0.95$ V, purple line in plots from Figure 5.12. This represents the offset at short-circuit in the total charge density between the two curves. In each simulated curve the offset is added to $n_{e^-}^t$ for all potentials – Figure 5.12c). Then the shift in V_{cb} (ΔV_{cb}) can be estimated directly from the plot by the lateral displacement of each curve – Figure 5.12c).

b) After ΔV_{cb} has been determined it can be added to the V_{cb} of each curve of Figure 5.12b), resulting in curves with a corrected conduction band potential $V_{cbc}= V_{cb}+\Delta V_{cb}$;

c) Then the V_{cbc} is used to plot J_{rec} versus $(V_{app}-V_{cbc})$ – Figure 5.12d). In this case, the V_{cb} was set at -1 V *vs.* electrolyte, which is a common accepted value for iodide/iodine based electrolytes. Afterwards, the curves are placed according to their recombination rate constants, independently of their $(E_{cb}-E_{redox})$ values, contrary to what is normally found in literature.

5.4.4   Optimization of electrode thickness

Throughout this work the influence of electron recombination and charge transport in the performance of DSCs was studied. Some critical aspects that must be taken into account in interpreting charge extraction results have been discussed. Now, the relevance of electron recombination and transport within the photoelectrode is evaluated in the design of solar cells. Figure 5.13 shows the *I-V* curves for DSCs with several photoelectrode layer thicknesses.
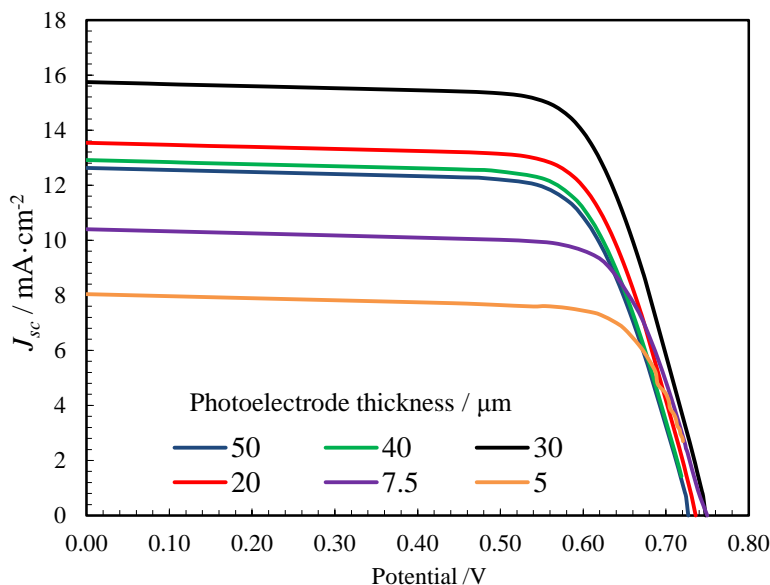
Figure 5.13 Influence of the photoelectrode thickness in the DSC *I-V* characteristics for $k_r = 50$ s^{-1}. All other parameters are given in Table 5.1, device B.

Figure 5.13 points out an obvious conclusion: for a given DSC system, there is an optimum thickness of semiconductor. This fact is many times observed in real devices, and is usually optimized experimentally[58,59]. The photo-electrode optimum thickness is related to the length that a generated electron can diffuse before recombining with electrolyte species; this is called diffusion length, L_n[26,60,61]. Given a certain effective electron diffusion coefficient, D_{eff}, a semiconductor thickness, L_f, and a recombination reaction rate constant, k_r, two parameters can be defined: the electron lifetime, τ_{e^-}, and the transport time, τ_{tr}. The lifetime depends on k_r, and the transport time on D_{eff} and L_f. The charge collection efficiency, η_{cc}, can now be written; it

depends of electron transport in the mesoporous semiconductor and recombination losses. If charge collection is much faster than charge recombination, then η_{cc} value will be higher. The electron collection efficiency, η_{cc}, can be given by[62]:

$$\eta_{cc} = \frac{\left[-L_n\alpha(\lambda)\cosh\left(\frac{L_f}{L_n}\right) + \sinh\left(\frac{L_f}{L_n}\right) + L_n\alpha(\lambda)e^{-\alpha(\lambda)L_f}\right]L_n\alpha}{\left(1 - L_n{}^2\alpha(\lambda)^2\right)\left(1 - e^{-\alpha(\lambda)L_f}\right)\cosh\left(\frac{L_f}{L_n}\right)} \qquad (5.36)$$

The relation between the ratio of lifetime and transport, and the active layer thickness and diffusion length has been established by Bisquert *et al.*[25] and included in eq. (5.36). When $L_n \gg L_f$, most electrons diffuse through the entire length of photoelectrode before recombining with the electrolyte. On the other hand, in the case of high reactivity, $L_n \ll L_f$, most electrons recombine at the TiO_2/electrolyte interface.

When recombination does not occur predominantly via the conduction band, the electron diffusion length can no longer be defined as previously, giving rise to a non-linear reaction order[29,30]. Assuming for a defined device that the two ruling processes of transport and recombination are held constant, increasing the semiconductor thickness will reduce the collection efficiency as shown in Figure 5.14; increasing the recombination, η_{cc} still decreases with L_f. This implies that the optimum thickness of active layer is highly dependent on the relation between transport and recombination in the solar cell.
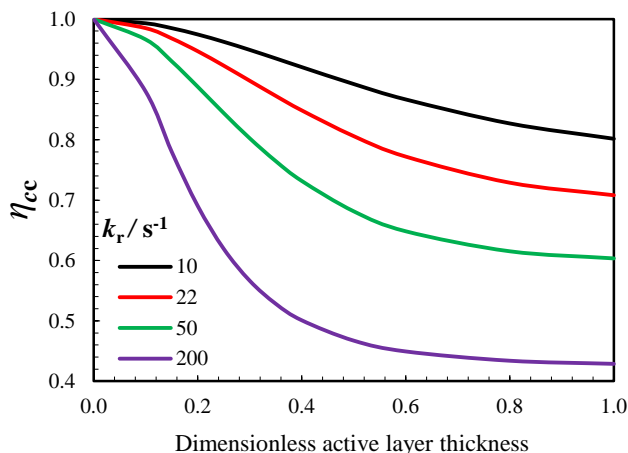

Figure 5.14 Collection efficiency determined as a function of the active layer thickness, for several recombination rate constants. All other parameters are given in Table 5.1, device B.

In the same way, the electron effective diffusion coefficient plays an important role in the collection efficiency. Using a constant value of k_r, the influence of D_{eff} in the performance of the DSC can be determined, as illustrated in Figure 5.15. By increasing D_{eff} the transport time becomes lower and η_{cc} and η increase. However, for the assumed device parameters (*cf.* Table 5.1, device B) it is necessary to increase D_{eff} two orders of magnitude to see a clear impact on the collection efficiency since the recombination is relatively small. Nonetheless, it is safe to state that the performance of the solar cell would greatly benefit from higher electron conductivities in the semiconductor.
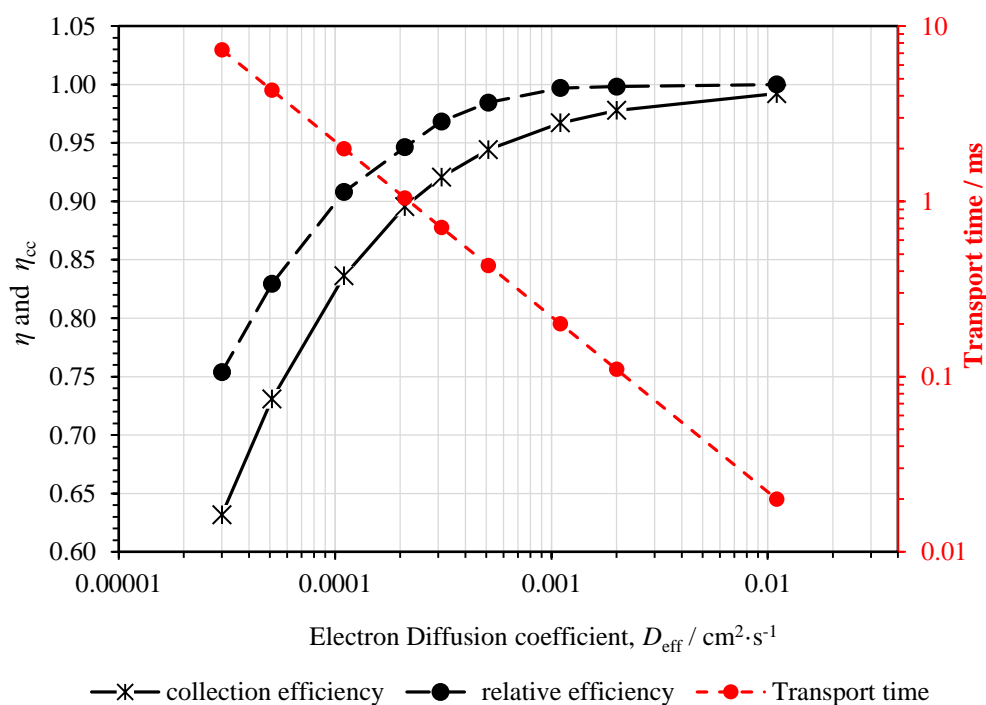
Figure 5.15 Collection efficiency, relative efficiency and transport time as a function of the diffusion coefficient. All other parameters are given in Table 1, device B.

Figure 5.16 shows the curves of efficiency as a function of active layer thickness assuming several k_r and D_{eff} values. The two plots highlight quantitatively the influence that recombination and transport have in the performance of DSCs. For example, assuming $k_r = 10$ s^{-1} (low recombination rate comparing to $k_r = 200$ s^{-1}), the optimum photoelectrode thickness is three times the normal thickness (from *ca.*10 μm to 30 μm)

and the DSC efficiency increases almost 5 percentage points (from *ca*. 5 % to 10 %). The highlighted points in the curves in Figure 5.16 (black diamonds) are the respective optimum thicknesses values. As expected, as the recombination rate decreases and/or the electron diffusivity increases, the optimum photoelectrode thickness increases. Figure 5.17 shows that the influence of k_r and D_{eff} at the optimum photoelectrode thickness is logarithmic.

Figure 5.16 a) Efficiency *vs*. photoelectrode thickness, for several k_r and $D_{eff} = 1.10 \times 10^{-4}$ $cm^{-2} \cdot s^{-1}$; b) Efficiency *vs*. photoelectrode thickness, for several values of D_{eff} and $k_r = 20$ s^{-1}. The black diamonds are the maximum efficiency values for each curve. All other parameters are given in Table 5.1, device B.
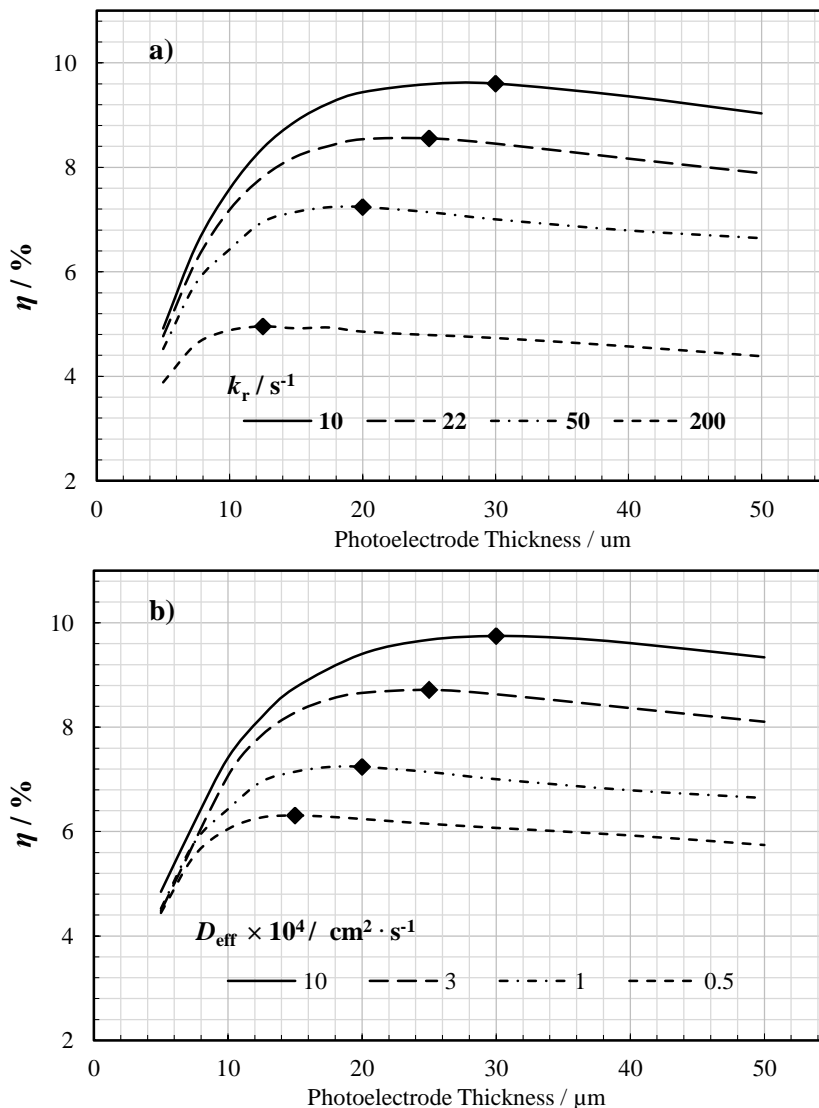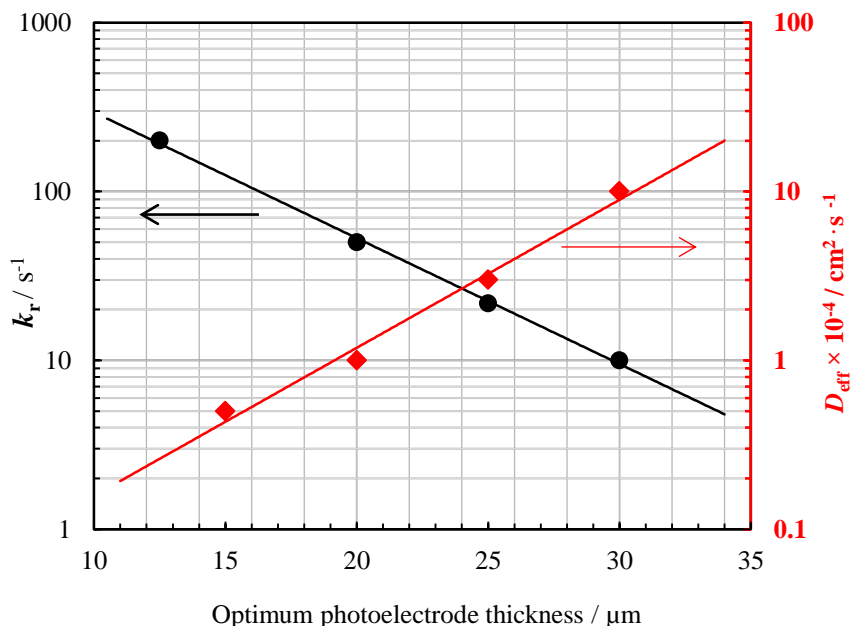
Figure 5.17 Influence of k_r and D_{eff} in the optimum photoelectrode thickness. The parameters used for the simulations are given in Table 5.1

In fact, a recent report by Crossland *et al.*[63] showed that a new mesoporous TiO$_2$ single crystal has electronic mobility values over one order of magnitude higher than the typical TiO$_2$ mesoporous film. This development resulted in an efficiency boost of almost 130 % in a solid state device. The reported electronic mobility should allow increasing the optimal thickness of the photoelectrodes in current DSC cells. Using the optimization curves of Figure 5.17 and 10^{-2} cm^2·s^{-1} as the new electron diffusion coefficient (typical coefficients values in anatase TiO$_2$ range between 10^{-4} and 10^{-5} cm^2·s^{-1} [10,63]), the optimum thickness for the new material should be around 40 μm and the energy efficiency could increase to 12 %. If one considers the use of the new porphyrin dye with cobalt (II/III)–based redox electrolyte for attaining open circuit voltages near 1 V [2], a 15 % efficient DSC could be expected in a near future.

5.5 Conclusions

Phenomenological modeling is a powerful tool to study the fundamentals of DSC operation. The transient model used considers the continuity equations for the three modeled species (electrons, iodide and triiodide) and their respective initial and boundary conditions. It is assumed that the cell is irradiated perpendicularly to the photoelectrode and that each absorbed photon generates one injected electron into the TiO_2 conduction band. Only one possible mechanism for electron loss is assumed, corresponding to the recombination reaction of electrons with electrolyte species. The presented phenomenological model is able to properly simulate steady state *I-V* curves of dye-sensitized solar cells. The model has been used as a simulation tool to assess the two processes that rule the performance of DSCs: electron transport and recombination. The quantitative effect of the recombination reaction rate constant, k_r, and the electron diffusion coefficient, D_{eff}, in the collection efficiency was shown and discussed. The influence of k_r in the V_{oc} and J_{sc} of DSCs has been determined and has been shown to be highly dependent on the recombination reaction kinetics.

The model was used to evaluate the influence that conduction band shifts have in charge extraction experiments. The described methodology is able to decouple the conduction band shifts from the recombination effect. This is particularly useful for material synthesis where charge experiments are used to assess changes in the recombination rate constants between different samples.

It simulated the influence that electron transport and recombination have in the optimization of the photoelectrode thickness. It was found that the optimum photoelectrode thickness varies logarithmically with the recombination rate and with the electron diffusion coefficient. The optimization procedure developed is particularly interesting when developing high efficiency DSCs.

Acknowledgements

References

1. J. H. Heo, S. H. Im, J. H. Noh, T. N. Mandal, C.-S. Lim, J. A. Chang, Y. H. Lee, H.-j. Kim, A. Sarkar, K. NazeeruddinMd, M. Gratzel and S. I. Seok, *Nat Photon*, 2013, **7**, 486-491.

2. A. Yella, H.-W. Lee, H. N. Tsao, C. Yi, A. K. Chandiran, M. K. Nazeeruddin, E. W.-G. Diau, C.-Y. Yeh, S. M. Zakeeruddin and M. Grätzel, *Science*, 2011, **334**, 629-634.

3. J. Burschka, N. Pellet, S.-J. Moon, R. Humphry-Baker, P. Gao, M. K. Nazeeruddin and M. Gratzel, *Nature*, 2013.

4. B. O'Regan and M. Grätzel, *Nature*, 1991, **353**, 737-740.

5. M. Grätzel, *Inorg. Chem.*, 2005, **44**, 6841-6851.

6. M. Grätzel and J. R. Durrant, in *Nanostructured and photoelectrochemical systems for solar photon conversion*, Imperial College Press, London, 2008, ch. 8.

7. M. D. Archer and A. J. Nozik, *Nanostructured and photoelectrochemical systems for solar photon conversion*, Imperial College Press ; World Scientific Pub. Co., London; Singapore; Hackensack, NJ, 2008.

8. L. R. Andrade, H. A.; Mendes, A, *Dye-Sensitized Solar Cells: an Overview, in Energy Production and Storage: Inorganic Chemical Strategies for a Warming World*, John Wiley & Sons, Ltd, Chichester, UK, 2010.

9. M. Wang, P. Chen, R. Humphry-Baker, S. M. Zakeeruddin and M. Gratzel,

ChemPhysChem, 2009, **10**, 290-299.

10.   G. He, L. Zhao, Z. Zheng and F. Lu, *Journal of Physical Chemistry C*, 2008, **112**, 18730-18733.

11.   J. Shi, B. Peng, J. Pei, S. Peng and J. Chen, *Journal of Power Sources*, 2009, **193**, 878-884.

12.   G. Boschloo, L. Haggman and A. Hagfeldt, *J. Phys. Chem. B*, 2006, **110**, 13144-13150.

13.   S. Y. Huang, G. Schlichthorl, A. J. Nozik, M. Gratzel and A. J. Frank, *The Journal of Physical Chemistry B*, 1997, **101**, 2576-2582.

14.   S. Nakade, Y. Makimoto, W. Kubo, T. Kitamura, Y. Wada and S. Yanagida, *J. Phys. Chem. B*, 2005, **109**, 3488-3493.

15.   S. Nakade, T. Kanzaki, W. Kubo, T. Kitamura, Y. Wada and S. Yanagida, *J. Phys. Chem. B*, 2005, **109**, 3480-3487.

16.   F. Matar, T. H. Ghaddar, K. Walley, T. DosSantos, J. R. Durrant and B. O'Regan, *Journal of Materials Chemistry*, 2008, **18**, 4246-4253.

17.   P. M. Sommeling, B. C. O'Regan, R. R. Haswell, H. J. P. Smit, N. J. Bakker, J. J. T. Smits, J. M. Kroon and J. A. M. vanRoosmalen, *J. Phys. Chem. B*, 2006, **110**, 19191-19197.

18.   N. Tetreault and M. Gratzel, *Energy & Environmental Science*, 2012.

19.   N. Tétreault, É. Arsenault, L.-P. Heiniger, N. Soheilnia, J. Brillet, T. Moehl, S. Zakeeruddin, G. A. Ozin and M. Grätzel, *Nano Letters*, 2011, **11**, 4579-4584.

20.   B. Mandlmeier, J. M. Szeifert, D. Fattakhova-Rohlfing, H. Amenitsch and T. Bein, *Journal of the American Chemical Society*, 2011, **133**, 17274-17282.

21.   S. Guldin, S. Hüttner, M. Kolle, M. E. Welland, P. Müller-Buschbaum, R. H. Friend, U. Steiner and N. Tétreault, *Nano Letters*, 2010, **10**, 2303-2309.

22.   J. N. Clifford, M. Planells and E. Palomares, *Journal of Materials Chemistry*, 2012, **22**, 24195-24201.

23.   J. Maçaira, L. Andrade and A. Mendes, *Renewable and Sustainable Energy Reviews*, 2013, **27**, 334-349.

24.   L. Andrade, J. Sousa, H. A. Ribeiro and A. Mendes, *Solar Energy*, 2011, **85**, 781-793.

25. J. Bisquert, *The Journal of Physical Chemistry B*, 2002, **106**, 325-333.

26. J. Bisquert and I. n. Mora-Seró, *The Journal of Physical Chemistry Letters*, 2009, **1**, 450-456.

27. Y. Liu, A. Hagfeldt, X.-R. Xiao and S.-E. Lindquist, *Solar Energy Materials and Solar Cells*, 1998, **55**, 267-281.

28. P. R. F. Barnes, L. Liu, X. Li, A. Y. Anderson, H. Kisserwan, T. H. Ghaddar, J. R. Durrant and B. C. O'Regan, *Nano Letters*, 2009, **9**, 3532-3538.

29. J. Villanueva-Cab, H. Wang, G. Oskam and L. M. Peter, *The Journal of Physical Chemistry Letters*, 2010, **1**, 748-751.

30. J. P. Gonzalez-Vazquez, G. Oskam and J. A. Anta, *The Journal of Physical Chemistry C*, 2012, **116**, 22687-22697.

31. J. A. Anta, J. Idigoras, E. Guillen, J. Villanueva-Cab, H. J. Mandujano-Ramirez, G. Oskam, L. Pelleja and E. Palomares, *Physical Chemistry Chemical Physics*, 2012, **14**, 10285-10299.

32. J. Ferber, R. Stangl and J. Luther, *Solar Energy Materials and Solar Cells*, 1998, **53**, 29-54.

33. K. Nithyanandam and R. Pitchumani, *Solar Energy*, 2012, **86**, 351-368.

34. M. Penny, T. Farrell and G. Will, *Solar Energy Materials and Solar Cells*, 2008, **92**, 24-37.

35. A. Ofir, L. Grinis and A. Zaban, *The Journal of Physical Chemistry C*, 2008, **112**, 2779-2783.

36. A. Hagfeldt, G. Boschloo, L. Sun, L. Kloo and H. Pettersson, *Chemical Reviews*, 2010, **110**, 6595-6663.

37. L. Petzold, *Siam J. Sci. Stat. Computing*, 1983, **4**, 136-148.

38. F. Ribeiro, Maçaira,J. , Cruz, R., Gabriel, J., Andrade, L., Mendes, A., *Solar Energy Materials and Solar Cells*, 2012, **96**, 43-49.

39. H. J. Snaith, *Advanced Functional Materials*, 2010, **20**, 13-19.

40. B. O'Regan, L. Xiaoe and T. Ghaddar, *Energy & Environmental Science*, 2012, **5**, 7203-7215.

41. S. Zhang, X. Yang, Y. Numata and L. Han, *Energy & Environmental Science*, 2013, **6**, 1443-1464.

42.   B. C. O'Regan and J. R. Durrant, *The Journal of Physical Chemistry B*, 2006, **110**, 8544-8547.

43.   P. Docampo, S. Guldin, U. Steiner and H. J. Snaith, *The Journal of Physical Chemistry Letters*, 2013, **4**, 698-703.

44.   P. R. F. Barnes, K. Miettunen, X. Li, A. Y. Anderson, T. Bessho, M. Gratzel and B. C. O'Regan, *Advanced Materials*, 2013, **25**, 1881-1922.

45.   L. M. Peter, *The Journal of Physical Chemistry C*, 2007, **111**, 6601-6612.

46.   S. A. Haque, E. Palomares, B. M. Cho, A. N. M. Green, N. Hirata, D. R. Klug and J. R. Durrant, *J. Am. Chem. Soc.*, 2005, **127**, 3456-3462.

47.   F. Fabregat-Santiago, J. Bisquert, G. Garcia-Belmonte, G. Boschloo and A. Hagfeldt, *Solar Energy Materials and Solar Cells*, 2005, **87**, 117-131.

48.   H. Wang and L. M. Peter, *The Journal of Physical Chemistry C*, 2012, **116**, 10468-10475.

49.   B. C. O'Regan, K. Bakker, J. Kroeze, H. Smit, P. Sommeling and J. R. Durrant, *The Journal of Physical Chemistry B*, 2006, **110**, 17155-17160.

50.   B. C. O'Regan, J. R. Durrant, P. M. Sommeling and N. J. Bakker, *The Journal of Physical Chemistry C*, 2007, **111**, 14001-14010.

51.   X. Wu, L. Wang, F. Luo, B. Ma, C. Zhan and Y. Qiu, *The Journal of Physical Chemistry C*, 2007, **111**, 8075-8079.

52.   E. Ronca, M. Pastore, L. Belpassi, F. Tarantelli and F. De Angelis, *Energy & Environmental Science*, 2013, **6**, 183-193.

53.   A. B. F. Martinson, M. r. S. Góes, F. Fabregat-Santiago, J. Bisquert, M. J. Pellin and J. T. Hupp, *The Journal of Physical Chemistry A*, 2009, **113**, 4015-4021.

54.   S. R. Raga and F. Fabregat-Santiago, *Physical Chemistry Chemical Physics*, 2013, **15**, 2328-2336.

55.   S. R. Raga, E. M. Barea and F. Fabregat-Santiago, *The Journal of Physical Chemistry Letters*, 2012, **3**, 1629-1634.

56.   H.-P. Wu, Z.-W. Ou, T.-Y. Pan, C.-M. Lan, W.-K. Huang, H.-W. Lee, N. M. Reddy, C.-T. Chen, W.-S. Chao, C.-Y. Yeh and E. W.-G. Diau, *Energy & Environmental Science*, 2012, **5**, 9843-9848.

57.   H.-P. Wu, C.-M. Lan, J.-Y. Hu, W.-K. Huang, J.-W. Shiu, Z.-J. Lan, C.-M. Tsai,

C.-H. Su and E. W.-G. Diau, *The Journal of Physical Chemistry Letters*, 2013, **4**, 1570-1577.

58. J.-Y. Liao, H.-P. Lin, H.-Y. Chen, D.-B. Kuang and C.-Y. Su, *Journal of Materials Chemistry*, 2012, **22**, 1627-1633.

59. S. Ito, S. Zakeeruddin, R. Humphry-Baker, P. Liska, R. Charvet, P. Comte, M. Nazeeruddin, P. Péchy, M. Takata, H. Miura, S. Uchida and M. Grätzel, *Advanced Materials*, 2006, **18**, 1202-1205.

60. H. Wang and L. M. Peter, *The Journal of Physical Chemistry C*, 2009, **113**, 18125-18133.

61. P. R. F. Barnes and B. C. O'Regan, *The Journal of Physical Chemistry C*, 2010, **114**, 19134-19140.

62. L. Bertoluzzi and S. Ma, *Physical Chemistry Chemical Physics*, 2013, **15**, 4283-4285.

63. E. J. W. Crossland, N. Noel, V. Sivaram, T. Leijtens, J. A. Alexander-Webber and H. J. Snaith, *Nature*, 2013, **495**, 215-219.

CHAPTER 6

High efficient DSC photoelectrode using a SiO_2 scaffold layer coated with a 3 nm TiO_2 film

"As soon we are shown something old in an innovation, we are at peace."

Friedrich Nietzsche

High efficient DSC photoelectrode using a SiO$_2$ scaffold layer coated with a 3 nm TiO$_2$ film

Abstract

A new photoelectrode (PE) architecture for incorporating in DSC devices was developed aiming to increase the electron mobility, the specific surface area and the transparency. The developed PE is made of a mesoporous SiO$_2$ scaffold layer covered by a conformal TiO$_2$ film deposited by atomic layer deposition (ALD). The shrinking core model was used to predict the minimum pulse time (25 s and $D_{TIP} = (4.23 \pm 0.65) \times 10^{-3}$) required for the complete coverage of the inner SiO$_2$ scaffold surface area (*ca.* 160 m^2·g^{-1}). The TiO$_2$ film thickness proved to be related to two DSC operation regimes: transport limited regime ($D_{eff} \propto$ TiO$_2$ thickness, where D_{eff} is the electron effective diffusivity) and a recombination limited regime (D_{eff} constant); in the latter regime, the minimum recombination rate constant, k_r, resulted in maximum DSC performance. DSCs based on the new PE coated with an optimized TiO$_2$ film thickness (3.3 nm, 150 ALD cycles) exhibited an average of 8 % higher energy conversion efficiency than the standard devices, $\eta = 8.43$ % *vs.* $\eta = 7.82$ % and 10 % more transmittance in the visible range. The superior performance exhibited by the new PE was ascribed to: higher surface area and lower electron recombination. The increased recombination resistance was attributed to lower morphological defects and better dye coverage of the TiO$_2$ layer. This work shows that an ALD deposited TiO$_2$ film with 3 to 4 nm thickness is suitable for the dye adsorption and electron transport; when applied over a large surface area scaffold, the TiO$_2$ nanolayer displayed the same transport abilities as conventional TiO$_2$ mesoporous films. The proposed PE opens the

doors to new architectures and the use of new semiconductors with better properties concerning electronic mobility, conduction band energy level, stability, transparency and recombination.

6.1 Introduction

Films assembled by nanoparticles have a much larger surface area then the corresponding bulk materials; this allowed dye sensitized solar cells (DSC) to emerge in 1991 amongst promising photovoltaic technologies[1,2]. Larger surface areas allow superior dye loading and therefore high current densities. However, nanoparticle films present much higher number of grain boundaries and morphological defects than their bulk counterparts[3]; this causes unavoidable interfacial electron recombination and reduces electron transport mobility in the film[4,5]. Photovoltaic (PV) performance results from balance between photocurrent density and electron transport and recombination in the photoelectrode, and then there is an optimum thickness of the mesoporous TiO$_2$ film[6]. The best performing DSC devices still use too thin photoelectrodes to harvest the incident solar radiation, making the research of new photoelectrodes arrangements a hot research topic[6-8].

One-dimensional structures such as nanowires[9,10], nanotubes[11-13] and nanorods[14,15] have been failed strategies in the pursuit of DSCs efficiency improvement. Although they provide higher electron transport properties, their low specific surface area limits the photocurrent generation. Photoelectrodes with hierarchical structures [16-18] are interesting assemblies that provide large dye adsorption surface areas and effective light scattering; nevertheless, they share the nanoparticle films transport and recombination limitations. Other interesting approaches use removable templates of *e.g.* polystyrene and polyacrylate before depositing metal-oxides by atomic layer deposition (ALD)[19-21]. This strategy originates hollow nanostructures where the inner surface area is defined by the size of the template particles. Although this approach offers a continuous 3D network for electron collection the reported works show no improved photocurrents due to the large size of the template particles employed[16,19].

In terms of DSC photoelectrodes, mesoporous TiO_2 films made of nanoparticles are still dominating the PV performance, because TiO_2 nanoparticles have the best balance between dye loading, electron transport and optical transparency [6,8]. This work uses an approach that separates the morphological features of the PE film from the electrochemical properties of the semiconductor. This is possible using different materials as surface area provider and layers of semiconductors, respectively. The idealized photoelectrode is illustrated in Figure 6.1. It comprises a porous SiO_2 scaffold layer, coated with a suitable metal-oxide semiconductor, TiO_2. The role of the scaffold is to provide a large surface area for the dye adsorption and consequently an efficient solar radiation harvest. The SiO_2 material is responsible for the final morphology of the photoelectrode and should be as transparent as possible to ensure that light reaches the adsorbed dye molecules. Although the pores of this layer should be as small as possible to ensure large surface areas, they must be large enough to allow the deposition of an optimized semiconductor coating thickness; the amount of TiO_2 deposited in the template pores determines the ability of the PE to adsorb dye and efficiently transport electrons to the FTO surface. To achieve a homogeneous dense coating of the scaffold particles, the TiO_2 film was deposited by ALD. The deposited film should be compact and uniform with minimum number of grain boundaries and morphological defects compared to conventional TiO_2 mesoporous photoelectrode. Therefore, it is reasonable to expect better transport characteristics and less electron/electrolyte recombination in the proposed architecture. Using a template that maximizes the surface area of the PE while maintaining pore size slightly larger than ALD deposited layer, the engineered PE architecture separates morphological features of the PE from electrochemical properties of the semiconductor. This opens opportunities for using new semiconductors without the usual concern of nanoparticle morphological control.

In this study the ALD process was optimized for deposition of TiO_2 within a mesoporous scaffold with pores of *ca*. 20 nm; the TiO_2 precursors were titanium isopropoxide (TIP) and water. The shrinking core model [22,23] was used to predict the minimum exposure time for TIP to diffuse and completely cover the scaffold inner surface area; the calculations were performed for TIP since this is the slower reactant.

The thickness of the deposited TiO$_2$ film was optimized, and its influence on the DSC transport and recombination assessed.
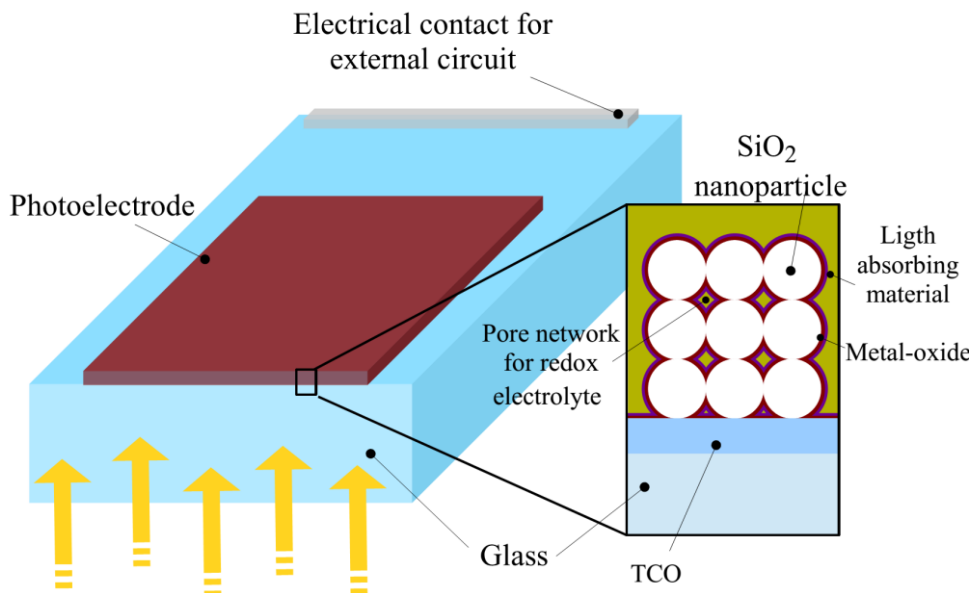
Figure 6.1 Schematic representation of the new photoelectrode architecture.

6.2 Materials and Methods

6.2.1 SiO$_2$ scaffold film

The properties of the SiO$_2$ nanoparticles (Sigma-Aldrich® ref. 637246) are given in Table 6.1. Brunauer-Emmett-Teller (BET) surface area analysis and Barrett-Joyner-Halenda (BJH) pore size analysis were conducted in the powder as received from the supplier (*cf*. appendix D, Figure D.1). A screen-printable paste formulation was developed to achieve optimum film characteristics, *i.e.*, suitable viscosity for screen printing, good particle packing, good adhesion to FTO substrate and no visible cracking of the film. The optimized paste formulation contains terpineol (Sigma-Aldrich® ref. W304506) as solvent and ethyl cellulose (Sigma-Aldrich® ref. 46070) as binder and is given in Table 6.1.

Table 6.1 SiO$_2$ particles morphological characteristics and paste formulation composition

SiO$_2$ particles (powder form)		Paste composition / wt. %			SiO$_2$ layer morphology (after sintering)	
d_{SiO_2} / nm	A_s / m$^2 \cdot$g^{-1}	SiO$_2$	Ethyl cellulose	Terpineol	d_p / nm	ε
15.0±0.5	159±0.55	20.0	10.0	70.0	21.0±0.6	0.63±0.09

The SiO$_2$ paste was applied by screen-printing (Rokuprint® screen printer) 5×5 mm^2 areas using a 43–80 mesh screen (43 threads/cm and 80 μm thread diameter) on previously cleaned FTO glasses. The printed samples were then fired in an infrared furnace (Nabertherm Gmbh model GF75) at 450 ºC during 30 min to remove the solvent and binder used, and to promote adhesion between particles and the FTO glass surface. Figure 6.2 shows a scanning electron microscopy (SEM) cross-section image of the SiO$_2$ film applied on a FTO glass. The porosity (ε) and average pore size (d_p) of SiO$_2$ layer were calculated based on the density of the SiO$_2$ particles and of the SiO$_2$ layer, as detailed in appendix D. The average pore size calculated for the sintered SiO$_2$ layer based on layer and particle densities (*ca*. 21.0 nm) is lower than the pore size obtained by BJH analysis (*ca*. 30 nm) to the a sample of SiO$_2$ particles. The difference was assigned to particle packing and necking between particles during the firing step. Actually, the sintered layer of SiO$_2$ was expected to display a smaller porosity than the corresponding powder sample.
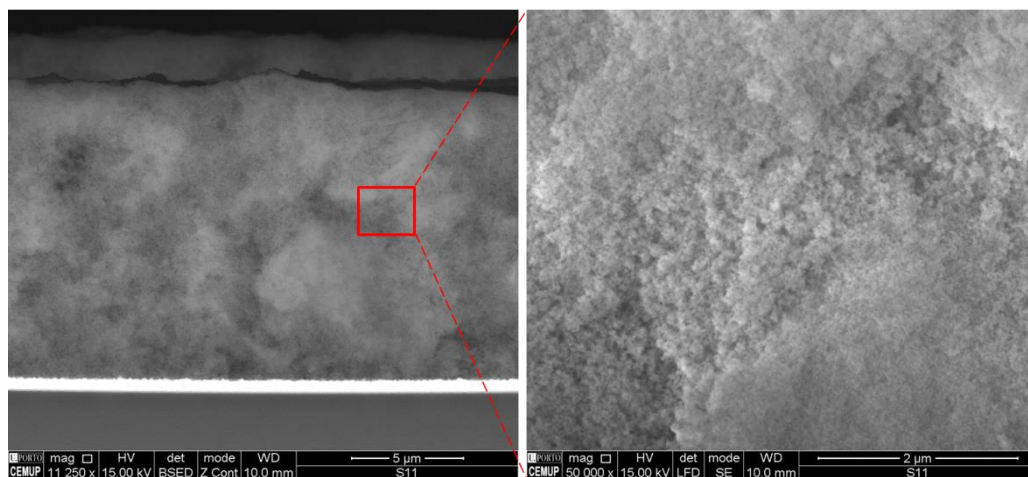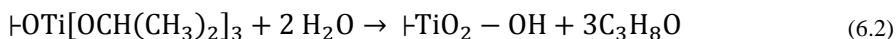

Figure 6.2 Cross section SEM image of the developed SiO$_2$ film applied by screen printing on FTO coated glass substrate (left) and respective magnification (right).

6.2.2   TiO$_2$ reaction mechanism in ALD

Atomic layer deposition of TiO$_2$ was accomplished using a titanium metal precursor, titanium isopropoxide (C$_{12}$H$_{28}$O$_4$Ti, titanium(IV) isopropoxide $\geq$ 97%, Sigma Aldrich®), and distilled water (H$_2$O) as oxidizing agent. The reaction mechanism is illustrated in Figure 6.3. First, the titanium precursor (TIP) was pulsed into the reaction chamber reacting with the OH groups present at the substrate surface until a monolayer has been chemisorbed and no more adsorption took place. Then, the reaction chamber is purged and the second precursor (water) is pulsed reacting with the chemisorbed TIP to form TiO$_2$ and propanol as byproduct. The reaction chamber is purged again and a monolayer of TiO$_2$ is obtained at the substrate. The half reactions of TIP and H$_2$O to produce TiO$_2$ are given by:

$$\vdash\!OH + Ti[OCH(CH_3)_2]_4 \rightarrow \vdash\!OTi[OCH(CH_3)_2]_4 + C_3H_8O \tag{6.1}$$

$$\vdash\!OTi[OCH(CH_3)_2]_3 + 2\,H_2O \rightarrow \vdash\!TiO_2 - OH + 3C_3H_8O \tag{6.2}$$

where the symbol $\vdash$ designates a surface bond.

This reaction cycle was repeated until the desired thickness has been reached. Therefore, the ALD growth rate is proportional to the number of cycles rather than the flux of the reactants.

The ALD deposition was conducted in a Beneq Oy thin film system equipped with a TFS 200 reactor. The process operation is described in detail in appendix C. The deposition of TiO$_2$ was assessed initially directly on FTO substrates. Table C1 (in appendix C) shows the operating variables used. The precursor pulse/purge times chosen took into account recommended values[24] and were chosen conservatively to prevent the mixture of the precursors either in the flow system tubing or in the reactor. For FTO glasses TIP pulse time ($\Delta t_{TIP,2}$) was set to 1 s while for the SiO$_2$ mesoporous layer this pulse time ($\Delta t_{TIP,2}$) was optimized. Nevertheless, for all tested $\Delta t_{TIP,2}$ values, the TIP to water pulse times ratio, the TIP purge to pulse times ratio and the water purge to pulse times ratio were kept constant according to equations C.2, C.3 and C.4 respectively, also presented in appendix C.
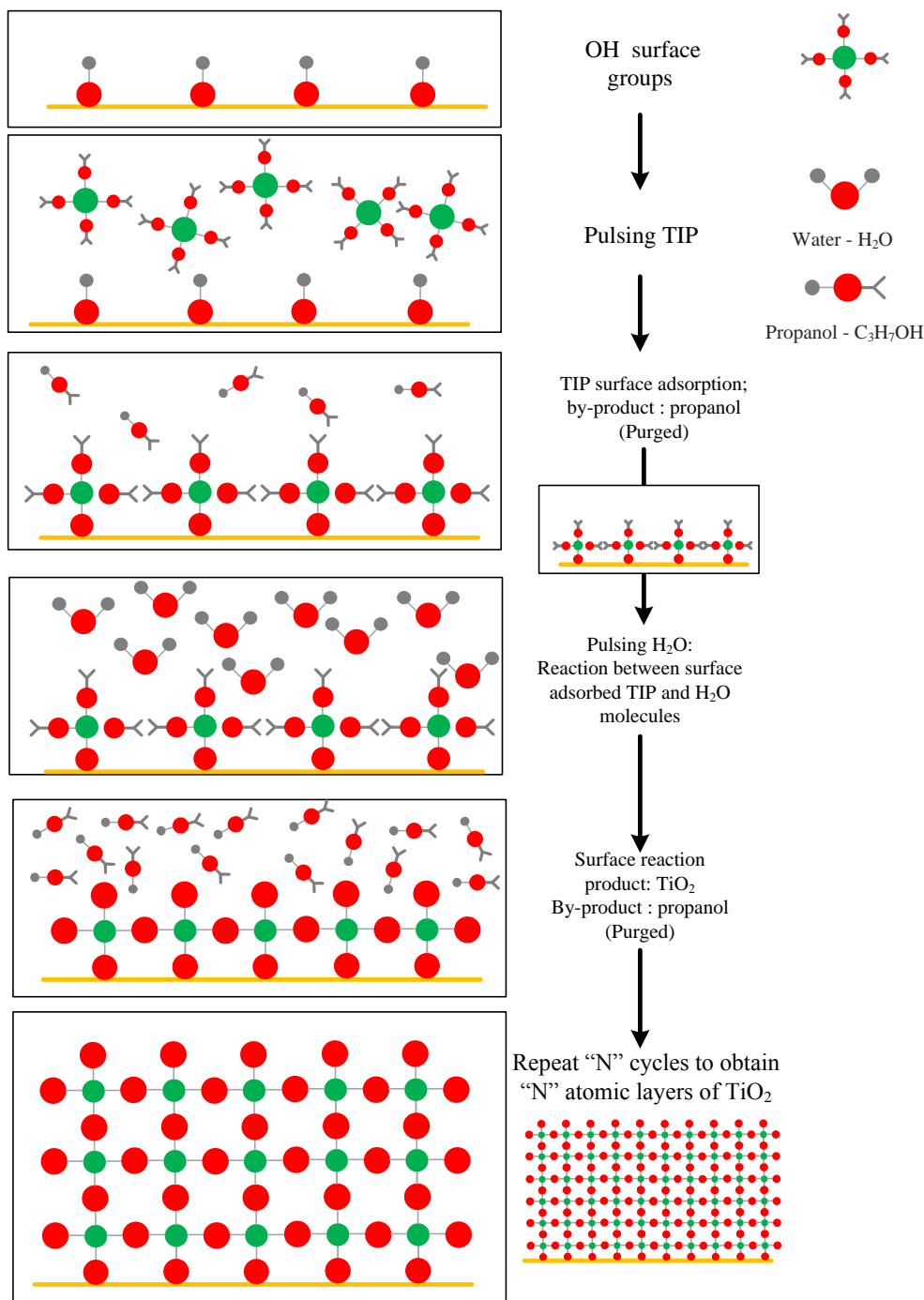
Figure 6.3 Schematic diagram of the ALD process for TiO_2 coating using TIP and H_2O.

6.2.3 Dye sensitized solar cells fabrication

Photoelectrodes were assembled on 7 Ω·□$^{-1}$ SnO$_2$-F (FTO) coated glass substrates (2.2 mm thick) from Solaronix®. The glass substrates were washed using a cleaning solution (Alconox®, VWR) in an ultrasonic cleaner (Amsonic TTC) at 55 ℃ for 15 min, followed by ultrasonic cleaning in deionized water at room temperature and dried with air at 50 ℃. Glass substrates were coated with the previously described SiO$_2$ paste by screen-printing followed by firing at 450 ℃ for 30 minutes. After firing the substrates were loaded into the ALD reactor and coated with TiO$_2$ with different thicknesses. The TiO$_2$/SiO$_2$ electrodes were then calcined at 450 ℃ during 30 min to promote the crystallization of the TiO$_2$ film. Dye adsorption was carried out dipping the electrodes in the dye solution (0.5 mM N719, ruthenizer 535-bisTBA from Solaronix®) during 24 hours. Afterwards, the electrodes were rinsed with ethanol and dried under nitrogen flow.

The counter-electrodes, prepared on the same type of glass substrates and cleaned as described before, were drilled previously with two holes of 1 mm diameter – Figure 2.19. A commercial platinum paste (Platisol T/SP from Solaronix®) was applied on the counter-electrode glass substrate by screen-printing followed by annealing at 400 ℃ for 15 minutes in an infrared furnace (Nabertherm Gmbh model GF75).

The two electrodes were assembled and sealed with a 60 μm Surlyn® film (Meltonix 1170-60, Solaronix®) using a hot press at 160 ℃, applying 10 bar for 20 s. After sealing, the electrolyte (EL-HPE, Dyesol) was injected trough the drilled holes, which were then sealed applying heat and pressure on a glass lamella / Surlyn® film sandwich. Solder bus bars were applied to the FTO surface of the photo and counter-electrodes using an ultrasonic soldering device (MBR electronics model USS-9210).

For comparison, reference DSCs were prepared using commercial TiO$_2$ paste (DSL 18NR-AO, Dyesol). Two layers were screen-printed using a 43-80 mesh screen with the same active area of the SiO$_2$ films (5 × 5 mm^2) and fired at 500 ℃ for 60 min. All other preparation details were similar to SiO$_2$/TiO$_2$ DSCs.

6.2.4 DSC performance characterization

The performance of the prepared DSCs was assessed from the *I-V* characteristics and from electrochemical impedance spectroscopy (EIS) analysis. The *I-V* curves were obtained at 100 mW·cm^{-2} (1 sun light intensity) and using a 1.5 air mass filter (Newport, USA) in a setup equipped with a 150 W xenon light source (Oriel class A solar simulator, Newport, USA). The simulator was calibrated using a single crystal Si photodiode (Newport, USA). The *I-V* characteristics were obtained applying an external potential load and measuring the generated photocurrent using an AUTOLAB electrochemical station (PGSTAT 302 N). The EIS measurements were performed in dark, from 100 kHz to 0.05 Hz with an AC modulation signal of 10 mV and at several loads between 0 V and the V_{oc}.

6.3 Shrinking core model

For depositing a TiO$_2$ film within the mesoporous SiO$_2$ scaffold the precursor reactants, in this case TIP or water vapor, are pulsed into the ALD reaction chamber infiltrating and adsorbing at the pore walls of the SiO$_2$ mesoporous layer. However, due to the very large surface area of the SiO$_2$ layer ($\approx$160 m^2·g^{-1}) the gas molecules may not reach all available adsorption sites. The screen-printed SiO$_2$ has a layer thickness (L_f) of *ca*. 20 ± 3 μm, and average pores size of 20 nm – see appendix C; therefore, it is reasonable to assume that the gas transport in the porous SiO$_2$ film falls in the Knudsen regime[22,25,26]. In the present work, the printed SiO$_2$ film was parallelepiped shaped with dimensions 5 mm × 5 mm × 20 μm, as illustrated in Figure 6.4a).
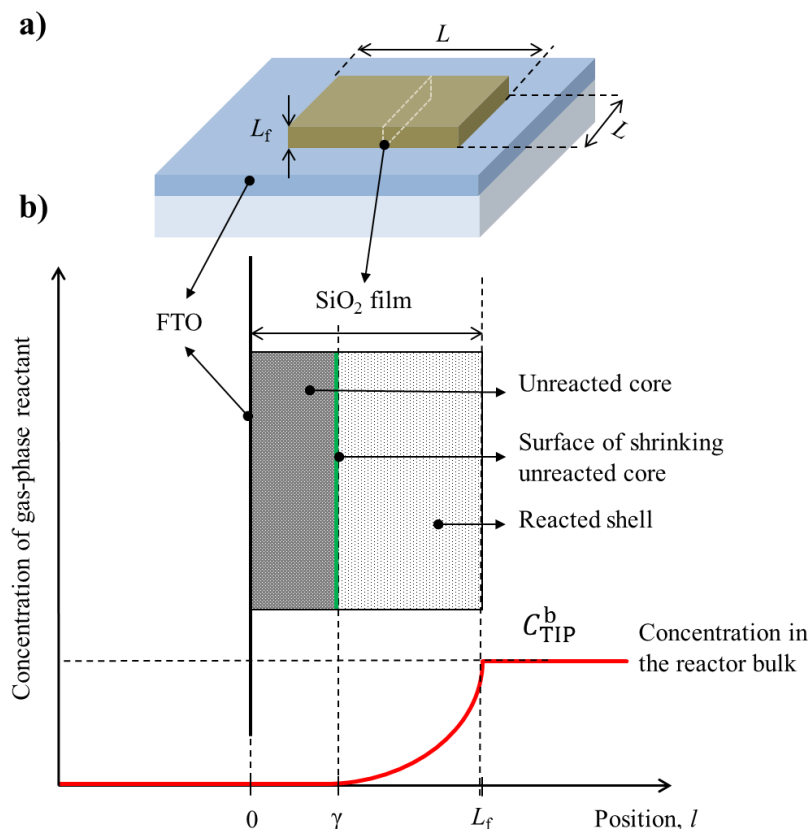
Figure 6.4 a) 3D illustration of the printed SiO$_2$ layer on FTO coated glass (not in scale) and b) model of reacting SiO$_2$ porous layer during precursor exposure. *L* represents the length and width of the printed SiO$_2$ layer, *L$_f$* the layer thickness and *γ* the position of the unreacted core.

Because $L \gg L_f$ ($L = 5$ mm and $L_f = 20 \pm 3$ μm), the top area of the SiO$_2$ layer is *ca*. 63 times larger than the lateral areas of the film (0.25 cm^2 *vs*. 0.004 cm^2); therefore, it was assumed a 1D diffusion model.

As the precursor molecules diffuse into the porous SiO$_2$ layer, two regions are defined: a region where the SiO$_2$ spheres were coated with a monolayer of one of the two reactants and an uncoated region, within the SiO$_2$ layer – Figure 6.4b. The uncoated region shrinks with time in a process analogous to a burning particle; the progressive coating can then be well represented by the so-called shrinking-core model (SCM)[22, 23]. Following the notation of this model, the uncoated region is named "core" while the coated region is named "shell". The boundary of the unreacted core

(represented in green color in Figure 6.4) moves inwards towards the FTO surface and its position is considered to be $l = \gamma$, the shrinking core position. For the gas/solid system under study, it is reasonable to consider that the unreacted core shrinkage is much slower than the flow rate of precursor molecules towards the unreacted core[22,23]. The main assumptions of the model are: one-dimensional mass transport, uniform morphologic characteristics of SiO_2 layer, isothermal transport, constant diffusion coefficient of TIP through the diffusion layer, constant bulk precursor concentration, TIP chemisorbs over the SiO_2 support as a monolayer originating TiO_2 upon reaction with water, and pseudo steady state. Of the two reactants, TIP is the heaviest and therefore the slowest one. Since the objective of the model was estimating the minimum pulse time, TIP gives the most conservative result and it was then used to compute the pulse time. Taking into account these assumptions the rate of TIP chemisorption at steady state on SiO_2 layer inner surface, at any instant t and position l, is given by[23]:

$$-\frac{dN_{TIP}}{dt} = Q_{TIP} \cdot A_s \tag{6.3}$$

where N_{TIP} and Q_{TIP} are the number of moles and the flux of TIP, respectively, and A_s is the reaction surface. The flux of TIP can be expressed according to the Fick's first law:

$$Q_{TIP} = D_{TIP} \cdot \frac{dC_{TIP}}{dl} \tag{6.4}$$

where D_{TIP} is the effective TIP diffusivity and C_{TIP} is the molar concentration of TIP at axial position l. Both Q_{TIP} and C_{TIP} are positive in the coordinates system presented in Figure 6.4. Combining (6.3) and (6.4) the following equation is obtained:

$$-\frac{dN_{TIP}}{dt} = A_s \cdot D_{TIP} \cdot \frac{dC_{TIP}}{dl} \tag{6.5}$$

Integrating (6.5) from the exterior surface $l = L_f$ (bulk concentration of TIP, C_{TIP}^b) to the boundary of the unreacted core surface $l = \gamma$ ($C_{TIP} = 0$) one obtains:

$$-\frac{dN_{\text{TIP}}}{dt} \int_{L_f}^{\gamma} \frac{dl}{l^2} = D_{\text{TIP}} \cdot \int_{C_{\text{TIP}}^b}^{0} dC_{\text{TIP}}$$

(6.6)

and after integration:

$$-\frac{dN_{\text{TIP}}}{dt} \left(\frac{1}{\gamma} - \frac{1}{L_f} \right) = D_{\text{TIP}} \cdot C_{\text{TIP}}^b$$

(6.7)

Equation (6.7) gives the moving boundary of chemisorbed TIP monolayer as it progress down in the SiO₂ mesoporous layer. According to the half reactions (6.1) and (6.2), TIP surface adsorption results in the same amount of loss in hydroxyl surface groups ($\vdash$OH):

$$-dN_{\text{TIP}} = -dN_{\text{OH}}$$

(6.8)

where N_{OH} is the number of moles of hydroxyl groups. Rewriting Eq. (6.8) using the molar density of OH and the volume of the unreacted core gives:

$$-dN_{\text{TIP}} = -dN_{\text{OH}} = -\rho_{\text{OH}}dV = -\rho_{\text{OH}}d(\gamma^3) = -3\,\rho_{\text{OH}}\gamma^2 d\gamma$$

(6.9)

Inserting equation (6.9) into (6.7), the rate of reaction in terms of the shrinking core position (γ) is:

$$-\frac{dN_{\text{TIP}}}{dt} = -3\,\rho_{\text{OH}}\,\gamma^2 \left(\frac{1}{\gamma} - \frac{1}{L} \right) \frac{d\gamma}{dt} = D_{\text{TIP}}\,C_{\text{TIP}}^b$$

(6.10)

Integrating and rearranging, the unreacted shrinking cores varies with time as follows:

$$t = \frac{\rho_{\text{OH}}L_f^2}{2D_{\text{TIP}}C_{\text{TIP}}^b} \left[1 - 3 \left(\frac{\gamma}{L_f} \right)^2 + 2 \left(\frac{\gamma}{L_f} \right)^3 \right]$$

(6.11)

For complete coverage of the SiO₂ surface area with TIP, $\gamma = 0$, the minimum pulse time, τ_{min}^p, can be written as:

$$\tau_{\text{min}}^p = \frac{\rho_{\text{OH}}L_f^2}{2D_{\text{TIP}}C_{\text{TIP}}^b}$$

(6.12)

Combining (6.11) and (6.12), the progression of the reaction can be written in terms of the time required for the full coverage, τ_{min}^p:

$$\frac{t}{\tau_{\text{min}}^p} = 1 - 3 \left(\frac{\gamma}{L_f} \right)^2 + 2 \left(\frac{\gamma}{L_f} \right)^3$$

(6.13)

and in terms of the surface coverage fraction:

$$\frac{t}{\tau_{min}^{p}} = 1 - 3(1 - X_f)^2 + 2(1 - X_f)^3 \tag{6.14}$$

where $X_f = 1 - \gamma/L_f$ is the surface coverage fraction. The effective TIP diffusivity, D_{TIP}, is given by[22, 28]:

$$D_{TIP} = D_k \frac{\varepsilon}{\xi} \tag{6.15}$$

where ε and ξ are the porosity and tortuosity of the SiO_2 and D_k is the Knudsen diffusivity given by:

$$D_k = \frac{d_p}{3} \sqrt{\frac{8RT}{\pi\, M_{TIP}}} \tag{6.16}$$

where d_p is the pore diameter, R the gas constant, M_{TIP} the molecular mass of the gas (TIP), and T the temperature. With the pore size for TIP diffusion and using eq. (6.16) and (6.12) it is possible to have an initial estimation of the minimum TIP pulse time, τ_{min}^{p}, for the complete coverage of the SiO_2 scaffold layer. Table 6.2 shows the parameters used for calculating D_k and τ_{min}^{p}. The results are plotted in Figure 6.5 for a range of pore sizes and show that for $d_p \leq 10$ nm, τ_{min}^{p} varies exponentially with pore size; for $d_p \geq 10$ nm τ_{min}^{p} is approximately linear with d_p. Because the pore size decreases with each ALD cycle, the Knudsen diffusivity is lower and the minimum pulse time required for complete diffusion of TIP in the porous layer increases. Therefore due to the increasingly lower d_p during ALD deposition, τ_{min}^{p} should be chosen accordingly to the required TiO_2 film thickness.

Table 6.2 Parameters used for computing the Knudsen diffusion coefficient, D_k, and the minimum TIP pulse time for complete coverage of the fresh SiO$_2$ scaffold, τ_{min}^p.

Variable	Description	Units	value
C_{TIP}^b	Bulk concentration of TIP	mol·cm^{-3}	2.33×10^{-7}
M_{TIP}	Molecular mass of TIP	g·mol^{-1}	284.22
d_p	Average pore diameter in SiO$_2$ film	nm	0-50
A_s	Superficial area of the SiO$_2$ film	m^2·g^{-1}	160
ρ_{OH}	Molar density of OH surface groups in SiO$_2$ porous film[*1]	mol·cm^{-3}	1.47×10^{-3}
L_f	SiO$_2$ layer thickness	μm	20 ± 0.5
T	Temperature	°C	250
P	Pressure	mbar	1.2

[*1] Calculated using 4.9 OH·nm^{-2} as reference value of –OH groups area density in SiO$_2$ [29].
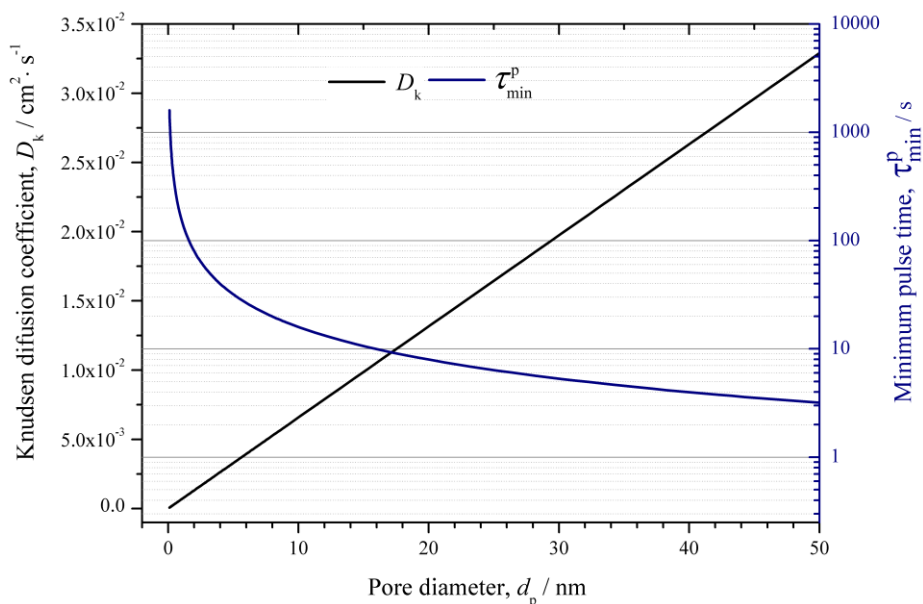

Figure 6.5 Knudsen diffusion coefficient, D_k, and minimum TIP pulse time for complete TiO$_2$ coverage of the fresh SiO$_2$ layer, τ_{min}^p. The parameters used are presented in Table 6.2.

6.4 Results and Discussion

6.4.1   Planar TiO$_2$ ALD films

TiO$_2$ films were deposited on FTO glass substrates according to the ALD operation conditions presented in appendix C, Table C1. The number of ALD cycles was varied from 100 to 4000. Figure 6.6 shows a SEM image of one of these films, obtained after 2000 ALD cycles. The deposited TiO$_2$ film is compact and very conformal, accompanying the irregular surface of the FTO. The optical characteristics of FTO glass and the ALD TiO$_2$ films were determined by spectrophotometry (Shimadzu UV-3600); their transmittance spectra are presented in Figure 6.7a). The deposition of 100 ALD cycles resulted in no noticeable changes in the transmittance spectrum (from 200 nm till 800 nm) compared with a reference FTO glass substrate; from 500 to 4000 ALD cycles the transmittance of the coated samples start decreasing due to the increased thickness of the TiO$_2$ deposited layer.
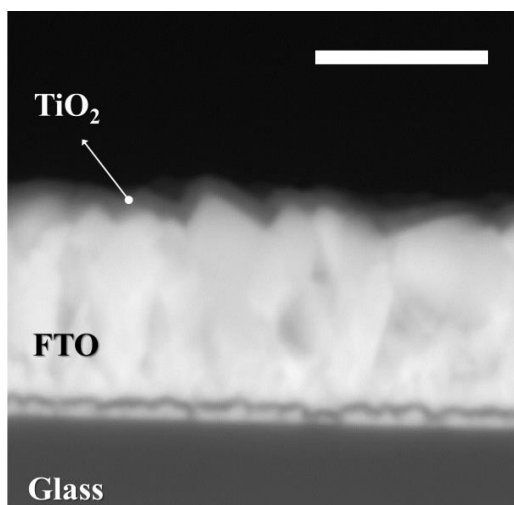

Figure 6.6 Cross sectional SEM image of a TiO$_2$ film produced after 2000 ALD cycles (white scale bar represents 500 nm). All other operating details are given in appendix C, Table C1.

The UV absorbance of the TiO$_2$ films was computed from transmittance and reflectance data. Figure 6.7b) shows that the UV absorbance (320 nm) of the TiO$_2$ films is linear with the ALD number of cycles. Thickness measurements by SEM

analysis showed a good linear fit between number of cycles and thickness of TiO$_2$ layer, a usual characteristic of ALD growth mechanism. The growth rate was determined to be 0.022 ± 0.003 nm/cycle, which is in agreement with literature[30,31].
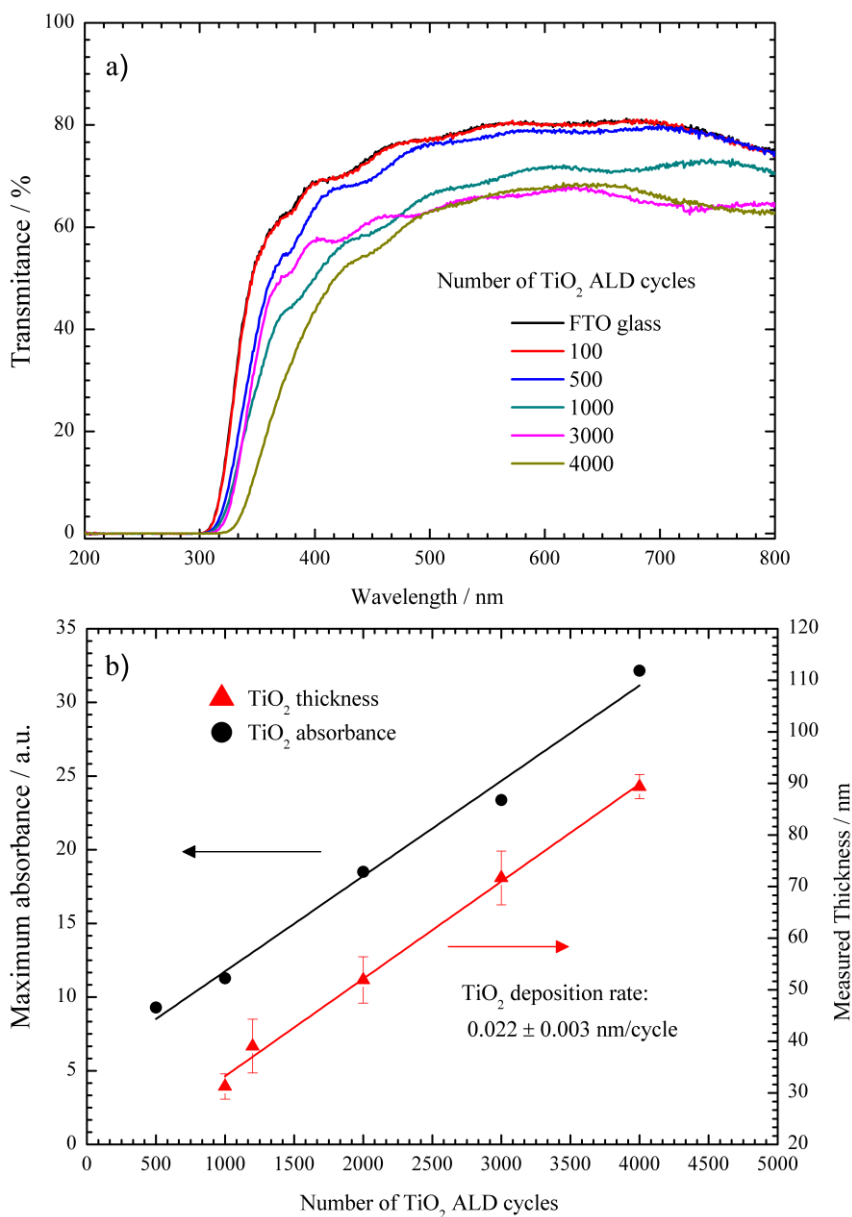

Figure 6.7 a) Transmittance spectra for FTO glasses coated with TiO$_2$ with different number of ALD cycles and b) calculated UV (320 nm) absorbance and SEM TiO$_2$ layer thickness.

6.4.2 Three-dimensional SiO$_2$/TiO$_2$ ALD layer

The success of the photoelectrode architecture highly depends on the ability to completely coat the surface area of the SiO$_2$ scaffold. Insufficient coverage of the SiO$_2$ scaffold results in poor electrical connection between the photoelectrode and the FTO, back contact. As starting point, the SiO$_2$ layer was infiltrated using the same pulse time used for planar TiO$_2$ coating on the FTO substrates ($\Delta t_{TIP,2} = 2$ s). The number of cycles was selected in order to deposit an amount of TiO$_2$ that would not cause pore blocking of the SiO$_2$ scaffold. According to the calculated average pore size of the "fresh" SiO$_2$ layer (no TiO$_2$ film, $d_p = ca.$ 20 nm, appendix D, Table D.1), it was determined to deposit 3 nm of TiO$_2$ film (*i.e.* total of 6 nm reduction in pore size); using a linear extrapolation of the fitted growth rate in Figure 6.7 this means *ca.* 140 ALD cycles.

Figure 6.8 shows a SEM cross-section image of a SiO$_2$ layer infiltrated with 140 cycles of TiO$_2$. Energy-dispersive X-ray spectroscopy (EDS) profile analysis was performed to check the infiltration of the TiO$_2$ deposited by ALD. The atomic count profile of Sn, Ti, Si and Na are plotted and overlapped over the SEM image. The atomic counts of these elements give a good indication of the relative position of the FTO layer, the infiltrated TiO$_2$ film, the SiO$_2$ nanoparticle layer and the glass substrate, respectively. The atomic count signal of Sn from the FTO (SnO$_2$-F) was used to set $L^* = 0$ in the SEM image. As expected, the atomic count of Si is constant across the SiO$_2$ layer. Because calcium is present only in the glass substrate its signal is mainly present at $L^* < 0$.

The Ti atomic count shows that the amount of titanium dioxide at the porous scaffold gradually decreases towards the interface with the FTO layer. Although the TIP pulse time $\Delta t_{TIP,2} = 2$ s was sufficient for covering planar structures such as FTO (showed in Figure 6.6), it is unsatisfactory to cover the mesoporous SiO$_2$ layer.
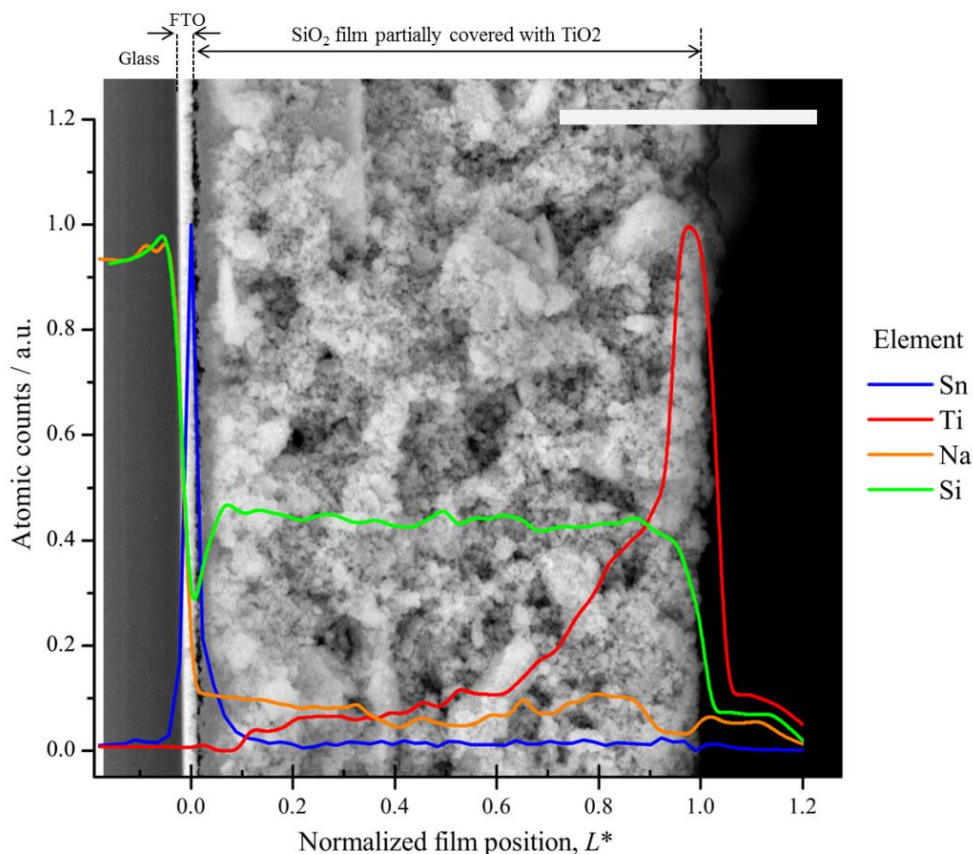
Figure 6.8 SEM cross-section of the partially infiltrated SiO_2 porous layer (white scale bar corresponds to 10 μm). Overlapped to the SEM image there are the EDS profiles (atomic counts) of Sn, Ti, Na and Si. $\Delta t_{TIP} = 2$ s, 140 cycles. All other ALD process parameters are appendix C, Table C1.

   To increase the surface coverage of the SiO_2 porous layer with TiO_2 film, the TIP pulse time was increased. Figure shows that the EDS Ti atomic counts on the SiO_2 mesoporous layer for TIP pulse times ($\Delta t_{TIP,2}$) from 2 s to 25 s. Assuming that the Ti atomic counts are proportional to the TiO_2 surface coverage fraction the integral of the yellow areas in Figure 6.9 gives the overall surface coverage fraction (X_f). The Ti counts increase with pulse time reaching 98 % coverage at $\Delta t_{TIP,2} = 25$ s.
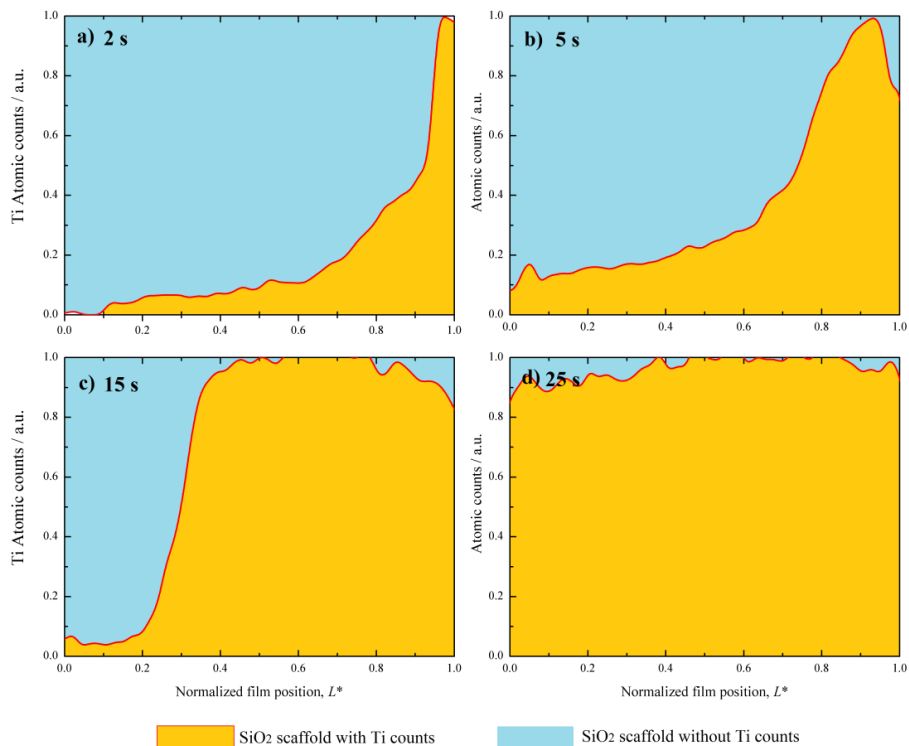
Figure 6.9 Titanium atomic counts profiles by EDS analysis in cross sections of the SiO_2 mesoporous layer infiltrated using 140 ALD cycles with different TIP pulse times: a) 2 s b) 5 s c) 15 s d) 25 s. All other ALD process parameters are presented in appendix C, Table C1.

Taking into account the reduction in the average pore size (from *ca.* 20 nm to *ca.* 14 nm) after the deposition of *ca.* 3 nm thick TiO_2 film (140 ALD cycles) the Knudsen diffusivity becomes $D_k = 8.75 \times 10^{-3}$ $cm^2 \cdot s^{-1}$ and a time of *ca.* 12 s would be necessary for the complete coverage of the SiO_2 layer – Figure 6.5. However, as shown by Figure 6.9, at least 25 s is required for the complete surface coverage. This difference was assigned to the wide range of pore sizes as well as the tortuosity of the pores. The experimental values of X_f as a function of TIP pulse time (shown in Figure 6.10) were fitted using equations (6.12) and (6.14) minimizing the sum of the square difference to obtain the effective diffusion coefficient of TIP in the SiO_2 film, D_{TIP}. The model fits well the experimental data, and D_{TIP} was found to be $(4.23 \pm 0.65) \times 10^{-3}$ $cm^2 \cdot s^{-1}$.
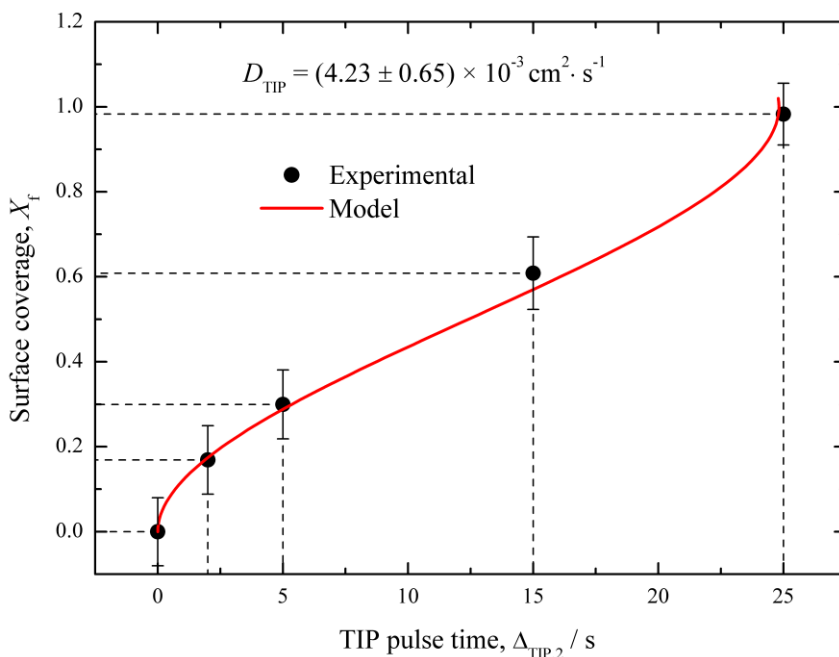
Figure 6.10 Experimental and predicted surface coverage (X_f) as a function of the TIP pulse time ($\Delta t_{TIP, 2}$).

Using the predicted D_k for the complete SiO$_2$ surface coverage taking into account the pore size reduction with 140 ALD TiO$_2$ cycles ($D_k = 9.83 \times 10^{-3}$ cm^2·s^{-1}), the fitted effective TIP diffusivity, $(4.23 \pm 0.65) \times 10^{-3}$ cm^2·s^{-1}, and the porosity of the film ($\varepsilon = 0.63$) then Eq. (6.16) allows computing the tortuosity of the SiO$_2$ porous layer – $\xi = 1.46$. The minimum pulse time, τ^p_{min}, can now be computed taking into account the tortuosity of the SiO$_2$ layer, and the size reduction caused by the deposition of the TiO$_2$ film; Figure 6.11 shows that the pore size reduction and τ^p_{min} as a function of the thickness of TiO$_2$ film. To assure the complete coverage in SiO$_2$ layer used for preparing DSC devices, the pulse time was set according to the amount of TiO$_2$ film to be coated in the scaffold layer, using Figure 6.11 and Table D1 presented in appendix D. All other ALD process variables were set according to Table C.1 and equations C.2, C.3 and C.4, presented in appendix C.
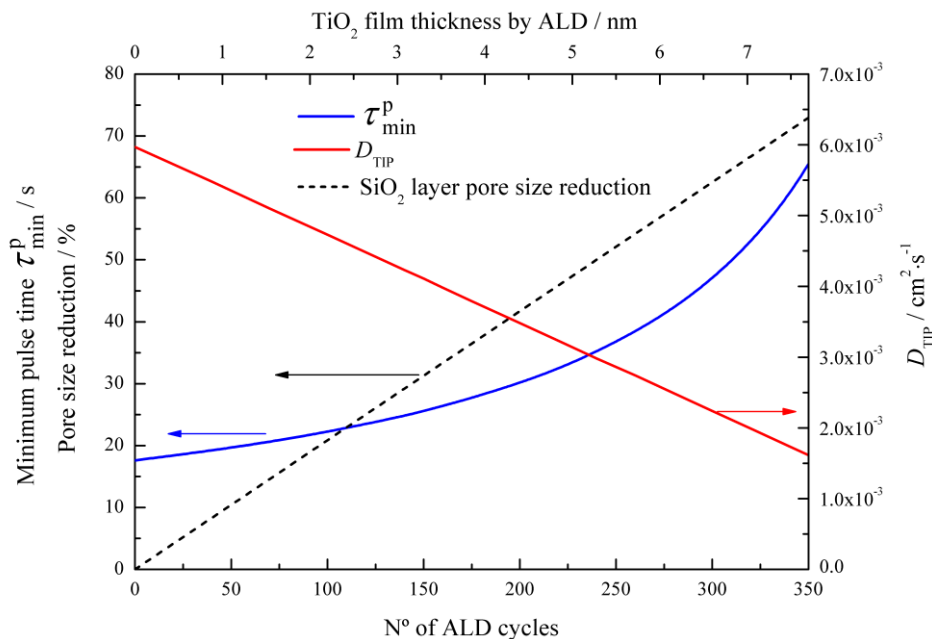
Figure 6.11 Minimum TIP pulse time, τ_{min}^{p}, required for complete TiO_2 coverage of the SiO_2 layer taking into account pore size reduction due to TiO_2 film ALD.

6.4.3 Optical characterization of SiO_2/TiO_2 films

SiO_2/TiO_2 composite layer (20 μm thick) on FTO glass substrate prepared with 140 ALD cycles and TIP pulse time according to Figure 6.11, were characterized optically using spectrophotometry; FTO glass substrate, FTO glass substrate with 3 nm ALD TiO_2 film, FTO glass substrate with the mesoporous SiO_2 layer (20 μm thick), and a conventional mesoporous TiO_2 film (20 μm thick, 18NR-AO-Dyesol®) were also analyzed. Figure 6.12a) and b) show the transmittance and reflectance spectra of these samples. The mesoporous SiO_2 layer shows a maximum of *ca.* 60 % transmittance and *ca.* 30% reflectance in the visible range. Adding 3 nm of ALD TiO_2 to the FTO glass substrate did not result in noticeably transmittance or reflectance changes; however, when 3 nm of TiO_2 are applied in the mesoporous SiO_2 layer, the optical characteristics of the sample change drastically. Due to the large inner surface area of the SiO_2 layer, the integral of TiO_2 film thickness becomes much higher than 3 nm. Therefore the transmittance of the sample decreases *ca.* 10 % and there is a significant increase (*ca.* 50 %) in reflectance that reaches 60 % at 400 nm. This is particular interesting for DSC

applications due to the strong absorption of N719 in this spectrum region, as showed by the dye absorption curve in Figure 6.12b).
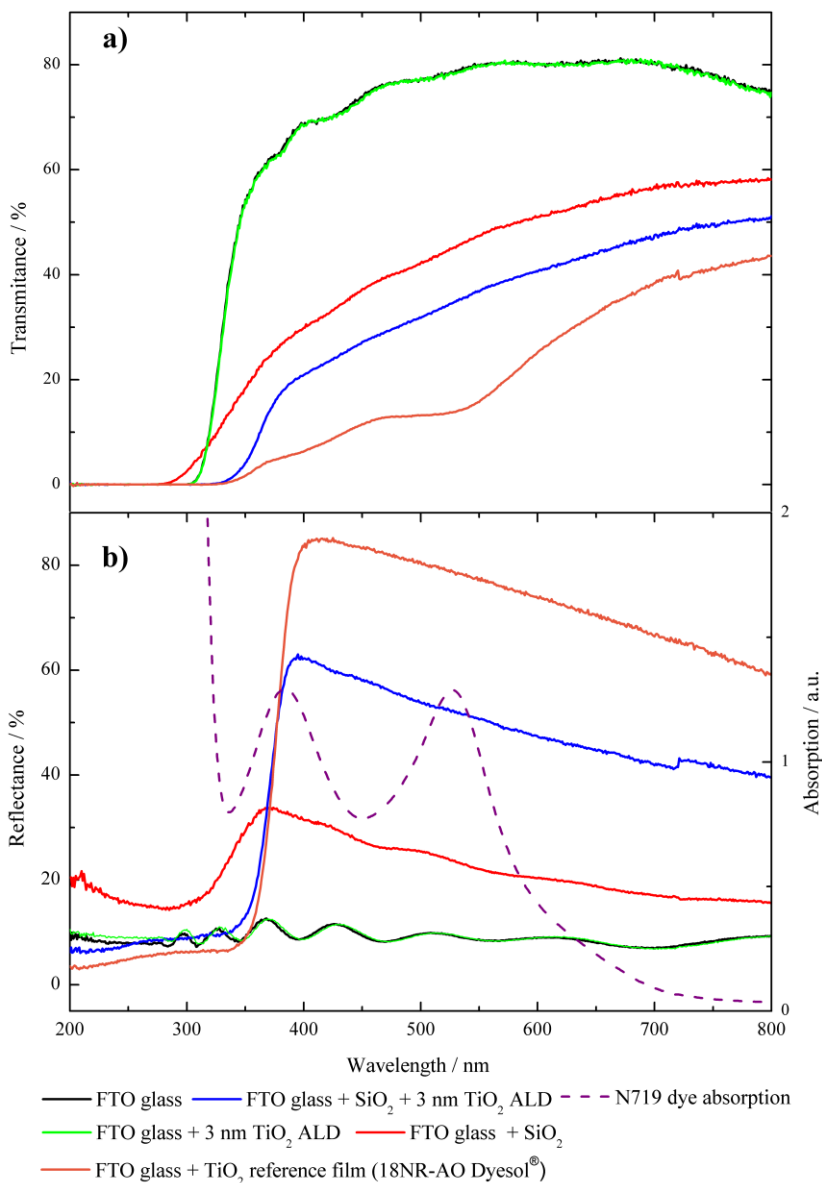

Figure 6.12 Optical characteristics of FTO glass substrate, FTO glass substrate with planar 3 nm ALD TiO₂ film, FTO glass substrate with 20 μm SiO₂ layer, FTO glass substrate with 20 μm SiO₂/TiO₂ composite layer, FTO with 20 μm of conventional TiO₂ layer (18NR-AO-Dyesol®). The absorption spectrum of N719 dye is also shown.

The optical bandgap (E_g) of the prepared SiO_2/TiO_2 composite layer was calculated from the Tauc plot [32] presented in Figure 6.13. The optical bandgap found for the TiO_2 in composite layer was 3.30 eV while for the conventional TiO_2 layer it was 3.25 eV. The increased TiO_2 bandgap when inserted in the composite layer, compared with the conventional TiO_2 layer, was assigned to the substrate effect; actually, a 3 nm TiO_2 film is expected to suffer optical deformations due to the scaffold layer [33].
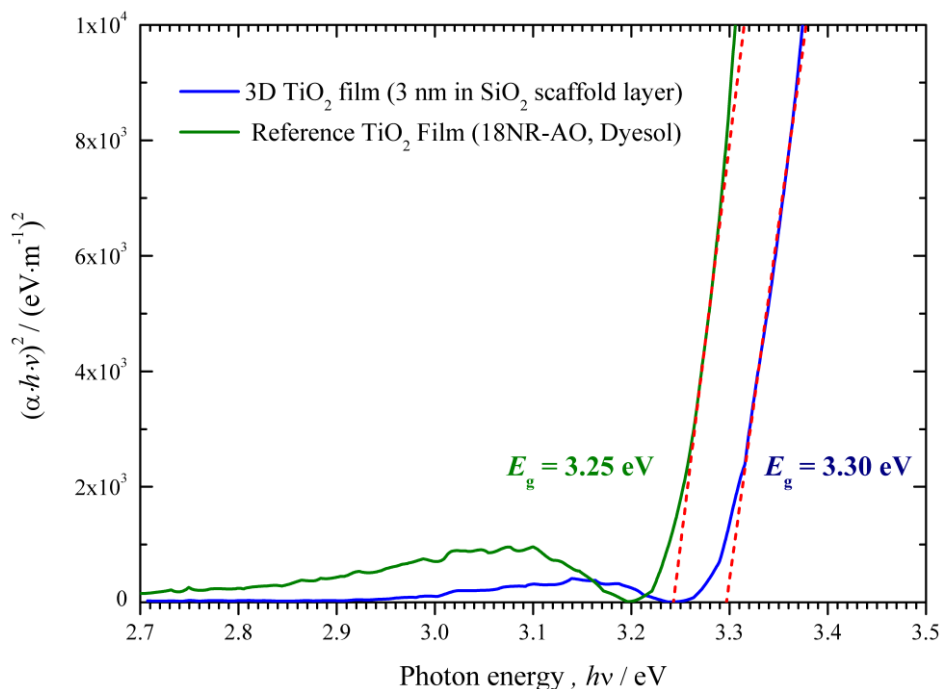
Figure 6.13 Tauc plot calculated from the absorption data of TiO_2 film (3 nm thick) deposited in the SiO_2 porous scaffold layer (20 μm) and of the conventional TiO_2 mesoporous layer (20 μm, 18NR-AO Dyesol®).

6.4.4 DSCs based on SiO_2/TiO_2 architecture

The prepared SiO_2/TiO_2 composite photoelectrodes were then used in DSC devices. Figure 6.14 shows the *I-V* curves obtained under illumination (AM 1.5, 100 mW·cm^{-2}) and in dark conditions for the SiO_2/TiO_2-DSCs, where the TiO_2 film thickness in the SiO_2/TiO_2 composite layer was varied from 40 to 200 ALD cycles (*ca.* 0.9 nm to 4.4 nm). The results presented are the average of a minimum of 3 DSC samples. Figure 6.14 shows that the TiO_2 number of cycles has a large influence in the

I-V curves and namely in the short-circuit current density (J_{sc}) and in the open circuit potential (V_{oc}). A preliminary analysis of the *I-V* curves obtained in dark conditions shows that the TiO_2 thickness has a large effect in the dark current, suggesting that recombination plays a major role in the DSCs performance.

Figure 6.15 shows the computed performance parameters (J_{sc}, V_{oc}, η, and FF) from the experimental *I-V* curves. The efficiency (η) of the DSC devices has an exponential increase with the number of TiO_2 cycles, up to 150 cycles where it reaches a maximum of 8.4 %; the η increase is driven mainly by the J_{sc}.
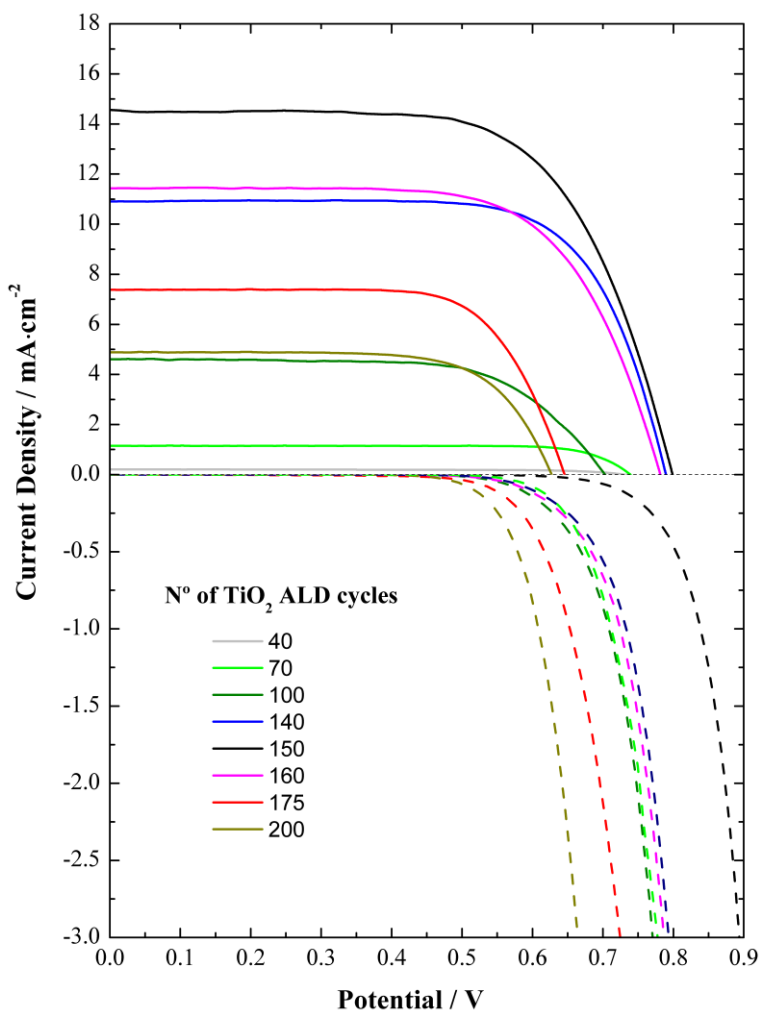

Figure 6.14 *I-V* curves obtained in light (AM 1.5 global 100 mW·cm⁻²) and dark conditions of DSCs prepared using the SiO_2/TiO_2 architecture, with varying the number of TiO_2 ALD cycles.

The minimum number of ALD cycles tested (40 cycles) resulted in very low efficient DSCs, $\eta = 0.1$ %; yet the V_{oc} and FF of this cell are relatively close to the values obtained for the optimum TiO_2 film thickness (150 ALD cycles). Hence, the reason for such low efficiency is related to the current output of the cell. Considering that the surface area of the electrode is approximately constant across all the experiments, dye loading is expected to be also approximately constant; therefore the reason for low J_{sc} should be related to the electron transport characteristics of the TiO_2 layer. Consequently increasing the number of ALD TiO_2 cycles results in enhanced electron transport characteristics.

The optimum number of ALD cycles was found to be 150, which mean *ca*. of 3.3 nm thick TiO_2 film, which cause a 6.6 nm pore size reduction. Considering 20 nm the average pore size the deposited TiO_2 film should not cause pore blockage, therefore the loss of J_{sc} and η was assigned to the inferior photoelectrode surface area and to the transport/recombination balance.
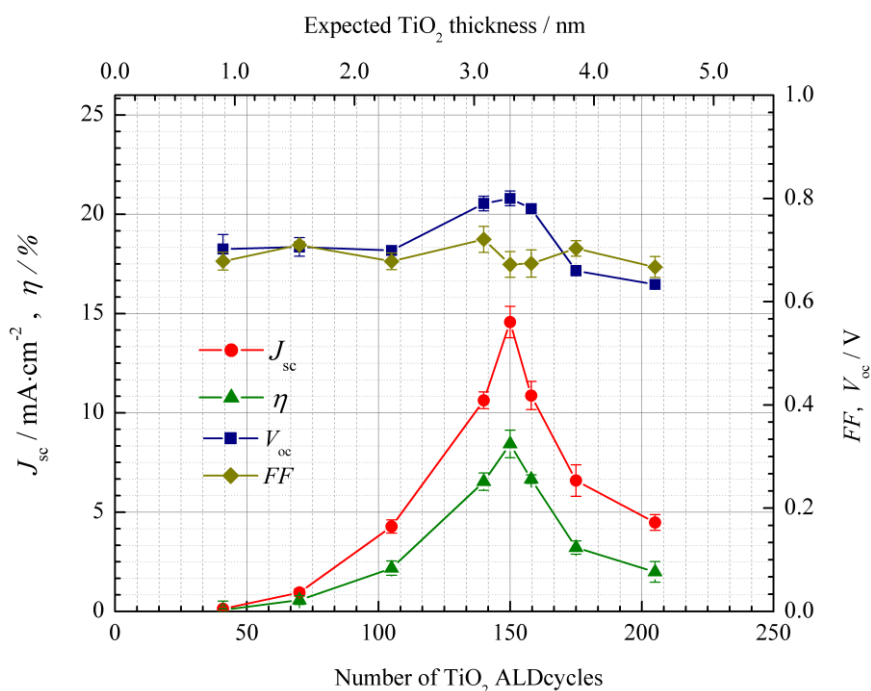

Figure 6.15 Calculated performance parameters from experimental *I-V* curves of SiO_2/TiO_2-DSCs, with TiO_2 ALD cycles ranging from 40 to 200. The error bars refer to the standard deviation of at least 3 samples.
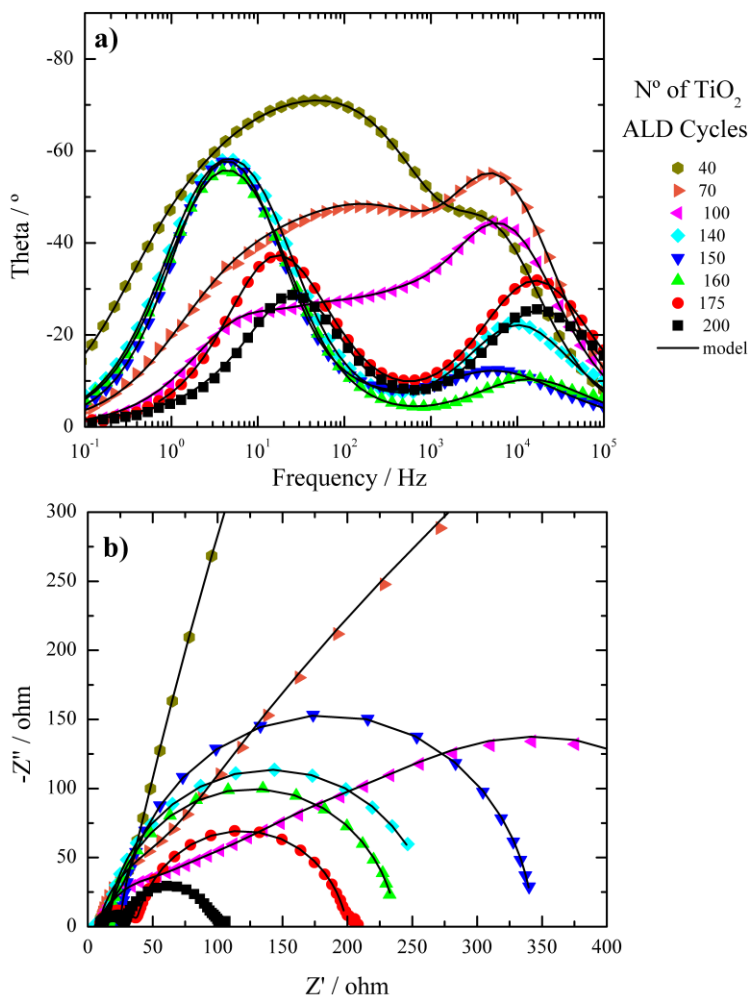
Figure 6.16 Bode (a) and Nyquist (b) plots obtained under dark conditions at the V_{oc} of the cells for a range of deposited ALD cycles of TiO₂.

Electrochemical impedance spectroscopy (EIS) was used to study the ALD TiO₂ thickness influence in recombination and transport characteristics of the prepared SiO₂/TiO₂-DSC. Figure 6.16 shows the obtained Bode (a) and Nyquist (b) plots in dark and at V_{oc}. Again, it is observed a large influence of the deposited TiO₂ film thickness in the recombination and transport properties. The Nyquist plots show semi-circles that change shape from 100 to 150 ALD cycles. Up to 100 ALD cycles, Nyquist plots show, a very large resistance associated with the electron transport resistance. To understand and quantify the influence of TiO₂ thickness on electron transport and

recombination, the EIS experimental data were fitted to an appropriate electrical analogue, namely using the transmission line model[34-37].

The computed parameters from the model fitting were used to assess transport and recombination in the DSCs based on SiO_2/TiO_2 composite photoelectrode. Electron diffusion coefficient, D_{eff}, and the recombination rate constant, k_r, were calculated according to equations presented elsewhere[6]. Figure 6.17 shows that between 140 to 200 TiO_2 deposition cycles, D_{eff} is similar and increases exponentially with the applied potential. However, for less than 140 cycles there are large differences in D_{eff} among cells and the potential influence is less pronounced.
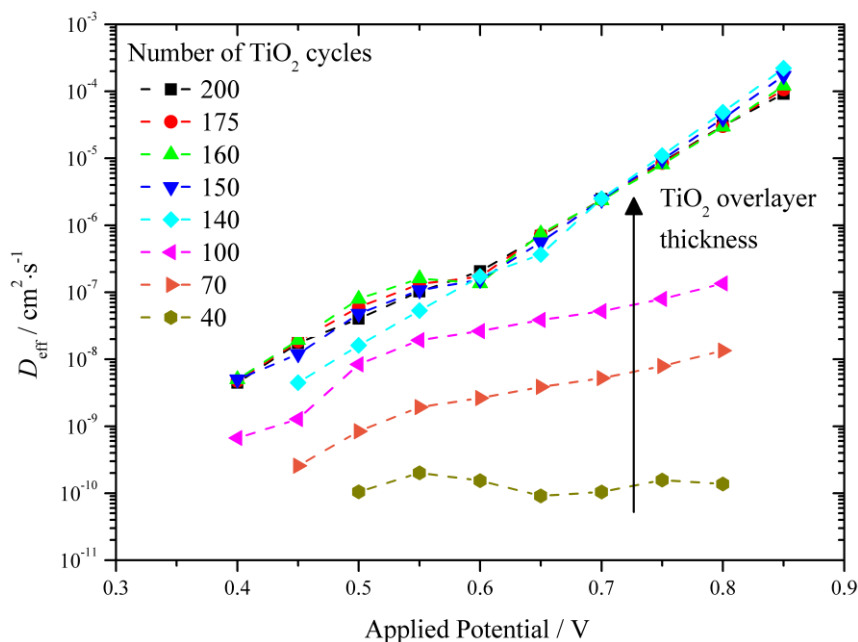
Figure 6.17 Electron diffusion coefficients, D_{eff}, as a function of the applied potential, calculated for DSCs based on SiO_2/TiO_2 composite photoelectrodes with several deposited number of TiO_2 ALD cycles.

Figure 6.18 shows k_r as a function of the applied potential for the same samples. Generally, the recombination rate increases with the potential. From 140 to 200 TiO_2 ALD cycles, recombination increases with TiO_2 thickness for all potentials; however, when analyzing recombination in SiO_2/TiO_2-DSCs with less than 140 ALD cycles, the influence of TiO_2 thickness in k_r is not clear.
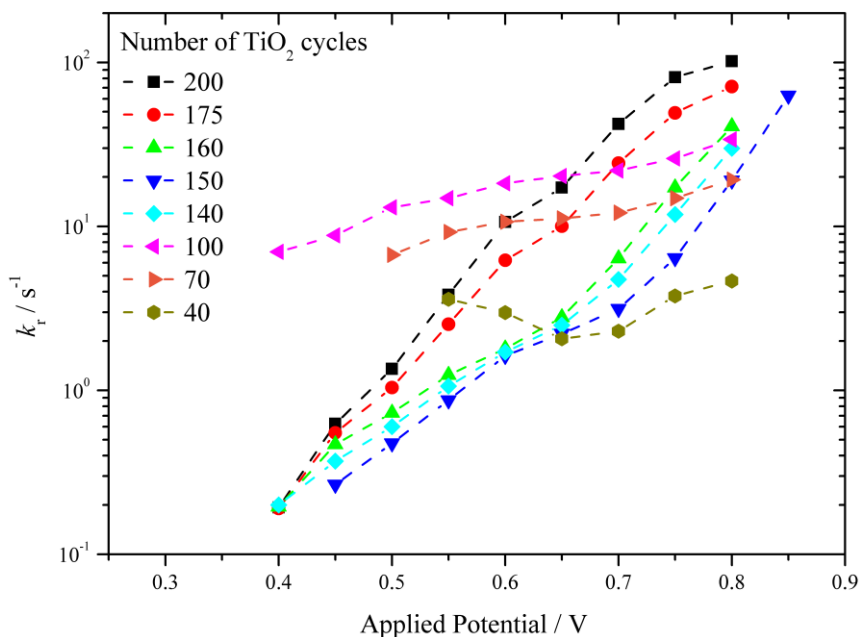
Figure 6.18 Recombination rate constants, k_r, as a function of the applied potential, calculated for DSCs based on SiO$_2$/TiO$_2$ composite photoelectrode with several deposited number of TiO$_2$ ALD cycles.

To elucidate the ALD TiO$_2$ thickness influence in recombination and transport, the electron lifetime, transport time and collection efficiency[38] (τ_{e-}, τ_{tr} and η_{cc}, respectively) were plotted at a fixed potential (0.7 V) against the number of TiO$_2$ ALD cycles. Figure 6.19 shows that up to 100 cycles, the transport time, τ_{tr} is greater than the electron lifetime, τ_{e-}; consequently the generated electrons in the SiO$_2$/TiO$_2$ porous layer tendentiously recombine before being collected, therefore the collection efficiency, η_{cc}, of the DSC is low. From the 100 cycle point on, $\tau_{e-} > \tau_{tr}$, so η_{cc} increases up to 140 cycles becoming the constant and approximately equal to 1. This shows that there is a minimum TiO$_2$ film thickness required for the efficient transport of electrons, which in the present case ranges between 3.0 nm and 3.5 nm.

Figure 6.20 allows distinguishing two regimes of operation of the SiO$_2$/TiO$_2$-DSCs. This figure shows that up to 140 ALD cycles of TiO$_2$ the prepared DSCs operate in a transport-limited regime; in this region the deposited thickness of TiO$_2$ (< 3 nm) is insufficient for efficiently transport the electrons, and D_{eff} increases exponentially with the deposition cycles of TiO$_2$. For more than 140 ALD cycles of

TiO$_2$, D_{eff} stabilizes at D_{eff} = (2.40 ± 0.05) × 10^{-6} cm$^2 \cdot$cm^{-1} at 0.7 V. This region is characterized by a constant D_{eff} and a minimum recombination rate, k_r, originating then the maximum current density, J_{sc}, and efficiency, η; in this region it is the recombination that determines the DSC efficiency. The increase of the recombination rate constant after 150 cycles could be ascribed to pore size reduction due to the excess of TiO$_2$ deposition; this originates: i) surface area decrease; ii) ionic transfer limitations and; iii) smaller surface area available for dye adsorption. The SiO$_2$ layer should display a wide range of pore sizes due to the particles assemble process. Since the average pore size of the SiO$_2$ scaffold decreases with the number of TiO$_2$ ALD deposition cycles, the smaller pores should reach a point where the bulky dye molecule hardly diffuses through, leaving uncoated surface areas. The smaller molecules of electrolyte, however, still diffuse through these small pores finding uncoated spaces where the recombination takes place, as illustrated in Figure 6.19 and Figure 6.20; this same effect was also observed by O'Regan & coauthors[39].
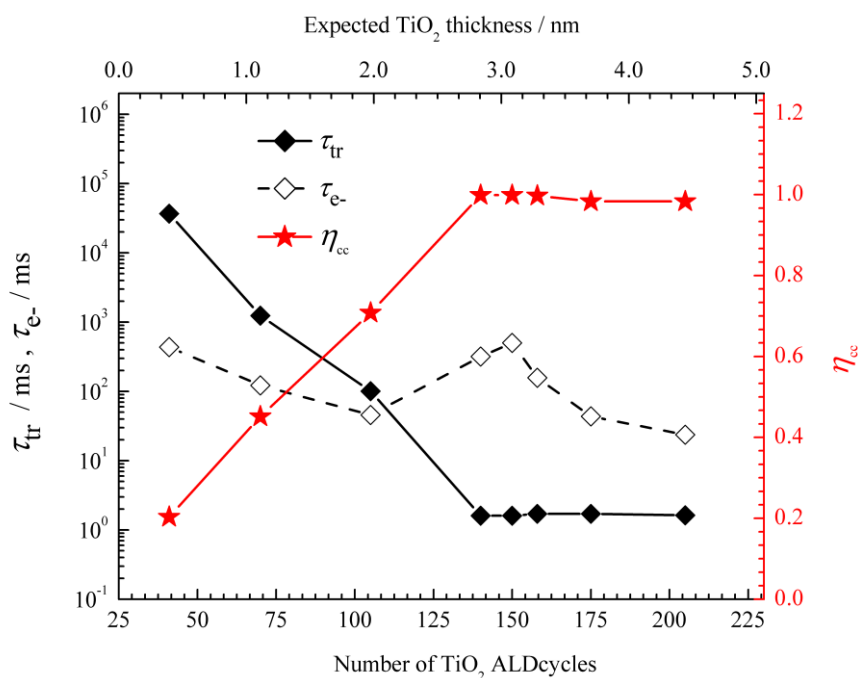

Figure 6.19 TiO$_2$ thickness influence in the electron lifetime, transport time and collection efficiency (τ_{e-}, τ_{tr} and η_{cc}, respectevely) for EIS conducted in dark conditions and at 0.7 V.
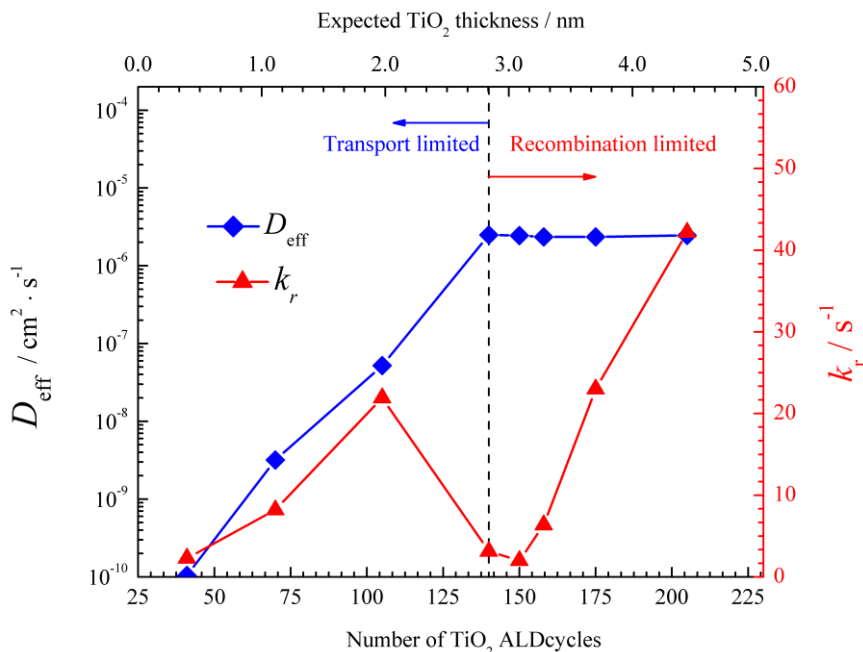
Figure 6.20 TiO$_2$ film thickness influence on transport (D_{eff},) and recombination (k_r) in the SiO$_2$/TiO$_2$-DSCs (EIS analysis conducted at dark conditions and at 0.7 V).

   DSCs prepared with the optimum amount of TiO$_2$ (150 ALD cycles, *ca*. 3.3 nm film thick) were compared with conventional cells using a nanoparticulate TiO$_2$ paste (DSL 18NR-AO, Dyesol). Figure 6.21 and Table 6.3 show *I-V* curves and the respective performance parameters in light and in dark conditions. The SiO$_2$/TiO$_2$-DSC cell shows enhanced current–density and open–circuit potential and less dark current than the reference cell. The increased current should be ascribed to the larger surface area of the porous layer (160 m^2·g^{-1} *vs*. 74 m^2·g^{-1} [40]). The increase in the V_{oc} is within the experimental error.

Table 6.3 Photovoltaic parameters of the reference DSCs and of the SiO$_2$/TiO$_2$-DSCs

Photo-electrode	Performance parameters			
	V_{oc} /V	J_{sc} / mA·cm^{-2}	FF	η / %
TiO$_2$ nanoparticle reference	0.78 ± 0.02	12.7 ± 0.1	0.71 ± 0.02	7.82 ± 0.05
SiO$_2$ / TiO$_2$	0.80 ± 0.05	14.6 ± 0.1	0.65 ± 0.04	8.43 ± 0.20

Figure 6.21 *I-V* curves of the prepared DSCs with the developed SiO_2/TiO_2 PE and a reference cell prepared with a commercial TiO_2 paste. (measurement at 1-sun, 1.5 AM illumination).
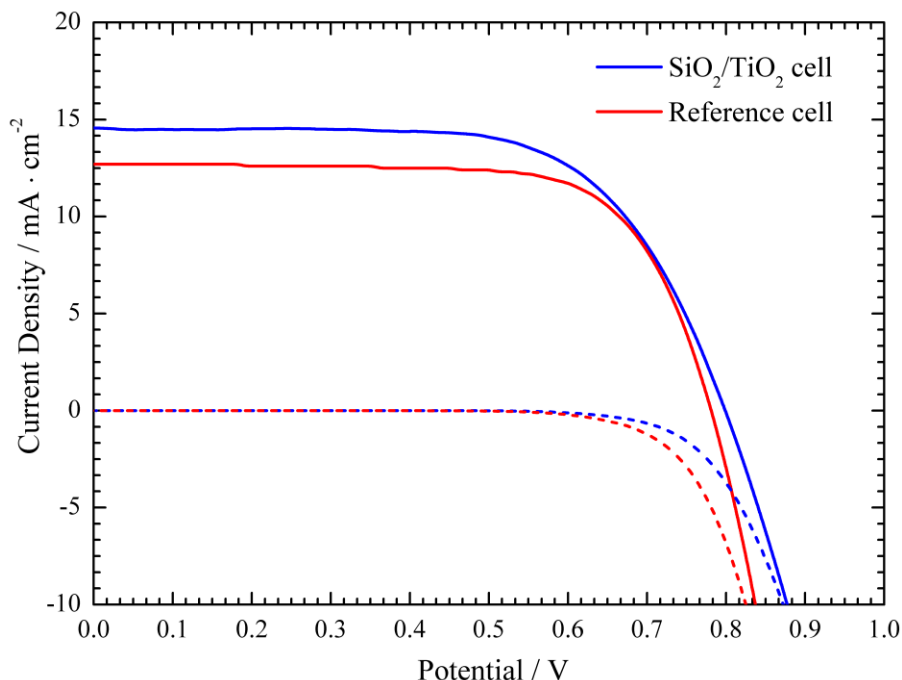
The recombination and charge transport resistances in both devices was obtained by EIS analysis at several potentials. Figure 6.22 shows the Nyquist and Bode plots for both devices at 0.8 V, 0.6 V and 0.4 V. At potentials close to the V_{oc} (0.8 V) Nyquist and Bode plots (Figure 6.22a and b) show that the difference between both cells is rather small. However, at potentials close to the maximum power point (0.6 V, (Figure 6.22c and d) there is a large difference in the second semicircle in the Nyquist plot and first frequency peak in Bode phase plot, showing that recombination resistance is lower in the reference cell at this potential. At 0.4 V, the difference is even more noticeable as the impedance spectra of the SiO_2/TiO_2-DSCs show recombination resistances orders of magnitude higher than the reference cell.

The recombination rate constants and diffusion coefficients in both devices were calculated as a function of the potential and plotted in Figure 6.23. There are two important observations: 1) electron transport, evaluated by D_{eff}, is similar between the devices; 2) electron recombination, characterized by k_r, is higher in the reference cell.

Taking into account these observations, the difference in the performance between both devices should be assigned to the electron recombination rate. Consequently, the lower recombination in the SiO₂/TiO₂-DSCs contributes, along with larger surface area, to the higher current delivered by this cell type.
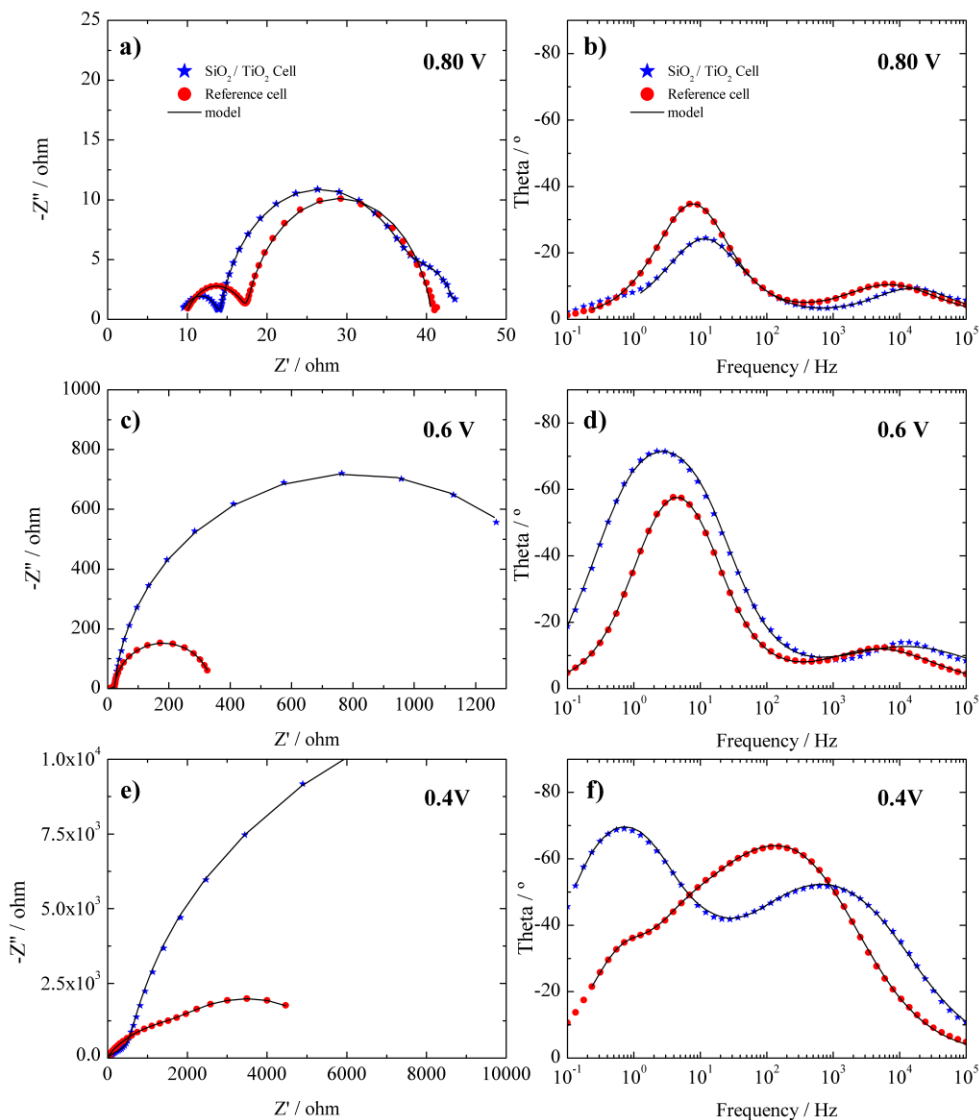

Figure 6.22 Impedance spectra obtained under dark conditions at 0.80 V, 0.6 V and 0.4 V for SiO₂/TiO₂-DSCs (150 ALD cycles of TiO₂) and reference DSCs (Dyesol® 18NR-AO TiO₂ paste).
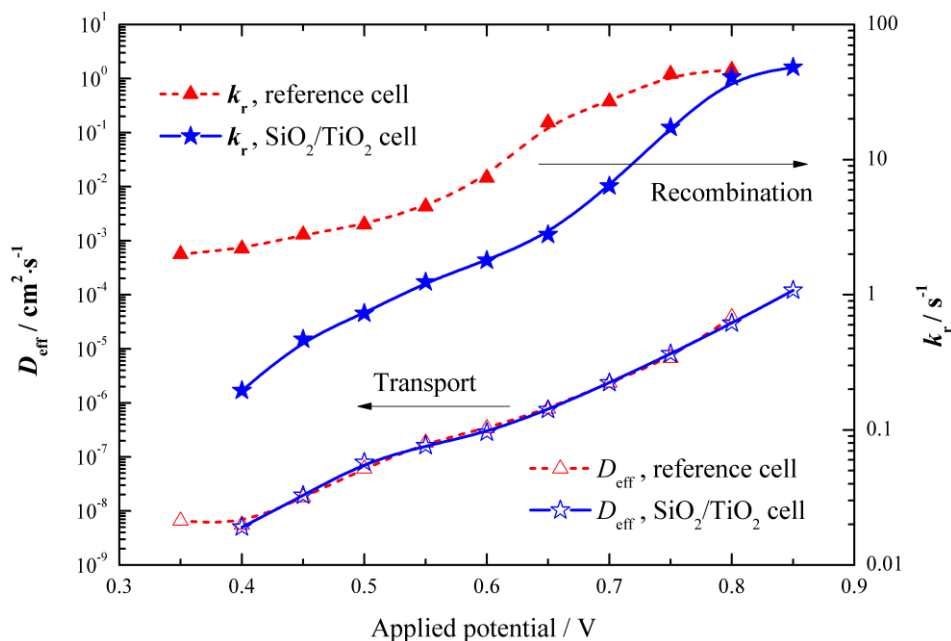
Figure 6.23 Comparison between electron transport (D_{eff},) and recombination (k_r) in the SiO_2/TiO_2-DSC (150 ALD cycles of TiO_2) and reference DSCs (Dyesol® 18NR-AO TiO_2 paste).

6.5 Conclusions

The performance of dye sensitized solar cells is ruled by two main competing processes: electron transport in the mesoporous semiconductor and recombination losses in the semiconductor/electrolyte interface. In order to increase the efficiency of DSCs, a new photoelectrode architecture is proposed that tackles the shortcomings of the usually employed TiO_2 nanoparticle films. The proposed photoelectrode employs a SiO_2 scaffold with superior surface area covered by a conformal layer of TiO_2 with *ca.* 3 nm.

The scaffold layer, made of *ca.* 15 nm SiO_2 nanoparticles, is infiltrated with a TiO_2 layer by atomic layer deposition. Due to the small size of the SiO_2 scaffold pores, the ALD process parameters had to be optimized to obtain the complete coverage of inner surface of the SiO_2 layer. The results show the reactant titanium isopropoxide (TIP) has Knudsen diffusion through the SiO_2 mesoporous layer. It was concluded that the TIP monolayer chemisorption penetration is well described by the so-called shrinking core

model. The diffusion coefficient for TIP in the fresh SiO_2 scaffold (D_{TIP}) was determined to be $(4.23 \pm 0.65) \times 10^{-3}$ cm^2·s^{-1}. Deposition cycle times of TIP of no less than 25 s are required to fully coat the 20 μm thick SiO_2 scaffold layer.

There were identified two DSC operation regimes: i) a transport limited regime, in which the TiO_2 film controls the electron transport, which is observed for film thicknesses smaller than *ca.* 3.5 nm; and ii) a recombination limited regime, where D_{eff} is constant (($2.40 \pm 0.05) \times 10^{-6}$ cm^2·s^{-1} at 0.7 V) and the DSC performance is determined by the recombination rate. The best DSC results were obtained for 150 ALD deposition cycles of TiO_2, corresponding approximately to a film thickness of 3.3 nm.

The SiO_2/TiO_2-DSC showed better energy performance than the conventional device, made with a nanoparticulated photoelectrode layer, due to enhanced current density (14.6 ± 0.1 *vs.* 12.7 ± 0.1 mA·cm^{-2}) owing to lower electron recombination and larger surface area; SiO_2/TiO_2-DSCs showed and average of $\eta = 8.43$ % *vs.* $\eta = 7.82$ % of the conventional DSC devices. The superior recombination resistance was assigned to more uniform TiO_2 photoelectrode film, which allows a better dye coverage. It must be emphasized that a *ca.* 3 nm thick ALD deposited film of TiO_2 is suitable for the electron transport of a DSC with over 8.4 % energy efficiency. The new SiO_2/TiO_2 composite layer also showed 10 % higher transmittance than the conventional mesoporous TiO_2 layer, making this PE more attractive to applications requiring semi-transparency such as building integrated photovoltaics (BIPV).

Due to the ability of ALD process to deposit a wide range of metal–oxides, the proposed photoelectrode architecture opens the doors for new materials to be tested as photoelectrodes in DSCs. Metal-oxides such as ZnO, SnO_2 and Nb_2O_5 (alone or combined with TiO_2) are examples of promising materials to serve as semiconductor layers in the proposed photoelectrode architecture.

Acknowledgements

References

1. J. Desilvestro, M. Grätzel, L. Kavan, J. Moser and J. Augustynski, *J. Am. Chem. Soc.*, 1985, **107**, 2988-2990.

2. B. O'Regan and M. Grätzel, *Nature*, 1991, **353**, 737-740.

3. E. J. W. Crossland, N. Noel, V. Sivaram, T. Leijtens, J. A. Alexander-Webber and H. J. Snaith, *Nature*, 2013, **495**, 215-219.

4. S. Mori, K. Sunahara, Y. Fukai, T. Kanzaki, Y. Wada and S. Yanagida, *The Journal of Physical Chemistry C*, 2008, **112**, 20505-20509.

5. M. Wang, P. Chen, R. Humphry-Baker, S. M. Zakeeruddin and M. Gratzel, *ChemPhysChem*, 2009, **10**, 290-299.

6. J. Maçaira, L. Andrade and A. Mendes, *Renewable and Sustainable Energy Reviews*, 2013, **27**, 334-349.

7. Q. Zhang and G. Cao, *Nano Today*, 2011, **6**, 91-109.

8. N. Tetreault and M. Gratzel, *Energy & Environmental Science*, 2012.

9. X. Gan, X. Li, X. Gao, F. Zhuge and W. Yu, *Thin Solid Films*, 2010, **518**, 4809-4812.

10. H. W. Wang, C. F. Ting, M. K. Hung, C. H. Chiou, Y. L. Liu, Z. W. Liu, K. R. Ratinac and S. P. Ringer, *Nanotechnology*, 2009, **20**, 9.

11. C. H. Lee, S. W. Rhee and H. W. Choi, *Nanoscale Research Letters*, 2012, **7**, 48.

12.   A. B. F. Martinson, M. r. S. Góes, F. Fabregat-Santiago, J. Bisquert, M. J. Pellin and J. T. Hupp, *The Journal of Physical Chemistry A*, 2009, **113**, 4015-4021.

13.   X. D. Li, D. W. Zhang, S. Chen, Z. A. Wang, Z. Sun, X. J. Yin and S. M. Huang, *Materials Chemistry and Physics*, 2010, **124**, 179-183.

14.   P. Zhong, X. Ma, X. Chen, R. Zhong, X. Liu, D. Ma, M. Zhang and Z. Li, *Nano Energy*, 2015, **16**, 99-111.

15.   J.-Y. Liao, B.-X. Lei, D.-B. Kuang and C.-Y. Su, *Energy & Environmental Science*, 2011, **4**, 4079-4085.

16.   C.-Y. Cho and J. H. Moon, *Langmuir*, 2012.

17.   Z. Zhao, G. Liu, B. Li, L. Guo, C. Fei, Y. Wang, L. Lv, X. Liu, J. Tian and G. Cao, *Journal of Materials Chemistry A*, 2015, **3**, 11320-11329.

18.   L. N. Quan, Y. H. Jang, Y. J. Jang, J. Kim, W. Lee, J. H. Moon and D. H. Kim, *ChemSusChem*, 2014, **7**, 2590-2596.

19.   N. Tétreault, É. Arsenault, L.-P. Heiniger, N. Soheilnia, J. Brillet, T. Moehl, S. Zakeeruddin, G. A. Ozin and M. Grätzel, *Nano Letters*, 2011, **11**, 4579-4584.

20.   P. Labouchere, A. K. Chandiran, T. Moehl, H. Harms, S. Chavhan, R. Tena-Zaera, M. K. Nazeeruddin, M. Graetzel and N. Tetreault, *Advanced Energy Materials*, 2014, **4**, n/a-n/a.

21.   N. Tétreault, G. von Freymann, M. Deubel, M. Hermatschweiler, F. Pérez-Willard, S. John, M. Wegener and G. A. Ozin, *Advanced Materials*, 2006, **18**, 457-460.

22.   G. F. Froment and K. B. Bischoff, *Chemical Reactor Analysis and Design*, John Wiley and Sons, 1990.

23.   O. Levenspiel, *Chemical reaction engineering*, Wiley, 1972.

24.   J. Aarik, A. Aidla, T. Uustare, M. Ritala and M. Leskelä, *Applied Surface Science*, 2000, **161**, 385-395.

25.   H.-Y. Lee, C. J. An, S. J. Piao, D. Y. Ahn, M.-T. Kim and Y.-S. Min, *The Journal of Physical Chemistry C*, 2010, **114**, 18601-18606.

26.   P. F. Lito, S. P. Cardoso, A. E. Rodrigues and C. M. Silva, *Separation & Purification Reviews*, 2015, **44**, 283-307.

27.   A. M. M. Mendes, C. A. V. Costa and A. E. Rodrigues, *Gas Separation & Purification*, 1994, **8**, 229-236.

28.   J. R. Welty, C. E. Wicks and R. E. Wilson, *Fundamentals of momentum, heat, and mass transfer*, Wiley, 1976.

29.   A. Mortensen, *Concise Encyclopedia of Composite Materials*, Elsevier Science, 2006.

30.   D. H. Kim, M. Woodroof, K. Lee and G. N. Parsons, *ChemSusChem*, 2013, **6**, 1014-1020.

31.   D.-J. Lee, K.-J. Kim, S.-H. Kim, J.-Y. Kwon, J. Xu and K.-B. Kim, *Journal of Materials Chemistry C*, 2013, **1**, 4761-4769.

32.   O. Stenzel, *The Physics of Thin Film Optical Spectra: An Introduction*, Springer Berlin Heidelberg, 2005.

33.   X. Zheng, S. Meng, J. Chen, J. Wang, J. Xian, Y. Shao, X. Fu and D. Li, *The Journal of Physical Chemistry C*, 2013, **117**, 21263-21273.

34.   J. Macaira, I. Mesquita, L. Andrade and A. Mendes, *Physical Chemistry Chemical Physics*, 2015, **17**, 22699-22710.

35.   J. Bisquert, M. Gratzel, Q. Wang and F. Fabregat-Santiago, *The Journal of Physical Chemistry B*, 2006, **110**, 11284-11290.

36.   L. Andrade, S. M. Zakeeruddin, M. K. Nazeeruddin, H. A. Ribeiro, A. Mendes and M. Grätzel, *ChemPhysChem*, 2009, **10**, 1117-1124.

37.   Q. Wang, J.-E. Moser and M. Grätzel, *The Journal of Physical Chemistry B*, 2005, **109**, 14945-14953.

38.   L. Bertoluzzi and S. Ma, *Physical Chemistry Chemical Physics*, 2013, **15**, 4283-4285.

39.   B. O'Regan, L. Xiaoe and T. Ghaddar, *Energy & Environmental Science*, 2012, **5**, 7203-7215.

40.   J. Lin, A. Nattestad, H. Yu, Y. Bai, L. Wang, S. X. Dou and J. H. Kim, *Journal of Materials Chemistry A*, 2014, **2**, 8902-8909.

CHAPTER 7

Concluding Remarks and Outlook

"One's destination is never a place, but rather a new way of looking at things"

Henry Miller

7

Concluding Remarks and Outlook

The work portrayed in this Thesis addresses relevant constraints that prevent dye-sensitized solar cell (DSC) technology to become a commercial photovoltaic (PV) solution. Regarding this matter two critical aspects were identified: device stability and solar energy conversion efficiency.

This chapter highlights the main achievements obtained. An outlook for the DSC technology and its challenges is also presented, alongside with suggestions for future research.

7.1 Main Conclusions

A broad state of the art study was conducted, revealing a vast amount of academic work done related to DSCs efficiency enhancement, but relatively scarce regarding DSC stability. Improvements in the photoelectrode (PE) were identified as the most promising route for increasing the efficiency of DSCs. The influence of the PE morphology in the DSC performance was analysed and discussed. Electron transport and recombination are key mechanisms that rule the DSC efficiency. Electrolyte leakage and the permeation of external contaminants into the cell were identified as the technology bottlenecks. Therefore, efficient encapsulation was targeted as a main goal concerning DSCs long-term stability.

Regarding stability, a new sealing process, based on laser assisted glass melting, was developed and optimized for sealing DSC devices. A response surface methodology was used to optimize the process parameters, where laser power was identified as the most important factor. The obtained empiric model relates the sealing

quality with the process parameters, and displayed good agreement with the experimental results. Glass samples sealed by the developed process passed the following international standards:

- Helium leak tests : MIL-STD-883H, "Encapsulation suitable for microcircuits for use within military and aerospace electronic systems" ;
- Thermal cycling tests : IEC 61646, "International standard for thin-film terrestrial PV modules";
- Shear strength tests: ISO 13445, "Adhesives - Determination of shear strength of adhesive bonds between rigid substrates by the block-shear method"; and EN 1279-4, "Glass in Buildings - Insulating glass units, requirements for sealants".

Though none of these standards address specifically DSCs, it is expected that an encapsulated cell meeting the above requirements endure 20 years of leak free operation. The laser sealing process takes place at 330 ℃, which is lower than the maximum tolerable temperature of commonly employed materials in the photoelectrode (PE) and counter electrode (CE) layers of DSC devices, *i.e.* titanium dioxide (~ 500 °C) and platinum (~ 450 °C) in the PE and CE respectively. *I-V* characteristics and electrochemical impedance spectroscopy analysis (EIS) were used to characterize the laser sealed DSCs, demonstrating that the sealing process had no influence in performance.

Laser assisted glass frit sealed DSCs were tested for stability against DSCs sealed with the commonly employed sealant (Surlyn® polymer). Accelerated aging was carried out during 1000 hours of continuous illumination (765 W·m^{-2}), temperature between 60 and 65 ℃, and electrical resistive load close to the cells operating maximum power point (~ 0.6 V). The periodic PV characterization showed excellent stability results for laser sealed devices, with minimal efficiency loss (-2.4%). As for Surlyn® sealed cells degradation onset after *ca*. 400 hours, and at the end of the test they presented 34 % efficiency degradation. EIS analysis showed that the increase of series resistances (R_s) and recombination rate are the main causes of performance loss in Surlyn® sealed cells. In turn, laser sealed cells showed nearly no R_s degradation (-3.9

%) and less recombination (+3% in electron lifetime, τ_{e-}) after 1000 h of test, contributing to their performance stability. The results showed that, contrary to Surlyn® sealant, the developed laser assisted glass frit sealing process guarantees efficient encapsulation for DSC cells, therefore providing the necessary durability of the devices.

Temperature, alongside with solar irradiance, is the most important operating factor of PV devices. Temperature influence in DSC performance was assessed for a wide range of temperatures, from -5 ºC up to 105 ºC. Within this temperature range, the laser sealed DSCs did not show any degradation and displayed full efficiency reversibility at 25 ºC. Temperature has an overall negative effect on the DSC performance; this effect was shown to be caused by the total electron/electrolyte recombination process that is enhanced by temperature. The temperature influence in the recombination reaction was quantified for SnO_2-F/electrolyte and TiO_2/electrolyte interfaces. The results showed that the energy level of electrons significantly affects the recombination reaction rate: when electrons are in a higher energy level (*i.e.* TiO_2 conduction band, CB) the driving force for recombination is lower comparing with lower energy level electrons (*i.e.* SnO_2-F conduction band). Thus, the activation energy was lower for the recombination taking place at TiO_2 interface (0.47 eV) than SnO_2-F (0.66 eV) interface with electrolyte. The Arrhenius plots for recombination rates in DSCs showed two different activation energies for temperatures below and above *ca.* 40 ºC. It was proposed a shift in the dominant recombination pathway from trapped electrons/electrolyte to CB electrons/electrolyte to explain the different activation energies. This work shows that electron recombination highly depends on the cell operating temperature but also on the semiconductor interfaces present in the solar cell.

Increasing the solar to energy conversion efficiency of DSCs requires a fundamental understanding of the solar cell operation mechanisms. Phenomenological modeling was used as a simulation tool to assess the two processes that rule the performance of DSCs: electron transport and recombination. The effect of the recombination reaction rate constant, k_r, and the electron diffusion coefficient, D_{eff}, in the collection efficiency, η_{cc}, of the DSC was discussed. The influence of k_r in the open-circuit voltage (V_{oc}) and short-circuit current density (J_{sc}) of DSCs has been

determined and has been shown to be highly dependent on the recombination reaction kinetics considered in the model. It was also shown that the optimum PE thickness varies logarithmically with k_r and with D_{eff}, showing that the thickness of the photoactive layer should be carefully designed for developing high efficiency DSCs.

In order to increase the efficiency of DSCs, a new photoelectrode architecture was explored that tackles the shortcomings of the usually employed TiO_2 nanoparticulated films. The new PE employs a SiO_2 scaffold layer with superior surface area than commercial TiO_2 films, covered by a thin nanometric film of TiO_2.

The scaffold layer is composed by SiO_2 nanoparticles of *ca.*15 nm and has surface area of *ca.* 160 $m^2 \cdot g^{-1}$. This film hosts a thin TiO_2 film deposited by atomic layer deposition (ALD). Due to the small pore size of the SiO_2 film, the ALD process parameters had to be optimized for complete coverage of the inner surface area of the SiO_2 layer. The results showed that titanium isopropoxide (TIP) has Knudsen diffusion through the SiO_2 mesoporous layer, and that the shrinking core model can predict the pulse time required for complete TiO_2 coverage. The diffusion coefficient for TIP in the SiO_2 scaffold (D_{TIP}) was determined to be $(4.23 \pm 0.65) \times 10^{-3}$ $cm^2 \cdot s^{-1}$ and the minimum TIP pulse time for complete SiO_2 coverage with the TiO_2 film was 25 s.

Two DSC operating regimes were determined based on the number of cycles deposited in the inner surface area of the SiO_2 layer:

1) < 140 cycles (*ca.* 3 nm): transport limited regime showing that the minimum TiO_2 thickness required for efficient transport of electrons ranged between 3.5 and 4 nm.

2) > 140 ALD cycles: recombination limited regime, where D_{eff} is constant $((2.40 \pm 0.05) \times 10^{-6}$ $cm^2 \cdot s^{-1}$ at 0.7 V) and efficiency is highly dependent on the recombination rate.

The best DSC results using the developed SiO_2/TiO_2 PE architecture used 150 ALD cycles which is *ca.* 3.3 nm thick film of TiO_2. The SiO_2/TiO_2-DSCs showed better overall PV performance than reference DSCs using a commercial TiO_2 paste: (8.43 ± 0.20) % *vs.* (7.82 ± 0.05) % and 10 % higher transmittance in the visible range. The increase in efficiency was ascribed to enhanced current density $(14.6 \pm 0.12$ *vs.* 12.7 ± 0.08 mA·cm^{-2}) due to lower electron recombination and higher surface area. The

superior recombination resistance characteristics were attributed to lower morphological defects and better dye coverage in the TiO_2 ALD layer.

The TiO_2 thin film displayed the same transport capabilities but less recombination rates than conventional TiO_2 nanoparticle films. Its effectiveness in preparing high efficient DSCs depends only on appropriated scaffold films (*i.e*. large surface area) and careful optimization of the ALD process (precursor pulse time and number of cycles). The proposed architecture considers a SiO_2 scaffold and coated with a very thin film (*ca*. 3.3 nm) of TiO_2 as semiconductor; therefore, it is expected that the overall material costs for fabricating the proposed architecture are lower than when using pure TiO_2 nanoparticle films. The higher transmittance than the conventional mesoporous TiO_2 layer, makes the new PE more attractive to applications requiring semi-transparency such as building integrated photovoltaics (BIPV).

7.2 Outlook for dye-sensitized solar cells

In 1991 O'Regan and Grätzel showed that dye sensitized solar cells could become a potential competitor to other photovoltaic technologies[1]. Since then, the DSC technology has struggled to stand out in the PV market mainly due to stability constraints. The work portrayed in this thesis has brought a realistic solution to this problem. The developed laser assisted glass sealing produces hermetic devices that are stable under standard and extreme operating conditions. An interesting extension of the laser assisted sealing is the adaptation of the process for sealing perovskite solar cells (PSCs). PSCs are solid-state mesoscopic solar cells that employ an extremely efficient sensitizer, $CH_3NH_3PbI_3$, coupled with a solid hole transport material (HTM). The high absorption of the perovskite film allowed ramping efficiencies from 3.81 % in 2012 to an impressive 20.1 % in 2015, making this technology a serious competitor to silicon based solar cells[2,3]. However, PSC technology has yet to prove its stability in standard operating conditions and at elevated temperatures[4]. With a certified efficiency of 20.1 %, PSCs future challenge will be its durability and stability, therefore making any

suitable encapsulation method extremely valuable. The developed laser assisted sealing should be adapted for sealing this type of devices; in particular the sealing temperature (330 ºC) should be lowered at least to *ca*. 120 ºC. The use of a similar laser system combined with an extremely low melting glass frit, alongside appropriate optimization of the process parameters should allow sealing at $\leq$ 120 ºC where the PSCs inner components are not damaged.

Concerning the fundamental understanding of the DSC operation, the used phenomenological modeling was proven to be an invaluable tool for optimizing the photoelectrode thickness in DSCs using commercial TiO_2 films. It would be particularly interesting to use the model to simulate the DSC operation using the newly developed SiO_2/TiO_2 photoelectrode. The results should allow optimizing the PE thickness and SiO_2 size in the new DSC architecture and study opportunities to increase conversion efficiency. Another important addition to the model should be the influence of temperature. Chapter 4 shows that temperature has a preponderant effect in the electron recombination reaction rate; in turn this process rules the overall efficiency dependence on temperature. The obtained experimental data allowed extracting the activation energies for the recombination reaction in TiO_2/electrolyte and SnO_2-F/electrolyte interfaces. This effect is not taken into account in the phenomenological model and should be included in the future. With this new feature, the model can accurately predict the DSC behavior in more real operating conditions. Furthermore, the recombination reaction activation energy should be determined for the new SiO_2/TiO_2 architecture. Assessing different metal oxides in place of TiO_2 it should be possible to determine the metal oxide (or combination of different metal oxides) that have the highest activation energy for recombination and electrical conductivity and a suitable conduction band energy position. Promising metal-oxides that can be processed by ALD include ZnO, SnO_2 and Nb_2O_5. Doped metal-oxides that should yield higher electrical conductivities than TiO_2 are AZO and TZO (ZnO doped with aluminum or titanium, respectively) [5, 6] and Nb-TiO_2 (niobium doped TiO_2)[7] .

Finally, a promising route to enhance the efficiency of the developed SiO_2/TiO_2 architecture is the substitution of the iodide redox electrolytes by cobalt redox

mediator. This new electrolyte shows negligible visible light absorption and is less aggressive than iodine towards metallic conductors, such as Ag, Au and Cu, allowing them to be used as current collectors in DSC modules. Most importantly cobalt redox electrolyte have larger redox potential than iodine based electrolytes, allowing open circuit voltages of *ca*. 1 V to be obtained[8,9]. Unfortunately, cobalt based electrolytes show recombination rates several orders of magnitude higher than iodine based electrolytes[10]; this led to the substitution of standard ruthenium dyes and to the molecular design of new dyes (such as zinc porphyrin dyes, silyl-anchor dye and carboxy-anchor dyes) that retard electron/electrolyte recombination given their better surface coverage of the TiO_2 nanoparticles[11, 12]. Although these dyes resulted in record efficient DSCs (12 % to 14 %) they require complex multi-step preparation processes that can hinder the promise of low cost PV solution by DSCs. The new SiO_2/TiO_2 photoelectrode showed exceptional electron recombination resistance compared to their nanoparticle counterparts; therefore it would be very interesting to see whether standard ruthenium dyes in combination with cobalt redox mediators would work well on this architecture, avoiding in this way the zinc porphyrin dyes which have prohibitive high manufacturing costs.

References

1. B. O'Regan and M. Grätzel, *Nature*, 1991, **353**, 737-740.

2. N. J. Jeon, J. H. Noh, W. S. Yang, Y. C. Kim, S. Ryu, J. Seo and S. I. Seok, *Nature*, 2015, **517**, 476-480.

3. H. Zhou, Q. Chen, G. Li, S. Luo, T.-b. Song, H.-S. Duan, Z. Hong, J. You, Y. Liu and Y. Yang, *Science*, 2014, **345**, 542-546.

4. G. Niu, X. Guo and L. Wang, *Journal of Materials Chemistry A*, 2015.

5. D.-J. Lee, K.-J. Kim, S.-H. Kim, J.-Y. Kwon, J. Xu and K.-B. Kim, *Journal of Materials Chemistry C*, 2013, **1**, 4761-4769.

6. T. Tommi and K. Maarit, *Semiconductor Science and Technology*, 2014, **29**, 043001.

7. A. K. Chandiran, F. d. r. Sauvage, M. Casas-Cabanas, P. Comte, S. M. Zakeeruddin and M. Graetzel, *The Journal of Physical Chemistry C*, 2010, **114**, 15849-15856.

8. S. M. Feldt, E. A. Gibson, E. Gabrielsson, L. Sun, G. Boschloo and A. Hagfeldt, *Journal of the American Chemical Society*, 2010, **132**, 16714-16724.

9. J.-H. Yum, E. Baranoff, F. Kessler, T. Moehl, S. Ahmad, T. Bessho, A. Marchioro, E. Ghadiri, J.-E. Moser, C. Yi, M. K. Nazeeruddin and M. Grätzel, *Nat Commun*, 2012, **3**, 631.

10. L. E. Polander, A. Yella, B. F. E. Curchod, N. Ashari Astani, J. Teuscher, R. Scopelliti, P. Gao, S. Mathew, J.-E. Moser, I. Tavernelli, U. Rothlisberger, M. Grätzel, M. K. Nazeeruddin and J. Frey, *Angewandte Chemie International Edition*, 2013, **52**, 8731-8735.

11. A. Yella, H.-W. Lee, H. N. Tsao, C. Yi, A. K. Chandiran, M. K. Nazeeruddin, E. W.-G. Diau, C.-Y. Yeh, S. M. Zakeeruddin and M. Grätzel, *Science*, 2011, **334**, 629-634.

12. K. Kakiage, Y. Aoyama, T. Yano, K. Oya, J.-i. Fujisawa and M. Hanaya, *Chem. Commun.*, 2015.

APPENDIX

Appendix A. Design of Experiments: Design matrix with coded and actual values

Appendix B. Developed LabVIEW control panel interfaces

Appendix C. Atomic layer deposition (ALD) operation details

Appendix D. Estimation of minimum TIP pulse time for complete coverage of SiO_2 scaffold layer with TiO_2

Appendix A. Design of Experiments: Design matrix with coded and actual values

For the design of experiments performed in Chapter 2, a three factor central composite design was built with three center points – Table 2.3, Chapter 2. The design matrix is presented in Table A1 where for each run the coded factors (X_i) ranging from -1 to +1 were computed from the actual values (x_i), middle value and the semi-variation interval as presented in Eq. 2.1.

Table A1. Design matrix with coded and actual values

Run #	Coded Values			Actual Values		
	X_1	X_2	X_3	x_1 (ºC)	x_1(W)	x_3 (mm.s^{-1})
1	1.0	1.0	-1.0	330	50	300
2	1.0	-1.0	-1.0	330	20	500
3	1.0	1.0	-1.0	330	50	500
4	1.0	-1.0	-1.0	330	20	300
5	1.0	0.0	0.0	330	35	400
6	1.0	-1.0	1.0	330	20	300
7	1.0	1.0	1.0	330	50	500
8	1.0	-1.0	1.0	330	20	500
9	1.0	1.0	1.0	330	50	300
10	0.0	0.0	-1.0	305	35	400
11	0.0	0.0	0.0	305	35	400
12	0.0	0.0	0.0	305	35	400
13	0.0	0.0	0.0	305	35	300
14	0.0	0.0	0.0	305	35	500
15	0.0	1.0	0.0	305	50	400
16	0.0	0.0	0.0	305	35	400
17	0.0	-1.0	0.0	305	20	400
18	0.0	0.0	0.0	305	35	400
19	0.0	0.0	0.0	305	35	400
20	0.0	0.0	1.0	305	35	400
21	-1.0	-1.0	-1.0	280	20	300
22	-1.0	1.0	-1.0	280	50	500
23	-1.0	1.0	-1.0	280	50	300
24	-1.0	-1.0	-1.0	280	20	500
25	-1.0	0.0	0.0	280	35	400
26	-1.0	1.0	1.0	280	50	300
27	-1.0	-1.0	1.0	280	20	500
28	-1.0	1.0	1.0	280	50	500
29	-1.0	-1.0	1.0	280	20	300

Appendix B. Developed LabVIEW Control panel interfaces
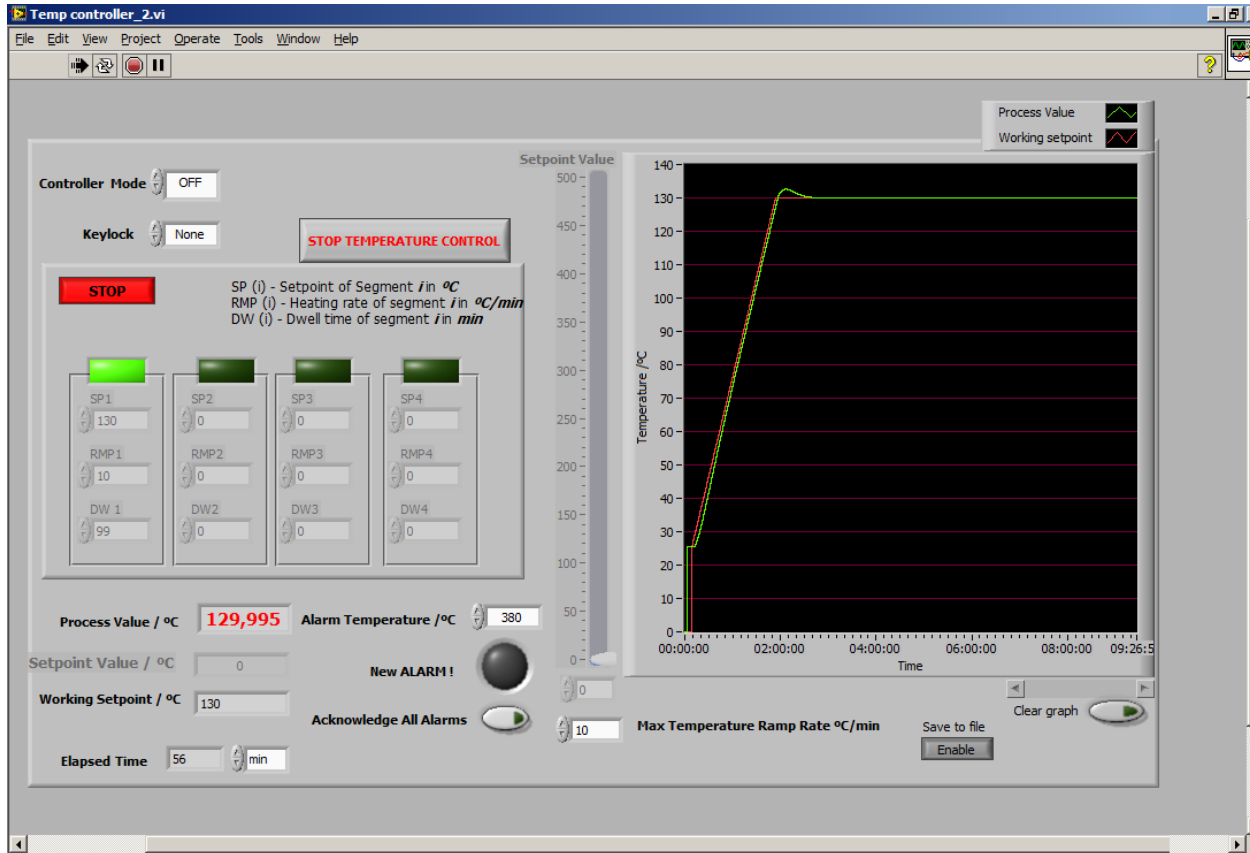

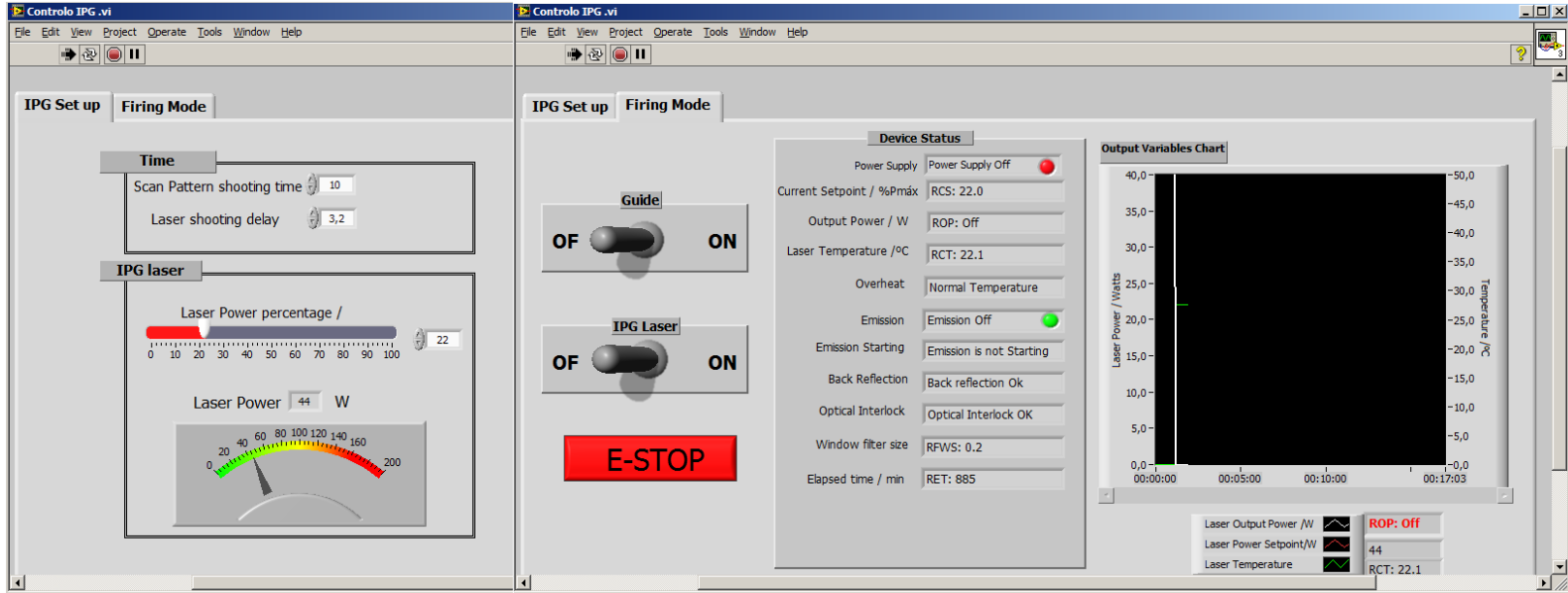**Figure B.1** LabVIEW control panel interface of the LaserBox heating plate.

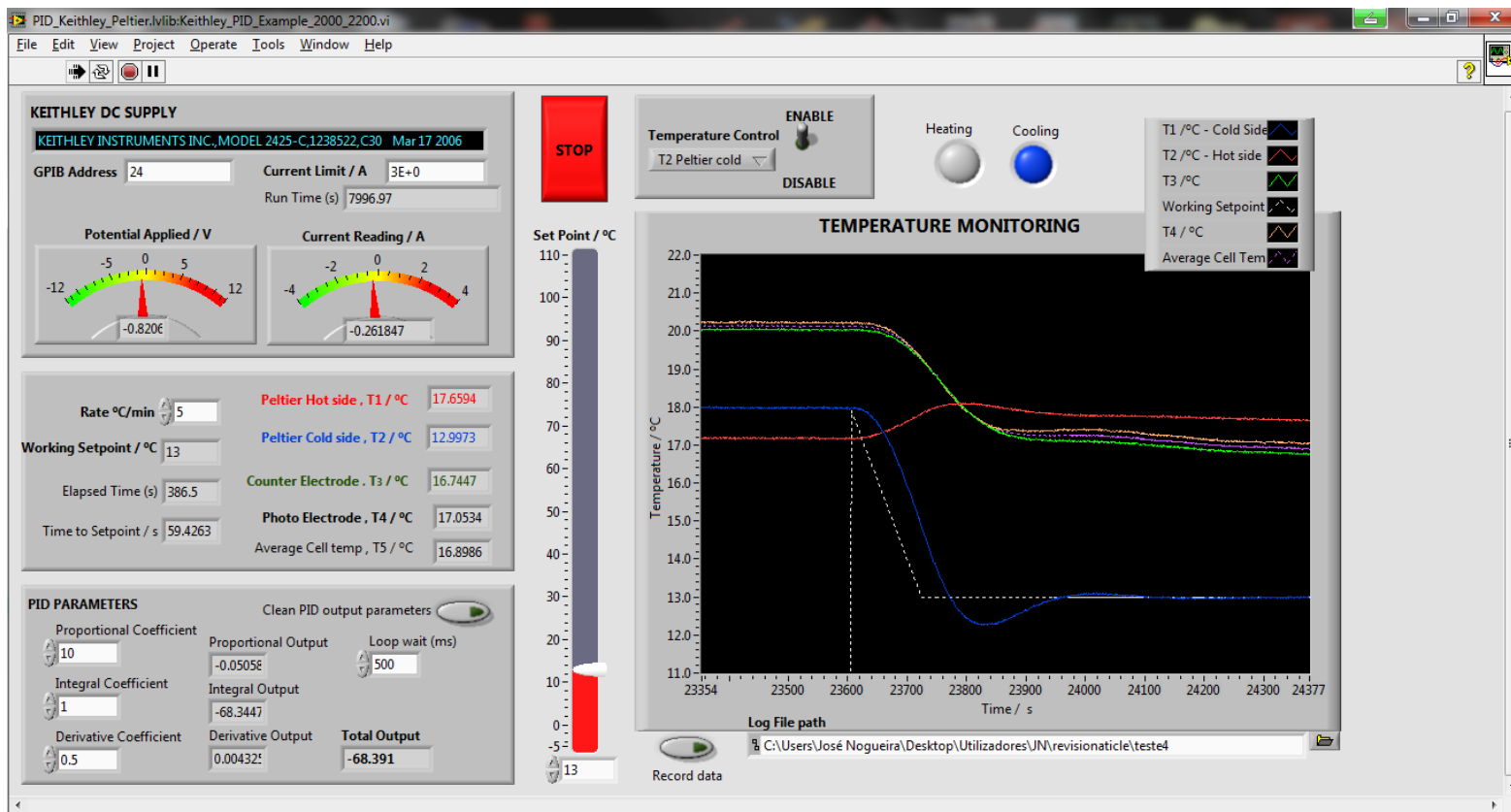**Figure B.2** LabVIEW control panel interface of the LaserBox IPG laser.

Figure B.3 LabVIEW control panel interface for the temperature control of an under illumination DSC.

Appendix C. Atomic layer deposition (ALD) operation details

The ALD relies on surface reactions that require precursors to diffuse and chemically adsorb in monolayer to the target surface. Therefore, it is essential that there is no gas mixture between both precursors in the reactor volume. The ALD deposition was conducted with a Beneq TFS 200 system. Figure C.1 sketches the experimental setup. The main elements of the ALD device comprise the carrier gas flow system, precursor containers, vacuum chamber, reaction chamber and a vacuum pump (Alcatel Adixen 2033C2). The ALD deposition is conducted using constant flow of nitrogen as carrier gas. The nitrogen feed is divided into two lines, in which the flowrate is controlled by two mass flow controllers (MFC-R and MFC-C). MFC-C controls nitrogen that flows through the vacuum chamber and MFC-R controls the flow used as carrier gas to the reactor. Nitrogen flowrates set by MFC-R and MFC-C determine the base pressures of the reactor and vacuum chamber.

During a typical operation, nitrogen is fed to the vacuum chamber that encloses the reactor. The reactor has a small aperture to the vacuum chamber and only the reactor is connected to the vacuum pump, as illustrated in Figure C.1. Therefore MFC-C sets the nitrogen flow, and then the pressures at the vacuum chamber and at the reactor; the pressure at the vacuum chamber is always higher than at the reactor. This prevents the precursors from escaping the reactor to the vacuum chamber. The vacuum pump is separated from the reactor by two pneumatic valves: DV-P1 for large flowrates and DV-P2 for accurate flowrate control. Between the reactor and DV-P1 and DV-P2, a particle filter is installed to prevent any solids to flow into the vacuum pump.

The precursors are enclosed in temperature controlled steel canisters that are connected to the flow system through hand valves and pneumatic valves. Each precursor has its carrier feeding line after MFC-R, and each one is connected to the reactor (represented as light blue for TIP and green tubing for H_2O). Each precursor can flow to the reaction chamber based on its vapor pressure or driven using a carrier gas. In the first mode, the precursor is pulsed into the reactor by opening the pneumatic pulsing valves (DV-PL1 for H_2O, or DV-PH1 for TIP). This mode requires that the precursors have a vapor pressure higher than the working pressure of the reactor. When

the precursor vapor pressure is lower than the reactor pressure, the carrier assisted mode is used: the carrier gas is pressurized inside the container (DV-BL1 for H_2O and DV-BH1 and DV-BHA1 for TIP) and pulsed (DV-PL1 for H_2O, or DV-PH1 for TIP) to the reactor.
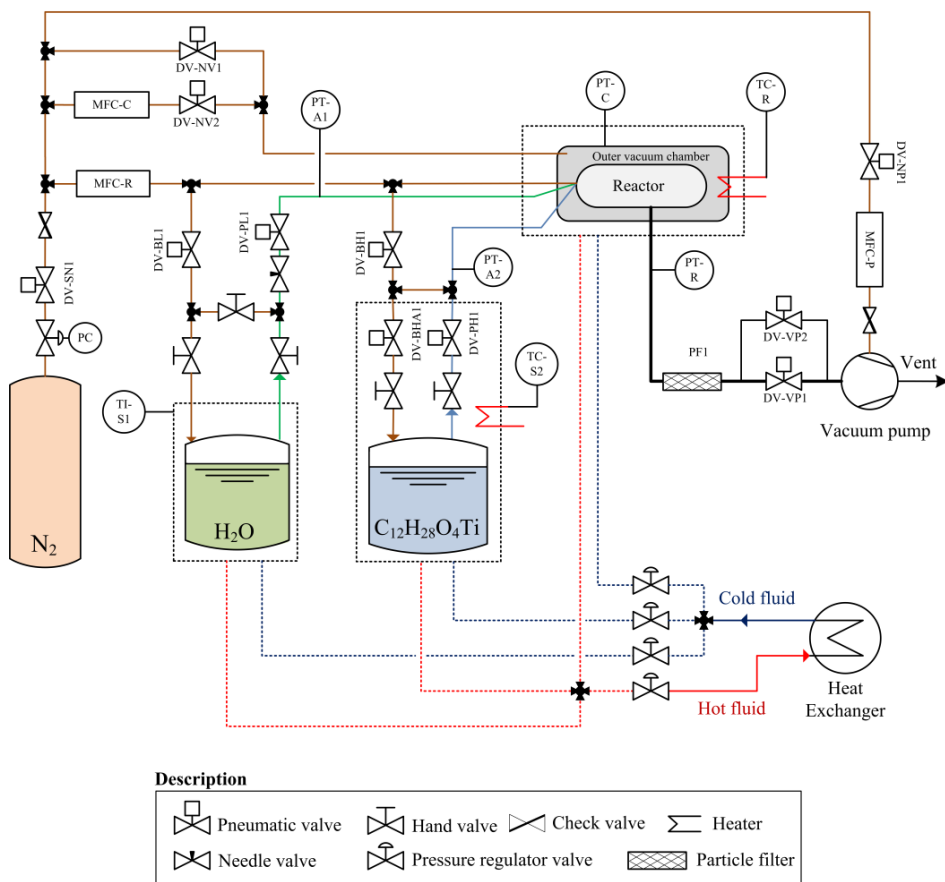

Figure C.1 Sketch of the experimental setup for the atomic layer deposition process of TiO_2 using titanium isopropoxide and water.

Figure C.2 shows the vapor pressure of TIP and H_2O as a function of temperature, calculated using the Antoine equation[1]. Because of its high vapor pressure at room temperature (~20 mbar @ 20 °C), H_2O was pulsed using its own vapor pressure (TI-S1 = 20 °C). In turn, since the TIP has a much lower vapor pressure at room temperature, the temperature of the TIP container was set to 50 °C (TC-SC2), where the pressure

vapor is *ca.* 1 mbar, and the carrier gas mode had to be used (charging time of $\Delta t_{\text{TIP},1} =$ 1 s).
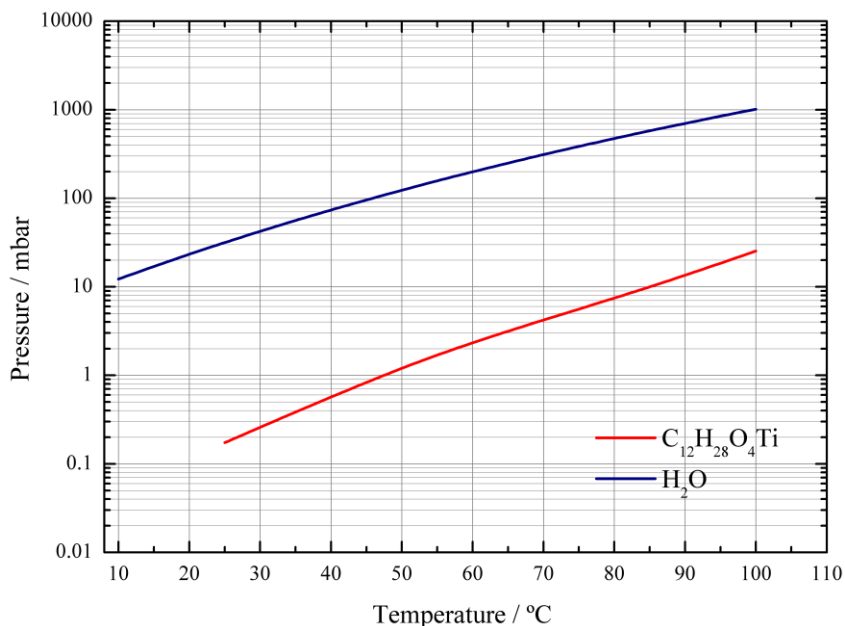

Figure C.2 Vapor pressure of water and titanium (IV) isopropoxide dependence with temperature. Values were determined using Antoine equation with coefficients given in reference [A1].

Figure C.3 illustrates the experimental procedure used for the atomic layer deposition of TiO_2. The procedure involves sequential pulsing/purging of each precursor into the reaction chamber. Each cycle comprises the following steps: pulse TIP; purge TIP; pulse H_2O and purge H_2O. The sequence is repeated *n* times to obtain the desired TiO_2 thickness.
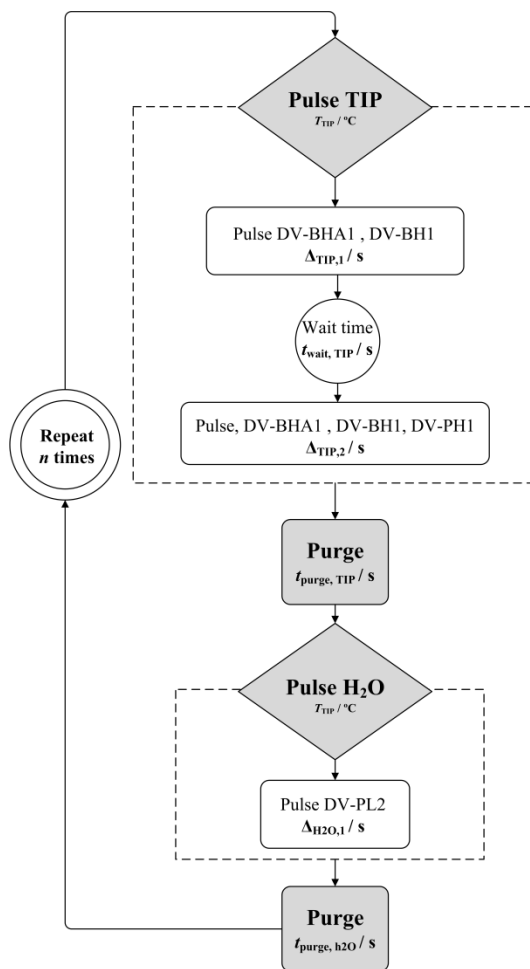
Figure C.3 Schematic representation of the ALD process operation according to the experimental setup presented in Figure C1.

Table C1 shows the operating variables used for the deposition of TiO_2 on FTO substrates. The TIP to water pulse time ratio, the TIP to water purge time ratio and the water purge to pulse time ratio were kept constant:

$$\frac{\Delta t_{TIP,2}}{\Delta t_{H2O,1}} = 2 \tag{C.1}$$

$$\frac{t_{purge,TIP}}{\Delta t_{TIP,2}} = 10 \tag{C.2}$$

$$\frac{t_{purge,H2O}}{\Delta t_{H2O,1}} = 3 \tag{C.3}$$

Table C.1 ALD process conditions for TiO$_2$ deposition on FTO glasses using C$_{12}$H$_{28}$O$_4$Ti (TIP) and H$_2$O as metal and oxidizing sources, respectively.

Process unit	Description	Variable	units	value
Reactor/vacuum chamber	flowrate (chamber)	MFC-C	cm$^3 \cdot$s^{-1}	10
	flowrate (reactor)	MFC-R	cm$^3 \cdot$s^{-1}	5
	temperature	TC-R	ºC	225
	working pressure	PT-V1	mbar	1
TIP source	temperature	TC-S2	ºC	50
	charge time	$\Delta t_{TIP,1}$	s	1
	pulse time	$\Delta t_{TIP,2}$	s	2
	purge time	$t_{purge, TIP}$	s	20
H$_2$O source	temperature	TI-S1	ºC	20
	pulse time	$\Delta t_{H2O,1}$	s	1
	purge time	$t_{purge, H2O}$	s	3

Figure C.4 shows the pressure history for the operating variables shown in Table C.1. The base pressures of the reactor and of the vacuum chamber were constant, respectively 1.2 and 5.4 mbar. The alternate pulse of TIP and water originate pressure pulses of *ca*. 11 and 23 mbar, respectively; these values are in line with the water vapor pressure at 20 ºC and with TIP vapor pressure at 50 ºC added of the carrier gas overpressure.
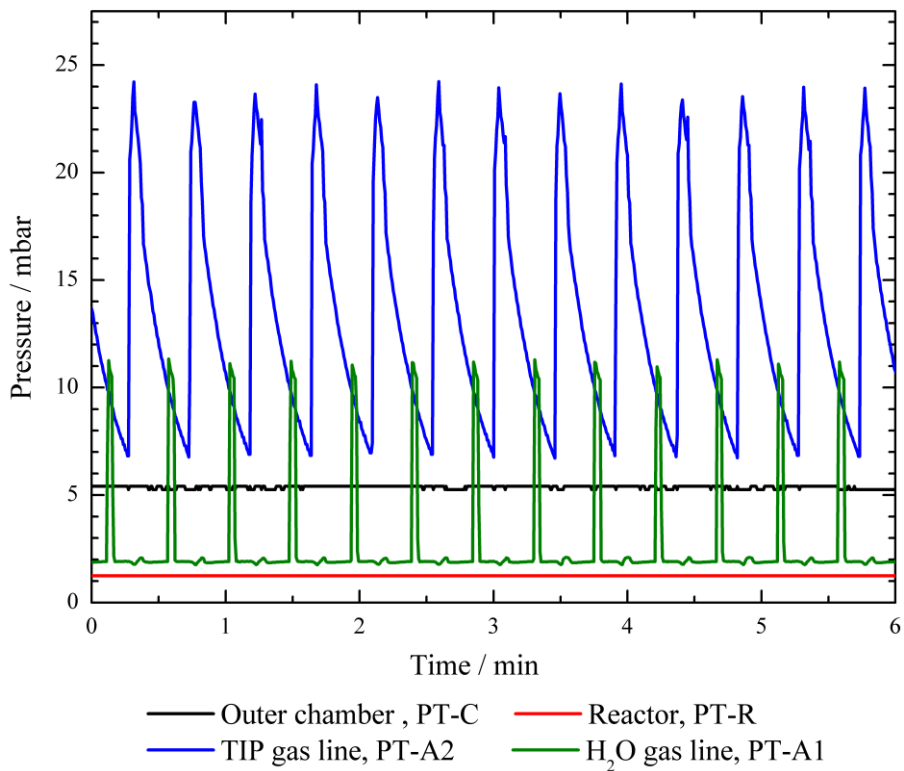
Figure C.4 Pressure monitoring during ALD operation. The process parameters are detailed in Table C.1

Appendix D. Estimation of minimum TIP pulse time for complete coverage of SiO$_2$ scaffold layer with TiO$_2$ film

Figure D.1. shows the N$_2$ adsorption/desorption isotherms obtained for the SiO2 nanoparticle powder. The BET surface area and BHJ average pore sizes are also presented.
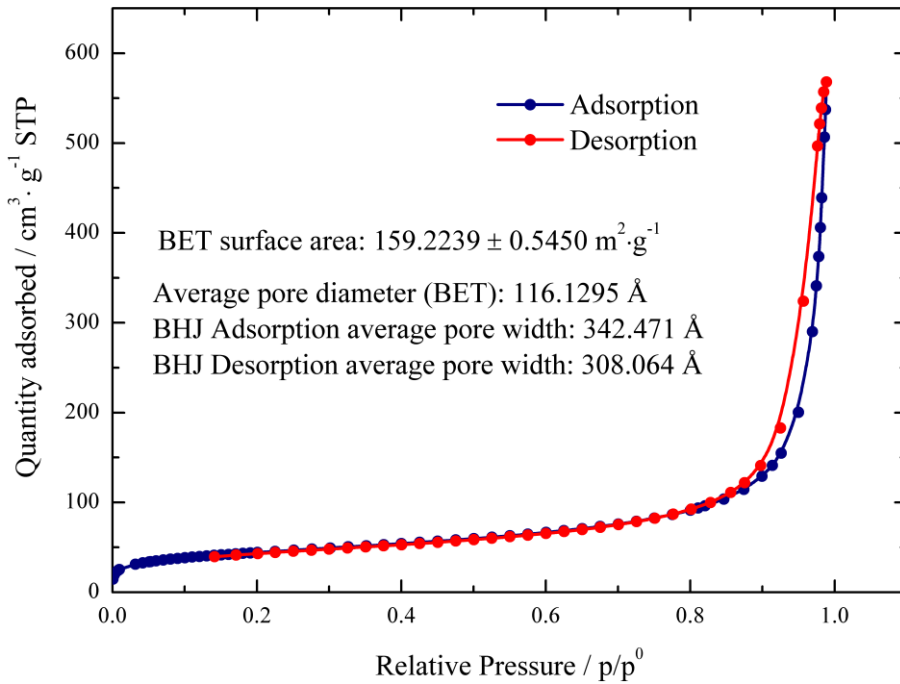

Figure D.1 Nitrogen adsorption / desorption isotherms performed in SiO$_2$ powder; values of BET surface area and BHJ pore size analysis are also presented.

The surface area of the SiO$_2$ layer is determined by it porosity and pore size. Considering uniform and spherical pores with diameter d_p, then the surface (S_p) to volume (V_p) ratio is given by:

$$\frac{S_p}{V_p} = \frac{6}{d_p} \qquad (D.1)$$

Assuming that the surface area of the SiO$_2$ layer (A_s) is approximately the surface area of its pores, and the volume of the pores is given by $V_p = \varepsilon \cdot V$, where ε is the

porosity of the SiO_2 layer and V its volume, then the average pore size of the SiO_2 layer is given by:

$$d_p = \frac{6 \cdot \varepsilon \cdot V}{S_p} \qquad (D.2)$$

The porosity of the SiO_2 layer was determined from:

$$\varepsilon = 1 - \frac{\rho_{SiO_2\ film}}{\rho_{SiO_2\ particle}} \qquad (D.3)$$

where $\rho_{SiO_2\ particle} = 2.5$ g·cm^{-3}, $\rho_{SiO_2\ film} = (0.98 \pm 0.03)$ g·cm^{-3}, $\varepsilon = 0.63 \pm 0.09$ and $A_s = 160$ m^2·g^{-1}. The mass was obtained using an analytical balance (Radwag® AS 60/220/C/2).

Table D.1 shows the calculated d_p and minimum TIP pulse time for complete coverage of the SiO_2 porous layer taking into account pore reduction due to the TiO_2 film thickness coated by ALD.

Table D.1 Minimum TIP pulse time, τ_{min}^p, for complete coverage of the SiO_2 porous layer taking into account pore size reduction by the TiO_2 film thickness coated by ALD

TiO$_2$ deposited		d_p / nm	Pore occlusion %	D_k / cm^2·s^{-1}	D_{TIP}/ cm^2·s^{-1}	τ_{min}^p / s
No ALD cycles	thickness / nm					
0	0	21.1	0.0	1.39×10^{-2}	5.97×10^{-3}	17.6
40.0	0.90	19.4	8.30	1.27×10^{-2}	5.48×10^{-3}	19.2
70.0	1.50	18.0	14.6	1.19×10^{-2}	5.10×10^{-3}	20.6
100	2.20	16.7	20.8	1.10×10^{-2}	4.73×10^{-3}	22.2
140	3.08	14.9	29.2	9.83×10^{-3}	4.23×10^{-3}	24.8
150	3.30	14.5	31.3	9.54×10^{-3}	4.11×10^{-3}	25.6
160	3.52	14.1	33.4	9.25×10^{-3}	3.98×10^{-3}	26.3
175	3.85	13.4	36.5	8.82×10^{-3}	3.79×10^{-3}	27.7
200	4.40	12.3	41.7	8.10×10^{-3}	3.48×10^{-3}	30.1

References

A1. J. Dykyj, J. Svoboda, R. C. Wilhoit, M. Frenkel and K. R. Hall, *Vapor Pressure and Antoine Constants for Oxygen Containing Organic Compounds*, Springer Berlin Heidelberg, 2000.